Intrinsic Properties and Fabric Anisotropy of Sands

by

Junxing Zheng

A dissertation submitted in partial fulfillment
of the requirements for the degree of
Doctor of Philosophy
(Civil Engineering)
in the University of Michigan
2017

Doctoral Committee:

      Professor Roman D. Hryciw, Chair
      Associate Professor Adda Athanasopoulos-Zekkos
      Professor Udo Becker
      Professor Radoslaw L. Michalowski

http://orcid.org/0000-0001-9428-3969

junxing@umich.edu

DEDICATION

To my parents, Haisheng Zheng and Qiuping Zhang for their love and support.

ACKNOWLEDGEMENT

I was so lucky to work with Professor Roman D. Hryciw in the last five years. He taught me how to conduct research, how to solve problems, publish papers, write proposals, prepare presentations, interview for a job and how to watch football games. We published many papers in top journals in the geotechnical engineering field. These helped me to obtain prestigious awards including the Rackham Predoctoral Fellowship and the Richard and Eleanor Towner Prize for Distinguished Academic Achievement. I am sure that Professor Hryciw will continue to provide great help and suggestions to my future career and life as my academic father. I have reserved innumerable thanks to him for my future.

I was so lucky to know Professor Radoslaw L. Michalowski, Professor Dimitrios Zekkos, and Professor Adda Athanasopoulos-Zekkos. They taught me various classes which established a solid foundation for my research. They wrote recommendation letters for my various award competitions and job applications. I want to thank Professor Michalowski for inviting me for Thanksgiving dinners. Those moments are my precious memories. Undoubtedly, I am sure that Professor Michalowski, Professor Zekkos and Professor Adda will continue to provide great help and suggestions to my future career and life. I also sincerely thank Professor Udo Becker for being my dissertation committee member. He took time from his busy schedule to attend my Preliminary exam and my dissertation defense, and reviewed my dissertation. I appreciate his help.

I met so many friends in Ann Arbor: Zhijie Wang, Xunchang Fei, Dan Wei, Qianru Guo, Xiaohu Fan, Yao Zhang, Athena Gkrizi and Jonathan Hubler. Because of them, I had a happy five years in Ann Arbor. I wish each of you the best in your future careers!

CONTENTS

LIST OF TABLES

LIST OF FIGURES

x

ABSTRACT

The intrinsic properties and fabric anisotropy of sands significantly affect their macroscopic engineering behavior including packing densities, compressibility and strength. However, due to difficulties in reliably and rapidly determining them, intrinsic properties such as gradation, particle roundness and sphericity as well as the related fabric anisotropy of soils have not received their deserved attention and usage in practice. This dissertation introduces research that has facilitated rapid and precise quantification of soil properties and fabric anisotropy using various newly developed image analysis techniques. Extensive laboratory tests were performed on sands of various gradations, roundnesses, sphericities and geologic origins to develop relationships between their intrinsic properties and macroscopic mechanical behavior. A gradation-shape-fabric based Distinct Element Modeling technique was developed to simulate the properties and fabric anisotropy of soils. Besides geotechnical engineering, the technique can be used by engineers and scientists in various disciplines including material science, geology, mining, powder sciences, pavement engineering and agriculture to simulate more realistic material particle geometries and microstructures.

CHAPTER 1

INTRODUCTION

1.1   Motivation

The engineering behavior of sands depends on both its intrinsic and state properties. Intrinsic properties include particle size distribution, particle shape and mineralogy. State properties include void ratio (particle packing), effective confining stress and fabric. Every sand has a fixed set of intrinsic properties but could be at various states. The intrinsic properties can be thought of as bracketing the range of soil behaviors while state properties control where in this range the soil is found.

Among the intrinsic and state properties, the particle shape and fabric have been found to significantly affect macro mechanical behavior of granular materials such as index void ratios, compressibility, strength, shear wave velocity, liquefaction susceptibility and erosion susceptibility. Previous studies on particle shapes include: Eisma (1965), Holubec and D'Appolonia (1973), Youd (1973), Zelasko et al. (1975), Edil et al. (1975), Sukumaran and Ashmawy (2001, 2003), Yasin and Safiullah (2003), Santamarina and Cho (2004), Cho et al. (2006), Rouse et al. (2008), Bareither et al. (2008), Cavarretta et al. (2010), Cabalar et al. (2013), Shin and Santamarina (2013), Zheng and Hryciw (2016a) and many others. The studies on fabric include: Oda (1972), Arthur et al. (1977), Tatsuoka et al. (1986), Guo (2008), Rodriguez and Lade (2013), Yang et al. (2015), Zeng et al. (2010), Li et al. (2010), Yan and Byrne (1990), Sully and Campanella (1995), Bellotti et al. (1996) and many others.

Despite ample evidence of the importance of particle shape and fabric, those two properties are usually not considered by practicing geotechnical engineers. The main reason is that they are very difficult to determine. For example, one of the particle shape descriptor, roundness, was defined as the ratio of the average radius of curvature of the corners of a

particle to the radius of the maximum inscribed circle (Wadell, 1932). Significant manual effort is needed to find those circles. To facilitate visual estimation of roundness, charts consisting of reference particles were developed by Krumbein (1941), Krumbein and Sloss (1951) and Powers (1953). The chart methods for roundness estimation have been extensively used in many disciplines. However, the subjective nature of chart methods limits its accuracy.

The first objective of this research was to develop image processing techniques to automate the particle shape and fabric determination so that the tedious manual measurements and subjective chart estimations could be eliminated. The image-based methods can accurately and rapidly quantify particle shape and fabric parameters.

The next issue is how to incorporate the shape parameters in geotechnical practice. This was the second objective of the research. Extensive laboratory tests including relative density (packing) and one-dimensional consolidation tests were performed on many soils with various gradations, roundnesses, sphericities and geologic origins to explore the relationship between the intrinsic properties and the macro mechanical behavior of soils including packing and compressibility. Rigorous mathematical formulas were developed based on the laboratory observations. The formulas can be used by geotechnical engineers to more accurately predict soil behavior, decrease uncertainties in geotechnical engineering analyses, make more reasonable designs, save construction costs and promote sustainability.

The intrinsic properties and fabric can also be used in Distinct Element Method (DEM) modeling to simulate more realistic soils. This research developed algorithms to generate realistic particle shapes based on user specified particle size and shape distribution curves and fabric anisotropy. Those distribution curves are either computed from real soil images or created by users. The ability of DEM simulations in parametrical studies will be greatly enhanced through this work. Beside geotechnical engineering, this technique can be used in various disciplines including material science, geology, mining, powder sciences, pavement engineering and agriculture to simulate more realistic material particle geometries and microstructures

1.2   Tasks and organization

This dissertation consists of the following chapters:

Chapter 1 provides a brief introduction of the motivation and objectives for this research.

Chapter 2 is a literature review of the existing efforts on particle shape and soil fabric studies and the DEM simulation.

Chapter 3 develops a computation method to automate particle shape determination.

Chapter 4 explores the effects of particle shapes and gradation on packing and compressibility of granular soils.

Chapter 5 develops a rotational Haar Wavelet Transform technique by simulating the human cognition process to automate soil fabric determination.

Chapter 6 develops a corner preserving technique to generate realistic DEM particles (clumps).

Chapter 7 develops a clump library technique to generate realistic soil specimens based on user-defined gradation, shape and fabric parameters.

Chapter 8 summarizes current research efforts and outlines future research needs.

CHAPTER 2

LITERATURE REVIEW

2.1   Particle shape quantification

Soil particle shape is defined by International Standards (ISO, 2008) as "the envelope formed by all the points on the surface of the particle". Using two-dimensional projections, it may be characterized at three observation levels as shown in Figure 2.1. From largest to smallest scale, particles are described by their: form, roundness and surface texture (ISO, 2008; Barrett, 1980; Mitchell and Soga, 2005). For soil particles, "sphericity" is commonly used for describing form while "roughness" is often used for surface texture. Therefore, in this research, the author will use the common geotechnical terms: sphericity, roundness and roughness. The three are considered to be independent descriptors of particle shape because each can vary with no change in the other two (Wadell, 1932; Barrett, 1980; Cho et al., 2006).
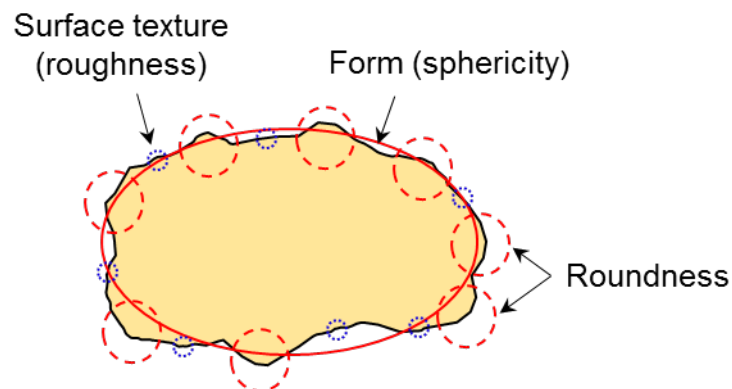
Figure 2.1 Particle shape characterization at different scales (after ISO, 2008; Barrett, 1980; Mitchell and Soga, 2005).

2.1.1 Sphericity

The first description of sphericity for "objects of sedimentological importance" is generally attributed to Wadell (1933). He defined "degree of true sphericity" as "the ratio of the surface area of a sphere of the same volume as the particle to the actual surface area of the particle". Recognizing the difficulty of measuring three-dimensional surface areas of soil particles, Wadell also offered a practical definition based on the projected area of a particle; he defined "degree of sphericity" as the diameter of a circle having an area equal to the largest projected area to the diameter of the smallest circle that will circumscribe the grain projection. Over the years, other definitions of sphericity have been proposed based on two dimensional maximum projections of particles. The five most commonly used definitions as reviewed by Mitchell and Soga (2005) and Rodriguez et al. (2012) are:

Area Sphericity: $$S_A = \frac{A_s}{A_{cir}}$$ Equation 2.1

Diameter Sphericity: $$S_D = \frac{D_c}{D_{cir}}$$ Equation 2.2

Circle Ratio Sphericity: $$S_C = \frac{D_{ins}}{D_{cir}}$$ Equation 2.3

Perimeter Sphericity: $$S_P = \frac{P_c}{P_s}$$ Equation 2.4

Width to Length Ratio Sphericity: $$S_{WL} = \frac{d_2}{d_1}$$ Equation 2.5

where:

A_s = projected area of a soil particle,

A_{cir} = area of the minimum circumscribing circle,

D_c = diameter of a circle having the same projected area as the particle,

5

D_{cir} = diameter of the minimum circumscribing circle,

D_{ins} = diameter of the largest inscribing circle,

P_c = perimeter of circle having the same projected area as the particle,

P_s = perimeter of the particle,

d_1 and d_2 = length and width of a particle.

Volume based sphericity definitions, such as proposed by Wadell (1933) also exist but they are not used in this section since the soil particles are being characterized strictly from two-dimensional projections.

Area sphericity was first proposed by Tickell (1931). Diameter sphericity is Wadell's (1933) original "degree of true sphericity". The area sphericity is the square of diameter sphericity. Riley (1941) defined $\sqrt{D_{ins}/D_{cir}}$ as sphericity which later evolved into S_c by Equation 2.3 in papers by Santamarina and Cho (2004), and Cho et al. (2006). Similarly, Cox (1927) defined sphericity by $(P_c/P_s)^2$ which evolved into S_P by Equation 2.4 in the works of Kuo and Freeman (2000) and Altuhafi et al. (2013). The S_P is identical to "circularity" in ISO (2008). For historical accuracy, neither Tickell (1931) or Cox (1927) actually used the term "sphericity"; in the pre-Wadell era, they used the term "roundness" for today's "sphericity". Krumbein and Sloss (1951) hinted that "sphericity could be related to the proportion between length and breadth of the particles". The author believes that Krumbein and Sloss must have had Equation 2.5 in mind. The reciprocal of S_{WL} is commonly referred to as "elongation ratio".

2.1.2 Roundness

Roundness quantifies the sharpness of particle corners. It was first distinguished from sphericity by Wadell (1932, 1933, 1935). Using two-dimensional projections of particles, Wadell defined roundness as the ratio of the average radius of curvature of the corners of a particle to the radius of the maximum inscribed circle:

$$R = \frac{\sum_{i=1}^{N_c} r_i \Big/ N_c}{r_{ins}}$$

Equation 2.6

where r_i is the radius of the i-th corner circle; r_{ins} is the radius of the maximum inscribed circle; and N_c is the number of the corners around particle perimeter.

This definition of roundness is still widely used today (Santamarina and Cho, 2004; Mitchell and Soga, 2005; Cho et al., 2006; Bareither et al., 2008; Chapuis, 2012; Shin and Santamarina, 2013; Cabalar et al., 2013). The original procedure for determination of Wadell's roundness requires considerable manual effort. Each corner on a particle's outline is compared to a series of transparent templates to find the maximum sized circle that will fit inside the corner. Despite being cumbersome and subjective, the procedure is still used today (Moroto and Ishii, 1990; Rouse et al., 2008; Oh et al., 2014).

2.1.3   Chart Methods for Roundness and Sphericity

In the 1950's, charts consisting of a set of reference particle silhouettes were prepared to facilitate rapid estimation of Wadell's particle roundness through visual comparisons to particles viewed under a microscope. Three such charts were developed by Krumbein (1941), Krumbein and Sloss (1951), and Powers (1953) as shown in Figures 2.2, 2.3 and 2.4.
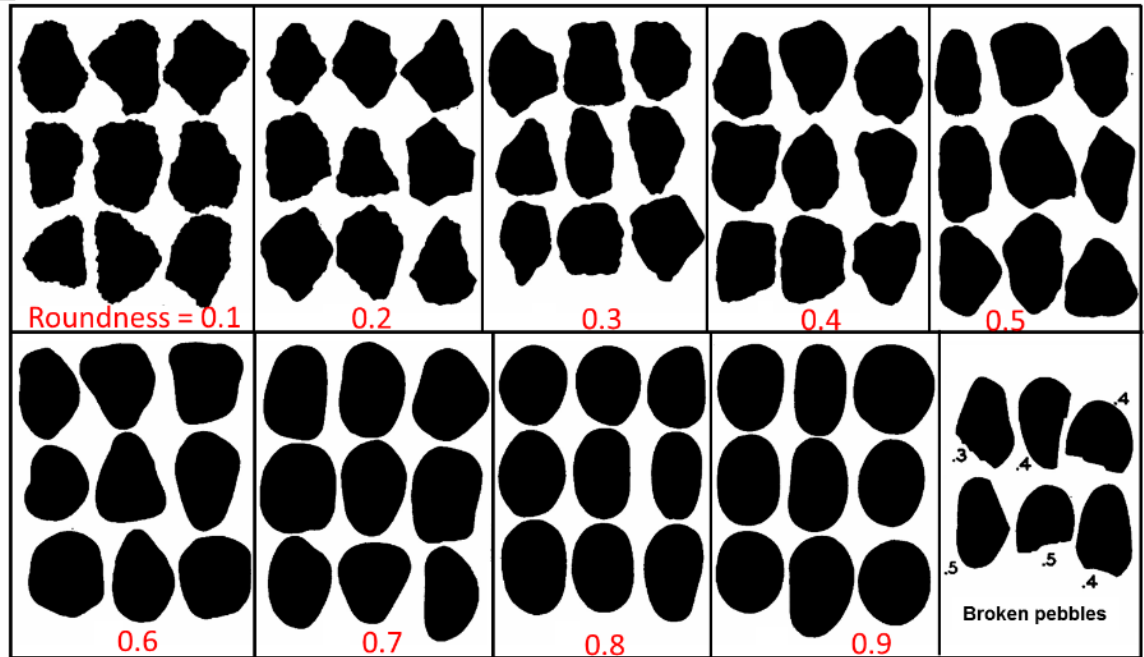
Figure 2.2 Chart for estimating particle roundness (after Krumbein, 1941)
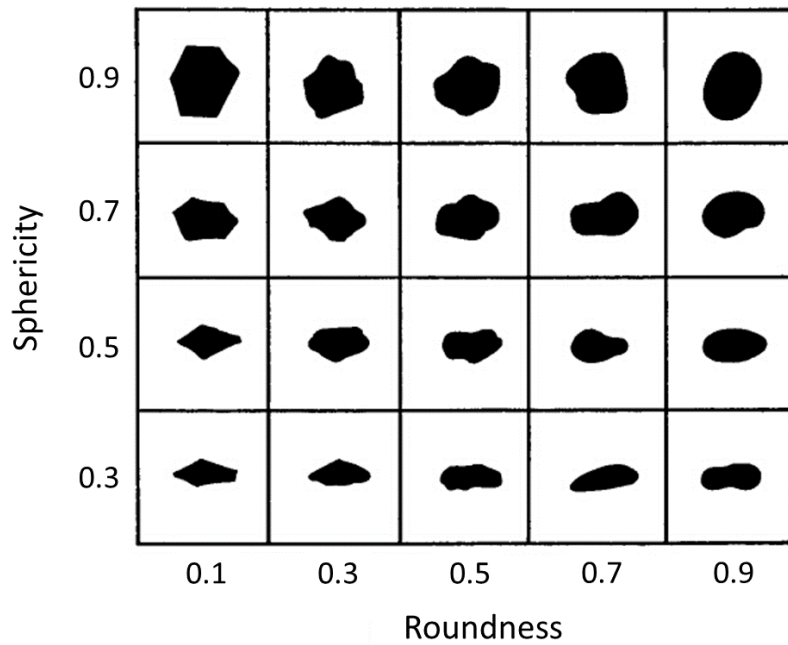
Figure 2.3 Chart for estimating particle roundness and sphericity (after Krumbein and Sloss, 1951)
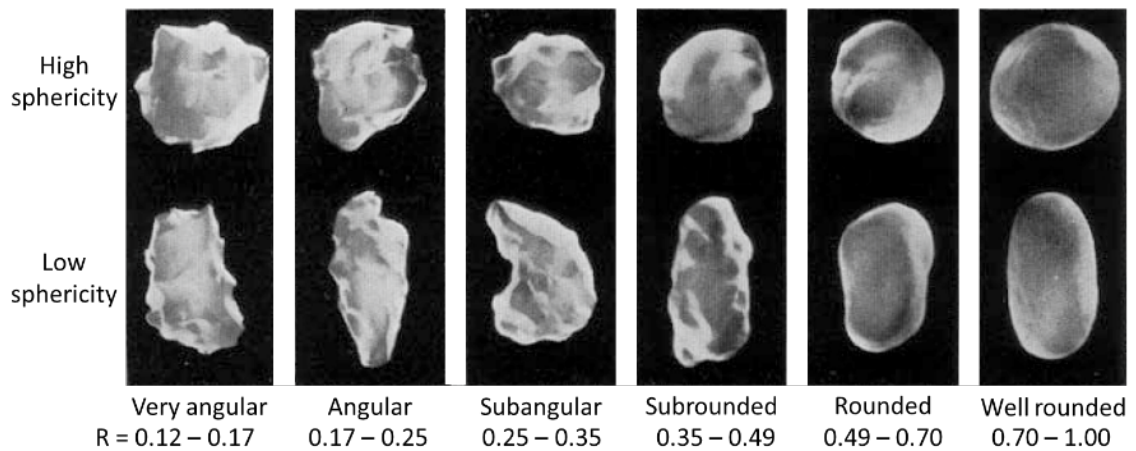
Figure 2.4 Chart for estimating particle roundness (after Powers, 1953)

The Krumbein (1941) chart, shown in Figure 2.2, contains 81 particles redrawn from pebbles for which R had been determined by Wadell's method. Krumbein placed the particles in 9 bins with R ranging from 0.1 to 0.9 in increments of 0.1. Several broken particles are also shown in the figure to indicate the effects of breakage on R. Compared with the other two charts, Krumbein's provides more reference particles and thus more opportunities for visual comparisons.

The Krumbein–Sloss (1951) chart, shown in Figure 2.3, provides 20 reference particles having S from 0.3 to 0.9 and R from 0.1 to 0.9, both in increments of 0.2. The Krumbein–Sloss chart pointed out that R and S are independent parameters because one could vary without change in the other. The Krumbein–Sloss chart may be the most widely used chart because it provides an opportunity to simultaneously estimate both R and S.

The Powers (1953) chart separates soil particles having Wadell roundness values from 0.12 to 1.00 into six classes, as shown in Figure 2.4. The ratio of the upper limit to the lower limit of R in each class is approximately 1.4. Each R range is exemplified by two particles: one with high S and one with low S. The Powers chart may have inspired the word descriptions of R in the current ASTM D2488 (ASTM 2009).

Obviously, the charts are even more subjective than Wadell's original template method. Nevertheless, they are used in many disciplines including geotechnical engineering, soil science, agriculture, powder engineering, pavement engineering and geology. Studies have compared the effects of soil particle shape and roundness as obtained from the charts on the macroscale properties and mechanical behavior of soil (Youd, 1973; Edil et al., 1975; Frossard, 1979; Sladen et al., 1985; Santamarina and Cho, 2004; Bareither et al., 2008; Chapuis, 2012; Shin and Santamarina, 2013; Cabalar et al., 2013; Kandasami and Murthy, 2014). In geomorphology, Eisma (1965) studied the influence of roundness of beach and dune sands on eolian sorting. Sagga (1993) assessed the roundness of sand grains in longitudinal dunes in Saudi Arabia. Mehring and McBride (2007) used the charts in studies on the origin of beach sands. Vepraskas and Cassel (1987) studied the influence of sphericity and roundness of coastal plain sands on soils' resistance to cone penetration, to bulk density, and on the angle of repose of dense sands. In all of the above mentioned research, roundness was determined using the charts. The charts have also been used for comparison to other roundness descriptors such as proposed by Masad et al. (2007) and Sukumaran and Ashmawy (2001).

2.1.4 Optical method for roundness and sphericity

Advances in optical image gathering have led to rapid digitization of soil particle projections and created a potential to automate Wadell's procedure. It has nevertheless been a mathematically challenging problem and thus, researchers have proposed alternative definitions of roundness which could be more easily computerized. Such alternate definitions have included: Fourier analysis (Bowman et al., 2001; Wettimuny and Penumadu, 2004; Wang et al., 2005), angularity index (Sukumaran and Ashmawy, 2001; Tutumluer and Pan, 2008), and a fractal technique (Arasan et al., 2011). A comprehensive review of these newer methods was provided by Masad et al. (2007). However, the alternative definitions of roundness have not yet prevailed over Wadell's due to the latter's longer history and numerous useful correlations to mechanical properties based on it. In light of its continuing popularity and wide usage, the first objective of this research is to develop an algorithm, based on computational geometry and statistics, to automate a rigorous and non-subjective determination of roundness according to Wadell's definition.

2.1.5 Surface Roughness

At the smallest observation scale, we have surface roughness. Surface roughness is a scale depend problem. All surfaces are rough even down to the atomic scale. In general, instruments with different resolutions and scan lengths will yield different roughness values for the same surface (Majumdar and Bhushan, 1990). Given measurements at a specific scale, the deviations of a surface from its mean plane are commonly used to characterize the roughness at the given scale. Such deviations are usually quantified by a *root mean squared roughness* (Otsubo et al., 2015; Alshibli and Alsaleh, 2004):

$$Roughness = \sqrt{\frac{1}{N}\sum_{i=1}^{N}\left(Z_i\right)^2} \qquad \text{Equation 2.7}$$

where N is the total number of data points; Z_i is the elevation of data point i relative to the reference surface.

2.2 Effects of Intrinsic properties on mechanical behavior of granular soils

It has been well-observed that the particle shape significantly affecting macro mechanical behavior of granular materials such as index void ratios, compressibility, strength, shear wave velocity, liquefaction susceptibility and erosion susceptibility. Some typical studies include: Eisma (1965); Holubec and d'Appolonia (1973); Youd (1973); Zelasko et al. (1975); Edil et al. (1975); Vepraskas and Cassel (1987); Sukumaran and Ashmawy (2001, 2003); Yasin and Safiullah (2003); Santamarina and Cho (2004); Cho et al. (2006); Guo and Su (2007); Rouse et al. (2008); Bareither et al. (2008); Cavarretta et al. (2010); Cabalar et al. (2013); Shin and Santamarina (2013); Zheng and Hryciw (2016) and many others.

2.3 Soil fabric

Soil particles that have been deposited through water generally align their largest projected surface area normal to the depositional direction. As such, cross anisotropic fabric

commonly develops in alluvial, coastal and lacustrine deposits. Accordingly, such geomaterials exhibit cross anisotropic mechanical and hydrologic behavior.

Anisotropic strength and dilation of sands have been studied in the laboratory by Oda (1972), Arthur et al. (1977), Tatsuoka et al. (1986), Guo (2008), Rodriguez and Lade (2013) and Yang et al. (2015). These studies showed that the friction angle of sands will typically vary by 4° to 16° depending on the angle between the loading direction and direction of deposition. Additionally, Oda et al. (1978) and more recently Azami et al. (2009) observed that bearing capacity was 25-34 % higher when the loading was in the deposition direction (normal to the fabric plane). Zeng et al. (2010) and Li et al. (2010) found that the fabric anisotropy strongly affects the deformation of retaining walls and settlement of its backfill. Yu et al. (2013) simulated seismic loading in centrifuge tests on sands with different deposition angles and found that specimens prepared at larger deposition angles were more vulnerable to liquefaction. Yan and Byrne (1990) and Sully and Campanella (1995) observed that fabric anisotropy significantly affects shear wave velocity. Bellotti et al. (1996) found that shear modulus, constrained modulus and elastic modulus are 20-30% higher for loading in the deposition plane than in the deposition direction.

In soil constitutive modeling, fabric is quantified by a fabric tensor. A popular tensor was developed for anisotropic fabric by Oda and Nakayama (1989). Oda and Nakayama's fabric tensor has been extensively used for formulation of anisotropic failure criteria and for investigation of anisotropic macro behavior of granular soils by Li and Dafalias (2002, 2004), Dafalias et al. (2004), Yang et al. (2008), Gao et al. (2010), Gao and Zhao (2012) and others. The Oda and Nakayama tensor was also used to describe the anisotropic behavior of pavement materials in the works of Masad et al. (2002, 2005), Tashman et al. (2005), Saadeh et al. (2007), Zhang et al. (2011) and others. The Oda and Nakayama fabric tensor will also be utilized in this research.

The Oda and Nakayama fabric tensor can be computed from the distribution of branch vectors, from contact normals, from void orientations or from particle long axes (Oda and Nakayama 1989; Fonseca et al. 2013). The distribution of particle long axes is most commonly used because they are relatively easy to determine visually. For example, Oda

and Nakayama (1989) injected glue into the pores of soil specimens which were then cut into thin sections. They manually recorded the particles' long axis orientations to determine the fabric tensor. Kuo et al. (1998), Yang et al. (2008) and Fonseca (2013) also used resin and cut specimens into thin sections but used an image thresholding technique to distinguish the particles from the resin. Such image thresholding greatly facilitates the fabric characterization but the resin must be chosen to create a high-contrast background. Therefore, this method can only be used on soils having coloration different from the matrix resin and under well-controlled laboratory conditions that allow the resin to be injected and solidified.

2.4   Realistic DEM particle generation

The Discrete Element Method (DEM) has become the preeminent numerical tool for study of granular material behavior. Typical DEM models use circular or spherical particles mainly due to the simplicity of contact detection and force calculations. However, such oversimplified particulate models cannot provide adequately accurate insight to the mechanical behavior of granular assemblies. Methods to better simulate irregular particle shapes for use in DEMs have therefore been sought. The use of ellipsoids (Lin and Ng, 1997; Mustoe and Miyata, 2001; Ouadfel and Rothenburg, 2001; Ng 2009; Fu and Dafalias, 2010), spherical cylinders (Pournin et al., 2005), pentagons (Azéma et al., 2007), rounded-cap elongated rectangles (Azéma et al., 2010), polyhedrons (Azéma et al., 2009; Galindo-Torres and Pedroso, 2010), and Non-Uniform Rational Basis Splines (NURBS) (Andrade et al., 2012) have led to some progress but these are all still idealized particle shapes. Another approach has used bonded non-overlapping spheres (or circles) or clumps of overlapping spheres (or circles) to create various particle shapes. Such approaches simulate real particle shapes while maintaining the ease of contact detection and force calculation.

Bonded non-overlapping spheres were originally used in the simulation of rocks (Potyondy, 2012). Wang et al. (2007) used this concept to render real particle shapes. As shown in Figure 2.5, an irregular particle is filled with small spheres, then adjacent small spheres are replaced by larger spheres to reduce the overall number of spheres. However, it is difficult

to determine the size of the small spheres to be used in the initial arrangement. Especially for angular particles, the spheres must be small enough to model sharp corners. This method will result in rough or "bumpy" surfaces which are relatively crude approximations of the real surface. Therefore, this non-overlapping method is rarely used today for simulation of soil particles.

(a) (b) (c)
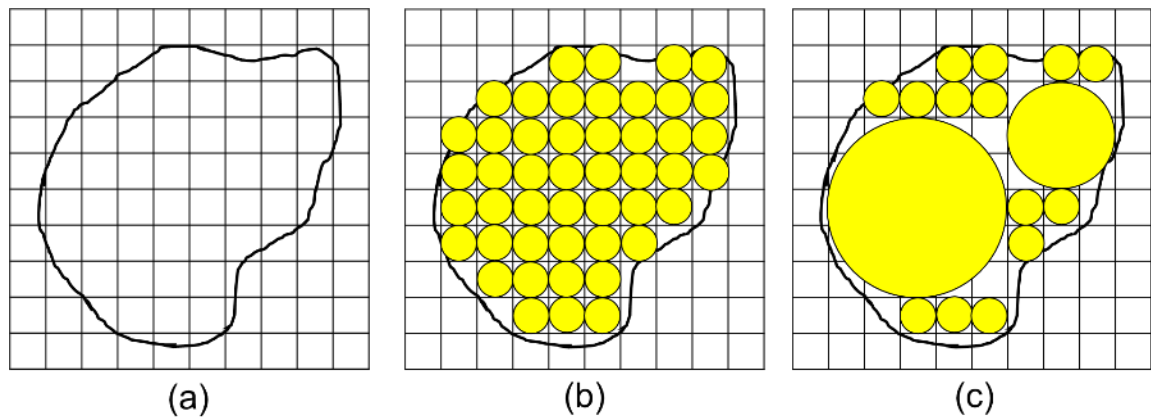
Figure 2.5 Bonded non-overlapping circles on a two-dimensional irregular shape

Clumps of overlapping spheres are currently the most widely used method to model real soil particles. The contacts between overlapped spheres are ignored and the clumps behave as rigid bodies. Since DEM computational load increases markedly with increasing numbers of spheres, the challenge is to generate clumps using a minimum number of spheres that will still effectively reproduce particle shapes. Many techniques have been developed to generate clumps such as by Matsushima et al. (2009), Ferellec and McDowell (2010), and Taghavi (2011). The Ferellec-McDowell and Taghavi methods are the most recently proposed and have become most popular. Therefore, they are described in the following section.

Ferellec and McDowell (2010) presented a conceptually simple method to generate clumps. From a randomly chosen point on the outline of the particle as shown in Figure 2.6, a circle is expanded internally along a normal to the outline. The circle is expanded to the maximum

extent possible within the particle boundary. The procedure is repeated for other points along the particle outline. For a particle surface with a dense point spacing, this method will generate thousands of circles. The majority of the circles are redundant. Therefore, Ferellec and McDowell introduced three parameters to limit the number of generated circles: the minimum distance between a surface point and the circle surface, d_{min}, a minimum radius for any circle, r_{min}, and the percentage of points used to generate the circles, p_{max}. This method involves considerable computational effort due to redundant circle generation and iterative expansion of circles within the soil particle perimeter.
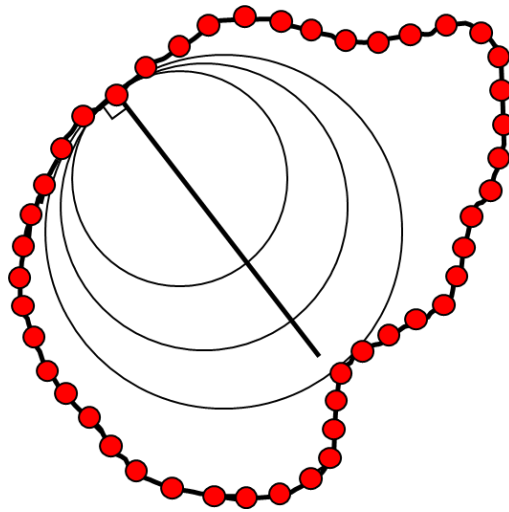
Figure 2.6 Clump generation by Ferellec and McDowell (2010)

Another limitation of Ferellec and McDowell's algorithm is that the three parameters d_{min}, r_{min}, and p_{max} will vary with particle size, particle shape, and image magnification. Thus, these parameters cannot be universally applied to all of the particles in a specimen. Both d_{min} and r_{min} are in distance units. Therefore, the two parameters will vary with the particle size: both d_{min} and r_{min} should be large for large particles and small for small particles. The d_{min} and r_{min} should also be based on particle angularities. For angular particles, both d_{min} and r_{min} must be small enough to capture small and sharp corners. For rounded particles, r_{min} should be set larger to limit the number of redundant small circles generated. The p_{max}

will be affected by image magnification. For the same particle, if it is captured under high magnification, its perimeter will contain more points (or pixels) and vise verse. Therefore, p_{max} should be set larger for high magnification particle images.

Taghavi (2011) proposed a "Bubble Packing" algorithm, which has been integrated into the widely used DEM software Particle Flow Code (PFC) program by Itasca (2015). Therefore, this bubble packing algorithm has gained great popularity in recent years. Given an irregular particle shape such as shown in Figure 2.7(a), a Delaunay tetrahedralization is firstly built in Figure 2.7(b). For each tetrahedron, its circumscribed sphere is computed as shown in Figure 2.7(c). This will generate a large number of spheres. Two parameters are defined to reduce the number of spheres: the circle to circle intersection angle φ as shown in Figure 2.7 and the radius ratio of smallest to the largest sphere ρ. Both φ and ρ are unitless and therefore independent of particle size and image magnification. However, ρ will be significantly affected by particle angularity. For angular particles with small and sharp corners, ρ must be set small enough to capture the corners. For rounded particles, ρ should be large to reduce the number of circles in the clumps. The angle φ essentially controls the clump smoothness. If φ is too small, the generated clump will have a bumpy surface. If φ is too large, an excessive number of unnecessary circles will be generated.
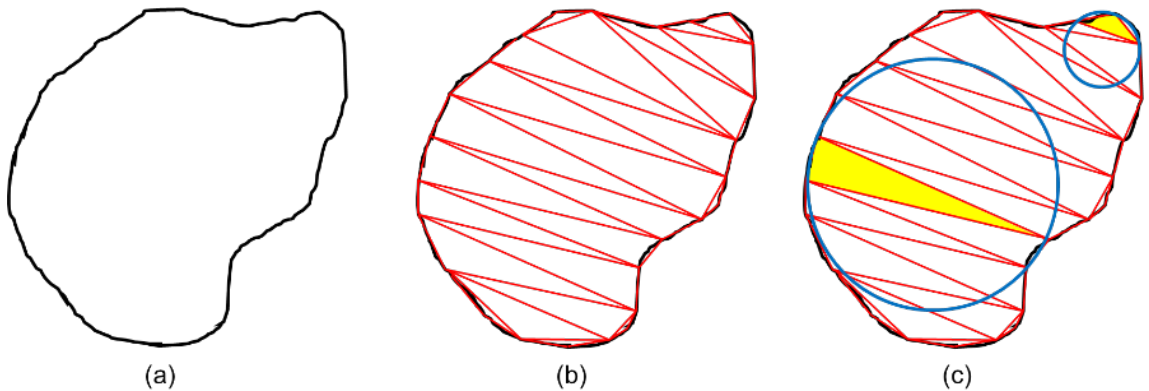
Figure 2.7 Tetrahedralization of a particle (after Taghavi, 2011)
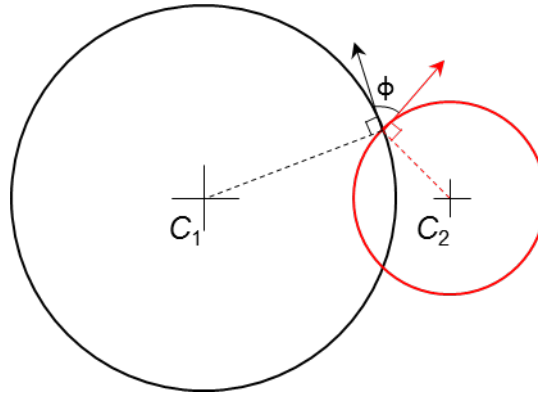
Figure 2.8 Definition of circle to circle intersection angle φ (after Taghavi, 2011)

The two just described methods are similar in that a large number of potential circles are first generated through considerable computational effort. Then, multiple parameters must be defined to restrict the number of circles used to generate the clumps. However, these parameters will vary from particle to particle depending on particle size, angularity and magnification. Therefore, for a soil with a wide range of particle sizes and angularities, user interaction is needed to tune the parameters until optimal values are found for each specific clump. Considerable effort is needed to create many clumps. Therefore, a method is sought that would automatically create many clumps at the same time for a specimen containing a range of particle sizes and angularities without the need to tune the parameters for each clump.

Another limitation of existing methods is the lack of a comparison mechanism to evaluate how accurately the generated clumps simulate or reflect the original soil particles. Figure 2.9(a) displays an example particle. By tuning φ and ρ, a series of clumps were generated, as shown in Figures 2.9(b) to 2.9(h), using the bubble packing algorithm. The displayed value N is the number of circles in each clump. The surface of the clumps is gradually simplified as the number of circles decreases although some of the simplifications are not distinguishable by eye. Nevertheless, users must choose a clump model that they feel represents the original particle with sufficient accuracy. It is a subjective process. Therefore, a criterion to automatically quantify clump accuracy would be desirable and should be integrated into the clump generation algorithm.
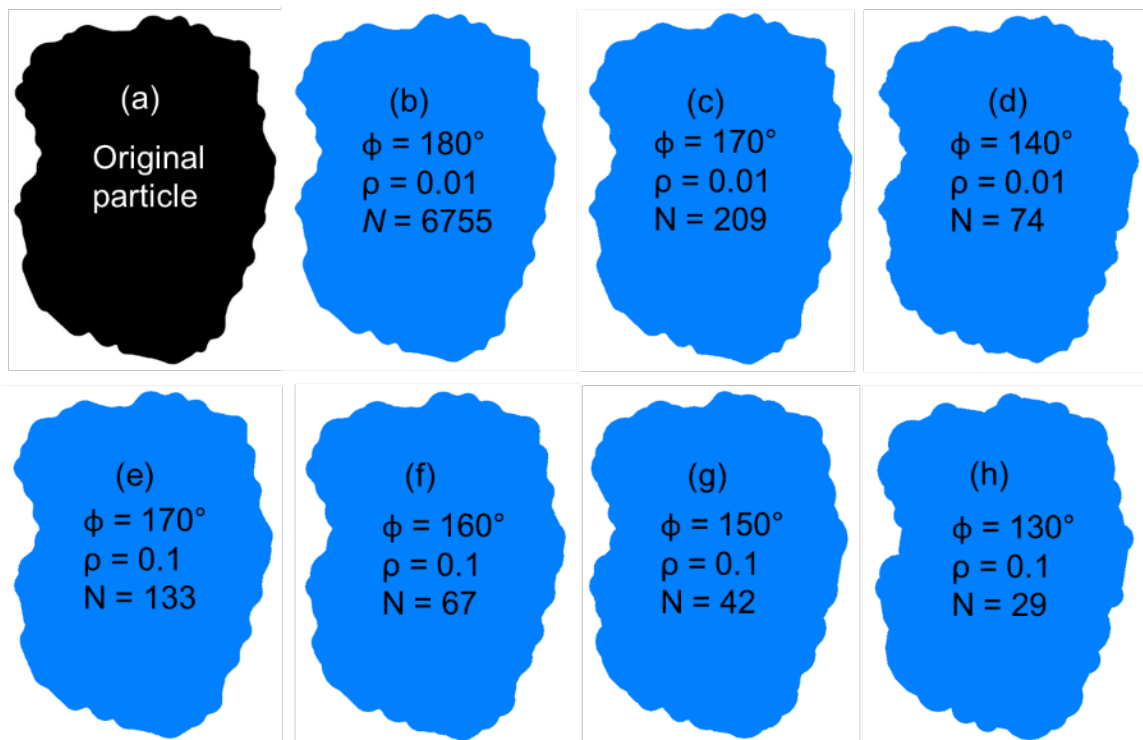
Figure 2.9 Clumps generated by varying φ and ρ in the bubble packing algorithm

CHAPTER 3

PARTICLE SHAPES BY COMPUTATIONAL GEOMETRY

3.1 Introduction

Definitions of soil particle sphericity, roundness and roughness have existed since at least the 1930s. In the 1950s, charts of typical sphericity and roundness values (Krumbein, 1941; Krumbein and Sloss, 1951; and Powers, 1953) were developed to alleviate tedious manual determination. They allowed users to classify particles by visual comparison to typical particles possessing ranges of sphericity and roundness. The original definitions and somewhat subjective chart methods are still widely used today. This chapter describes robust numerical methods based on computational geometry to determine precisely the traditional particle shape definitions from two-dimensional images of particles. The computational geometry method eliminates the need to use Wadell's manual method and approximations based on the chart method.

3.2 Sphericity by Computational Geometry

A computational geometry technique is developed to automate the computation of five commonly used sphericity definitions (Equations 2.1 to 2.5). The area and perimeter of a soil particle can be easily determined in Matlab, the image processing package from MathWorks (2016). However, the minimum circumscribing circle; the maximum inscribing circle; the particle length and width must be determined through additional "computational geometry" as follows.

The outline of a soil particle can be discretized as shown in Figure 3.1(a). The process of finding the minimum circumscribing circle is shown in Figures 3.1(b), 3.1(c) and 3.1(d).

First, the minimum number of *outer points* which when connected will bound all of the others is found. This is shown by the eight points in Figure 3.1(b). The two points which are farthest from each other such (#1 and #5) define the diameter of a trial circle as shown in Figure 3.1(c). If all of the other points are within this circle, then this is the minimum circumscribing circle. If not, the point which lies furthest outside of the circle (#7) is added to the first two points and a new circle is fitted to the three points (#1, #5 and #7). If all the other points are within this circle, this is a minimum circumscribing circle. If not, the point which lies furthest outside of the circle is added and a new circle is found using any two or three of the four points. The procedure is repeated until no points lie outside the circle. This yields the minimum circumscribing circle for the original set of points as shown in Figure 3.1(d).

The measurements of length and width of soil particles in this chapter mimics the procedure of ASTM D4791-10 and ASTM D2488-09a. Conceptually, the soil particle is circumscribed by a rectangular bounding box. Trial boxes with orientations ranging over 180 degrees are fitted to circumscribe the eight outer points as shown in Figures 3.1(e) through 3.1(h). The box that displays the largest single dimension (Figure 3.1(f)) defines both the length and width of the particle.
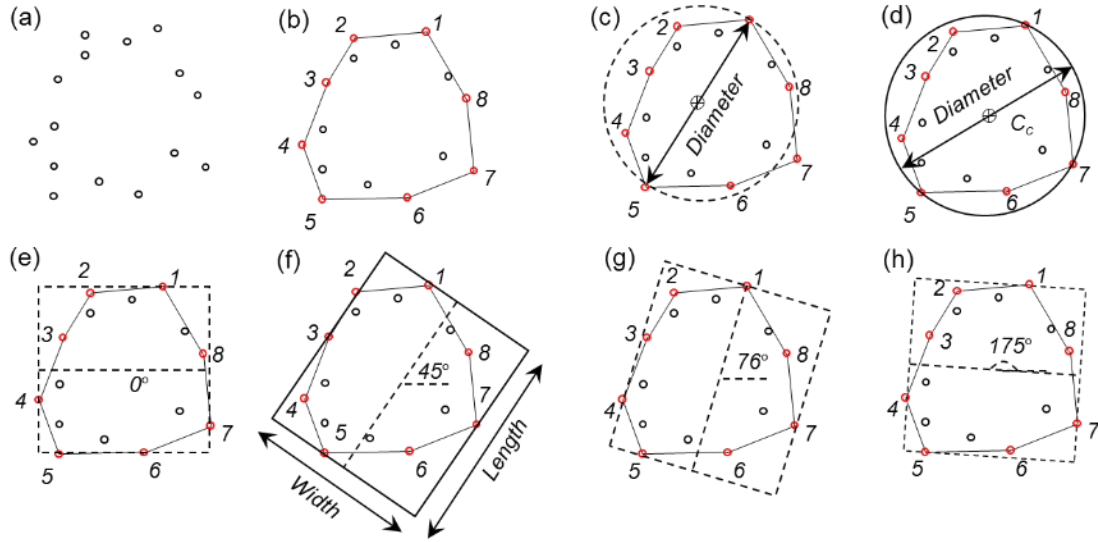
Figure 3.1 Finding the minimum circumscribing circle, length and width of a particle.

The maximum inscribed circle may be determined using a *Euclidean Distance Map*. For each pixel inside the soil particle in Figure 3.2(a), the distance to the nearest boundary pixel is computed resulting in the Euclidean distance map is shown in Figure 3.2(b). The largest distance value and its location identify the radius, R_i, and the center of the maximum inscribed circle, C_i, as shown in Figure 3.2(b). The results (in pixel units) are summarized in Figure 3.2(c).
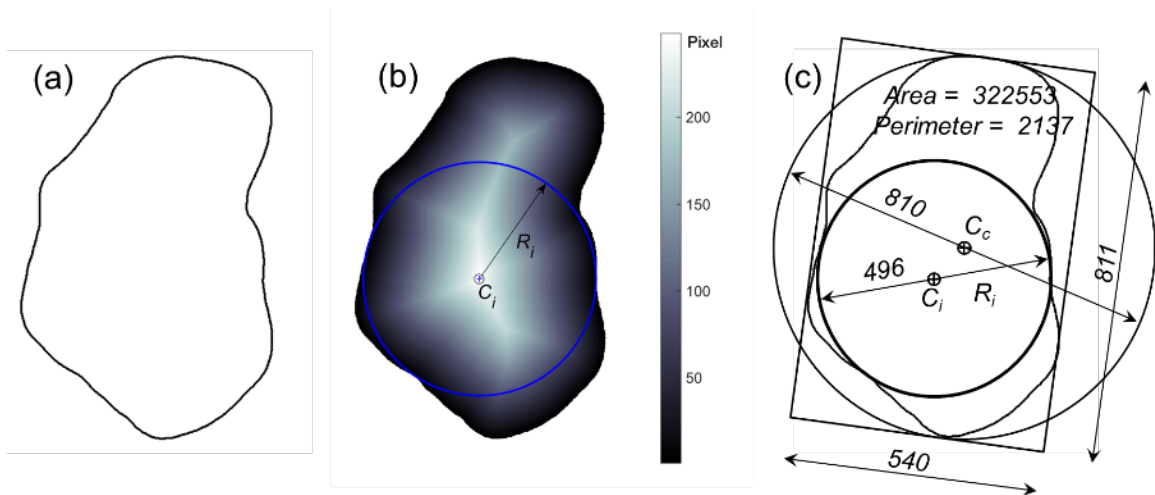
Figure 3.2 Finding the maximum inscribed circle of a soil particle: (a) particle outline; (b) Euclidean distance map; (c) result in pixel units.

3.3 Surface Roughness by Computational Geometry

To quantify surface roughness using Equation 2.7, the mean surface must be determined in prior. However, because of highly irregular soil particle surfaces, there is generally no functional form to describe the mean surface. This problem can be addressed by nonparametric fitting techniques. Such techniques fit a smooth curve to the measured points without any prior specification of a functional relationship between the points. One of the most popular nonparametric smoothers is "locally weighted scatter plot smoothing" (LOESS) which was proposed by Cleveland and Devlin (1988). An example of the LOESS procedure in shown in Figure 3.3. In Figure 3.3(a), a mean surface was assumed to be defined by the arbitrary function: $y = 2 - \cos(0.6x) - \sin(0.6x) - \cos(1.2x) - \sin(1.2x)$. Over the X-range shown in Figure 3.3(a), the function could be representing a corner of a subangular soil particle. The authors added Gaussian noise around the mean surface to generate a "rough" surface. The "roughness" could be actual particle roughness or digital rounding to pixels or simply electrical noise in the measurement system (e.g. camera, scanner or profilometer). In any case, the open circles in Figure 3.3(a) represent an instrument's measurements of this surface. The measurement could be optical or

22

physical and they could be at any scale depending on the instrument used. The measurement interval depends on the resolution of the instrument at this scale. The actual mean surface is now presumed to be unknown. The goal of LOESS is to predict the mean surface from the rough measurements.
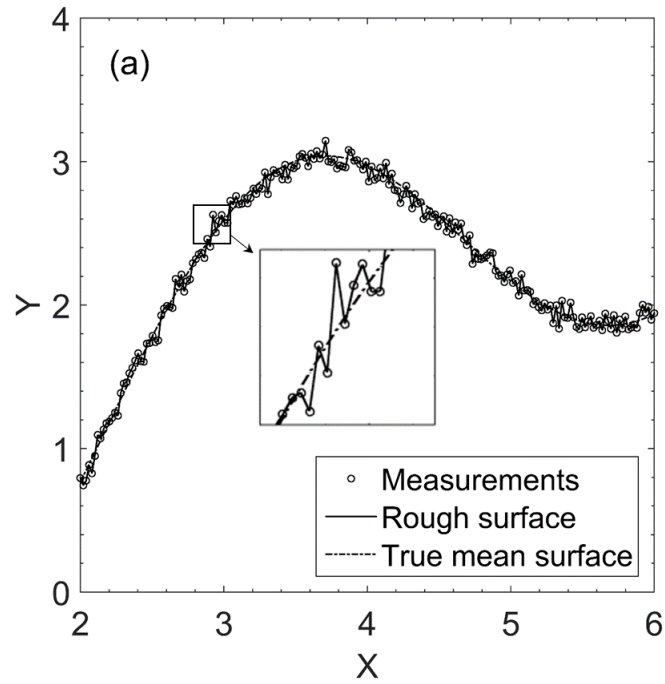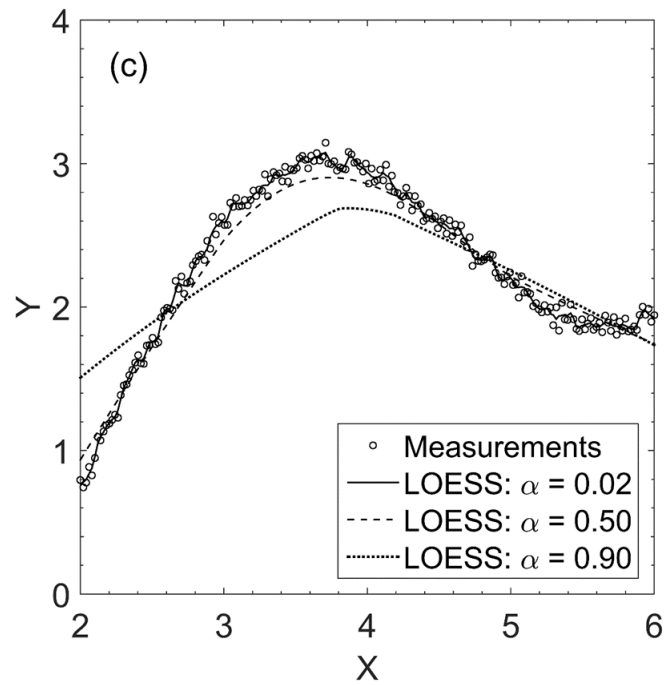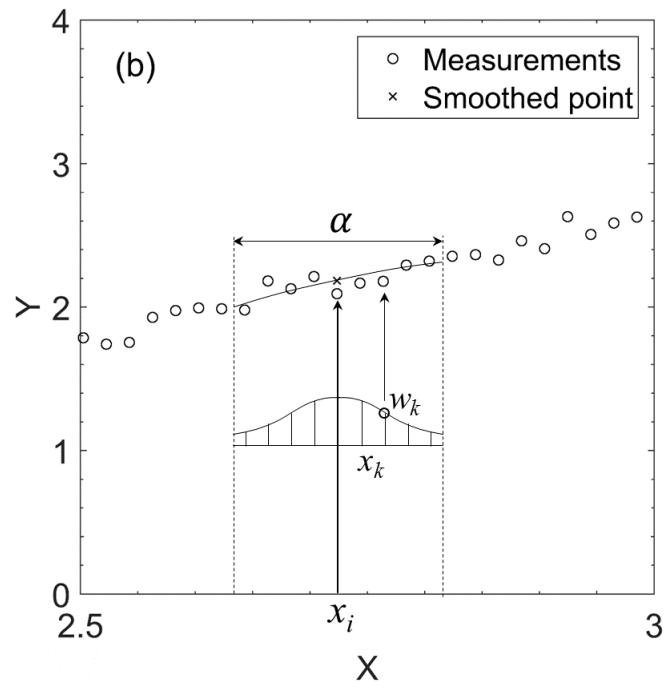
Figure 3.3 The LOESS procedure and results by various α values.

LOESS replaces each data point with the smoothed value determined by a locally weighted regression. Figure 3.3(b) shows how a smoothed value is found for a point x_i located between $X=2.5$ and $X=3.0$. The point x_i and its nearest neighboring points over a span distance α are used in the process. The span α is the ratio of the number of data points used for fitting to the total number of data points. Therefore, α is a value between 0 and 1.0. In this example, there are a total of 200 measurement points in a range between $X=2.0$ and $X=6.0$. If $\alpha=0.045$ then 9 points would be used for each smoothing. For each point in the span, a weight is applied based on its distance to the center point x_i. For example, the weight for the k-th point in Figure 3.3(b) could be:

$$w_k = \exp\left(-\frac{(x_i - x_k)^2}{2\alpha^2}\right)$$
Equation 3.1

The function is plotted in Figure 3.3(b). It shows that points closer to x_i have larger weights and therefore more influence on the fitting.

After applying weights to the data points in the span, a second-degree polynomial is fitted to the points using least-square regression. The smoothed value at point x_i will be given by the weighted regression as shown in Figure 3.3(b). This smoothing process progresses from data point to data point to obtain the smoothed value of each point. Clearly, the computed smoothed values will be affected by the specified α. Figure 3.3(c) shows three LOESS curves that were fitted to the same measured data with α having been varied from 0.02 to 0.90. It is evident that small α values could not filter out the roughness while large α values yield curves that fail to follow the local curvilinearity. The selection of an appropriate α must compromise between the "over-fitting" and "under-fitting" to produce a LOESS curve which is as close as possible to the mean surface. A strategy for finding the proper α follows.

The optimal α value can be determined by cross-validation techniques (Efron and Tibshirani, 1993). Cross-validation is essentially a trial and error approach. A total of say N different α values are tested one by one. The α producing the minimum fitting error is the optimum. A popular cross-validation technique is called *K-fold cross-validation*. The procedure is diagramed in Figure 3.4. All of the measured data points defining a particle's

outline are randomly partitioned into K roughly equal-sized sets. As shown by the rows in Figure 3.4, each of the sets will, in turn, be used as a validation set while the remaining sets are training sets. For example, in the k-th row, the k-th set is the validation set while the others are training sets. The data from all of the training sets is fitted with a LOESS curve which is defined by the α-value being tested. The validation set is then used to calculate a residual error for this LOESS curve. For the i-th α value and the k-th row it is $\varepsilon_k(\alpha_i)$. This process is repeated K times for $k = 1, 2, \ldots K$. The error for each tested span α_i is then calculated as the Average Residual Error (ARE) of $\varepsilon_k(\alpha_i)$:

$$\hat{\varepsilon}(\alpha_i) = \frac{1}{K}\sum_{k=1}^{K}\varepsilon_k(\alpha_i)$$

<div align="right">Equation 3.2</div>

The α with the minimum $\hat{\varepsilon}$ is the optimal span value. A series of K values was tried in this study. The results showed that $K = 10$ is adequate for soil particle roughness analysis.
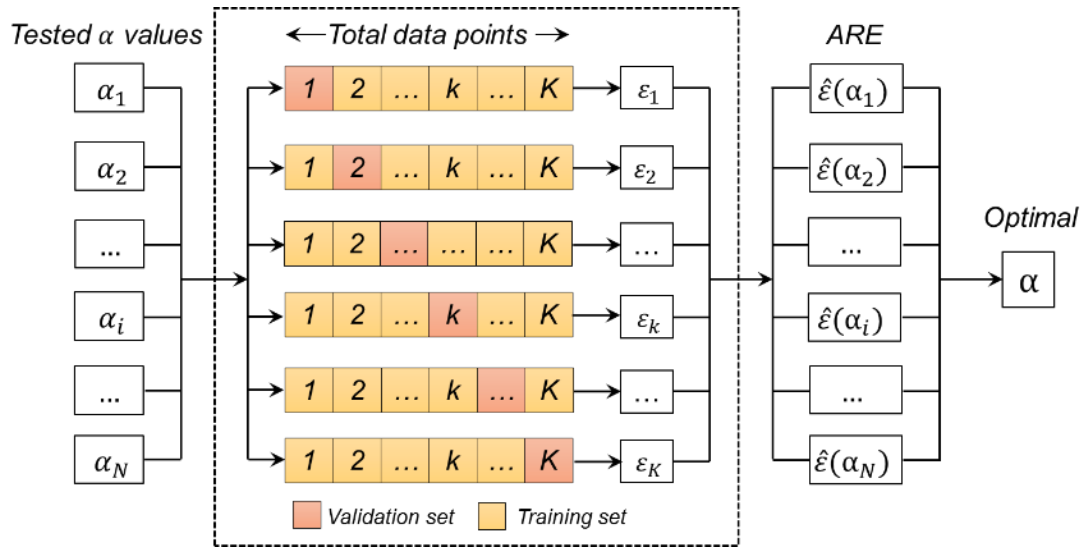
Figure 3.4 Procedure for K-fold cross-validation.

Back to the example given in Figure 3.3, in order to find the optimal α, a series of values from 0.01 to 0.99 with increments of 0.0098 (a total of 100 α values) were evaluated using 10-fold cross-validation. A total of 200 data points were randomly divided into 10 sets.

Each set contained 20 points. For every tested span α_i (i = 1, 2,…, 100), a training set containing 180 data points was fitted by a LOESS curve as shown in Figure 3.5(a). The validation set, consisting of the remaining 20 points was then used to compute the residual error. This process was repeated 10 times for each α_i to obtain its average residual error $\hat{\varepsilon}(\alpha_i)$. The optimal α was found to be 0.3367 based on the minimum ARE. Using $\alpha = 0.3367$, the LOESS curve is fitted using all of the measurements. The result is shown in Figure 3.5(b). The LOESS curve overlaps the true mean surface almost perfectly. The largest discrepancy between the two curves is 0.001. In summary, provided the roughness measurements, LOESS combined with K-fold cross-validation effectively predicts the mean surface.
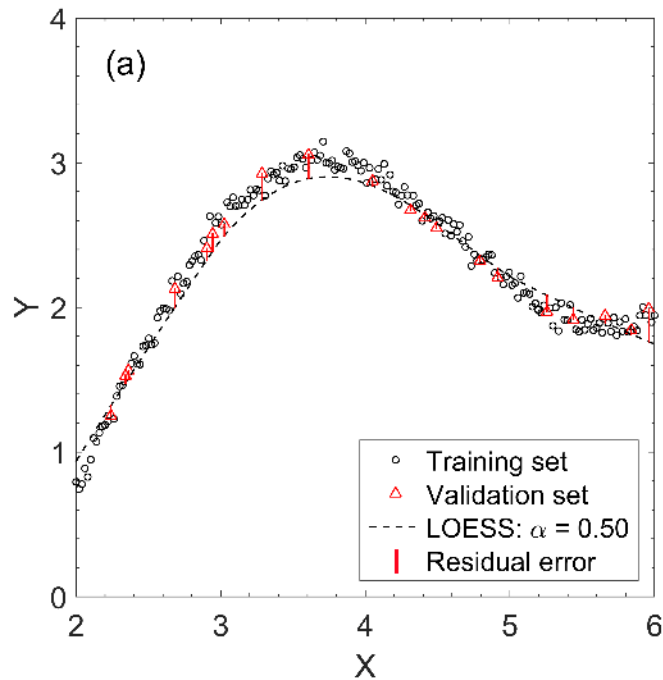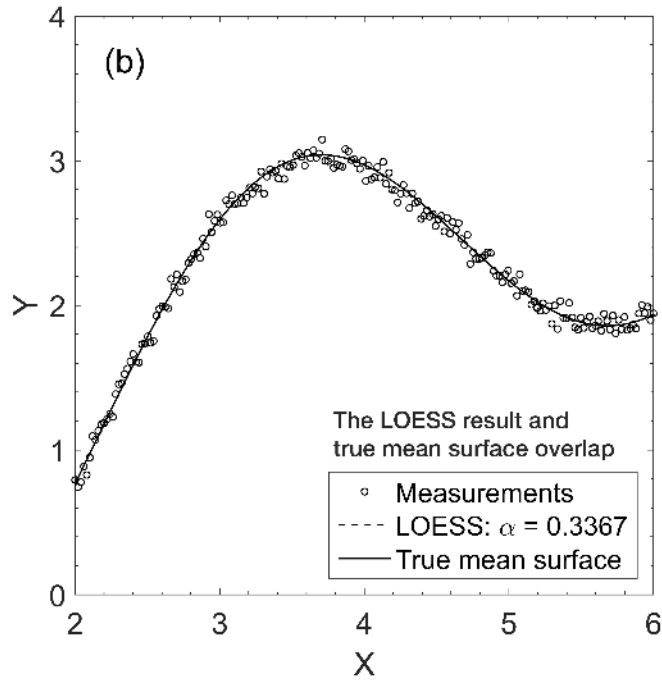
Figure 3.5 A 10-fold cross-validation result.

Having established the smoothed surface, the commonly used *root mean squared roughness* in Equation 2.7 can be rewritten as:

$$Roughness = \sqrt{\frac{1}{N}\sum_{i=1}^{N}\left(y_i - y_{i-loess}\right)^2}$$

Equation 3.3

where y_i is i-th measurement; $y_{i\text{-}loess}$ is the smoothed i-th measurement on the LOESS curve and N is the total number of measurements. It should be noted that roughness values computed from Equation 3.3 would vary with different scales. Therefore, Equation 3.3 must be used at the scale relevant to the problem being addressed.

To assess the roughness of a soil particle such as the one shown in Figure 3.6(a), the points on the particle outline are traced out using polar coordinates as shown in Figure 3.6(b). This particle image has a resolution of 40 pixel/mm. The (θ, ρ) coordinates of a total of 1980 points are plotted in Figure 3.6(b) and 3.6(c). Using LOESS and 10 fold cross validation, the optimal α was found to be 0.015. The predicted mean surface of this soil

particle is shown as the dash line in Figure 3.6(c). The computed roughness using Equation 3.3 is 0.1 mm.
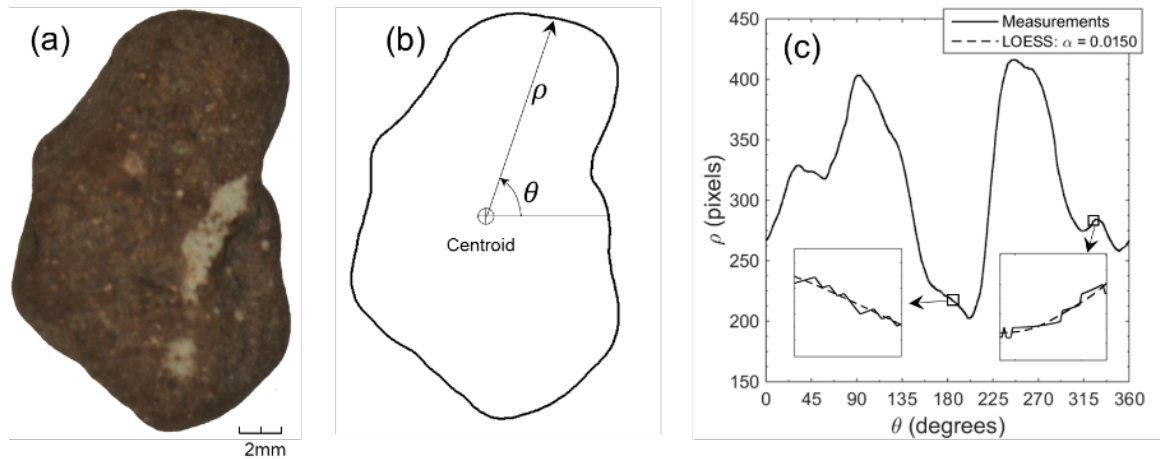
Figure 3.6 Particle perimeter profile and roughness assessment: (a) original particle image; (b) particle outline; (c) roughness smoothing by LOESS.

3.4 Roundness by Computational Geometry

Until now, the computation of roundness has been difficult to automate as it required human judgment. First, the corners on the soil particle had to be identified. Large variations in the number of corners per particle; their curvilinearity and the size of the particles made it difficult to establish a rigorous and repeatable procedure. There are no universal guidelines for identifying corners and for fitting appropriate circles to them. As a result, different human evaluators could find considerably different values for roundness. Secondly, particle roughness is superimposed over the particle corners. The roughness can be intuitively filtered out by humans when fitting circles to the corners. By contrast, computers have to be taught or programmed to distinguish roughness from small sharp corners. This section will attempt to solve these various challenges.

3.4.1   Removing roughness from particle corners

Previous researchers sought to remove the effects of roughness by discretizing the outline of a particle into an N-sided equal-angled polygon. The selected N value would therefore serve as the cutoff between angularity and roughness. Sukumaran and Ashmawy (2001) suggested that $N = 40$ would be an appropriate value while Tutumluer and Pan (2008) believed $N = 24$ to be satisfactory. In reality, a single N value cannot be applicable to all soil particles; N should vary from particle to particle depending on the particles' individual angularities and roughnesses. Another limitation of this N-approach is that small sharp corners can easily be missed. As such, it is ineffective for very angular particles. This will be demonstrated by example later in the chapter.

The previous section of this chapter showed that LOESS and K-fold cross validation effectively estimate the mean surface. This technique can be used to remove particle roughness. An example soil particle surface was represented using polar coordinates as shown in Figure 3.6. After finding the mean surface, (θ, ρ) could be plotted to show the new "smoothed" soil particle outline as in Figure 3.7. Having the smoothed particle outline, the next step towards computing Wadell's *roundness* is to fit an appropriate circle to each corner.
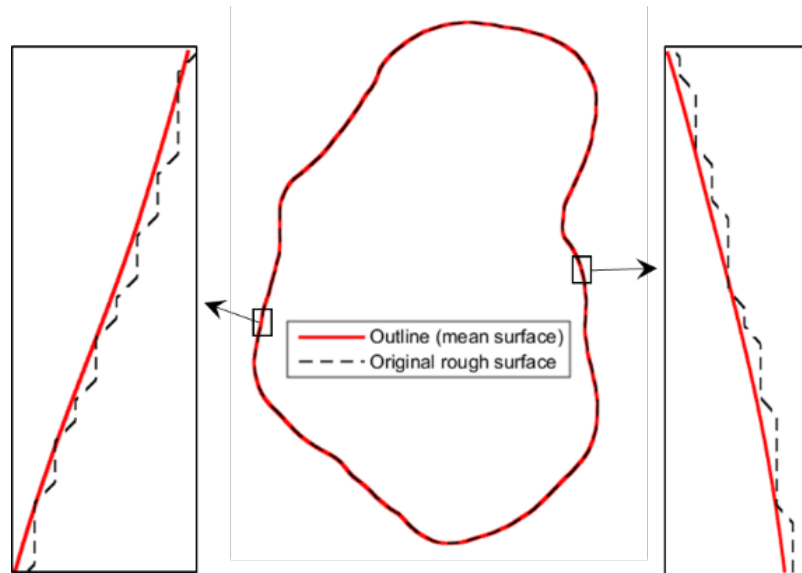
Figure 3.7 Removing roughness from the particle outline.

3.4.2 Corner identification

Determination of Wadell's *roundness* requires identification of each particle corner and assessment of its sharpness. In manual methods, judgment and intuition are used to identify the corners as done, for example, by the authors in Figure 3.8. By contrast, newer definitions of roundness using Fourier analysis, angularity index, and the fractal technique measure curvatures over the entire particle outline instead of just corners. As shown in Figure 3.8, the full outline of a particle contains both corner (convex) portions and non-corner (concave and flat portions). An algorithm is now presented to extract only the corner portions.

31
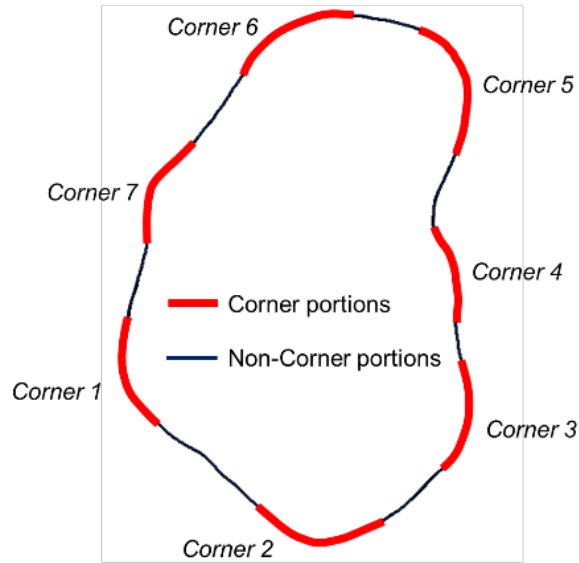
Figure 3.8 Corner and non-corner portions of a particle outline.

The smoothed outline of a particle can be discretized by "key points" connected by line segments. An example is given in Figure 3.9 where the curve EF represents the full perimeter of the particle in which the amplitudes are radial distances from the particle centroid as in Figure 3.6(b). A line $\overline{EF}$ is first drawn connecting the first and last point of the curve $\widetilde{EF}$ (Figure 3.9(a)). Point E is the first point on the discretized curve and F is the last one. The distance from the maximum divergent point G on $\widetilde{EF}$ to $\overline{EF}$ is defined by δ. If δ is larger than a predefined threshold δ_0, point G becomes the new end point of the line and line $\overline{EF}$ is shorted to $\overline{EG}$ as shown in Figure 3.9(b). The maximum divergence, δ, between $\widetilde{EG}$ and $\overline{EG}$ is now computed. The iteration continues until a point such as H in Figure 3.9(c), is found for which δ is smaller than δ_0. The curved segment $\widetilde{EH}$ is then permanently replaced by the line segment $\overline{EH}$. Point H now becomes the beginning point of the next straight-line segment to be found and $\overline{HF}$ becomes the new starting line segment as shown in Figure 3.9(d). The previously described procedure continues as shown in Figure 3.9(e). In the end, the entire originally curved perimeter $\widetilde{EF}$ will have been discretized into small piecewise linear segments connecting the key points as shown in Figure 3.9(f).

32
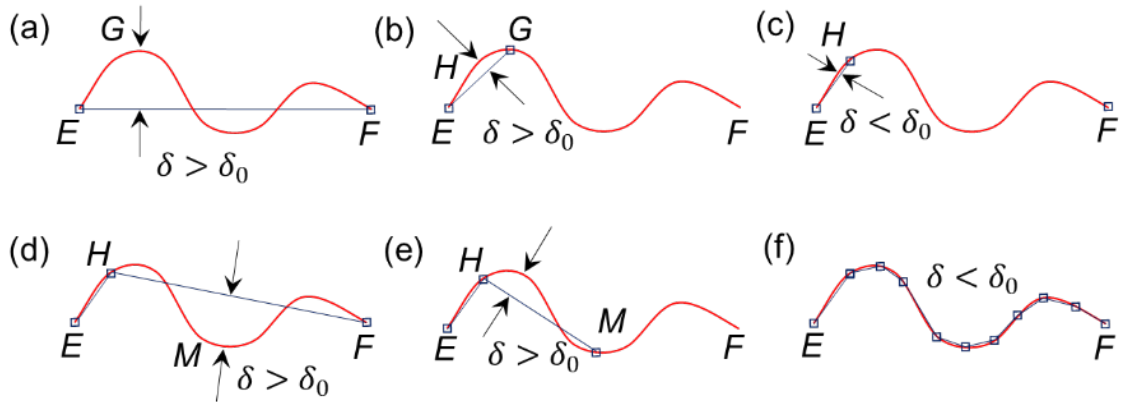
Figure 3.9 Discretizing the particle boundary.

The smoothed outline of the soil particle shown in Figure 3.8 was discretized using the above described procedure and the result is shown in Figure 3.10. The diamond points on the outline are the starting or ending points of the line segments (i.e. the key points). Naturally, the sharper corners having larger curvature require more line segments while flatter portions need fewer key points and line segments. Obviously, the threshold δ_0 is the critical parameter controlling corner identification; its selection will be addressed in detail later.

The next step is to identify the key points as belonging to either corner or non-corner segments. The centroid of the soil particle, O, is selected as the reference point. We use point C and its closest neighboring points on both sides, A and B to explain the next step. Straight line segments OC and AB are constructed as shown. If necessary, the line OC is extended to its intersection with AB at point D. The distances OD and OC are compared. If OC ≤ OD, then point C is a non-corner point. Conversely, if OC > OD then it is a corner point. This procedure is repeated for every key point on the particle outline. The final result is shown in Figure 3.10(b) where corner points are distinguished from non-corner points. Every stretch of consecutive corner points can now be fitted with a circle.
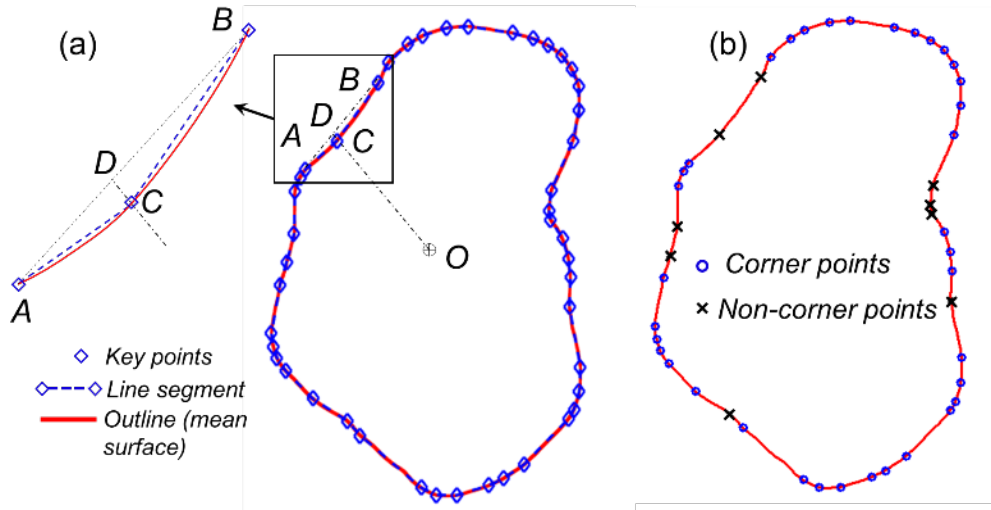
Figure 3.10 Identification of particle corners.

Gander et al. (1994) introduced a method for fitting a circle to a series of data points. The best fit circle is found by minimizing the sum of the squares of the distances between the points and the circle. Using this approach, the appropriate circle for each corner of a particle can be found. An example is shown in Figure 3.11. All of the corner points from 1 to 36 are initially used to compute a best fit circle as shown in Figure 3.11(a). The center of this circle is C and the radius is R. The minimum distance from C to the particle boundary is computed as T. If T is smaller than R, the fitted circle is not tangent to the particle boundary at T but secant to it. As such, it is not an acceptable circle. If this happens, the end point 36 is eliminated and point 35 becomes the new last point. The points from 1 to 35 are now used to fit a new circle. The recomputed T and R values are compared. If T is still smaller than R, point 35 is eliminated and 34 becomes the new last point. The process continues until a circle is found satisfying $T \approx R$ or if point 3 becomes the last point. Figures 3.11(b) and 3.11(c) show that the last point moved from point 20 to point 19, then 18, 17… and all the way to point 3 without finding an acceptable circle. If this happens, the loop ends without an acceptable circle having been found. In the next loop, point 2 becomes the first point as shown in Figure 3.11(d). This time, points 2 to 36 are used to fit a circle and if once again $T<R$ the last point is reassigned to sequentially lower number points in search of a satisfactory circle. Figure 3.11(e) shows point 20 as that last point. A proper circle C_1

for which $T = R$ is finally found when point 5 became the last point as shown in Figure 3.11(f). The circle C_1 is the best fitting circle found using points 2 to 5 for corner 1. The first point now moves to point 6 and point 36 once again becomes the last point in Figure 3.11(g). The next satisfactory circle is C_2 fitting points 8 to 10 as shown in Figure 3.11(h) which describes the roundness of corner 2. The procedure continues with point 34 finally becoming the first point and point 36 the last.
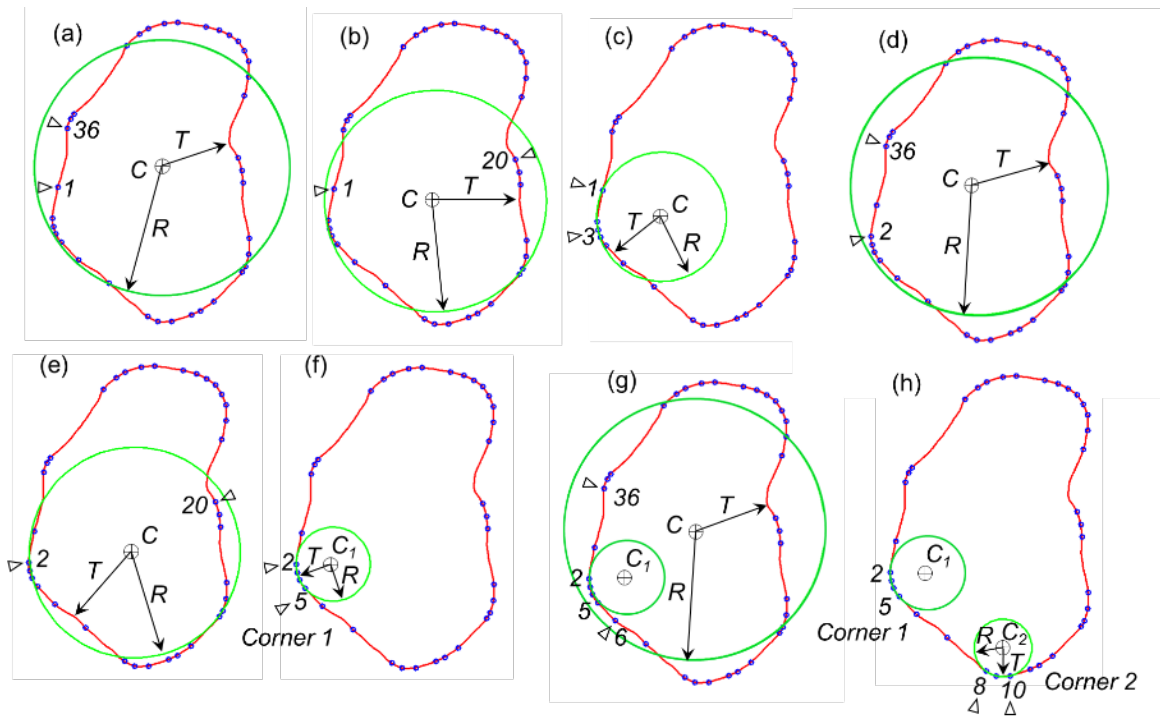
Figure 3.11 The circle-to-corner fitting process.

A special situation must be considered. The first several points (such as points 1 to 3) and the last several points (such as points 34 to 36) may be on the same corner and therefore could be fitted to a same circle in some cases. Therefore, after the last loop, the algorithm needs to check if this may have occurred.

Based on visual observation, the soil particle shown in Figure 3.10 appears to have seven corners. For comparison, the results of the "looping computation" are shown in Figure 3.12.

Seven circles have been fitted to the corners. The maximum inscribed circle (red circle with center C_i) is shown in Figure 3.12. After determining all the corner circles, the roundness was computed to be 0.49.
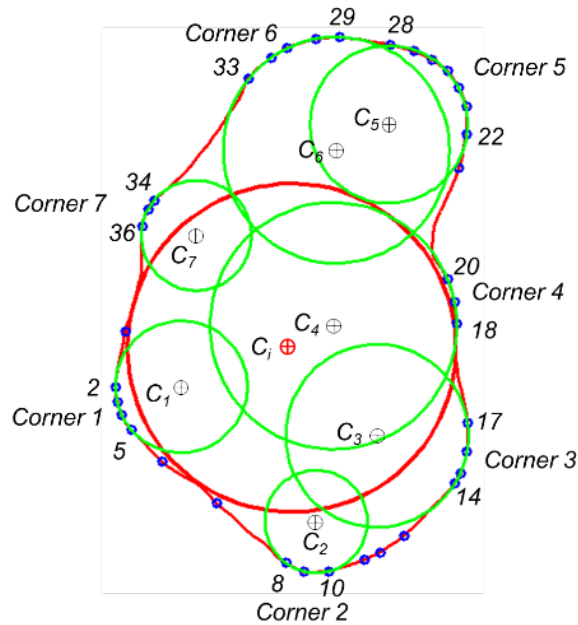
Figure 3.12 The final corner fitting of the particle from Figures 3.10 and 3.11.

In the above procedure, the tangent circle is found by finding the condition where T approximately equals R. However, it is very rare that T is exactly the same as R due to computational roundoff. In fact, the numerous calculations performed for this chapter indicate that $0.98 \leq T/R \leq 1$ is accurate enough for determining roundness.

3.4.3 Analysis of δ_0 and Image Resolution

Discretizing the soil particle outline by a sufficient number of key points connected by line segments is essential to identifying the particle corners. A threshold δ_0 must be selected for the discretization. This δ_0 is the maximum allowed divergence of the curve from the straight line segment approximating it between key points. The chosen value of δ_0

essentially sets the threshold between corners and non-corners. For example, the curve in Figure 3.13 will be either identified as a straight line or a corner depending on the chosen value of δ_0. Naturally, δ_0 should be set as small as possible to capture all the corners. However, this would generate more corner points and thus significantly increase the computational effort because the algorithm requires approximately N^N (where N is the number of corner points) operations to find all the corner circles.
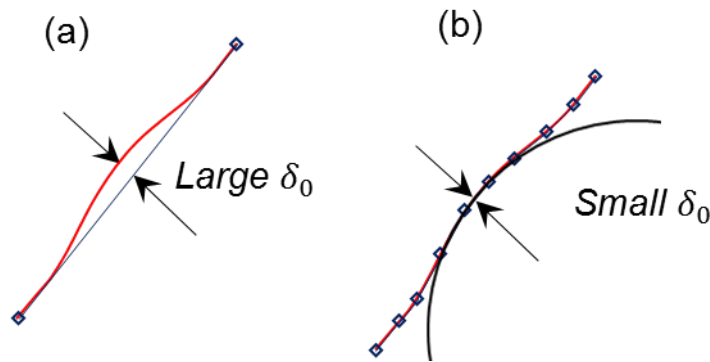
Figure 3.13 The definition and significance of δ_0.

Numerous computations were performed to investigate the influence of δ_0 on the final results. They showed that the more angular a soil particle is, the more sensitive the roundness results are to δ_0. A very angular soil particle shown in Figure 3.14(a) appeared in Powers (1953) and was reported to have a roundness of only 0.12. It has a very complex outline containing many small-sharp corners (e.g. corners 1, 10, and 12) as well as low-curvature corners (e.g. corners 13 and 15). Thus, it is a particularly challenging particle for the algorithm to compute roundness numerically. As such, it is used here to illustrate the significance of δ_0. A series of δ_0 values were tried and the results are shown in Figure 3.14. The original outline of this soil particle contained 3147 points. The δ_0 was first set at 0.01 in Figure 3.14(b). A total of 1455 key points including 782 corner points and 673 non-corner points were found. The corner points are plotted on the outline and were fitted by circles. As shown in Figure 3.14(b), all 17 corner circles were successfully identified. The

computed roundness was 0.12 which agrees perfectly with the value reported by Powers (1953). The δ_0 was then gradually increased from 0.01 to 0.50. Although progressively fewer key points approximated the outline, the computed roundness was exactly the same. However the computation time was shortened from 2 min for δ_0=0.01 to less than 1 sec for δ_0 = 0.50. When δ_0 was further increased to 1.00 (Figure 3.14(e)), corners 1, 10, 13, and 15 were not identified and the computed roundness jumped up accordingly. Corners 1 and 10 are very small and sharp while corners 13 and 15 have low curvature. These two types of corners are easily missed when using a large δ_0.

δ_0	0.01	0.1	0.5	1.0
Computed R	0.12	0.12	0.12	0.14
Corner points	782	252	109	72
Non-corner points	673	208	94	60
Computing time	2 min	40 sec	<1 sec	<1 sec
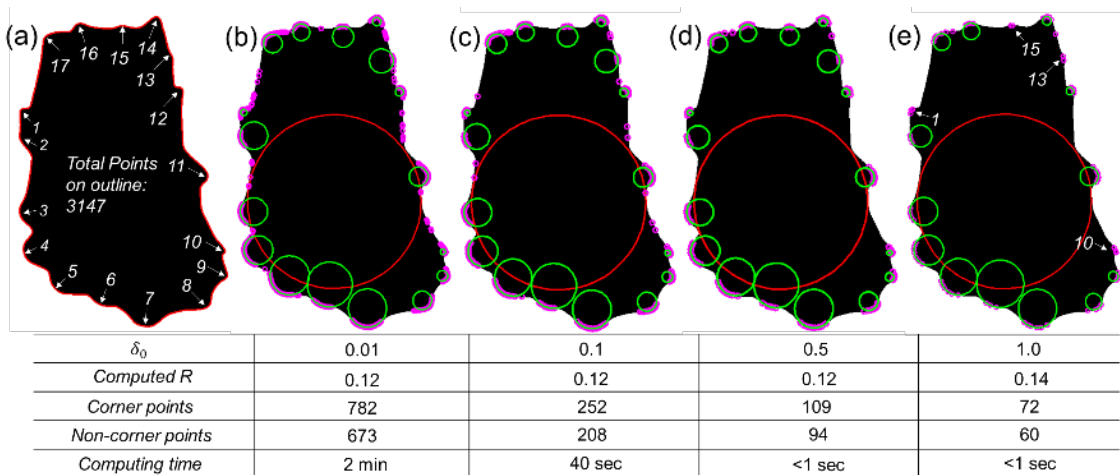
Figure 3.14 The effect of different δ_0 values on computed values of roundness.

It is evident from Figure 3.14 that the computed roundness is not very sensitive to δ_0 for values below a specific threshold, δ_{0max}. When $\delta_0 < \delta_{0max}$ all of the meaningful particle corners are successfully identified. As such using values smaller than δ_{0max} serves no purpose as it merely decreases computational efficiency. However, the threshold δ_{0max} will vary with image resolution (camera magnification). Image resolution is a key factor in the computation of particle roughness, sphericity and roundness. As previously discussed, roughness is a scale-dependent value. For the same surface, different instrument resolutions (e.g. cameras versus microscopes) will yield different roughness values. While there is an obvious dependence of the computed roughness on image resolution, the stability of the

computed values of particle sphericity and roundness to different image resolutions is more difficult to assess. To quantify the effect of particle image resolution, the concept of Pixels per Circumscribed Circle Diameter (*PCD*) is introduced. Obviously, the same soil particle will have different *PCD*s when captured under different camera resolutions.

Compared to rounded particles, the computation of roundness for angular particles is more sensitive to *PCD* because small sharp corners may be lost at low *PCD*. The particle shown in Figure 3.14 is again used to demonstrate the influence of *PCD* on sphericity and roundness. The soil particle was digitally downscaled and upscaled to generate different *PCD*s as shown in Figure 3.15. Sphericity was computed using all five definitions given by Equations 2.1 to 2.5. Interestingly, the five sphericity values were virtually unaffected when *PCD* was varied from 100 to almost 12,000. This shows that the sphericity is not sensitive to image resolutions of soil particles for *PCD*>100. Roundness values were also computed using the different *PCD*s and they too are reported in Figure 3.15. Several conclusions could be drawn from the results:

1) When *PCD* is smaller than 200 pixels significant aliasing was observed along the particle outline. Even when using an extremely small δ_0, the small corners could not be clearly delineated and non-corner parts may have been identified as corners. Therefore, to accurately compute roundness, the particle must be captured with a *PCD* of at least 200 pixels. Once *PCD* is larger than 200 pixels, the image resolution is sufficient to delineate even a fairly complex outline.

2) It was earlier shown that as long as $\delta_0 \leq \delta_{0max}$, the computed roundness will not be affected. However, the δ_{0max} depends on the image resolution as shown in Figure 3.15. The *PCD* of the soil particle will change under different resolutions. The authors found that δ_{0max} should be no larger than 0.03% of *PCD*.
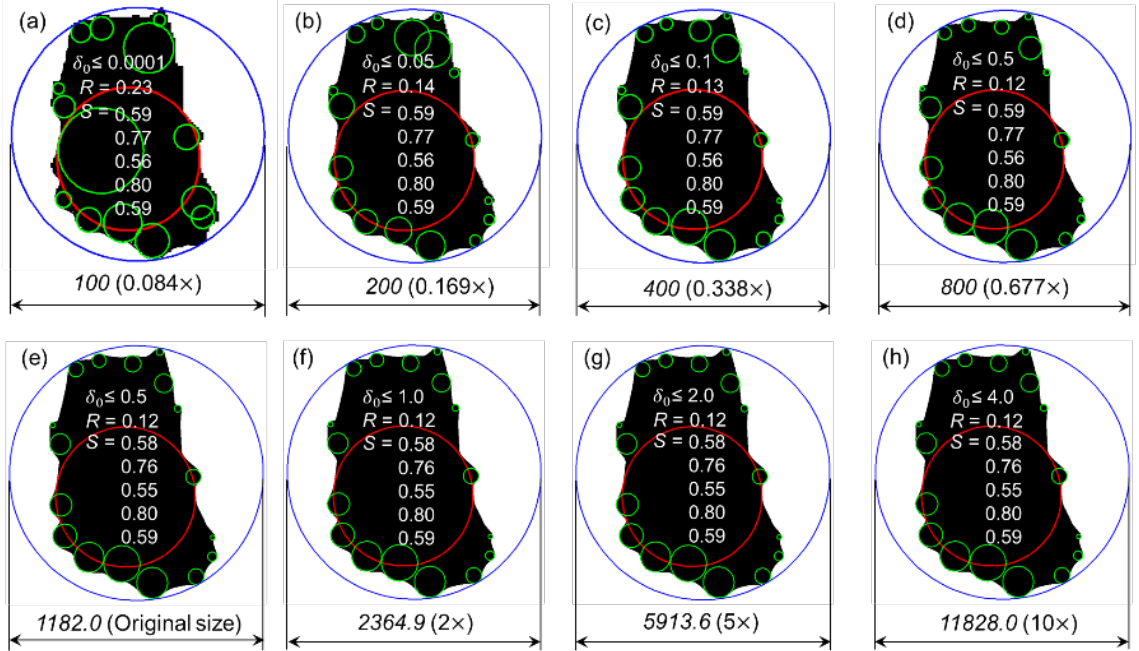
Figure 3.15 The influence of PCD on computed values of roundness and sphericity.

3.5   Comparison to Previously Reported Sphericity and Roundness Values

The roundness of the two quartz particles shown in Figures 3.16(a) and 3.16(c) were computed manually by Wadell (1935). For comparison, the corner circles were determined using the computational geometry method presented in this chapter. The results are shown in Figure 3.16(b) and 3.16(d). The positions and sizes of the circles fitted to the corners, as well as the computed roundness values are very close to those reported by Wadell. Diameter sphericity (Equation 2.2) which was used by Wadell is also determined by computational geometry. The results again agree with the previously reported values.
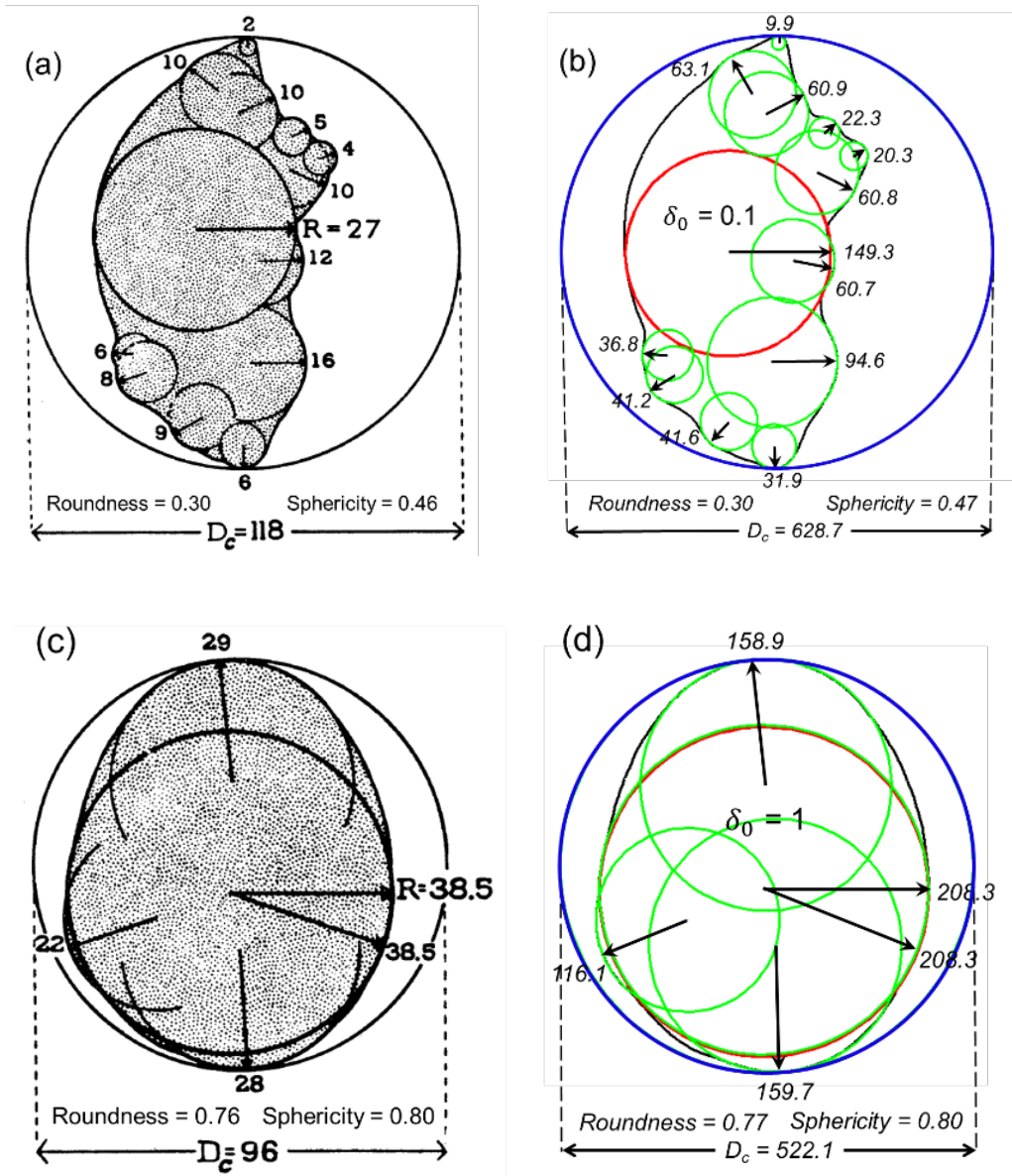
Figure 3.16 Comparison to the results of Wadell (1935): (a) and (c) are from Wadell (1935) units are millimeters; (b) and (d) are computational geometry results in pixel units (sphericity is the diameter sphericity by Equation 2.2).

Krumbein and Sloss (1951) were first to combine particle sphericity and particle roundness into one chart as shown in Figure 3.17. They evaluated roundness using Wadell's (1935) method although they did not provide the hand-drawn circles in their published work. The same 20 particles were evaluated for roundness (R) in this chapter. The computed maximum inscribed circles and corner circles are shown in Figure 3.17. The R values agree

well with the values reported by Krumbein and Sloss. Since the proposed computational geometry method appears to yield the same roundness values as by Wadell's manual means or through Krumbein-Sloss chart estimates, the required time, tedium and imprecision of the older methods can now be eliminated.
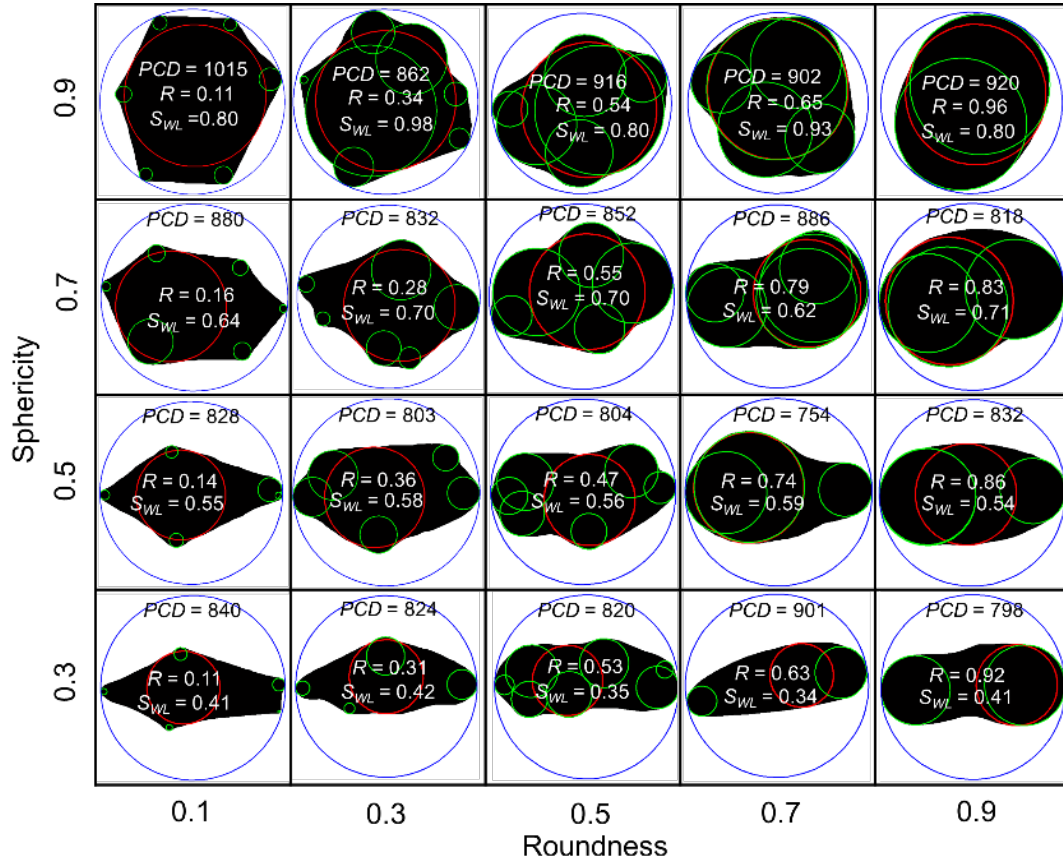
Figure 3.17 Comparison of computational geometry results to Krumbein and Sloss (1951).

The method used for computing sphericity by Krumbein and Sloss (1951) is somewhat unclear. They suggested that the sphericity values were S_{WL}, which are shown in Figure 3.17. However, Santamarina and Cho (2004) and Cho et al (2006) believed the sphericity values in the Krumbein-Sloss charts were S_C. The authors computed sphericity for each soil particle using Equations 2.1 to 2.5 and compared them with the Krumbein-Sloss chart

values in Figure 3.18. By observation, it appears clear that Krumbein and Sloss (1951) used S_{WL} in their well-known and often used sphericity chart.
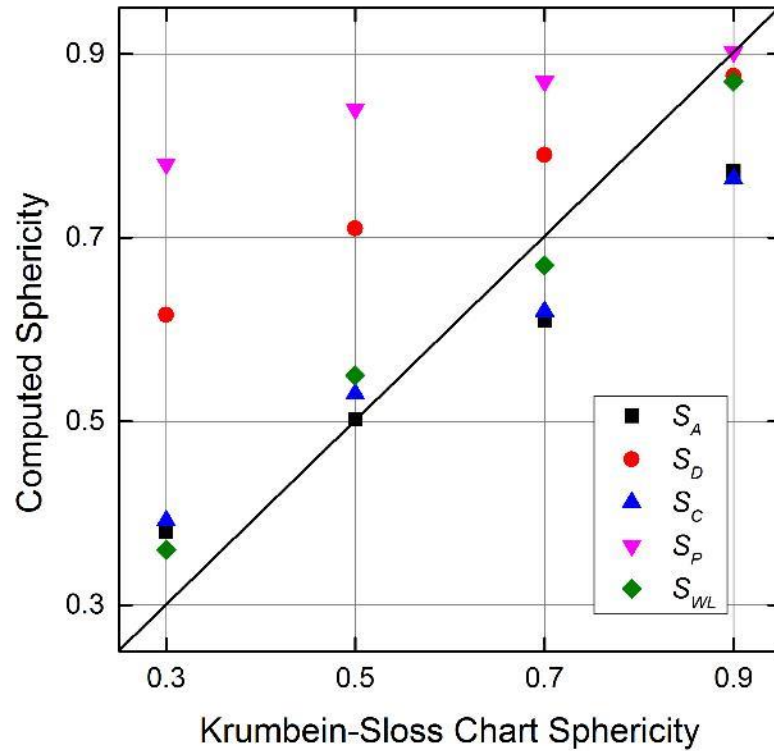
Figure 3.18 Comparison of sphericity by various definitions to Krumbein and Sloss (1951) chart values.

In addition to Figure 3.17's widespread historical usage, there are additional reasons that support the use of the S_{WL} for defining sphericity. First, S_{WL} is conceptually simple, intuitive and easily determined from images. Secondly, S_{WL} appears to be completely independent of roundness. Thirdly, of all five definitions, it utilizes the largest range of values between 0 and 1.0 thereby making it the most practical and attractive measure of particle form.

The Krumbein chart, proposed by Krumbein (1941), contains 81 reference particles redrawn from pebbles and manually assessed by Wadell's method. As shown in Figure

3.19, the 81 reference particles were binned by Krumbein into 9 groups having R increments of 0.1. The authors determined the R values of all 81 particles using computational geometry. The spatial resolution was set to have a PCD of approximately 1200 pixels for all of the particles and δ_0 was set to 0.3 for all computations. The resulting corner circles and maximum inscribed circles are plotted in Figure 3.19. The computed R values are shown with two significant figures over each of the particles in Figure 3.19. They are in excellent agreement with the one significant figure values provided by Krumbein (1941) at the bottom of each of the nine groups. When the computational results are rounded to one significant figure, perfect agreement is found for 79 of the 81 particles. The only exceptions are two very well rounded particles that had $R = 0.97$ which rounds to 1.0.

Figure 3.19 Comparison to results reported by Krumbein (1941)

45

It is clear that the computational method furnishes a precise computation of R while the chart methods provide only estimates of it. Indeed, the successful development of the former eliminates the need for the latter.

Another widely used chart for estimating particle sphericity and roundness was provided by Powers (1953). He separated particles having Wadell R values from 0.12 to 1.00 into six roundness classes as shown in Figure 3.20. The ratio of the upper limit to the lower limit of R in every class is 0.7. Each roundness range is illustrated with two particles: one having high S and one with low S. The R values of the 12 soil particles were determined using the computational methods described in this chapter with δ_0 set to 0.3. The results are shown in Figure 3.20. The computed R values of the two particles in each class are very close to the upper and lower limit in each class. The particles having high S displayed the upper R value while the particle having low S displayed the lower R value in each range. The computed values agree remarkably well with the values reported by Powers (1953). As such, we again conclude that the computational geometry method proposed herein can replace the imprecise and subjective chart method.

High Sphericity

PCD = 1097.7
R = 0.16
S = 0.81, 0.90
0.81, 0.86
0.98

PCD = 1076.7
R = 0.25
S = 0.69, 0.83
0.72, 0.86
0.82

PCD = 932.1
R = 0.33
S = 0.75, 0.87
0.77, 0.87
0.86

Low Sphericity

PCD = 1182.0
R = 0.12
S = 0.58, 0.76
0.55, 0.80
0.59

PCD = 1363.1
R = 0.18
S = 0.41
0.63
0.41
0.76
0.47

PCD = 1210.4
R = 0.26
S = 0.58, 0.76
0.54, 0.79
0.54

Very angular
0.12 – 0.17

Angular
0.17 – 0.25

Subangular
0.25 – 0.35

High Sphericity

PCD = 969.7
R = 0.47
S = 0.82, 0.90
0.79, 0.92
0.87

PCD = 943.7
R = 0.66
S = 0.90, 0.95
0.89, 0.94
0.94

PCD = 1038.4
R = 0.96
S = 0.91, 0.96
0.92, 0.94
0.93

Low Sphericity

PCD = 1331.3
R = 0.36
S = 0.49, 0.70
0.47, 0.83
0.50

PCD = 1154.6
R = 0.52
S = 0.61, 0.78
0.60, 0.89
0.50

PCD = 1285.3
R = 0.72
S = 0.57, 0.75
0.54, 0.89
0.54

Subrounded
0.35 – 0.49

Rounded
0.49 – 0.70

Well rounded
0.70 – 1.00

Figure 3.20 Comparison of computational method to estimates of angularity by Powers (1953)

3.6   Application of the algorithm to particle assemblies

Provided binary particle images, the computational algorithm can directly extract a particle's outline and compute the Wadell roundness. Therefore, it could be readily integrated into existing optical soil characterization systems capturing binary soil images. Some of the systems include: the University of Illinois Aggregate Image Analyzer (UIAIA) (Rao and Tutumluer, 2000; Tutumluer and Pan, 2008); the Aggregate Imaging System (AIMS) (Fletcher et al., 2003; Chandan et al., 2004; Mahmoud and Masad, 2007; Mahmoud et al., 2010); the Qicpic system (Altuhafi et al., 2013); and the Translucent Segregation Table (TST) system (Ohm and Hryciw, 2013). In all of these systems the particles are prepared to lie detached from one another thereby facilitating image collection for simple analysis.

By contrast to the systems listed above, in other image-based soil characterization systems the soil particles are not or cannot be detached. For example, in the Sedimaging system (Ohm and Hryciw, 2014) a 213 cm (7 ft.) tall sedimentation column is used to rapidly sort soil particles by size prior to image capture. In these images, the sedimented soil particles are in three-dimensional contacting assemblies. The Vision Cone Penetrometer (VisCPT) developed by Raschke and Hryciw (1997) captures images in-situ without taking soil specimens from the ground. Obviously, the soil particles in VisCPT images are also in three-dimensional assemblies. Finally, some particles such as fine sands are so small that it is unrealistic to separate them prior to image capture, even in a laboratory. Therefore, a procedure was sought that could computationally extract particles from images of three-dimensional assemblies so that the new computational algorithm for Wadell roundness could be used on them.

In 3D assemblies, particles are not only in contact with each other, they also block and are blocked from view by other particles. Some soil particles may have a full projection of their area in view while others will be occluded by foreground particles. Secondly, the voids between soil particles are hard to distinguish from actual particles. Naturally, only particles exhibiting full projections are useful for characterization of form and roundness.

Therefore, the challenge is to distinguish particles with full projections from voids and occluded particles. Ideally, a computer algorithm would make these distinctions. However, this is a daunting task as soils have various colors, size distributions, internal textures, particle forms and roundnesses. The authors' future research efforts will aim to teach computers to pick out the particles with full projections through machine learning and pattern recognition techniques. However, to date, only human judgment is capable of making the selections. Therefore, a semi-automated approach is utilized in this chapter; it combines human judgment with a computer's rapid computational abilities. In this hybrid approach, operators first pick out the particles with full projections. Then, binary particle images are automatically generated. Finally, roundness and other descriptors of particle geometry are determined using the computational methods described in this chapter.

Figure 3.21(a) shows a natural soil aggregate image called Brown Fused Alumina Oxide sand (BFAO). The particles are brown and have a complex texture. The particles whose projections are fully visible can be manually picked out using the image processing software "Photoshop". To begin, the operator can trace the particle boundaries using the Photoshop tools: *polygonal lasso* or *magnetic lasso*. When using the polygonal lasso, users must manually specify the perimeter points and Photoshop will connect the points to generate particle boundaries. The magnetic lasso automatically detects the particle boundaries. Although it is a very powerful tool that does not require much human interaction, the magnetic lasso is ineffective for particles that exhibit complex textures due to roughness or mineral variability.

As such, the polygonal lasso was used for the BFAO. A total of 89 fully projected particles were identified. After delineating the boundaries, the regions within them are filled with a distinct color as shown in Figure 3.21(b). Figure 3.21(b) is the input into the computational geometry program previously described. The program easily extracts the newly colored particles and computes the *PCD* of each one. Each particle is then upscaled or downscaled so that *PCD* equals 1000 pixels and δ_0 is set to 0.3. The results have been superimposed on the original image in Figure 3.21(c). The dashed circle is the maximum inscribed circle and the solid circles are the corner circles.

Figure 3.21 Circle fitting results for BFAO sand: (a) image of the three-dimensional assembly of BFAO; (b) delineated particles using Photoshop; (c and d) fitted corner circles (solid) and maximum inscribed circles (dashed).

Images of two other soils were collected using different optical systems. Figure 3.22 shows standard Ottawa #20 - #30 sand captured using the VisCPT. The particles are light brown, rounded and spherical. The soil in Figure 3.23 is called "2NS" by the Michigan Department of Transportation; an image of its 1.4 mm to 2.0 mm size increment was captured in the Sedimaging device. The detailed Sedimaging test procedures are provided by Ohm and Hryciw (2014). The 2NS particles have a variety of colors, shapes and roundnesses. In the Ottawa sand image, 129 particles showed full projections while 203 particles were found in the 2NS image. The computational results for the two soils are superimposed on the original images. Once again, the maximum inscribed circles are in dashed lines while the corner circles are solid lines. They again appear to nicely fit the particles and their corners.
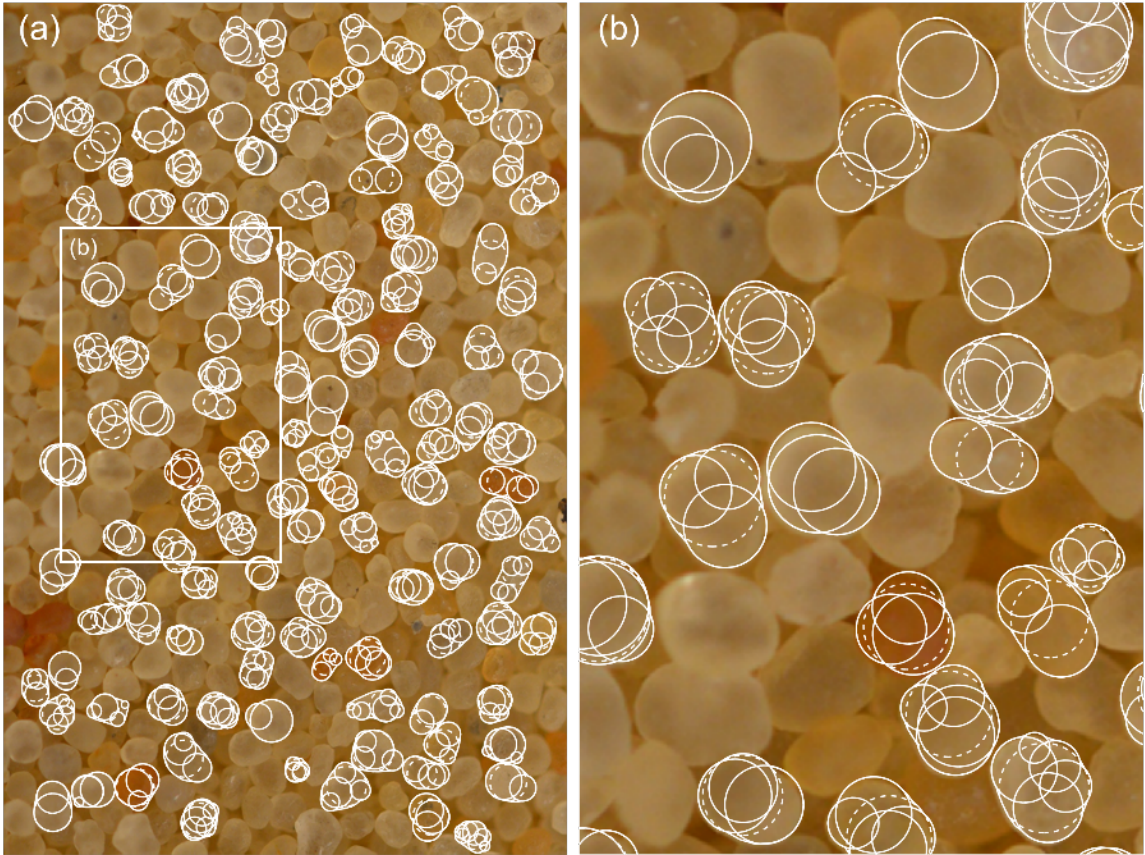
Figure 3.22 Circle fitting results for Ottawa #20–#30: (a) image of the three-dimensional assembly of Ottawa #20–#30 by VisCPT; (b) fitted corner circles (solid) and maximum inscribed circles (dashed).
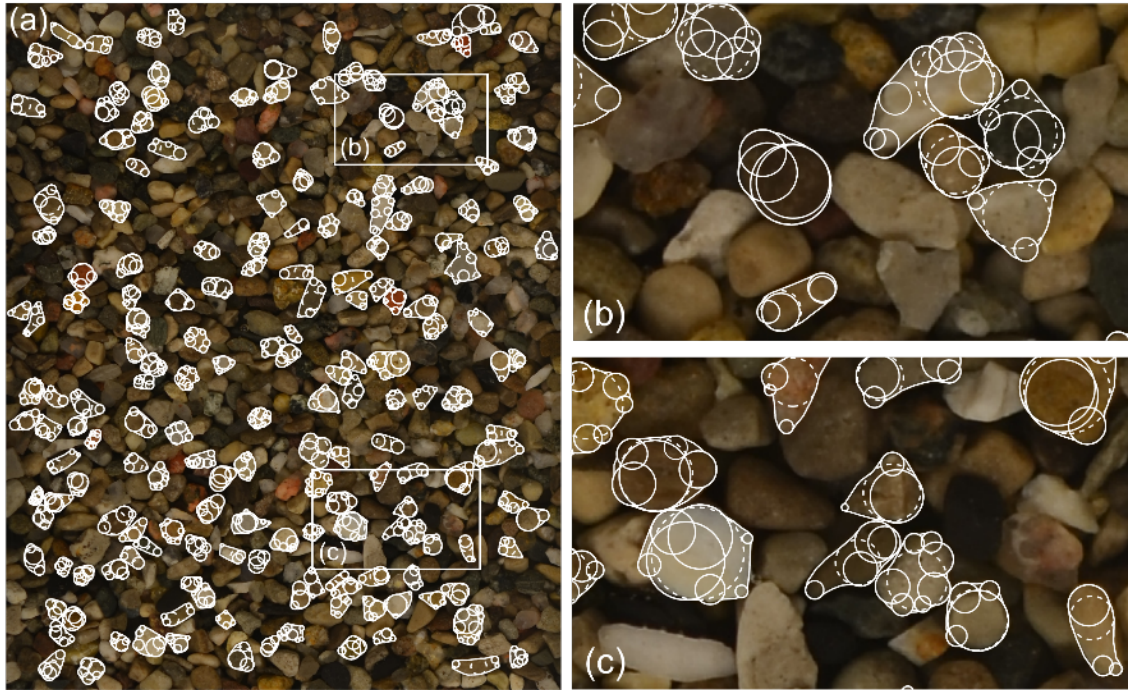
Figure 3.22 Circle fitting results for 2NS sand: (a) image of a three-dimensional assembly of 2NS sand by sedimaging; (b and c) fitted corner circles (solid) and maximum inscribed circles (dashed).

After identifying the maximum inscribed circle and corner circles, the Wadell roundness of each particle is easily computed. Other geometric descriptors such as length (d_1), width (d_2), sphericity, aspect ratio, orientation can also be readily obtained. Assuming the soil particles are ellipses, a "relative volume" of each particle can be computed as $d_1 \times d_2 \times d_2$. The distribution of Wadell R by volume for the three soils was computed and is shown in Figure 3.23. The use of volume-based distributions for civil engineering (geomechanics) applications is more logical and appropriate than simple distributions based on particle counts. Nevertheless, it's recognized that for relatively uniform sized soil particles the distributions will be similar.

Powers' classification of R (according to Figure 3.20) is also shown in Figure 3.23. As shown, the Ottawa sand is 75% by volume well-rounded with about 25% rounded; 2NS contained about 45% rounded and 35% subrounded with smaller volumes of well-rounded

(10%) and subangular (10%); the BFAO was 50% subangular, 20% angular and 30% subrounded by volume.
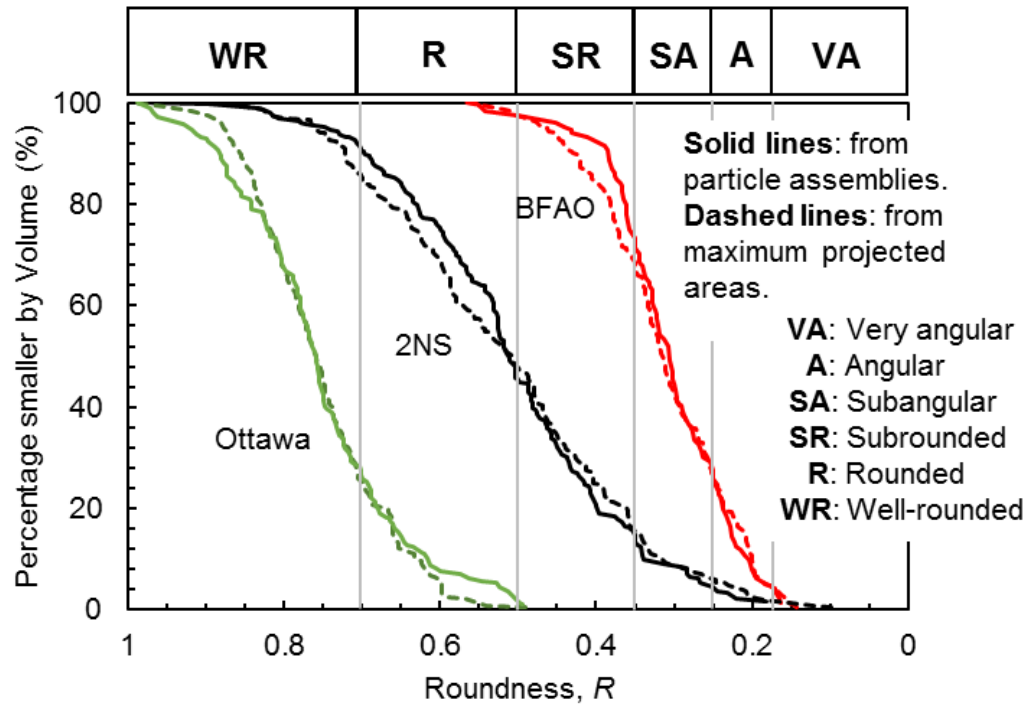
Figure 3.23 Wadell roundness cumulative distributions

By convention, roundness should be evaluated in the view showing the largest projected area of a particle (Sneed and Folk, 1958). Therefore, approximately 200 random particles from each of the three sands were laid out on a flat surface exposing their largest area. Images were captured and analyzed using the computational method. The results, shown by dashed lines in Figure 3.24 are in very good agreement with those obtained from the images of three-dimensional assemblies. As summarized in Table 3.1, the difference between the average R determined from images of assemblies and the average R from images of detached particles was +/- 0.01 for all three soils.

Having identified particles with full projections, particle sphericities can also be computed following Equations 2.1 to 2.5 and their distributions can also be developed. Figures 3.24(a), 3.24(b), and 3.24(c) are the sphericity distributions for BFAO, Ottawa #20-#30 and 2NS, respectively. The results confirm that S_{WL} indeed gives a widest numerical range for sphericity. The dashed lines in the three figures are the sphericity distributions obtained using the largest projected areas of the same particles as were used for computing roundness. Table 3.1 tabulates the average values for all three soils by all five definitions of sphericity. As observed, the differences in average values were at most +/- 0.02.

Table 3.1 Mean R and S from Images of Assemblies and Images of Maximum Area Projections

Soil	R		S_A		S_D		S_C		S_P		S_{WL}	
	IA	MP	IA	MP	IA	MP	IA	MP	IA	MP	IA	MP
BFAO	0.31	0.32	0.62	0.62	0.78	0.78	0.62	0.62	0.88	0.89	0.69	0.70
Ottawa	0.75	0.76	0.75	0.77	0.87	0.88	0.74	0.76	0.96	0.96	0.79	0.80
2NS	0.53	0.52	0.62	0.64	0.78	0.79	0.62	0.63	0.91	0.92	0.67	0.67

Note: IA = from images of assemblies; MP = from images of maximum area projections.
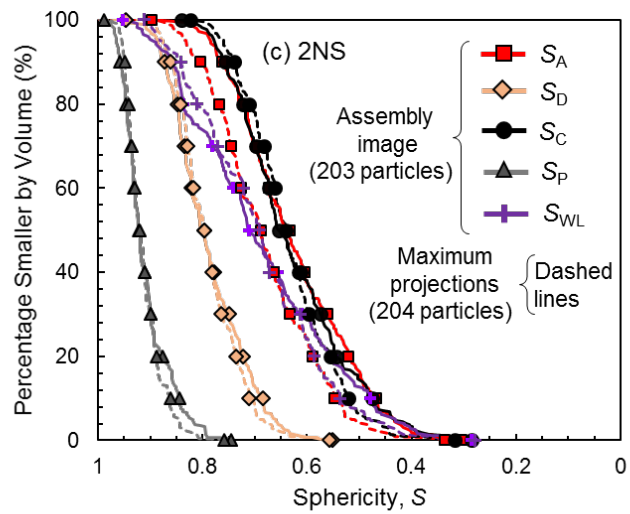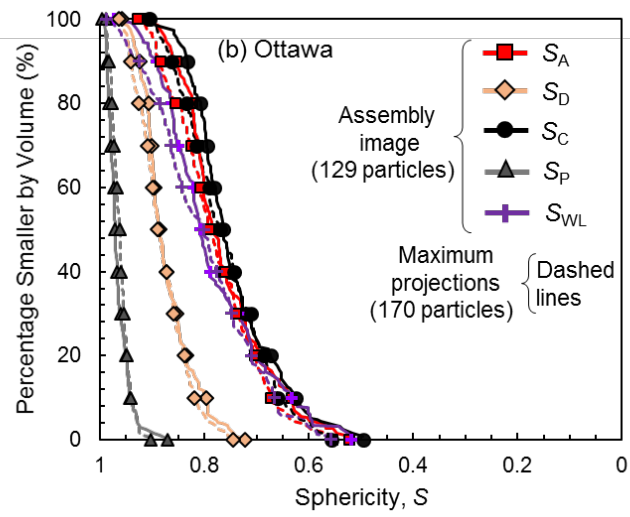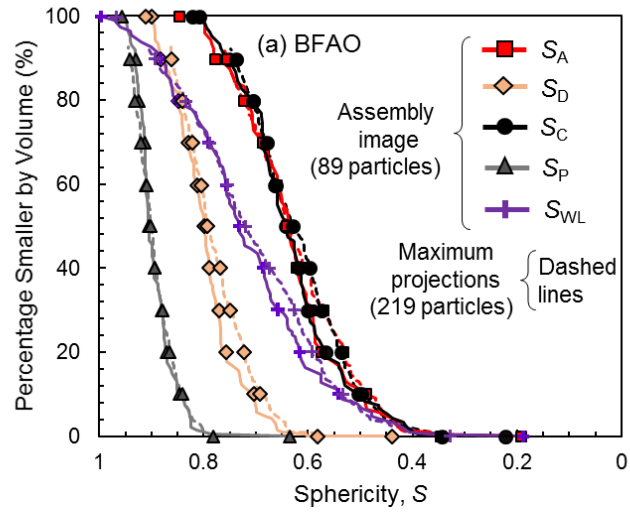
Figure 3.24 Sphericity distributions for (a) BFAO; (b) Ottawa #20-#30; (c) 2NS

3.7   Required sample size for determining particle roundness of a soil

In most earlier studies, only a mean R value for a soil was determined. The ability to rapidly determine R for numerous particles in a specimen raises the question of how many are needed to obtain statistically valid value. To obtain an average R for a soil specimen, Youd (1972) reported that at least 50 particles are needed. Edil et al. (1975) estimated R for sand particles by Krumbein's chart and reported that viewing at least 25 particles were needed to yield a reliable mean. Cho et al. (2006) visually compared 30 particles to obtain the mean. Rouse et al. (2008) concluded that at least 30 particles are needed to compute the mean R based on the probability theorem 'law of large numbers'. Bareither et al. (2008) used 50 particles. Yang and Wei (2012) reported using 40 particles. Others who computed and reported average R values include Eisma (1965); Frossard (1979); Sladen et al. (1985); Vepraskas and Casselkan (1987); Sagga (1993); Frossard (1979); Mehring and McBride (2007); Bareither, et al. (2008); Chapuis (2012) and Cabalar et al. (2013). In summary, the typical sample size used to compute an average R value has been in the range of 30 to 50 particles.

From statistics, for normal distributions the minimum sample size, n_{min} necessary for reliably estimating the mean value of a population is computed by:

$$n_{min} = \left[\frac{z_{\alpha/2} \sigma}{E} \right]^2 \qquad \text{Equation 3.4}$$

where E is the allowed error between the estimated population mean and the actual population mean; σ is the population standard deviation and $Z_{\alpha/2}$ is a value related to the confidence level of $100(1 - \alpha)\%$ which is obtained from a Z-table.

If we establish a maximum E of 0.05 for the mean roundness and wish to know it with a confidence level of 98%, then $\alpha = 0.02$ and $Z_{\alpha/2} = Z_{0.01} = 2.33$ from the Z-table. From study of over 20 different sands, the authors have observed standard deviations of no more than 0.17 for roundness, with most values below 0.15. Using the worst case $\sigma = 0.17$ with $E = 0.05$ and a 98% desired confidence ($\alpha = 0.02$), the computed n_{min} is 63. Since this chapter presents a more rapid and precise method for computing Roundness than by chart methods,

it is also logical that more particles could and should be used than the previously used 30 to 50.

Eight natural and two crushed sands from various locations in Michigan, Texas, Missouri New Mexico and California having various particle shapes were evaluated using the computational geometry methods for roundness and sphericity. In each case, the average value of 64 particles was computed. The mean R values with their standard deviations and the mean S_{WL} with their standard deviations are shown in Figure 3.25. As expected, the two crushed sands, 30A ($R=0.15$) and a crushed Gabbro rock ($R=0.23$) were the most angular, as expected. Fort Davis, TX ($R=0.41$) is very recent colluvium. Scotts Valley, CA ($R=0.40$) is a residual sand from a mildly cemented sandstone. Rincon, NM ($R=0.55$) is a dessert sand, probably windblown. Capitola, CA ($R=0.48$) is an alluvial river bed sand. The most rounded soils, are a Mississippi River alluvium from New Madrid, MO ($R=0.57$), a glaciofluvial sand from Oakland County, MI ($R=0.65$) and a Lake Michigan Dune sand ($R=0.62$).

Visual observation of the images appears to confirm the reasonableness of the roundness values and classifications. Just as importantly, the inscribed circles and circles fitted to corners are correctly constructed. The largest observed standard deviation was 0.17 confirming the reasonableness of using $\sigma = 0.17$ in Equation 3.4 to compute n_{min}.
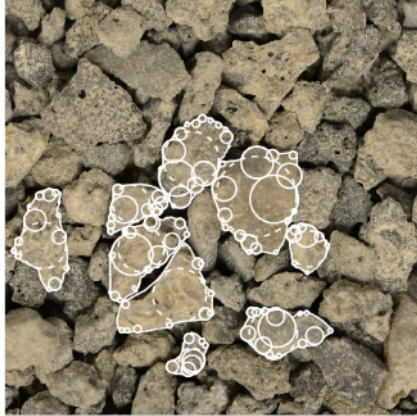
(a) Michigan 30A
R = 0.15, σ = 0.08
S_{WL} = 0.69, σ = 0.15

(b) Crushed Gabbro
R = 0.23, σ = 0.08
S_{WL} = 0.56, σ = 0.14
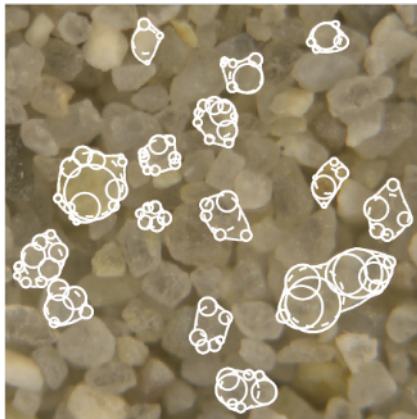
(c) Scotts Valley, CA
R = 0.40, σ = 0.09
S_{WL} = 0.73, σ = 0.13

(d) Fort Davis, TX
R = 0.41, σ = 0.09
S_{WL} = 0.68, σ = 0.14

(e) Capitola, CA
R = 0.48, σ = 0.12
S_{WL} = 0.72 , σ = 0.11

(f) Upper Peninsula, MI
R = 0.51, σ = 0.17
S_{WL} = 0.69, σ = 0.14

Figure 3.25 Mean R and S values and their standard deviations for sands of various geologic origins: (a) Michigan 30A; (b) Crushed Gabbro; (c) ScottsValley,California; (d) FortDavis,Texas; (e) Capitola,California; (f) UpperPeninsula,Michigan; (g) Rincon,NewMexico; (h)NewMadrid, Missouri; (i) Lake Michigan Dunes; (j) Oakland County, Michigan

3.8   Conclusion

This chapter presented methods for determination of soil particle sphericity, roundness and surface roughness using their traditional definitions but obtained numerically through

computational geometry. Values for sphericity computed by five existing definitions, all based on 2D particle projections, were compared. The analysis showed that the simple ratio of particle width to length, S_{WL} provides the best distribution of sphericity values between 0 and 1.0 and is also independent of particle roundness.

A surface roughness assessment was proposed based on statistical methods: locally weighted regression (LOESS) and K-fold cross validation. A mean surface is determined from which a root mean squared roughness is computed. Determination of the mean surface is also a prerequisite to determining particle roundness.

The digitization of Wadell's roundness computation is complex for two reasons. First, the roughness needs to be removed. Secondly, the particle's corners need to be identified and fitted with appropriate circles. These two challenges were overcome by the computational geometry methods proposed in this section. The accuracy of the computational algorithm was verified by excellent agreement with Wadell's (1935) original hand computations of roundness. The computational results were also compared to three widely utilized charts of Krumbein (1941), Krumbein and Sloss (1951), Powers (1953) to show that the chart's particle silhouettes approximated Wadell's roundness reasonably well. The computational geometry method essentially eliminates the need to use Wadell's manual method and approximations based on the chart method.

Parametric evaluation of computational geometry results revealed two rules of thumb for obtaining reliable values of sphericity and roundness. First, the resolution of images should be at least 200 pixels per circumscribing circle diameter (*PCD*) and secondly, the maximum departure of linear segments approximating the particle perimeter (δ_{0max}) should be no more than 0.03% of *PCD*.

The computational geometry methods were extended to particles in three-dimensional assemblies that exhibited full and unobscured projections. For particles exhibiting uniform internal textures, Photoshop's magnetic lasso tool was used to define the perimeter while for particles with complex internal textures, Photoshop's polygonal lasso was used. Cumulative volume-based distribution of particle roundness and sphericity were developed for uniformly textured Ottawa sand and Michigan 2NS as well as for a highly textured

Brown Fused Oxide Sand (BFAO). As expected, the Ottawa sand proved to be mostly well-rounded (75%) with about 25% by volume rounded particle; 2NS ranged from 35% subrounded to 45% rounded with smaller volumes of well-rounded (10%) and subangular particles (10%); the BFAO was 50% subangular, 20% angular and 30% subrounded. Sphericity distributions for these three soils confirmed that the ratio of particle width to length (as sphericity was defined by Krumbein and Sloss, 1951) provides a broader range of values than four other occasionally used definitions of sphericity. Average values of roundness and sphericty obtained from the images of three-dimensional assemblies were also compared to average values obtained from images of detached particles of the same sands laid out to expose their largest projected areas. The differences in computed roundness and sphericity were insignificant.

Finally, mean roundness was computed for 10 different sands of various geologic origins. Their values ranged from 0.22 and 0.25 for crushed sands to 0.56 to 0.59 for alluvial and glacio-fluvial sands. It was shown that 64 particles were adequate to compute a mean roundness with +/- 0.05 accuracy and 98% confidence.

CHAPTER 4

LABORATORY MECHANICAL BEHAVIOR

4.1   Index void ratios

4.1.1   Introduction

Particle packing is a primary state parameter controlling a soil's mechanical response to a change in applied loads (effective confining stress is the other major state parameter). Contraction in loose packing states and dilation in dense states during shearing inspired the development of critical state soil mechanics and stress-dilatancy theories. One way to quantify packing for geomechanics purposes is through a soil's relative density, D_r. It expresses the degree of compactness of a sand with respect to experimentally determined "very loose" and "very dense" index states. It is defined as $(e_{max} - e)/(e_{max} - e_{min})$ where e is the void ratio. The two index void ratios, e_{max} and e_{min}, establish very loose and very dense index packing states which a sand achieves under specific laboratory testing conditions prescribed by ASTM D4253 and ASTM D4254 respectively.

Angular, non-spherical and uniform-sized sands tend to have larger values of e_{max} and e_{min} than rounded, spherical and well-graded sands (Santamarina and Cho, 2004; Youd, 1972; Cubrinovski and Ishihara, 2002; Cho et al., 2006; Bareither et al., 2008; Rouse et al., 2008; Koerner, 1969 and Shin and Santamarina, 2013). However, only Koerner (1969) and Youd (1972) considered the coupled effects of several intrinsic properties. Others generally studied the effects of only one intrinsic property at a time. Most commonly, the effect of particle roundness of relatively uniform-sized soil particles on e_{max} and e_{min} was evaluated.

In this section, 25 particulate materials having various shapes, sizes and gradations were investigated. High quality e_{max} and e_{min} tests were performed on them. The primary intrinsic properties affecting e_{max} and e_{min} including particle size distribution, particle roundness (R)

and sphericity (S) were obtained by image-based computational geometry algorithm of chapter 3. As a compliment to the newly obtained lab data, previously published $e_{\max}$ and $e_{\min}$ values for 142 other sands were added to the dataset. Using the combined data, this chapter quantifies the influence of particle size distribution, R and S on the index void ratios and a new model is presented for predicting $e_{\max}$ and $e_{\min}$ using all three intrinsic properties.

4.1.2 Materials and test procedures

Twenty one sands of various shapes, sizes and gradations were collected. In addition, two different sized glass bead specimens and two kinds of rice were included to increase the range of particle shapes. The average R and S values of the 100 particles was computed for each soil. Sieving was employed to obtain the 50% size (D_{50}) and the coefficient of uniformity (C_u). Table 4.1 summarizes these values as well as $e_{\max}$ and $e_{\min}$ for each material.

Table 4.2 lists information that was available for the additional 142 sands found in the geotechnical engineering literature. The particle size distributions, R and S were extracted whenever such information was available. In some of the previous works, only images of the sand grains were available instead of actual R and S values. In such cases, the computational geometry algorithm was used to determine R and S from the images.

Table 4.1 Test results for 25 sands by this study.

Soil	Gradation		Shape		Packing	
	D_{50}	C_u	R	S	e_{max}	e_{min}
Chesterton, IN Dunes	0.26	1.3	0.64	0.76	0.87	0.57
Ottawa 20-30	0.71	1.4	0.75	0.82	0.74	0.49
Michigan 2NS	0.50	2.3	0.53	0.67	0.82	0.54
New Madrid, MO	0.32	2.2	0.57	0.73	0.81	0.52
Michigan Dunes	0.30	1.5	0.62	0.72	0.85	0.56
Oakland Co., MI	0.31	1.6	0.65	0.72	0.86	0.53
Michigan 30A	0.58	7.0	0.15	0.69	0.92	0.55
Fused AI Oxide	1.80	1.6	0.30	0.69	0.92	0.63
Scotts Valley, CA	0.33	1.5	0.40	0.73	0.94	0.60
Upper Peninsula, MI	0.60	2.8	0.51	0.69	0.85	0.54
Fort Davis, TX	0.44	8.6	0.41	0.68	0.85	0.51
Rincon, NM	0.36	3.0	0.55	0.82	0.80	0.51
Crushed Gabbro	0.80	5.5	0.23	0.56	0.96	0.60
Capitola, CA	0.35	1.6	0.48	0.72	0.89	0.57
Small Glass Beads	0.70	1.1	1.00	1.00	0.75	0.50
Large Glass Beads	0.97	1.1	1.00	1.00	0.74	0.50
Brady, TX	0.61	1.4	0.68	0.76	0.84	0.57
Class IIA, MI	0.21	1.9	0.62	0.69	0.86	0.56
Griffin, IN	0.74	4.3	0.60	0.69	0.79	0.51
Chesterton, IN Beach	0.64	2.9	0.64	0.66	0.85	0.54
Muskegon, MI	0.40	1.6	0.55	0.74	0.84	0.56
Nevada Sand	0.16	1.3	0.61	0.72	0.88	0.58
Treasure Island, CA	0.25	1.8	0.56	0.72	0.85	0.57
Long-grain rice	1.51	1.1	0.62	0.40	1.08	0.85
Short-grain rice	1.91	1.1	0.54	0.55	0.97	0.65

Note: D_{50} = 50% size (mm), C_u = coefficient of uniformity, R = roundness, S = sphericity, e_{max} and e_{min} = index maximum and minimum void ratios.

Table 4.2 The results of 142 sands from literatures.

Source	Soil	Gradation		Shape		Index Packing	
		D_{50}	C_u	R	S	e_{max}	e_{min}
Sladan et al. (1985)[b]	Nerlerk	0.28	2.0	0.43	0.75	0.94	0.62
	Leighton Buzzard	0.86	1.2	0.50	0.82	0.82	0.54
Cho et al. (2006)[b]	Nevada sand	0.15	1.8	0.60	0.85	0.85	0.57
	Ticino sand	0.58	1.5	0.40	0.80	0.99	0.57
	Margaret River sand	0.49	1.9	0.70	0.70	0.87	-
	ASTM 20/30 sand	0.60	1.4	0.80	0.90	0.69	-
	Ponte Vedra sand	0.18	1.8	0.30	0.85	1.07	-
	8M8 crushed sand	0.38	3.3	0.20	0.70	0.97	-
	9C1 crushed sand	0.52	2.3	0.25	0.70	0.91	-
	Jekyll Island sand	0.17	1.7	0.30	0.85	1.04	-
	ASTM graded sand	0.35	1.7	0.80	0.90	0.82	0.50
	Blasting sand	0.71	1.9	0.30	0.55	1.03	0.70
	Glass beads	0.32	1.4	1.00	1.00	0.72	0.54
	Granite powder	0.09	6.2	0.40	0.24	1.30	-
	Ottawa #20/30 sand	0.72	1.2	0.90	0.90	0.74	0.50
	Ottawa F-110 sand	0.12	1.7	0.70	0.70	0.85	0.54
	7U7 curshed sand	0.30	3.2	0.20	0.80	0.79	-
	1K9 crushed sand	0.30	3.4	0.20	0.40	1.16	-
	2Z8 crushed sand	0.48	5.0	0.10	0.60	0.86	-
	5Z9 crushed sand	0.40	3.6	0.30	0.90	0.89	-
	6H1 crushed sand	0.33	3.8	0.20	0.80	0.97	-
	9F1 crushed sand	0.33	3.5	0.20	0.80	0.90	-
	3P3 crushed sand	0.27	2.2	0.20	0.70	0.95	-
	6A2 crushed sand	0.33	5.5	0.20	0.75	0.93	-
	5U1 crushed sand	0.32	3.5	0.15	0.70	0.84	-
	Sandboil sand	0.36	2.4	0.55	0.70	0.79	0.51
	1O2 crushed sand	0.25	2.9	0.25	0.80	0.83	-
	1O6 crushed sand	0.21	2.8	0.30	0.70	0.77	-
	6F5 crushed sand	0.25	3.3	0.25	0.80	0.91	-
	8B8 crushed sand	0.32	3.7	0.25	0.80	0.85	-
	3C7 crushed sand	0.26	3.2	0.25	0.80	0.85	-
	2L6 crushed sand	0.28	3.5	0.25	0.80	0.84	-
Sukumaran and Ashmawy (2001)[b]	Daytona Beach sand	0.23	1.4	0.30	0.70	1.00	0.64
	Fraser River sand	0.30	1.9	0.43	0.50	1.13	0.78
	Ottawa #20/70 sand	0.53	2.4	0.32	0.81	0.78	0.47
	Ottawa #45 sand	0.57	2.1	0.24	0.68	1.11	0.75
	Ottawa #60/80 sand	0.21	2.4	0.65	0.78	0.85	0.55
	Ottawa #90 sand	0.27	2.2	0.16	0.60	1.10	0.73
	Syncrude tailings	0.18	2.5	0.20	0.62	1.14	0.59
	Ottawa 20 - 30	0.74	1.1	0.78	0.90	0.74	0.51

DeJong and Christoph (2009)[a]	Q-Rok	0.75	1.5	0.20	0.50	1.14	0.70
Guo and Su (2007)[a]	Sand O	0.38	1.8	0.41	0.93	0.81	0.50
	Sand L	1.64	2.0	0.14	0.57	1.20	0.62
Bolton (1987)[c]	Toyoura sand	0.16	1.5	0.35	0.65	0.97	0.61
Ezaoui and Benedetto (2009)[c]	Hoston sand	0.47	1.4	0.30	0.62	1.04	0.64
Lings and Dietz (2004)[c]	Abraded Leighton Buzzard	0.76	1.3	0.75	0.80	0.80	0.51
Cabalar et al. (2013)[c]	Narli	1.00	3.7	0.75	0.65	0.83	0.52
	Crushed Stone Sand	1.40	2.5	0.45	0.61	0.93	0.62
	Birecik	0.86	3.3	0.65	0.72	0.80	0.55
	Trakya	0.72	6.3	0.35	0.65	0.70	0.49
Barden et al. (1969)[c]	Bronze Ballotini	-	1.6	0.80	0.80	0.74	0.54
	River Welland sand	-	1.7	0.40	0.60	0.94	0.62
	Crushed feldspar	-	6.4	0.25	0.65	0.90	0.56
Tsomokos and Georgiannou (2010)[c]	Ham River sand	0.30	1.3	0.55	0.75	0.87	0.53
	Fontainebleau sand	0.21	1.2	0.65	0.71	0.87	0.54
	M31 sand	0.30	1.3	0.75	0.70	0.87	0.53
	Longstone sand	0.15	1.3	0.30	0.65	1.00	0.61
Coop and Lee (1993)[c]	Ham River	0.28	1.6	0.45	0.65	0.92	0.59
Roberts (1964)[c]	Hawaiian sand	0.60	1.5	0.60	0.75	0.86	0.52
DeBeer (1963)[c]	Mol sand	0.19	1.5	0.65	0.65	0.89	0.56
Rouse et al. (2008)[c]	Badger sand	-	1.3	0.81	0.90	0.69	0.49
Zelasko et al (1975)[b]	Ottawa 20-30	0.72	1.2	0.65	0.87	0.78	0.46
	Ottawa 35-45	0.42	1.2	0.60	0.90	0.82	0.48
	Ottawa 50-70	0.25	1.2	0.52	0.90	0.89	0.53
	Ottawa 70-100	0.18	1.2	0.50	0.90	0.92	0.54
	Ottawa 100-140	0.12	1.2	0.50	0.90	0.92	0.54
	Evanston Beach 20-30	0.72	1.2	0.44	0.71	0.92	0.55
	Evanston Beach 35-45	0.42	1.2	0.43	0.73	0.90	0.52
	Evanston Beach 50-70	0.25	1.2	0.41	0.73	0.92	0.54
	Evanston Beach 70-100	0.18	1.2	0.42	0.72	0.93	0.53
	Franklin Falls 20-30	0.72	1.2	0.36	0.52	1.08	0.62
	Franklin Falls 35-45	0.42	1.2	0.35	0.52	1.04	0.63
	Franklin Falls 50-70	0.25	1.2	0.34	0.52	1.10	0.64
Thomann (1990)[c]	Ottawa 20-30	0.75	1.2	0.75	0.90	0.72	0.51
	Ottawa 50-70	0.22	1.1	0.70	0.80	0.84	0.57
	Ottawa 100-200	0.13	1.9	0.60	0.60	0.90	0.59
	Douglas Lake Sand	0.23	2.4	0.45	0.75	0.83	0.54

	Lake Ackerman Sand	0.34	2.5	0.60	0.80	0.72	0.48
	Agsco 50 - 80	0.25	1.3	0.20	0.50	1.24	0.79
	Daedalus Sand	0.60	4.7	0.75	0.90	0.61	0.36
Yasin and Safiullah (2003)[b]	Teesta sand	0.50	2.5	0.40	0.65	0.92	0.57
	Meghna sand	0.23	1.9	0.20	0.74	0.97	0.66
	Jamuna sand	0.13	1.9	0.10	0.68	1.14	0.72
Moroto and Ishii (1990)[a]	Gabbro	-	1.6	0.27	0.74	0.90	0.65
	Greywacke	-	1.6	0.31	0.65	0.97	0.72
	Onahama	-	1.6	0.32	0.72	0.99	0.71
	Dolelite	-	1.6	0.39	0.76	0.96	0.69
	River gravel	-	1.6	0.43	0.71	0.84	0.55
	Beach gravel	-	1.6	0.58	0.74	0.74	0.53
Shahanazari and Rezvani (2013)[c]	Bushehr Port	0.78	4.5	0.35	0.60	0.91	0.63
	Hormuz Island	0.43	3.2	0.20	0.50	1.05	0.72
Georgiannou and Konstadinou (2013)[c]	M31 sand	0.30	1.6	0.62	0.70	0.87	0.53
	Ottawa sand	0.72	1.4	0.80	0.90	0.74	0.50
Baxter and Mitchell (2004)[c]	Evanston Beach sand	0.30	1.8	0.75	0.80	0.79	0.50
	Density sand	0.50	1.9	0.80	0.90	0.72	0.48
Yang et al. (2010)[c]	Fontainebleau sand	0.21	1.5	0.45	0.75	0.90	0.51
Kumar and Madhusudhan (2012)[c]	Clean sand	0.75	3.8	0.40	0.68	0.90	0.48
Bareither et al. (2008)[b]	P1-S2	0.38	2.2	0.61	-	0.67	0.42
	P1-S4	0.30	2.7	0.59	-	0.70	0.40
	P1-S5	0.44	2.6	0.62	-	0.76	0.43
	P1-S6	0.34	2.4	0.62	-	0.69	0.43
	P1-S1	0.31	1.9	0.50	-	0.76	0.48
	P1-S3	0.31	2.3	0.40	-	0.83	0.50
	P1-S7	0.29	2.0	0.42	-	0.81	0.52
	P2-S3	0.16	2.3	0.24	-	0.96	0.58
	P3-S3	0.54	2.5	0.59	-	0.64	0.37
	P3-S5	0.48	3.0	0.56	-	0.62	0.38
	P3-S6	0.29	2.1	0.36	-	0.77	0.50
	P3-S7	0.22	1.8	0.46	-	0.80	0.51
	P2-S1	0.30	1.9	0.31	-	0.80	0.51
	P2-S2	0.20	2.1	0.29	-	0.83	0.56
	P2-S4	0.32	5.3	0.40	-	0.68	0.39
	P2-S9	0.50	4.2	0.43	-	0.56	0.33
	P2-S10	0.20	2.3	0.31	-	0.75	0.46
	P2-S11	3.50	3.4	0.52	-	0.43	0.26
	P3-S1	0.63	3.2	0.50	-	0.58	0.35
	P3-S2	0.48	4.8	0.48	-	0.70	0.39

		D_{50}	C_u	R		S	e_{max}	e_{min}
	P4-S1	0.58	2.0	0.42	-	0.84	0.56	
	P5-S1	0.69	5.3	0.38	-	0.55	0.31	
	P2-S5	0.64	2.8	0.33	-	0.69	0.44	
	P2-S6	0.27	3.8	0.25	-	0.76	0.46	
	P2-S7	0.15	3.2	0.22	-	0.86	0.52	
	P2-S8	0.50	3.1	0.37	-	0.64	0.40	
	P2-S12	0.42	3.1	0.42	-	0.64	0.39	
	P3-S4	0.70	2.9	0.52	-	0.60	0.37	
	P4-S2	0.48	2.9	0.31	-	0.72	0.44	
	P4-S3	0.77	6.5	0.35	-	0.62	0.33	
Youd (1973)[a]	Mixed sand 1	0.74	1.4	0.34	-	0.80	0.46	
	Mixed sand 2	0.74	2.5	0.35	-	0.69	0.37	
	Mixed sand 3	0.74	4.3	0.37	-	0.58	0.30	
	Mixed sand 4	0.74	8.0	0.37	-	0.49	0.27	
	Mixed sand 5	0.74	4.3	0.37	-	0.64	0.36	
	Mixed sand 6	0.74	1.4	0.19	-	1.26	0.71	
	Mixed sand 7	0.74	2.5	0.19	-	1.10	0.59	
	Mixed sand 8	0.74	4.3	0.19	-	0.93	0.48	
	Mixed sand 9	0.74	8.0	0.19	-	0.80	0.43	
Herle and Gudehus (1999)[c]	Hochstetten sand	0.2	1.6	0.30	-	0.95	0.55	
	Hostun RF sand	0.35	1.7	0.30	-	0.98	0.61	
	Karlsruhe sand	0.4	1.9	0.45	-	0.84	0.53	
	Lausitz sand	0.25	3.1	0.51	-	0.85	0.44	
	Toyoura sand	0.16	1.5	0.30	-	0.98	0.61	
	Zbraslav sand	0.5	2.6	0.30	-	0.82	0.52	

Notes:

D_{50} = 50% particle size (mm), C_u = coefficient of uniformity, R = roundness, S = sphericity, e_{max} and e_{min} = index void ratios.

[a]Roundness and sphericity computed by Wadell's manual procedure.

[b]Roundness and sphericity estimated by visual comparison with standard charts developed by Krumbein and Sloss (1951) or Krumbein (1941).

[c]Roundness and sphericity estimated based on written descriptions or particle images given in the reference.

Figure 4.1(a) shows the R and S pairs for all of the soils. It should be noted that the S values for most of the sands are between 0.6 and 0.8. This is expected. Slender elongated particles are rarely found in nature because they are vulnerable to breakage. The R values range from 0.1 to 1. Extremely angular particles with R less than 0.1 are also rare in nature. Figure 4.1(b) shows the materials are fine to coarse sands with C_u values as high as 9. Thus, the sands range from highly uniform to well-graded.
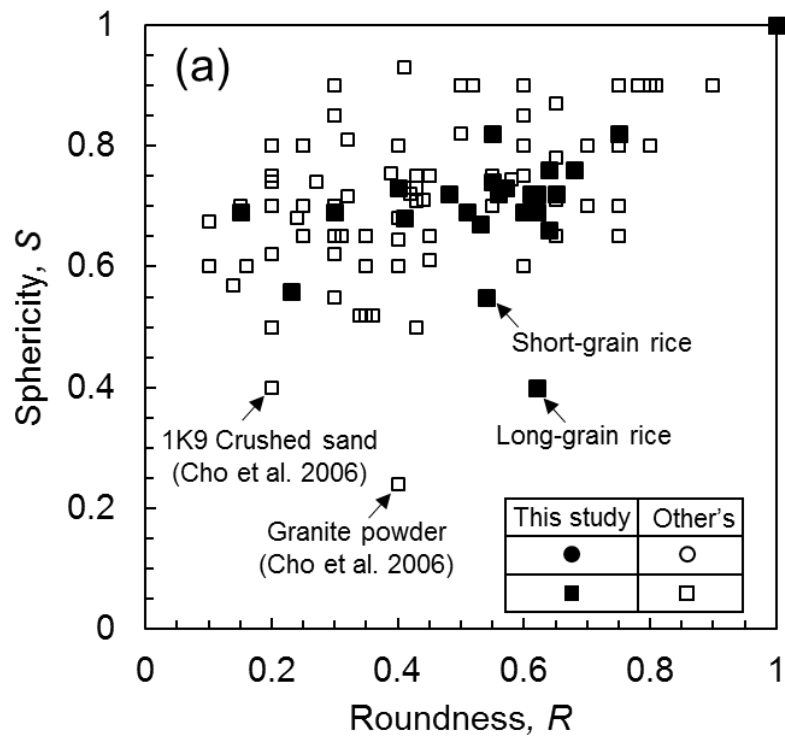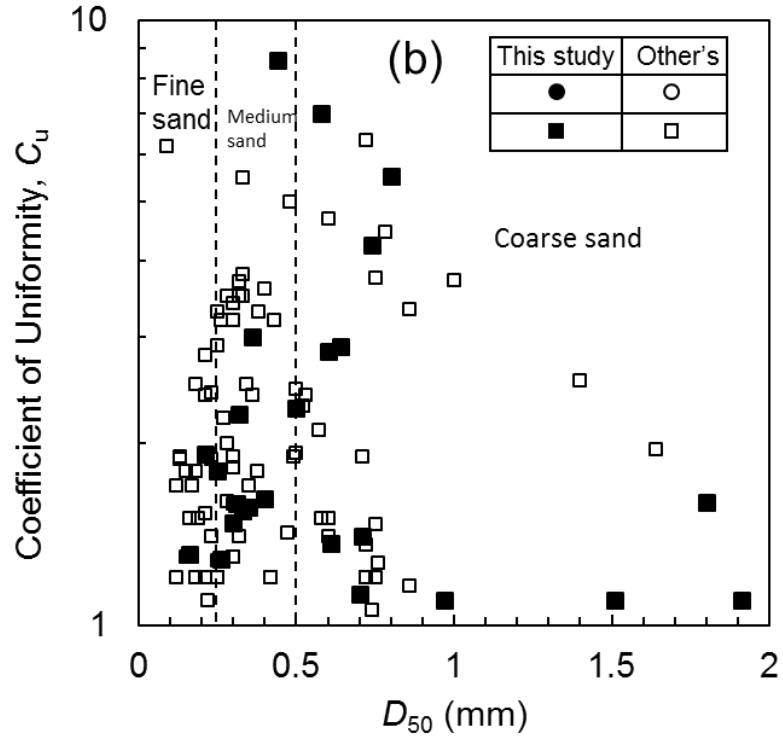
Figure 4.1 Intrinsic properties of the collected soils.

4.1.3   Relationship between Packing and Intrinsic Properties

The influence of roundness (R), sphericity (S), coefficient of uniformity (C_u) and 50% size (D_{50}) on e_{max} and e_{min} was analyzed using the soils in Tables 4.1 and 4.2. First, to focus only on the effects of R and S, only uniform soils with $C_u < 2.5$ were considered. Figures 4.2 and 4.3 were developed using only such relatively uniform sands. They show that both e_{max} and e_{min} decrease nonlinearly with increasing R and S. When initially poured through a funnel to create the e_{max} condition, angular (low R) particles do not pack easily as they do not roll and slide as well as more rounded particles. Elongated (low S) particles could bridge over each other generating high local porosities (Santamarina and Cho 2004). While the general trends of decreasing index void ratios with R and S are unmistakable, there is large scatter in the data and functional relationships based on the data in Figures 4.2 and 4.3 yielded very low correlation coefficients.
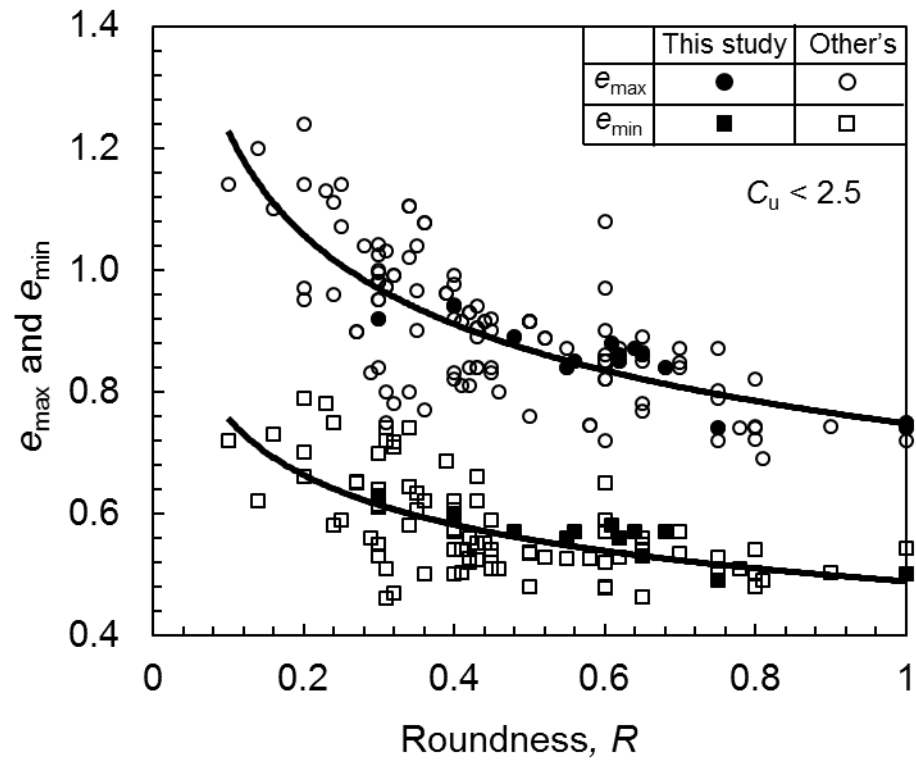
Figure 4.2 Influence of roundness (*R*) on index void ratios.
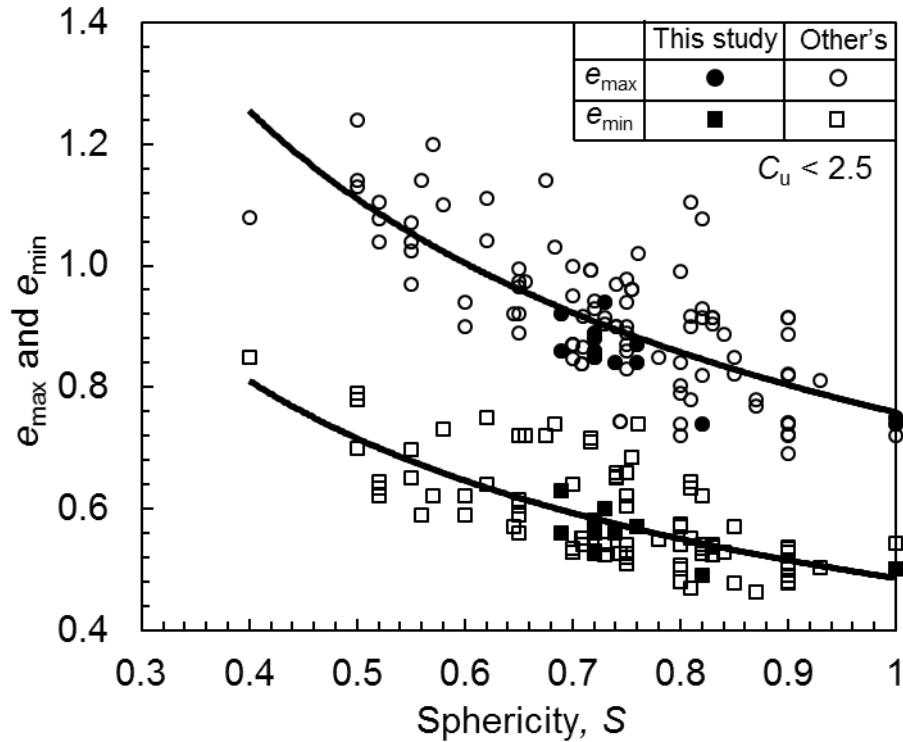
Figure 4.3 Influence of sphericity (*S*) on index void ratios.

Particle gradation is certainly known to affect packing. For well-graded soils, the voids within a skeleton of larger particles will be filled by smaller particles. This will reduce both e_{max} and e_{min} as shown by the trends in Figure 4.4. In this figure, the effects of particle roundness are illustrated through use of different symbols for three *R* ranges: 0.15 to 0.25; 0.26 to 0.49 and 0.50 to 1.00. These three ranges correspond to the "angular", "subangular to subrounded" and "rounded to well-rounded" qualitative descriptions proposed by Powers (1953). While correlations based on Figure 4.4 were slightly better than those based on Figures 4.2 and 4.3, they were still low.
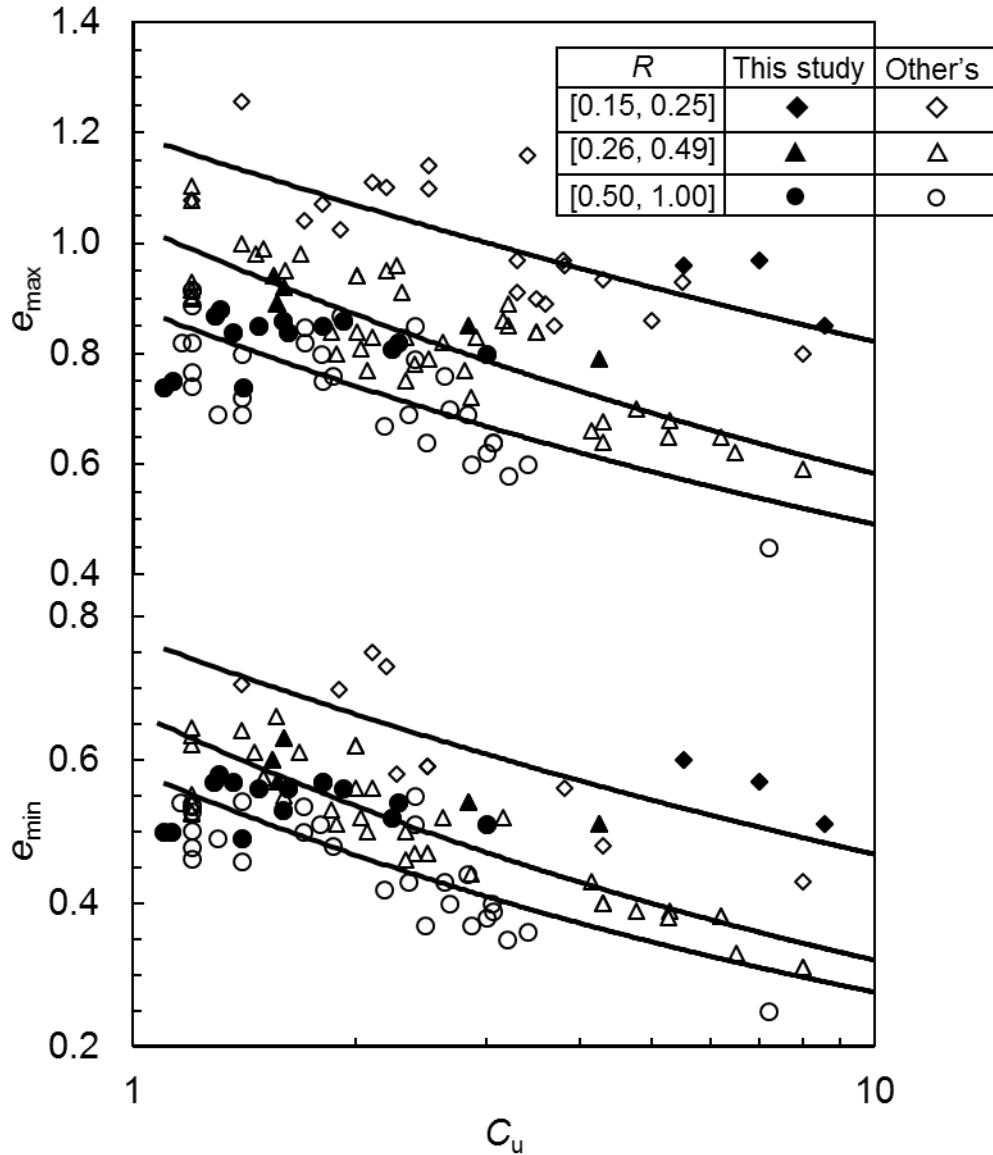
Figure 4.4 Influence of coefficient of uniformity on index void ratios.

Cubrinovski and Ishihara (2006) and Bareither et al. (2008) suggested that e_{max} and e_{min} decrease slightly with increasing D_{50}. The data from Tables 4.1 and 4.2 when plotted in Figure 4.5(a) appears to show this slight trend. However, the previous researchers did not isolate and account for the effects of R, S, and C_u. To minimize these effects, the authors selected the sands in Tables 4.1 and 4.2 having R, S, and C_u in the following narrow ranges: $0.40<R<0.70$; $0.71<S<0.93$ and $1.1<C_u<2.5$. When this reduced data set is plotted in Figure

4.5(b), it shows that D_{50} does not affect e_{max} and e_{min}. This confirms the findings by Dickin (1973). Therefore, the trends observed in Figure 4.5(a) are attributable to the combined effects of R, S, and C_u but not to D_{50}. As such, only R, S, and C_u will be used to develop a comprehensive model to predict e_{max} and e_{min} in the following section.
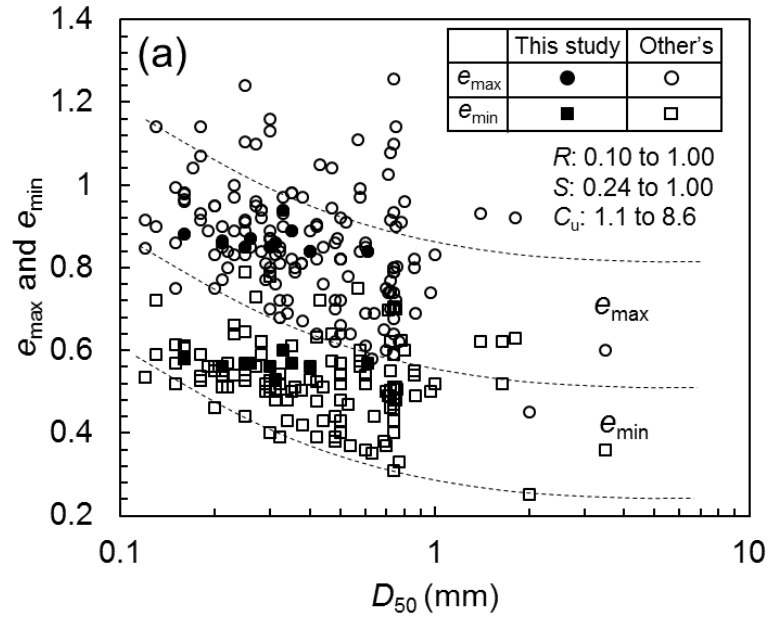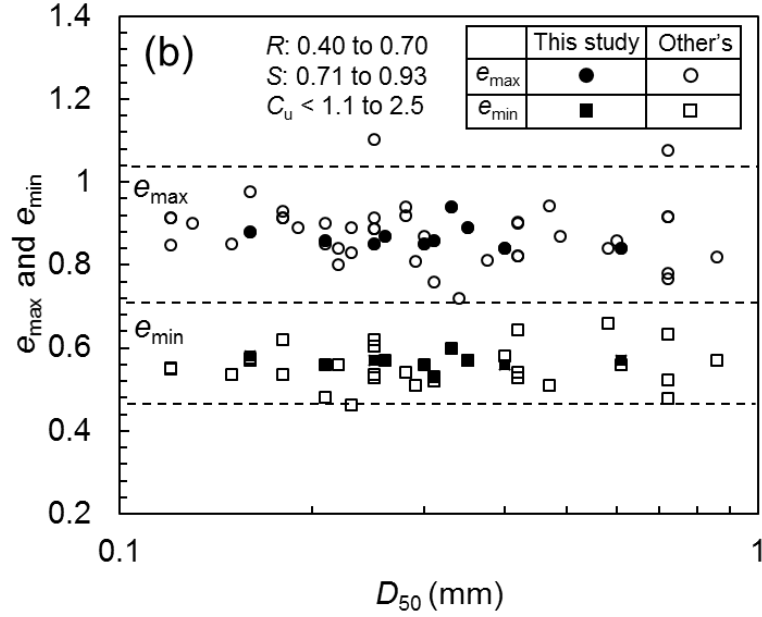
Figure 4.5 Influence of particle size on index void ratios.

4.1.4 Predictive model for e_{max} and e_{min} based on intrinsic soil properties.

To develop the predictive model, the maximum and minimum void ratios of spherical uniform glass beads having $R = S = C_u = 1.0$ were used as reference index void ratios e_{max}° and e_{min}°. The e_{max} and e_{min} of other soils can be related to e_{max}°, and e_{min}° using influence factors I^R, I^S, and I^C that reflect the effects of R, S, and C_u respectively:

$$e_{max} = I_{max}^{R} I_{max}^{S} I_{max}^{C} e_{max}^{\circ} \qquad \text{Equation 4.1}$$

$$e_{min} = I_{min}^{R} I_{min}^{S} I_{min}^{C} e_{min}^{\circ} \qquad \text{Equation 4.2}$$

From ASTM tests for index void ratios, $e_{max}^{\circ} = 0.75$ and $e_{min}^{\circ} = 0.50$.

Using a best fit to the data in Tables 4.1 and 4.2, the influence factors were found and Equations 4.1 and 4.2 became:

76

$$e_{max} = R^{-0.20} S^{-0.25} C_u^{-0.10} e_{max} \qquad \text{Equation 4.3}$$

$$e_{min} = R^{-0.15} S^{-0.25} C_u^{-0.15} e_{min} \qquad \text{Equation 4.4}$$

Equations 4.3 and 4.4 are visualized in Figure 4.6. Each shaded band is for a fixed value of R with two fixed S values establishing the upper and lower boundaries for each band. The upper boundary is for S=0.6 and the lower boundary is for S=0.8. Figure 4.6 reveals that while R has the largest impact on e_{max} and e_{min}, the effect of C_u is also significant. The effect of S is somewhat smaller when considering its typical natural range of 0.6 to 0.8.
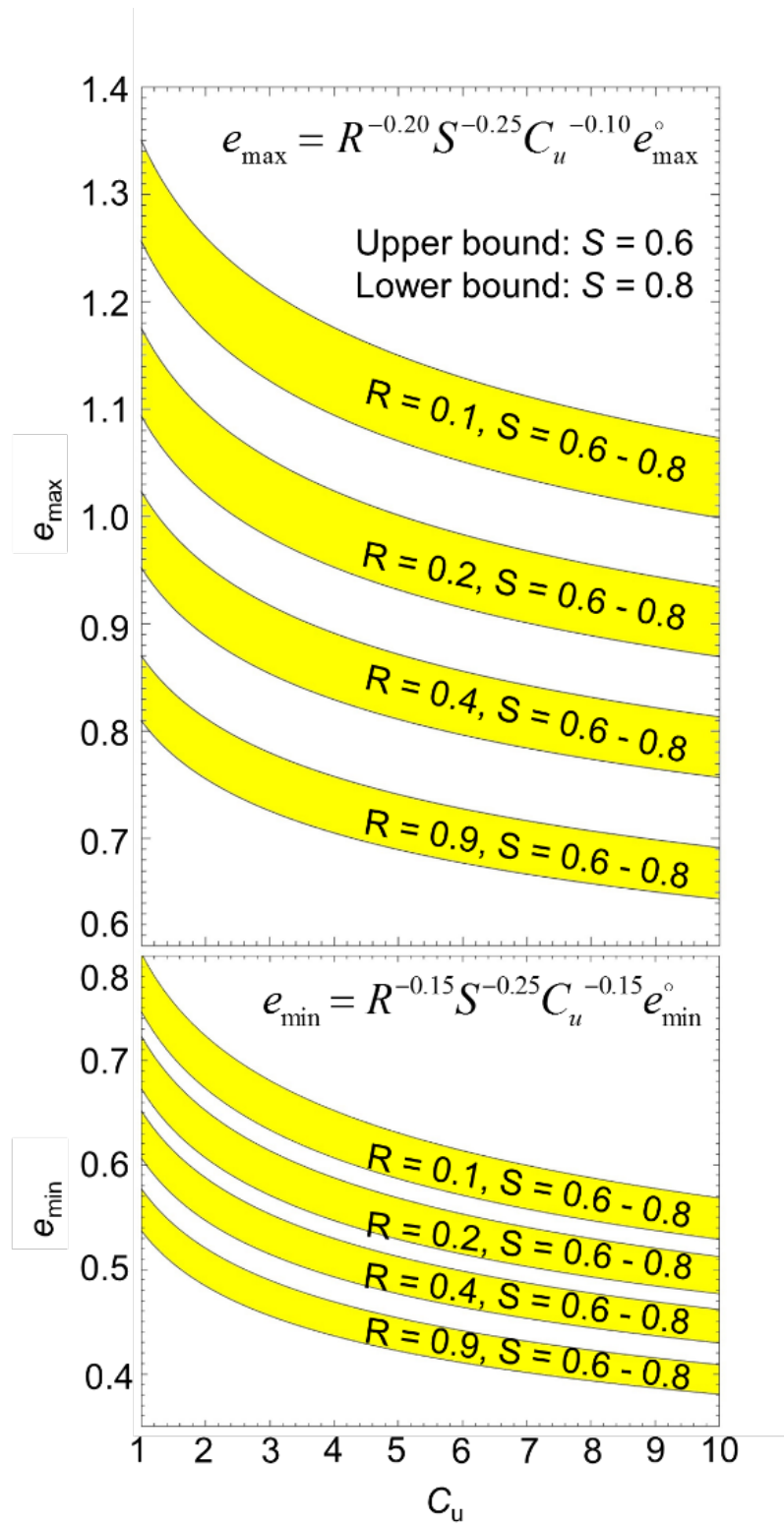
Figure 4.6 Graphical visualization of Equations 4.3 and 4.4.

Interestingly, Equations 4.3 and 4.4 imply that the ratio e_{max}/e_{min} is a function of C_u/R:

$$\frac{e_{max}}{e_{min}} = \left(\frac{C_u}{R}\right)^{0.05} \frac{e_{max}}{e_{min}} \qquad\qquad \text{Equation 4.5}$$

While uniform spheres ($R = C_u = 1.0$) exhibit $e_{max}/e_{min} = 1.5$, sub-rounded borderline SP/SW (C_u=6) sands would have $e_{max}/e_{min} = 1.75$ and very angular well-graded sands would show e_{max}/e_{min} approaching 2.0.

Equations 4.3 and 4.4 were used to predict e_{max} and e_{min} based on R, S, C_u for all of the soils in Tables 4.1 and 4.2. The results are shown in Figures 4.7(a) and 4.7(b) respectively. Most of the predicted values are within ±0.05 (shown by dashed lines in Figure 4.7) of the measurements. The prediction accuracy is quantified by the Mean Absolute Difference (*MAD*) between predictions and measurements. The *MAD* for e_{max} and e_{min} are 0.047 and 0.035 respectively.
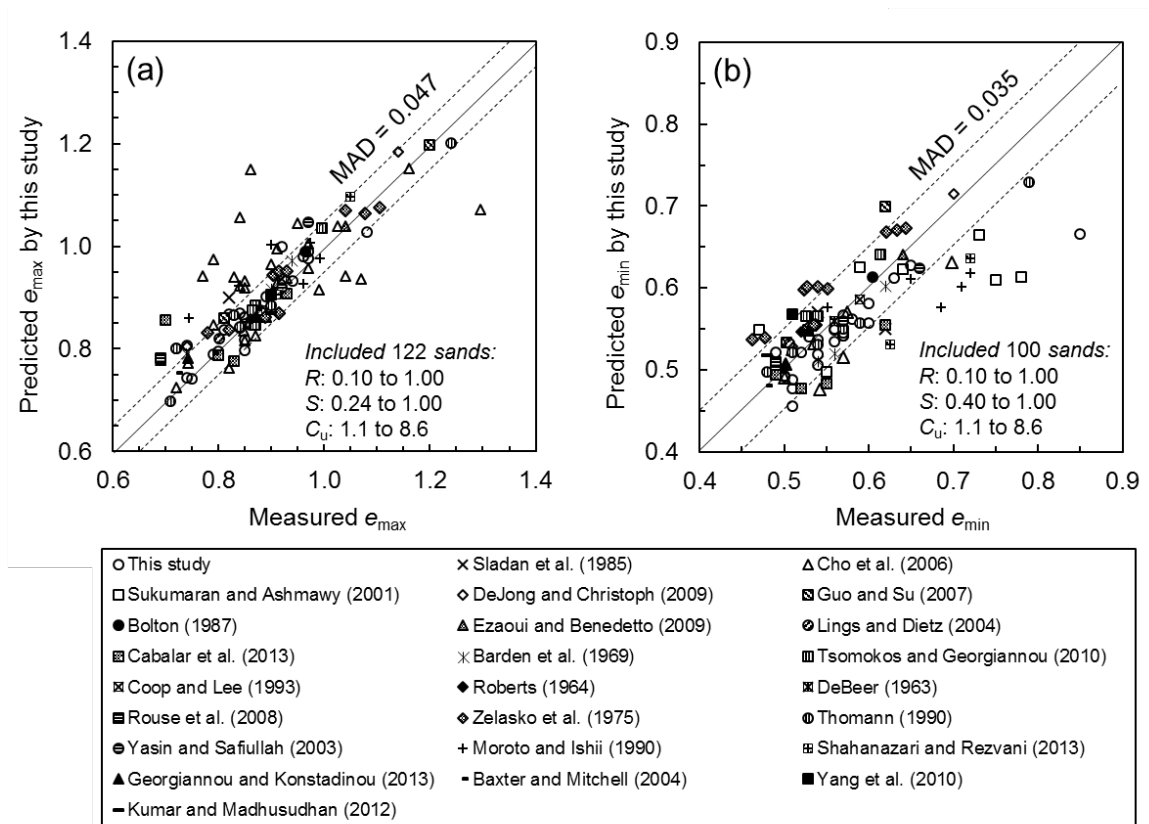
Figure 4.7 Comparisons between observed values and model predictions for index void ratios by Equations. 4.3 and 4.4.

Youd (1973) also developed a generalized set of curves to estimate e_{max} and e_{min} based on C_u and R. His model was therefore used to predict e_{max} and e_{min} for the sands in Tables 4.1 and 4.2. The comparisons between predictions and measurements are shown in Figures 4.8(a) and 4.8(b). Youd's model typically underestimated e_{max} and e_{min} with *MAD* values of 0.180 for e_{max} and 0.186 for e_{min}. The low agreements may be attributed to two factors. First, artificial mixes were used instead of a large range of natural sands. Secondly, sphericity was not considered to be a factor. This study shows that *S* does have some effect on e_{max} and e_{min}.
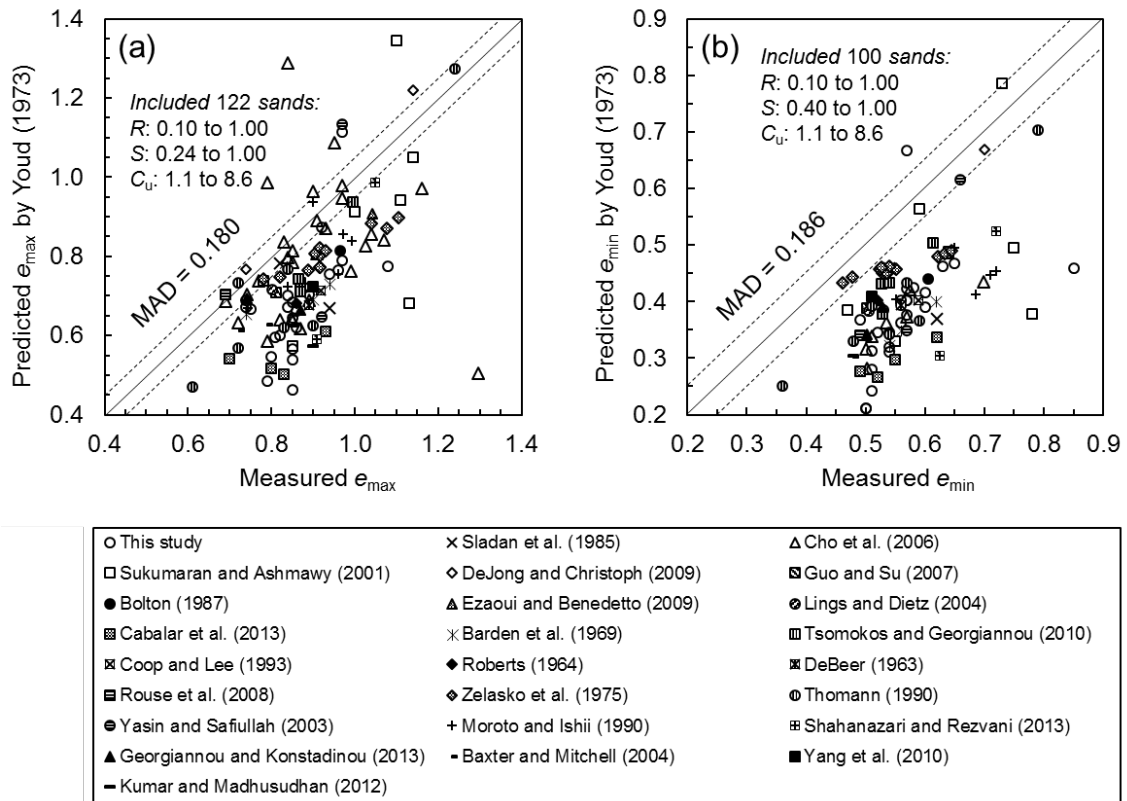
Figure 4.8 Comparisons between observed values and model predictions for index void ratios by Youd (1973).

An earlier model for index packing densities was also developed by Koerner (1969). The comparisons between predictions and measurements are shown in Figures 4.9(a) and 4.9(b). Overall, Koerner tended to overpredict e_{max} at low values of e_{max} and underpredict it at high values of e_{max} with a *MAD* of 0.150. Koerner's predictions for e_{min} were much better with a *MAD* of only 0.064.
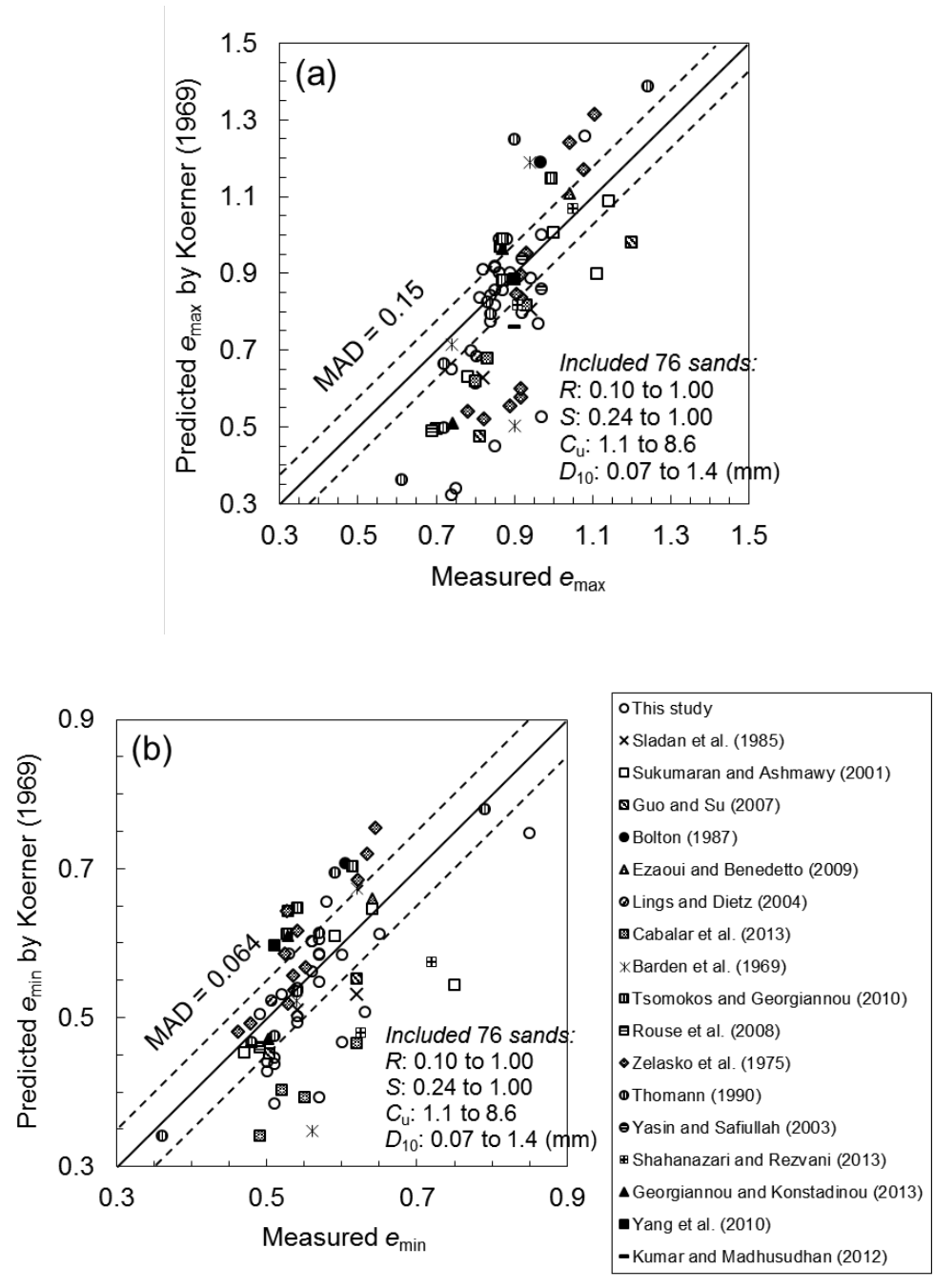
Figure 4.9 Comparisons between observed values and model predictions for index void ratios by Koerner (1969).

4.1.5   Discussion

As observed in Figures 4.7(a) and 4.8(b), the e_{max} and e_{min} for some soils were still not accurately predicted. There may be several reasons for this. First, in the database collected from the literature some values of R and S may not be accurate, particularly if they were estimated from the Krumbein and Sloss (1951) chart which provides particle silhouettes for only five values of R and four values of S (0.2 units apart in each case). It is also well known that experimentally determined e_{max} and e_{min} values for the same soil can vary considerably when tests are performed in different laboratories (Cubrinovski and Ishihara, 2002). In light of these sources of error, the authors also compared the model predictions to only the soils tested for index void ratios in their laboratory. More importantly, the new data set in Table 4.1 reports R and S values obtained by the precise image-based method using large numbers of particles. The results are plotted in Figure 4.10. They show considerably reduced deviations between predicted and measured values with $MAD = 0.022$ for e_{max} and 0.021 for e_{min}.
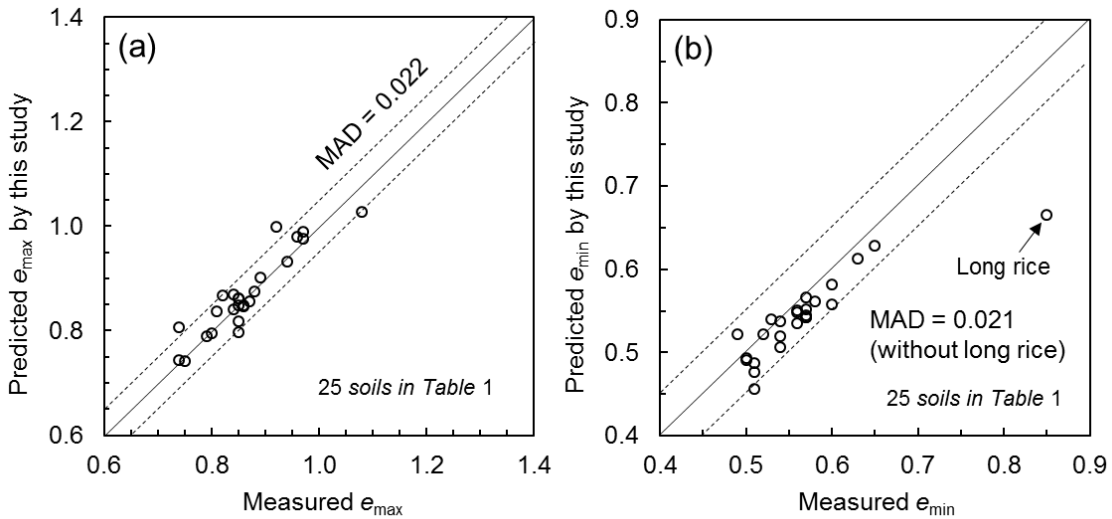
Figure 4.10 Comparisons between observed values and model predictions for index void ratios by Equations 4.3 and 4.4 when using only image-based computational geometry methods for R and S.

There are still other properties including fabric (uniform or random orientation of non-spherical particles) and mineralogy (crushability and surface roughness) that were not considered in this study. For example, Figure 4.10(b) suggests that the model does not handle very elongated particles such as long-grain rice ($S= 0.40$) which may develop a strong fabric during deposition. The rice is also more crushable than most earth materials. Therefore, further investigation is needed to assess the roles of these other properties on index void ratios. Finally, the models developed in this study should not be used for gap-graded soils. Additional research is needed on such soils.

4.1.6 Conclusions

A comprehensive study using sands of various shapes and gradations was conducted to develop models for the index void ratios, e_{max} and e_{min}, as a function of particle roundness (R), sphericity (S) and coefficient of uniformity (C_u). The models utilize the index void ratios of perfectly uniform glass beads ($R = S = C_u = 1.0$) as baseline values to which factors are applied to account for the effects of R, S and C_u in real sands.

The models achieve better predictions for e_{max} and e_{min} compared to previous attempts for three reasons: 1) all of the major intrinsic properties affecting e_{max} and e_{min} were considered; 2) a large database of sands having different R, S and C_u was employed; and 3) image-analysis and computational geometry allowed for precise determination of R and S of for a large and therefore statistically reliable number of particles. The study also yielded a simple expression for the ratio e_{max}/e_{min} as a function of C_u/R.

4.2 Compressibility of sands

4.2.1 Introduction

The linearity between soil void ratio, e, and the logarithm of effective vertical stress, σ_v', has been known since early in the last century. It led to standardized oedometer testing for estimation of soil compression and settlement of ground surfaces due to structural loading, groundwater lowering or other causes of increase in effective stress. While the relationship

is commonly associated with consolidation of clayey soils, the linear trend is also observed in coarse-grained soils as long as particle crushing does not occur.

Idealized 1D compression behavior of a sand is illustrated in e - log σ_v' space in Figure 4.11 from Vesić and Clough (1968). It shows relatively small compressibility during the pre-crushing stage. Subsequently, even if a soil is compressed from different initial void ratios, at high pressures the e-logσ_v' lines converge to a unique Limiting Compression Curve (LCC).
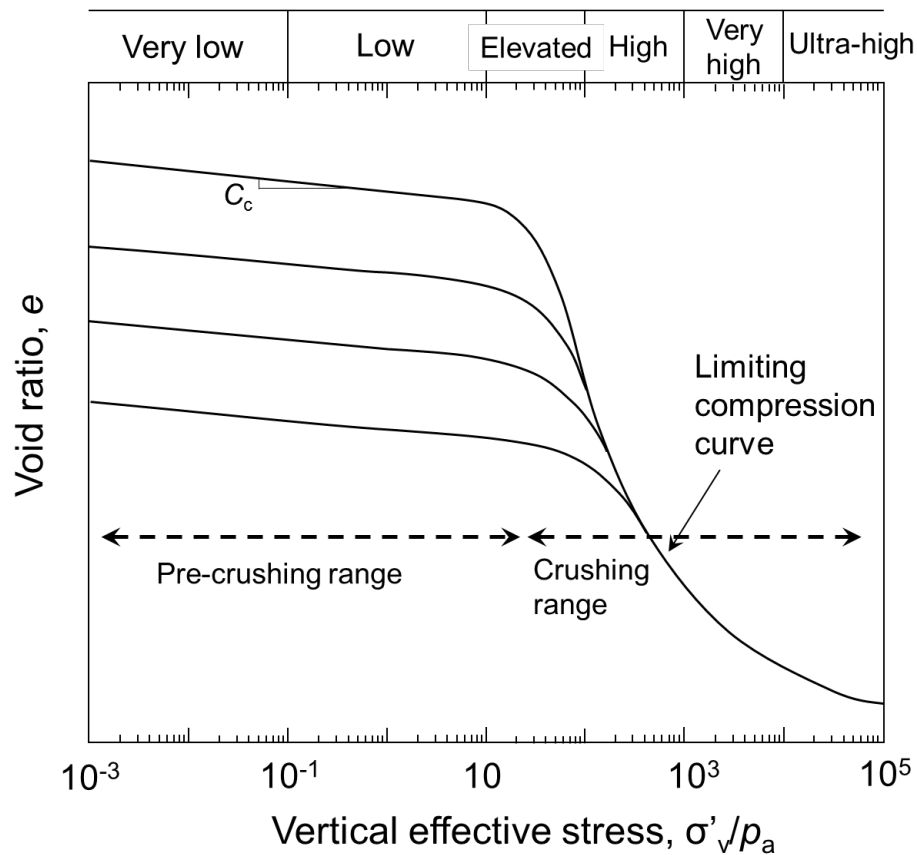
Figure 4.11 Conceptual interpretation of one-dimensional compression for cohesionless soils (After Vesić and Clough, 1968).

The compression index, $C_c = \Delta e / \Delta \log \sigma_v'$ during the pre-crushing stage is approximately constant and in the range between 0.001 and 0.10 (Nakata et al., 2001a; 2001b; Cho et al., 2006; Mesri and Vardhanabhuti, 2009). At elevated stress levels, compression increases

significantly with C_c jumping to between 0.10 and 1.0. Such values are more typical of normally consolidated clays (Pestana and Whittle, 1995; Miura et al., 1984).

The stress level marking the onset of crushing was referred to as a yield stress σ_Y' by Mesri and Vardhanabhuti (2009). However, it should not be mistaken for the preconsolidation (maximum historic) effective stress which marks the onset of irreversible compression. The pre-crushing stage is not elastic and the recompression index, $C_r = \Delta e / \Delta \log \sigma_v'$ during unloading & reloading is typically 0.3 to 0.7 of C_c as will be confirmed in this chapter. The σ_Y' threshold depends mainly on soil mineralogy. Mesri and Vardhanabhuti (2009) concluded that σ_Y' may range from 0.3 MPa for biogenic carbonate sands to 30 MPa for quartz sands.

Both laboratory tests (Roberts and de Souza, 1958; Hendron, 1963; Hardin, 1985; Nakata et al., 2001a; 2001b; Chuhan et al., 2002; 2003; Mesri and Vardhanabhuti, 2009; Altuhafi and Coop 2011) and Discrete Element Method (DEM) studies (Bolton et al., 2008) show progressive particle damage during compression of cohesionless soils. Prior to crushing, compression is achieved by abrasion of particle surface asperities and breakage of sharp particle corners. These have been defined as Level I and Level II damage respectively (Nakata et al., 2001b; Mesri and Vardhanabhuti, 2009). At elevated stress levels, compression is induced by splitting of the more heavily loaded particles into two or more pieces. Most researchers refer to this as particle crushing. This crushing of the load-bearing structure under very high pressures is defined as Level III damage (Nakata et al., 2001b; Mesri and Vardhanabhuti, 2009).

The compression index of coarse-grained soils depends on both intrinsic and state properties. The intrinsic properties could include particle size distribution, particle shape and mineralogy. Particle size distribution may be quantified by the 50% size by weight, D_{50} and the coefficient of uniformity, C_u. Particle shape includes sphericity S, roundness R, and surface roughness. State properties include void ratio e, relative density D_r, effective confining stress and fabric. A given soil has a fixed set of intrinsic properties but can be at various states that could change with time or stress history.

The geologic transport mode and the distance travelled strongly affect the shape of soil particles. For example, glacial soils tend to be more angular than fluvial deposits due to their lower time in transport (Bareither et al. 2008). Parker (2008) observes that even within the same water system, fluvial soils downstream (i.e. a longer travel distance) had on average more rounded particle shapes than their upstream counterparts. Margolis and Krinsley (1974) note that eolian soil particles have an overwhelmingly high roundness, while weathered regolith have largely angular particles. It is also worth noting that particles with extremely angular shape are rarely found in nature and are more commonly formed by manually crushing coarser materials in laboratories or industrial settings. Examples of these highly angular materials include the W30A crushed concrete and the brown fused aluminum oxide abrasive used in this study.

At pre-crushing stress levels, the amount of Level I and Level II damage is controlled predominantly by particle shape, relative density and particle size distribution. Non-spherical, angular and rough soils sustain more Level I and Level II damage and thus exhibit a higher C_c. Naturally, D_r plays a role as it reflects the average numbers of intergranular contact points per grain and thus affects the contact stress levels. It also reflects the availability of void space for particles to pack into. The previous section showed that size distributions and particle shapes establish the limit index void ratios, e_{max} and e_{min} needed to compute D_r. Level III damage (crushing) is mainly controlled by particle mineralogy and stress levels.

This section investigates and quantifies the influence of intrinsic soil properties including R, S, D_{50}, C_u and D_r on C_c and C_r of sands at pre-crushing stress levels. Twenty four sands exhibiting a wide range of particle shapes, gradations, and geologic origins were collected for the study. Particle size distributions were determined by sieve analysis according to ASTM C 136 (2014). The particle shapes were determined using a computational geometry algorithm developed in chapter 3 which allows characterization of a statistically large number of particles in each specimen. One dimensional oedometer tests were performed on the soils. The new data was augmented with previously published results where compressibilities, size distributions and shapes were reported or could be deduced.

Through statistical analyses, functional relationships are developed for C_c and C_r. The accuracy of the model is assessed by comparison of predicted and observed values.

4.2.2 Materials and test procedures

The twenty four newly collected soils are listed in Table 4.3. The soils are grouped in the table according to geologic origin in order of decreasing R. Within each group by geologic origin, the soils are also arranged according to decreasing R. In the case of the old marine seabed, glacial, and alluvial soils, the specimens are arranged according to their presumed travel distance. For example, among the alluvial soils, the New Madrid sand was carried much further by the Mississippi River than was the Capitola sand within the Soquel Creek, and as such the New Madrid sand is listed above the Capitola sand in Table 4.3. This relationship with travel distance can in part explain why the New Madrid sand has a significantly larger R than the Capitola sand. Two different sized glass beads were also included in Table 4.3 to increase the range of R and S values. The intrinsic properties investigated to develop the models for C_c and C_r included R, S and particle size distribution as defined by D_{50} and C_u. Table 4.3 summarizes these parameters for all of the soils in the study. It is noted that the well graded 30A (W30A) soil was sieved to also yield a uniform version of 30A (P30A).

Table 4.3 Test results for 24 specimens in this study.

Geologic Origin	Soil Type	Description	Shape		Gradation		Packing		Compressibility		
			R	S	D_{50}	C_U	e_{max}	e_{min}	D_r	C_c	C_r
Manufactured to be Round	Small Glass Beads	Synthetic silica spheres	1.00	1.00	0.70	1.1	0.75	0.50	0.92	0.0020	0.0017
									0.52	0.0120	0.0064
									0.12	0.0220	0.0100
	Large Glass Beads	Synthetic silica spheres	1.00	1.00	0.97	1.1	0.74	0.50	0.92	0.0020	0.0016
									0.50	0.0100	0.0060
									0.08	0.0200	0.0090
Old Marine Seabeds (Former Beach)	Ottawa 20-30	Silica mined from St. Peter's Sandstone	0.75	0.8	0.71	1.4	0.7	0.49	0.92	0.0035	0.0021
									0.84	0.0060	0.0026
									0.64	0.0150	0.0040
									0.40	0.0200	0.0100
									0.28	0.0220	0.0130
									0.08	0.0300	0.0140
	Brady, TX	Silica sand mined from Riley Formation's sandstone	0.68	0.8	0.61	1.4	0.8	0.57	0.89	0.0040	0.0027
									0.52	0.0200	0.0100
									0.19	0.0260	0.0130
	Scotts Valley, CA	Zayante soil mined from Santa Margarita Formation's sandstone	0.40	0.7	0.33	1.5	0.9	0.60	0.97	0.0070	0.0038
									0.56	0.0280	0.0095
									0.18	0.0320	0.0120
Current Beach	Chesterton, IN Dunes	Beach sand	0.64	0.87	0.26	1.3	0.87	0.57	0.90	0.0047	0.0023
									0.50	0.0230	0.0090
									0.13	0.0300	0.0130
	Chesterton Beach, IN	Beach sand	0.64	0.7	0.64	2.9	0.9	0.54	0.87	0.0060	0.0040
									0.55	0.0160	0.0078

Category	Location	Description									
									0.13	0.0360	0.0130
	Michigan Dunes	Beach sand	0.62	0.72	0.30	1.5	0.85	0.56	0.97	0.0048	0.0023
									0.52	0.0240	0.0110
									0.17	0.0360	0.0150
	Muskegon, MI	Beach sand	0.55	0.7	0.40	1.6	0.8	0.56	1.00	0.0046	0.0035
									0.43	0.0180	0.0090
									0.00	0.0300	0.0130
Eolian	Nevada Sand	Fine eolian silica dune sand	0.61	0.72	0.16	1.3	0.88	0.58	0.87	0.0060	0.0040
									0.43	0.0200	0.0079
									0.13	0.0340	0.0150
	Rincon, NM	Recent eolian deposit	0.55	0.70	0.36	3.0	0.80	0.51	0.90	0.0073	0.0050
									0.62	0.0220	0.0090
									0.17	0.0360	0.0140
	Oakland Co., MI	Glacio-fluvial	0.65	0.72	0.31	1.6	0.86	0.53	0.94	0.0042	0.0026
									0.33	0.0210	0.0090
									0.03	0.0340	0.0130
	Class IIA, MI	Glacio-fluvial	0.62	0.69	0.21	1.9	0.86	0.56	0.90	0.0042	0.0029
									0.57	0.0250	0.0090
									0.10	0.0320	0.0130
Glacial	Griffin, IN	Glacio-fluvial	0.60	0.69	0.74	4.3	0.81	0.51	0.93	0.0061	0.0028
									0.43	0.0260	0.0090
									0.00	0.0380	0.0130
	Michigan 2NS	Glacio-fluvial	0.53	0.7	0.5	2.3	0.8	0.54	1.00	0.0041	0.0021
									0.46	0.0190	0.0120
									0.14	0.0320	0.0140
	Upper Peninsula, MI (UP)	Glacial	0.51	0.69	0.60	2.8	0.85	0.54	0.94	0.0065	0.0048
									0.48	0.0220	0.0100

Origin	Location	Soil description	D_{50}	S	R	C_u	e_{max}	e_{min}	D_r	C_c	C_r
									0.10	0.0380	0.0150
Alluvial	New Madrid, MO	Old Mississippi river alluvium	0.57	0.73	0.32	2.2	0.81	0.52	1.00	0.0032	0.0025
									0.41	0.0250	0.0100
									0.00	0.0300	0.0120
	Treasure Island, CA	Dredged San Franscisco Bay alluvium	0.56	0.7	0.25	1.8	0.9	0.57	0.93	0.0046	0.0034
									0.46	0.0260	0.0100
									0.00	0.0350	0.0150
	Capitola, CA	Soquel Creek alluvium	0.48	0.72	0.35	1.6	0.89	0.57	0.94	0.0069	0.0036
									0.50	0.0220	0.0100
									0.13	0.0300	0.0120
Colluvial	Fort Davis, TX	Weathered volcanic colluvium	0.41	0.68	0.44	8.6	0.85	0.51	0.91	0.0080	0.0052
									0.50	0.0300	0.0150
									0.12	0.0450	0.0160
Manufactured to be Angular	Brown Fused Aluminum Oxide (BFAO)	Coarse commercial abrasive	0.30	0.69	1.80	1.6	0.92	0.63	0.93	0.0110	0.0066
									0.48	0.0280	0.0120
									0.07	0.0450	0.0170
	Crushed Gabbro	Crushed igneous rock	0.23	0.6	0.8	5.5	1	0.60	0.94	0.0180	0.0090
									0.58	0.0320	0.0140
									0.14	0.0480	0.0180
	P30A	Poorly-graded crushed concrete	0.15	0.7	0.72	1.2	1.20	0.87	0.94	0.0220	0.0150
									0.52	0.0420	0.0180
									0.12	0.0600	0.0210
	W30A, MI	Well-graded crushed concrete	0.15	0.69	0.58	7.0	0.97	0.57	0.93	0.0170	0.0110
									0.50	0.0380	0.0170
									0.10	0.0580	0.0200

Note: D_{50} = 50% by weight size (mm), C_u = coefficient of uniformity, R = roundness, S = sphericity, e_{max} and e_{min} = limit index void ratios, D_r = relative density, C_c and C_r = primary compression index and recompression index.

The compression and recompression indices C_c and C_r were determined by oedometer testing at dry conditions following ASTM D2435. A 6.35 cm (2.5 in) diameter ring was used and the specimens were prepared in loose, medium dense, and dense conditions. The specimens were loaded in approximately doubling increments up to 300 kPa then unloaded to 50 kPa. The maximum vertical stress of 300 kPa corresponds to stress magnitudes commensurate with Level I and Level II damage where the effects of mineralogy are not yet felt (Mesri and Vardhanabhuti 2009; Cho et al. 2006). The results for W30A and P30A, which are typical, are shown in Figure 4.12. The observed C_c and C_r values for all of the soils are provided in Table 4.3.
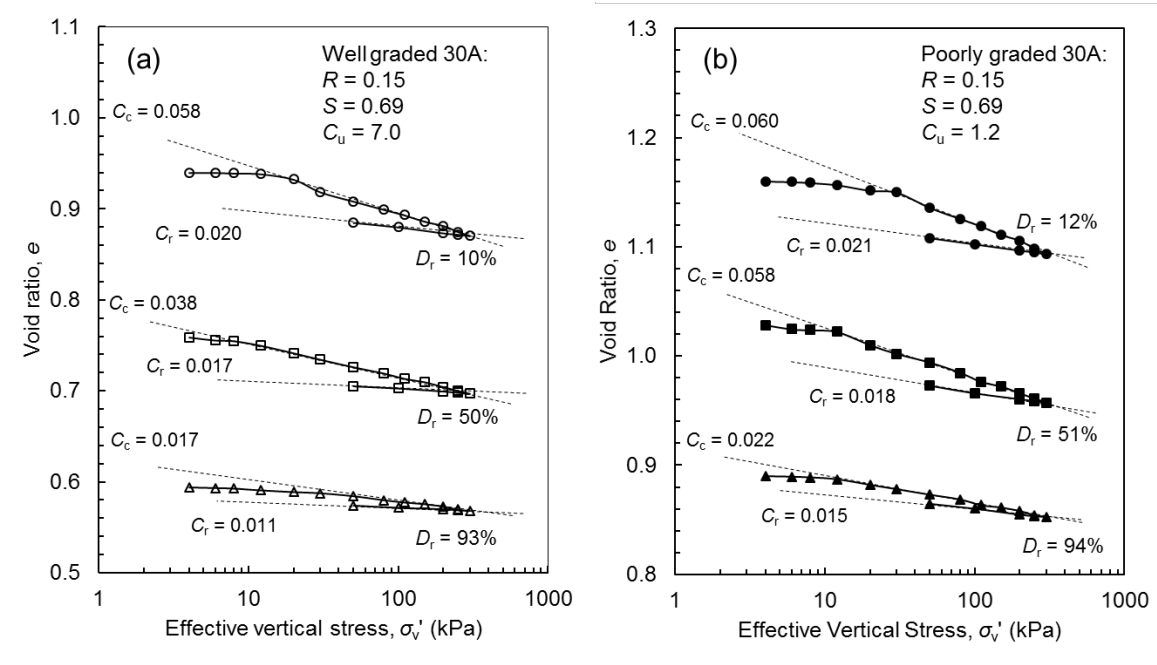
Figure 4.12 Typical oedometer test results on: a) W30A and b) P30A.

As a supplement to the new data in Table 4.3, the authors also compiled results from 52 other sands found in previously published works in which D_{50} and C_u were provided. This supplemental data is included in Table 4.4. The study by Cho et al. (2006) reported R and S values for each sand. However, other works did not provide R values. They gave only qualitative descriptions of particle roundness. In such cases, the R values were estimated by the authors. In other cases, images of the sands were shown which allowed for the

deployment of computational geometry method for R and S. The C_c and C_r values reported in Table 4.4 were all obtained in the stress range between 10 kPa and 300 kPa which is comparable to the test range used in this study.

Table 4.4 Data on fifty two sands from previously published papers

Source	Soil type	Gradation		Shape		Packing		Compressibility		
		D_{50}	C_u	R	S	e_{max}	e_{min}	D_r	C_c	C_r
Pestana and Whittle (1995)[c]	Quiou	0.60	1.5	0.35	-	1.20	0.78	0.40	0.0260	-
								0.71	0.0160	-
								0.88	0.0100	-
	Feldspar	0.70	4.5	0.35	-	1.10	0.89	0.05	0.0400	-
								1.29	0.0080	-
Nakata et al. (2001)[b]	Glass beads	0.93	1.2	1.00	1.00	0.70	0.60	1.00	0.0004	-
	Toyoura sand	0.20	1.3	0.35	0.65	0.98	0.61	0.45	0.0220	-
								0.80	0.0150	-
								0.98	0.0060	-
Nakata et al. (2001b)[c]	Silica	0.75	2.1	0.35	-	0.86	0.43	0.42	0.0300	-
								0.96	0.0070	-
	Aio	1.14	1.2	0.30	-	0.97	0.70	1.00	0.0100	-
Rahim (1989)[c]	Ganger	0.17	2.5	0.15	-	-	-	0.40	0.0400	-
Hendron (1963)[c]	Wabash River sand	0.56	3.0	0.65	-	-	-	0.05	0.0340	-
								0.71	0.0160	-
	Pennsylvania sand	1.35	1.5	0.50	-	0.88	0.60	0.63	0.0170	-
								0.74	0.0120	-
Debeer (1963)[b]	Mol sand	0.19	1.5	0.65	0.65	0.89	0.56	0.68	0.0150	-
Lee and Seed (1967)[b]	Sacramento River	0.21	1.5	0.45	0.70	1.03	0.61	0.38	0.0240	-
								0.60	0.0150	-
								0.76	0.0100	-
								1.00	0.0050	-
Robert (1964)[b]	Hawaiian	0.60	1.5	0.45	0.75	0.86	0.72	0.14	0.0350	-
								1.00	0.0040	-
Coop and Lee (1993)[b]	Ham River	0.20	2.4	0.65	0.75	0.92	0.59	0.39	0.0200	-
Thomann (1990)[b]	Ottawa 100-200	0.13	1.9	0.60	0.60	0.90	0.59	1.00	0.0060	0.0030
								0.03	0.0400	0.0160
	Douglas Lake sand	0.23	2.4	0.45	0.75	0.83	0.54	0.00	0.0400	0.0160
								1.00	0.0100	0.0050

Reference	Sand	D_{50}	C_u	R	S	e_{max}	e_{min}	D_r	C_c	C_r
	Agsco 50-80 Sand	1.30	1.2	0.20	0.50	1.24	0.79	0.00	0.0380	0.0170
								1.00	0.0065	0.0034
	Ottawa 20-30 Sand	0.75	1.2	0.75	0.80	0.72	0.51	0.00	0.0300	0.0130
								1.00	0.0025	0.0018
	Daedalus sand	0.60	4.7	0.75	0.80	0.61	0.36	0.00	0.0400	-
								0.20	0.0360	-
								0.52	0.0280	-
								0.72	0.0180	-
								0.76	0.0180	-
Cho et al. (2006)[a]	Nevada sand	0.15	1.8	0.60	0.85	-	-	-	0.0059	0.0034
	Ticino sand	0.58	1.5	0.40	0.80	-	-	-	0.0050	0.0042
	Margaret river sand	0.49	1.9	0.70	0.70	-	-	-	0.0046	0.0034
	ASTM 20/30 sand	0.60	1.4	0.80	0.90	-	-	-	0.0038	0.0029
	Ponte Vedra sand	0.18	1.8	0.30	0.85	-	-	-	0.0052	0.0036
	8M8 crushed sand	0.38	3.3	0.20	0.70	-	-	-	0.0220	0.0042
	9C1 crushed sand	0.52	2.3	0.25	0.70	-	-	-	0.0050	0.0038
	1K9 crushed sand	0.30	3.4	0.20	0.40	-	-	-	0.0160	0.0059
	5Z9 crushed sand	0.40	3.6	0.30	0.90	-	-	-	0.0067	0.0042
	6H1 crushed sand	0.33	3.8	0.20	0.80	-	-	-	0.0170	0.0088
	9F1 crushed sand	0.33	3.5	0.20	0.80	-	-	-	0.0080	0.0042
	3P3 crushed sand	0.27	2.2	0.20	0.70	-	-	-	0.0180	0.0046
	6A2 crushed sand	0.33	5.5	0.20	0.75	-	-	-	0.0100	0.0042
	2Z8 crushed sand	0.48	5.0	0.10	0.60	-	-	-	0.0088	0.0034

Note: D_{50} = 50% by weight size (mm), C_u = coefficient of uniformity, R = roundness, S = sphericity, e_{max} and e_{min} = limit index void ratios, D_r = relative density, C_c and C_r = primary compression index and recompression index.
[a]The R and S were estimated by visual comparison with standard charts developed by Krumbein and Sloss (1951).
[b]The R and S were estimated by authors based on particle images
[c]The R and S were estimated by authors based on descriptions given in the paper

The intrinsic properties of all the collected soils from Tables 4.3 and 4.4 are plotted in Figure 4.13. The S values of most sands fall in the range of 0.6 to 0.8 as shown in Figure 4.13(a). This relatively narrow range is fully expected since very elongated particles are rarely found in nature as they are vulnerable to breakage. The R values range from 0.1 to 1.0. Extremely angular particles with R less than 0.1 are also rare in nature, as noted previously. Figure 4.13(b) shows the studied material range from fine to coarse sand and the C_u values show the sands ranging from uniform to well-graded.
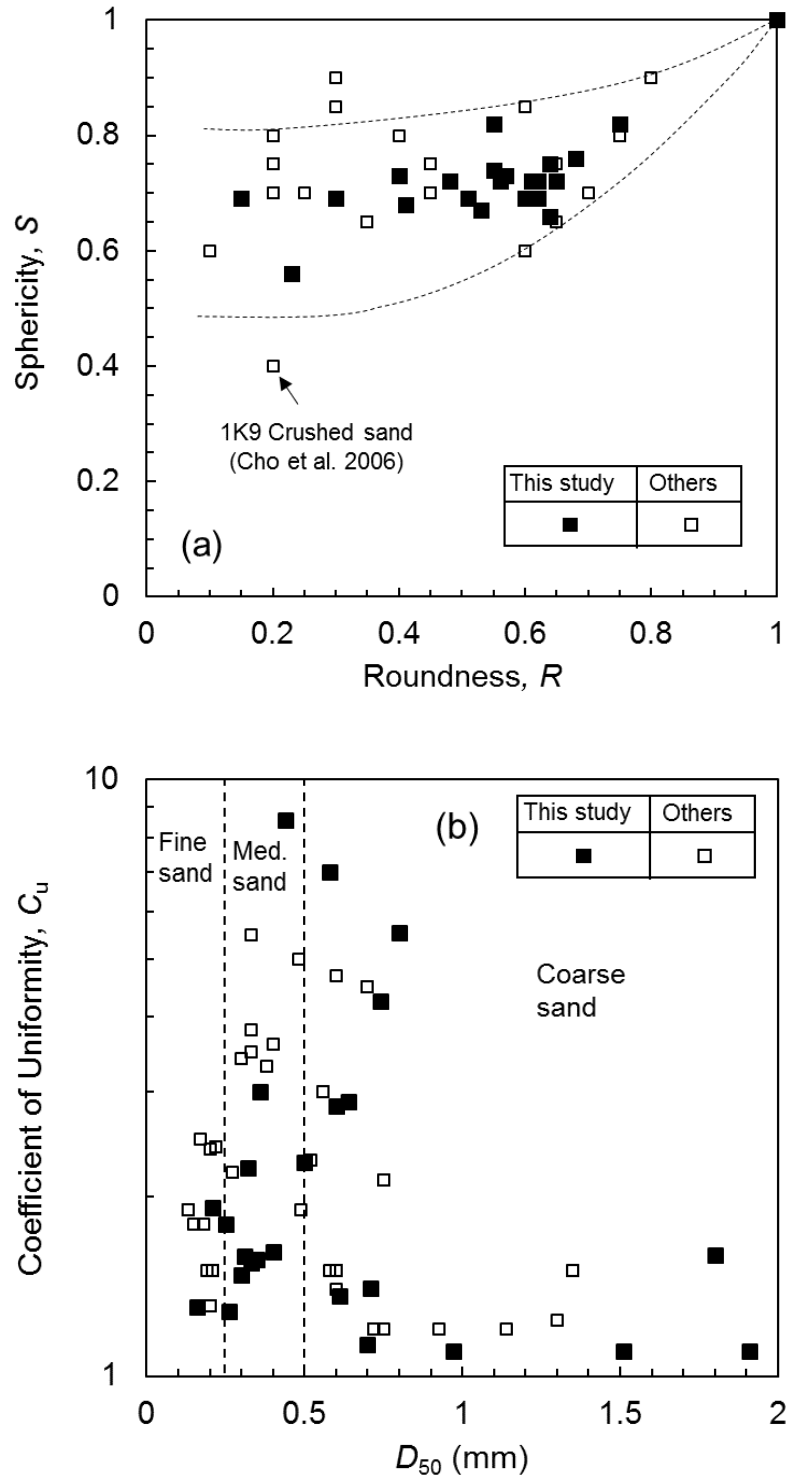
Figure 4.13 The intrinsic properties of the collected soils: (a) roundness and sphericity; (b) mean particle size and gradation.

4.2.3 Compression index

The effects of R, S, C_u, and D_{50} on C_c are now evaluated. As shown in Figure 4.14, C_c decreases with increasing R and with increasing S. In Figure 4.14(b), the C_c values of both W30A and P30A do not follow the trend lines of the other sands. This is because 30A is an extremely angular material ($R = 0.15$) which dominates the sand's behavior. Angular particles have more surface protrusions, sharp corners and initial high void ratios. Therefore, during compression, larger particle movements will occur due to more abrasions and breakages of the protrusions and sharp corners. More particle breakage induces large vertical movements and thus larger C_c.
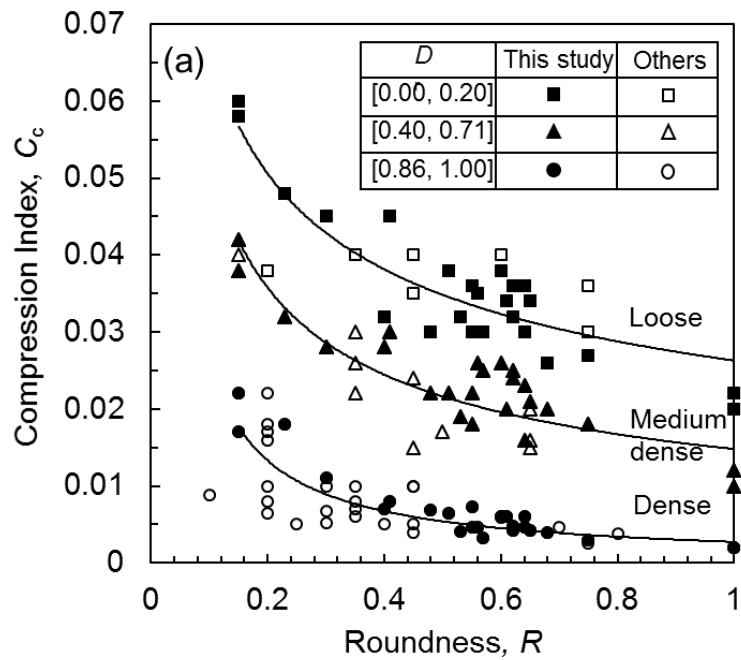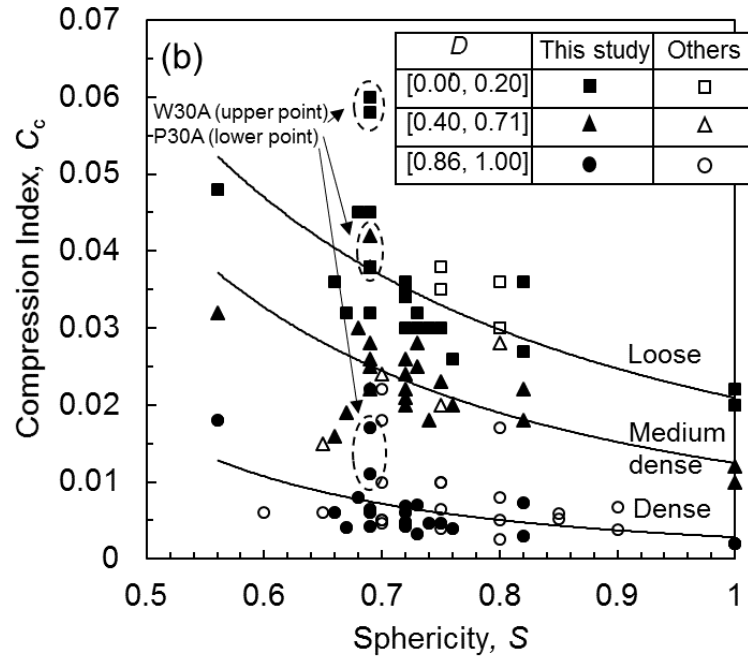
Figure 4.14 The influence of: a) roundness and b) sphericity on compression index.

In order to examine the effect of C_u on C_c, W30A with $C_u = 7.0$ was compared to P30A with $C_u = 1.2$. These two specimens have similar R, S, and D_{50} values and therefore their effects are discounted. The oedometer results for these two soils is shown in Figure 4.12. The C_c values for W30A and P30A are compared in Figure 4.15(a). As expected, the C_c decreases only slightly when C_u increases from 1.2 to 7.0. Naturally, this is because the P30A has more voids ($e_{max}=1.20$; $e_{min}=0.87$) compared to the W30A ($e_{max}=0.97$; $e_{min}=0.57$). Particle size appears to have no direct influence on C_c as revealed by Figure 4.15(b).
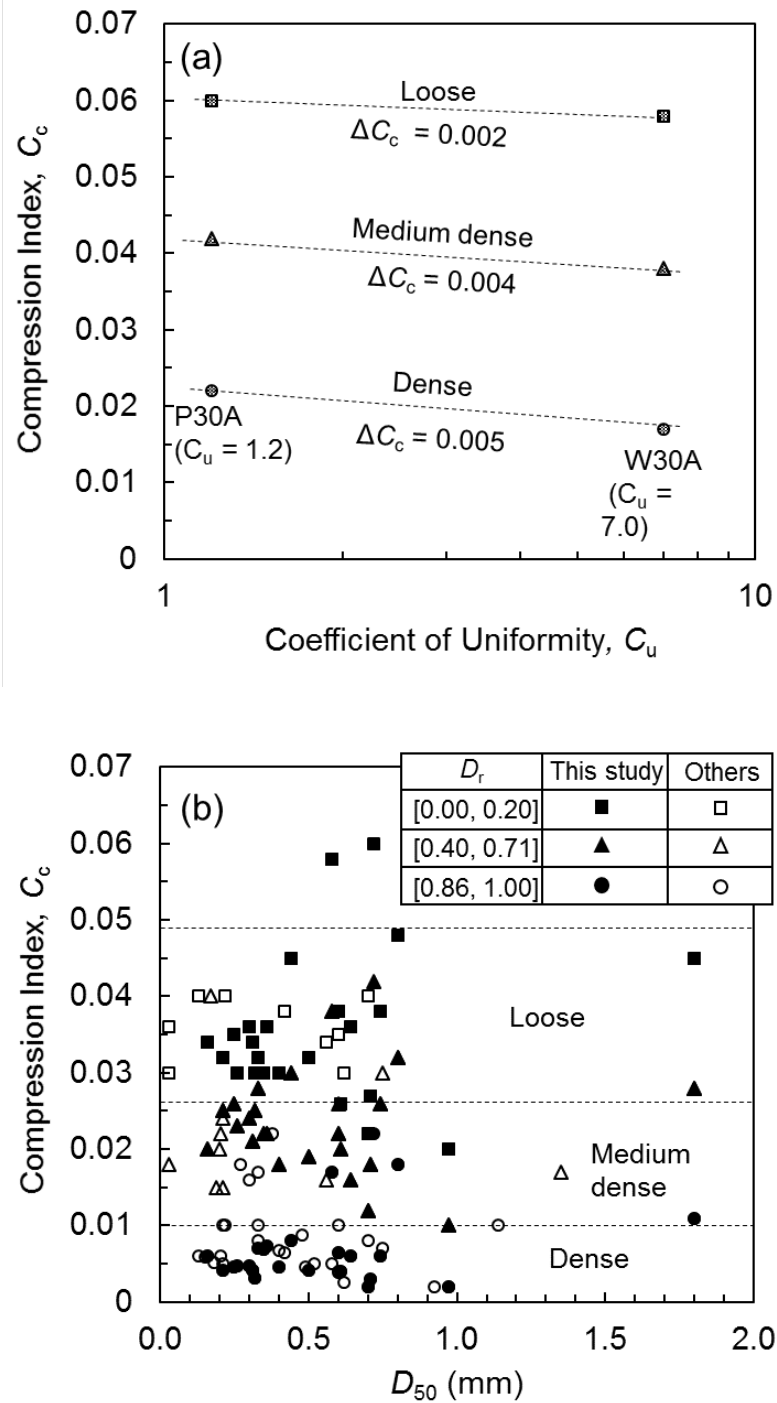
Figure 4.15 The influence of: (a) coefficient of uniformity; (b) 50% size by weight on compression index.

Having observed that S, C_u and D_{50} appear to have limited direct effect on C_c it is worth pointing out that Zheng and Hryciw (2016a) showed that e_{max} and e_{min} depend on the three

intrinsic properties R, S, and C_u by Equations 4.3 and 4.4. Therefore, particle sphericity and size distribution indirectly affect C_c and C_r through D_r which in turn will affect C_c as follows.

This research found that $(1 - D_r/2)$, rather than simply D_r, has the strongest correlation with C_c. Therefore, a relationship between C_c and $(1 - D_r/2)$ was sought. Ottawa sand was tested at D_r = 0.08, 0.28, 0.40, 0.64, 0.84, and 0.92. The six resulting C_c values are plotted in Figure 4.16. The C_c increases linearly with $(1 - D_r/2)$. The results of four other materials having different R and C_u, each tested at three different D_r's, are also shown in Figure 8 and fitted by the solid lines. The slopes of the lines, k depend primarily on R, although, there may be secondary effects of other intrinsic properties. The k value certainly increases with increasing particle angularity (decreasing R).

Figure 4.16 The influence of relative density and roundness on compression index.

99

4.2.4 C_c Model development

A functional model for C_c at pre-crushing stress levels could be developed by combining the previously described effects of intrinsic (R, S, C_u and D_{50}) and state (D_r) properties. However, the authors found that using only R and D_r yields very acceptable predictions for C_c. This may be attributed to two factors: first, the S value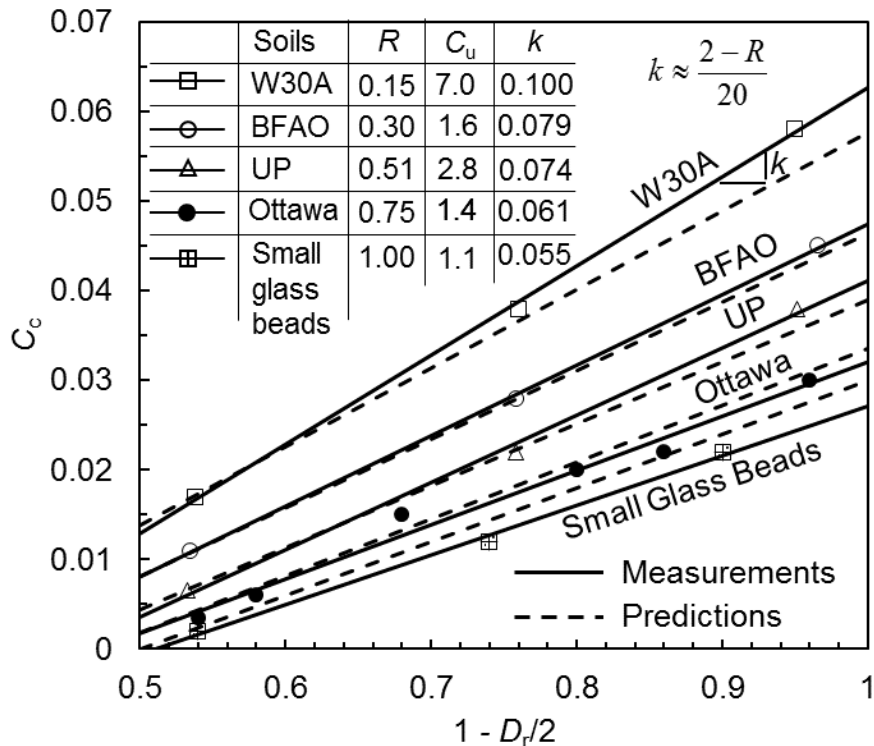s for the majority of soils fall in a fairly narrow range between 0.6 and 0.8. While occasional individual particles of sand (more typically aggregate) could have S values lower than 0.6, it is rare that natural soils possess average S values below 0.6. In Figures 4.15(a), C_u ranges from 1.2 to 8.5. Yet, C_u has only a limited effect on C_c. Figure 4.16 discloses a linear relationship between C_c and $(1 - D_r/2)$ in which the slope k is related to R. It was hoped that k and R would be linearly related and indeed, k is approximately equal to $(2-R)/20$. However, the fit was not as good as by a power law. Therefore, the following model form is proposed:

$$C_c = A \cdot R^m \left(1 - \frac{D_r}{2}\right) - B \qquad \text{Equation 4.6}$$

where A, B, and m are empirical coefficients. The precision offered by using three coefficients will be revealed shortly.

A Robust Multiple Linear Regression (RMLR) analysis was used to find A, B, and m. The RMLR minimizes the effects of outliers to the overall fitting model. This is achieved by assigning weights to each data point and tuning them iteratively using a process called "iteratively reweighted least squares" (Holland and Welsch 1977). In the first iteration, each point is assigned an equal weight. Then the weighted least square method is used to estimate the coefficients for fitting a model to the data points. In the second iteration, the weights of all the points are recomputed based on their divergence from the model's first iteration prediction such that the points further from the predictions are given lower weights. The weighted least square process is again used to fit a new model to the reweighted data points in the second iteration. The process is repeated in subsequent iterations so that the weights of outliers will become progressively lower resulting in their influence being minimized in the fitting. The iterations terminate when the values of the coefficient converge to a specified tolerance. In this study, the tolerance was set to 0.001.

There are 113 sets of data in Tables 4.3 and 4.4 having all of the requisite parameters (R, D_r, and C_c) for model development. Of these, 56 tests were randomly selected for training data and the remaining 57 tests were test data that will be used for evaluation. The training data was used by the RMLR to search for the optimal coefficients A, B, and m for Equation 4.6. The model with these determined values is then evaluated by the test data. The Mean Average Difference (*MAD*) between the predicted C_c and measured values from the test data is computed as MAD_1. A different set of 56 sands is then randomly selected as the training data and the second model is developed. The computed *MAD* for the second C_c model is MAD_2. The process is repeated 1000 times and the model having the smallest *MAD* (=0.0029) was found to be:

$$C_c = 0.06R^{-0.2}\left(1 - \frac{D_r}{2}\right) - 0.03 \qquad \text{Equation 4.7}$$

Equation 4.7 was plotted using dashed lines for the five soils shown in Figure 4.16. In Figure 4.17, lines of equal C_c are shown in R-D_r space according to Equation 4.7 with the 75 test results from Table 4.3 superimposed for comparison.

Figure 4.17 Visulization of the proposed model for compression index.

The predictions of C_c by Equation 4.7 are also plotted versus the measured values in Figure 4.18(a). The C_c values are larger than 0.01 for sands in the medium and loose states while being less than 0.01 in dense states. The dense state region is enlarged in Figure 4.18(b). For the medium and loose states, most predicted C_c values are within ±0.005 of the actual measured values as shown by the dashed lines in Figure 4.18(a). The MAD for all of the sands is 0.0029. Most of the predictions in the dense state were within ±0.002 of the measurements as shown by the dashed lines in Figure 4.18(b). In this region, the MAD was only 0.0015. Overall, Equation 4.7 does a very good job of predicting C_c. It is worth

noting that the model predicts essentially $C_c=0$ for very dense ($D_r=1.0$) perfectly round ($R=1.0$) spheres. At the other extreme, for very loose ($D_r=0$) crushed material (say $R=0.1$) C_c approaches 0.07.

(a)

Includes 113 tests:
R: 0.15 to 1.00
D_r: 0.00 to 1.29

MAD = 0.0029

Predicted C_c by this study

Measured C_c

○ This study
△ Penstana and Whittle (1995)
✕ Nakata et al. (2001a)
◉ Nakata et al. (2001b)
◇ Rahim (1989)
▦ Hendron (1963)
● Debeer (1963)
✳ Lee and Seed (1967)
▲ Robert (1964)
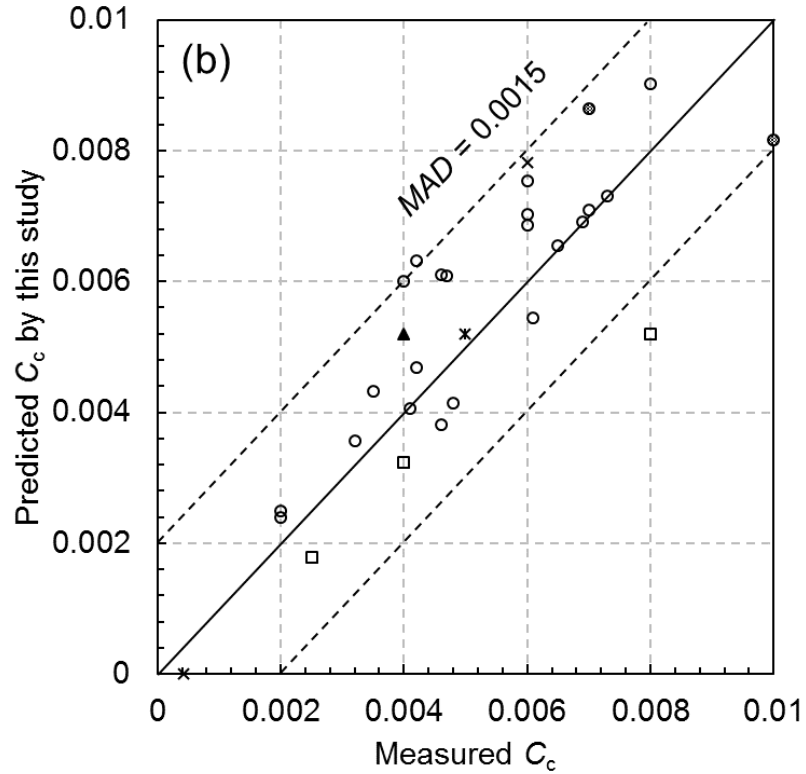■ Coop and Lee (1993)
□ Thomann (1990)
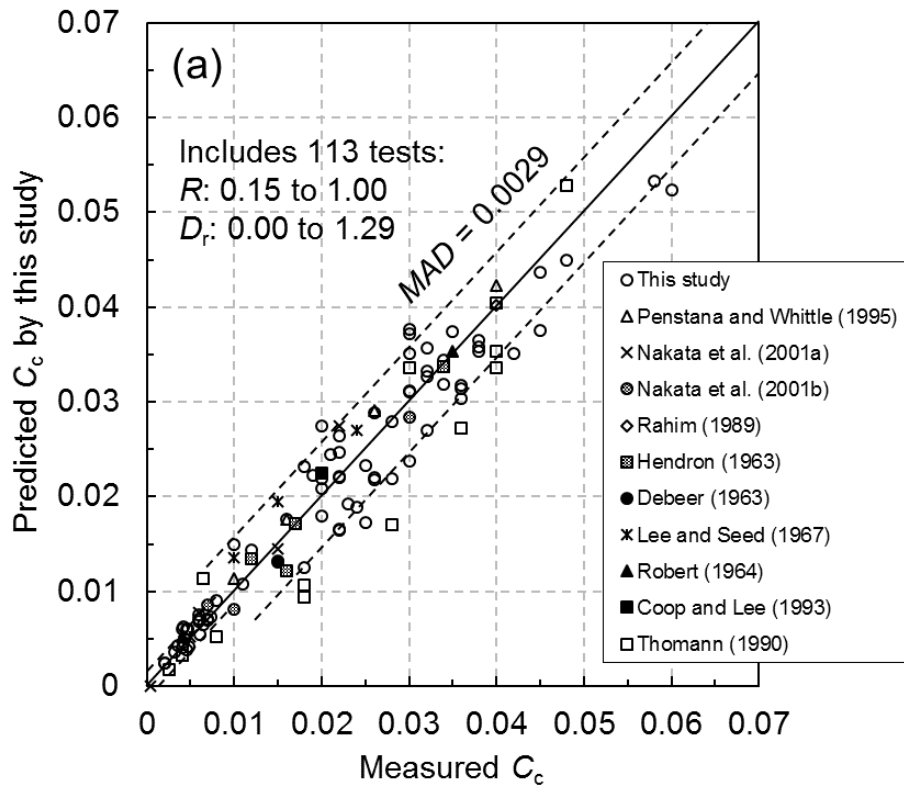
Figure 4.18 Comparisons of predicted and measured compression index: a) 0 to 0.07 range; b) expansion of the 0 to 0.001 range.

Cho et al. (2006) performed a series of oedometer tests on uniform sands at dense conditions. Their tests results are included in Table 4.4. They introduced regularity, ρ, as the average of roundness and sphericity and proposed: $C_c = 0.0032\rho^{-1.5}$ for dense conditions. The equation was therefore used to predict C_c for 36 sands in this study that had D_r between 0.76 and 1.00 and for which both R and S were available. The results are shown in Figure 4.19. Most of the predictions are within ±0.002 of the measurements and the MAD is 0.0038. As such, for dense sands Cho et al.'s equation is virtually as good as the model developed in the present study. However, whereas it is only for high D_r, Equation 4.7 is usable for the full range of D_r.
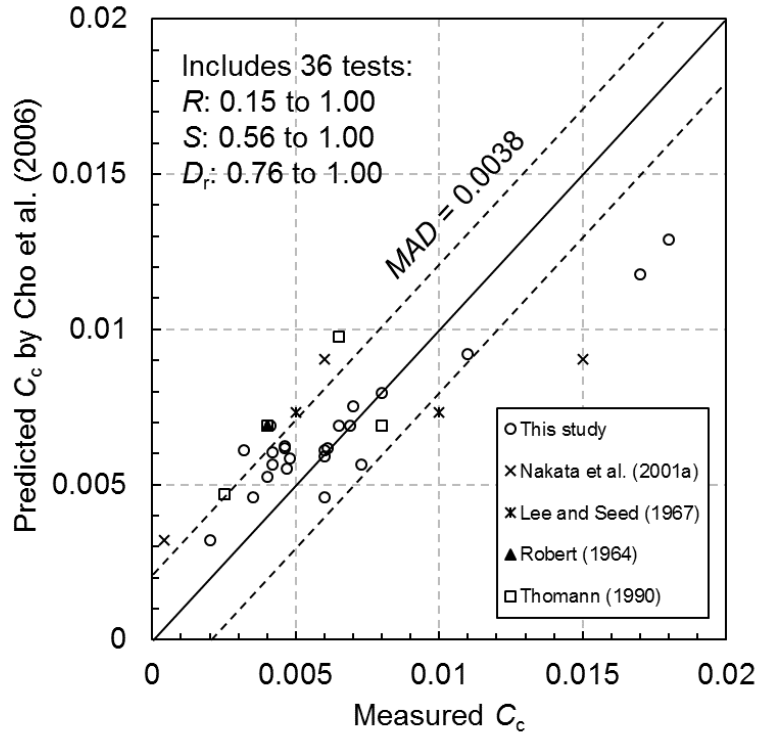
Figure 4.19 Comparison between measurement and prediction of compression index by Cho et al. (2006).

4.2.5   Recompression Index

The recompression index C_r is often related to C_c through the ratio C_r/C_c. The ratio reflects the reversibility or elasticity of a soil with $C_r/C_c = 1.0$ indicating completely reversible elastic deformation. For clays, C_r/C_c is typically between 0.10 and 0.20. For sands, C_r/C_c should logically be larger for looser while smaller for denser sands. The authors therefore selected soils from Table 4.3 having D_r at three distinct levels around 0.13, 0.50, and 0.90. The observed C_r/C_c ratios of these three D_r groups are plotted versus R in Figure 4.20. As expected, C_r/C_c increases with D_r. At each relative density, the C_r/C_c also increases linearly with R. That is also quite rational. Rounded sands tend to behave more elastically since there are no protrusions on the particles to suffer damage. By contrast, in angular sands irreversible deformations occur due to Level I and Level II particle damage at small and sharp corners. Of course, this is not yet Level III particle crushing.
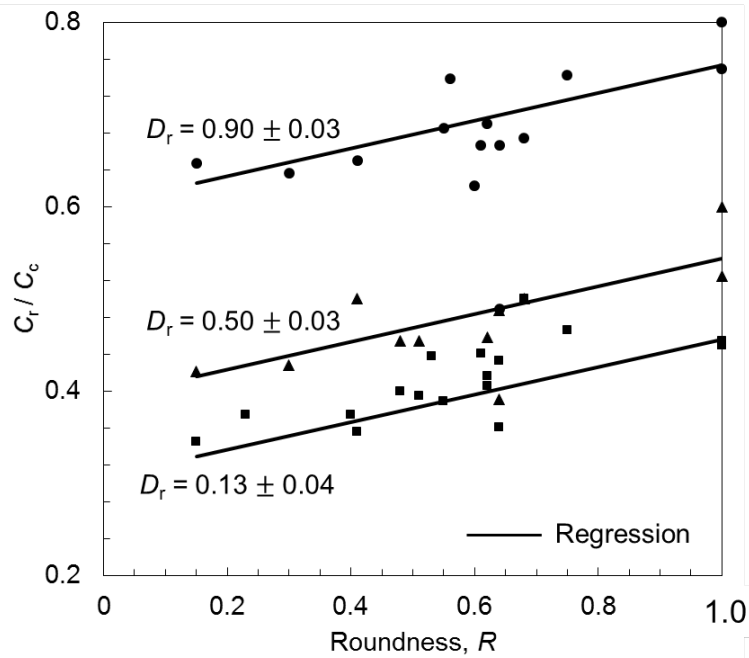
Figure 4.20 The influences of roundness and relative density on the ratio of compression index to recompression index.

Fortuitously, the slopes of all three lines in Figure 4.20 are nearly identical thus yielding a simple linear approximation for C_r/C_c:

$$\frac{C_r}{C_c} = 0.15\left(R + 2.5D_r^2 + 2\right)$$

Equation 4.8

Since R of sands ranges from 0.1 to 1.0 and D_r ranges from 0 to 1.0, the C_r/C_c predicted by Equation 4.7 will range between 0.3 for very loose very angular sands to over 0.8 for very dense rounded sands. By comparison, C_r/C_c is typically 0.1 to 0.2 for clays. Equations 4.7 and 4.8 were used to predict C_r for the soils in Tables 4.3 and 4.4. The comparisons between predictions and measurements are shown in Figure 4.21(a).
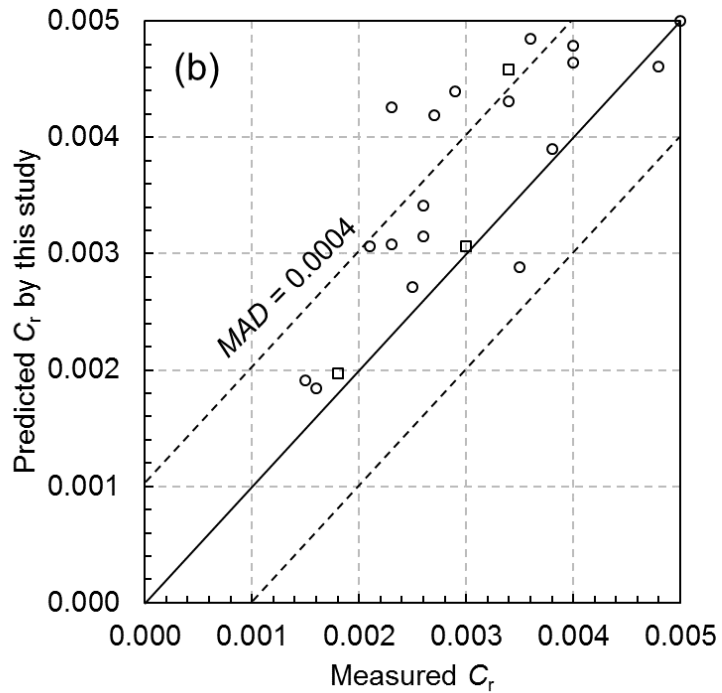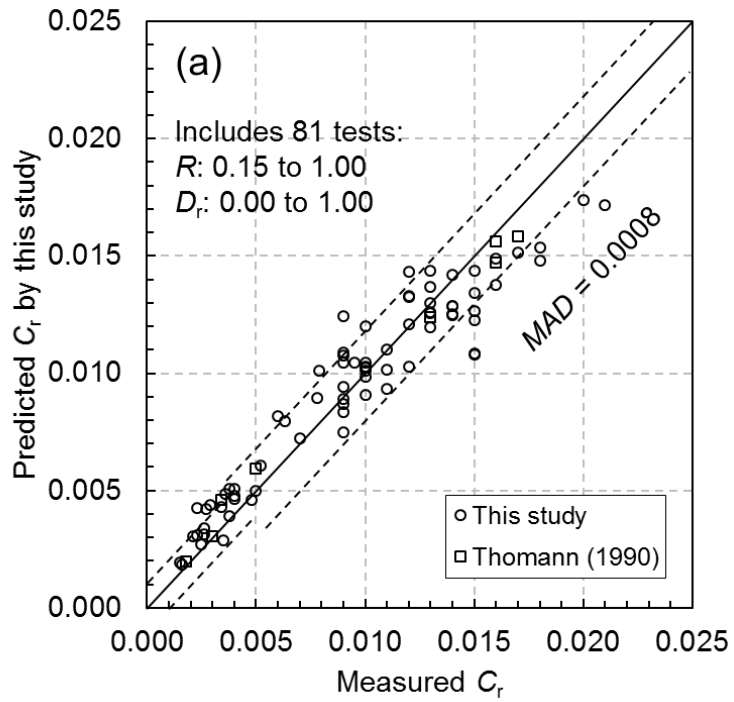
Figure 4.21 Comparisons between measurements and prediction of recompression index: (a) 0 to 0.025 range; (b) expansion of the 0 to 0.005 range.

The C_r values are typically larger than 0.005 for sands in the medium and loose states while being less than 0.005 for dense states. The dense state region is enlarged in Figure 4.21(b). Although it reveals that Equation 4.8 slightly overpredicts C_r/C_c for very dense sands, the actual C_r values are so small that the underpredictions are of no practical significance for settlement estimates. For the medium and loose states, the predicted C_r values are within ±0.001 of the measured values which are shown by dashed lines in Figure 4.21(a). Most of the predictions in the dense state are also within ±0.001 of the measurements as shown by dashed lines in Figure 4.21(b). The MAD is 0.0008 over the full range of C_r values but only 0.0004 for the dense range. Overall, Equations 4.7 and 4.8 provide very good practical predictions of C_r for sands.

As they did for C_c, Cho et al. (2006) also used regularity, ρ to predict C_r of dense sands by the equation: $C_r = 0.0028\rho^{-0.6}$. Twenty nine tests from Table 4.3 and Thomann (1990) having D_r from 0.76 to 1.00 were used to evaluate the equation. The results are shown in Figure 4.22 and the computed MAD is 0.0013. Cho et al.'s equation for C_r is also applicable only for dense sands.
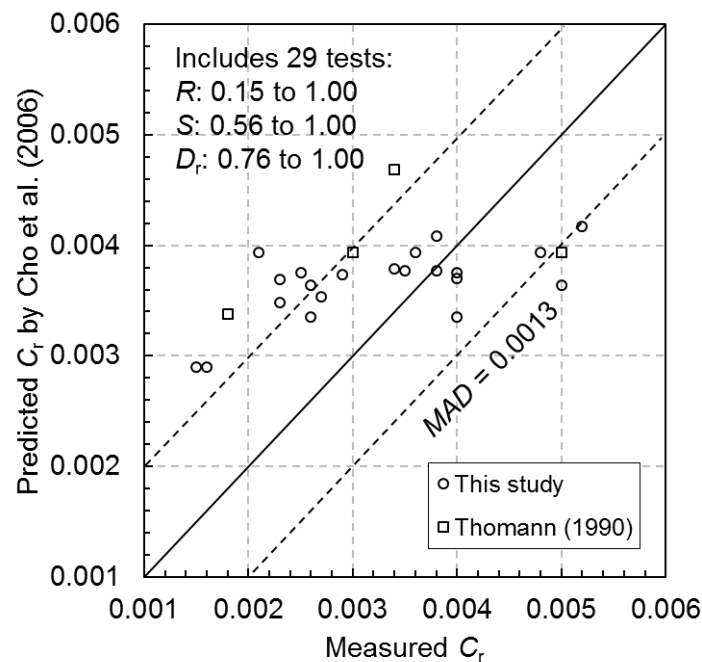

Figure 4.22 Comparisons between measurements and prediction of recompression index by Cho et al. (2006)

4.2.6 Conclusions

Based on tests performed on 24 materials spanning a wide range of shapes, size distributions, and geologic origins, and 52 other sands described previously in the geotechnical engineering literature, a simple model was developed for the 1-D compression index, C_c, of sands at pre-crushing stress levels. The model shows C_c being linearly related to $(1 - D_r/2)$ and inversely related to $R^{0.2}$. The model is an excellent fit to experimental data with the mean average difference (MAD) between observation and prediction being only 0.0029. For C_c values below 0.01 the MAD was only 0.0015. As expected, C_c values approaching zero were observed when R and D_r simultaneously approached 1.0. The highest C_c values of about 0.07 were observed when R and D_r approached values of 0.1 and 0 respectively. A second simple model for the ratio of recompression index to compression index, C_r/C_c as a function of R and D_r was also developed. The ratio ranged between 0.3 for very loose highly angular sands to over 0.8 for very dense well rounded sands. This model also showed excellent agreement with observed values.

CHAPTER 5

SAND FABRIC CHARACTERIZATION

5.1 Introduction

A Rotational Harr Wavelet Transform (RHWT) method that mimics human cognition to automate soil fabric characterization is presented in this chapter. An image of a soil is divided into numerous subareas for which pattern directions are obtained then used to develop a fabric rose diagram and the parameters for a cross-anisotropic fabric tensor. Based on images of eleven sands and three rice specimens at loose and dense conditions, a strong functional relationship for the fabric vector magnitude based on particle sphericity and relative density was shown. Furthermore, a very simple and practical relationship was presented for the fabric vector magnitude based only on relative density and the void ratio at 50% relative density.

5.2 The fabric tensor

The fabric anisotropy of granular material is usually quantified by a fabric tensor. We define the orientation of the long axis of a single particle by its unit vector **n** having orthogonal components (n_1, n_2, n_3). A fabric tensor for discrete granular materials using the **n** for many particles was proposed by Satake (1982):

$$\varphi_{ij} = \frac{1}{N}\sum_{k=1}^{N} n_i^k n_j^k = \frac{1}{N}\begin{bmatrix} \sum_{k=1}^{N} n_1^k n_1^k & \sum_{k=1}^{N} n_1^k n_2^k & \sum_{k=1}^{N} n_1^k n_3^k \\ \sum_{k=1}^{N} n_2^k n_1^k & \sum_{k=1}^{N} n_2^k n_2^k & \sum_{k=1}^{N} n_2^k n_3^k \\ \sum_{k=1}^{N} n_3^k n_1^k & \sum_{k=1}^{N} n_3^k n_2^k & \sum_{k=1}^{N} n_3^k n_3^k \end{bmatrix} \qquad \text{Equation 5.1}$$

where N is the number of particles used. A detailed explanation of Equation 5.1 is provided by Oda and Nakayama (1989). The **n** could also be obtained from branch vectors or contact normals, but in this study, the particle long axis vectors are used. For a three-dimensional soil specimen, the computed φ is a third–rank symmetric tensor which can be represented by three principal values φ_1, φ_2, and φ_3 and principal directions α_1, α_2, and α_3.

Directly computing the fabric tensor φ_{ij} is difficult because it requires identifying the orientations of many particle long axes in three-dimensional space. However, this problem can be simplified by recognizing that most soils display cross-anisotropic fabric as shown in Figure 5.1.
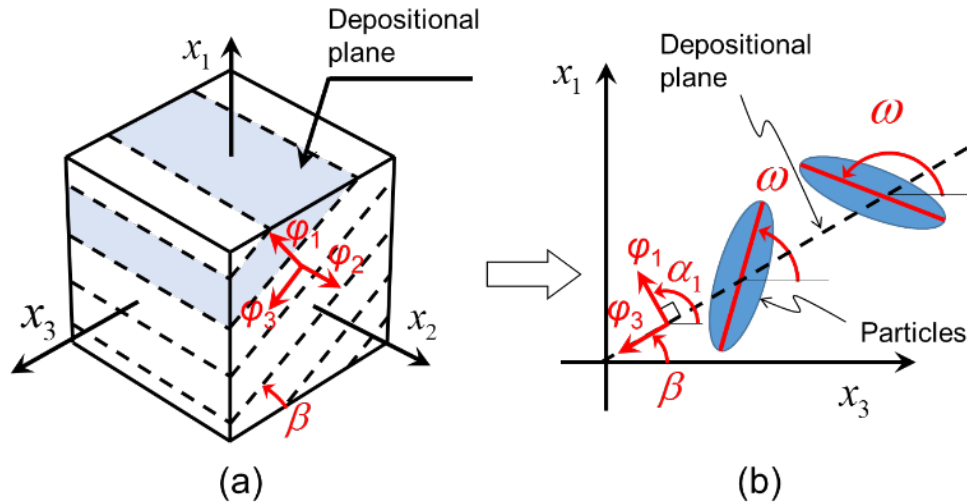

Figure 5.1 The cross–anisotropic fabric structure.

The particles develop an isotropic fabric in the depositional plane and therefore φ_2 is equal to φ_3. As such, only the angle α_1 is required to describe the fabric direction β as shown in Figure 5.1. The absolute difference between β and α_1 is ninety degrees. We only need to analyze particle orientations in the x_1 - x_3 plane, say from a two-dimensional image, to determine β, φ_1, and φ_3 as shown in Figure 5.1(b).

In the x_1 - x_3 plane, Equation 5.1 simplifies to a second-rank tenor: $\bar{\varphi} = [\bar{\varphi}_{11}, \bar{\varphi}_{13}; \bar{\varphi}_{31}, \bar{\varphi}_{33}]$ (the bar indicates it is a two-dimensional fabric tensor). Oda and Nakayama (1989) and Curray (1956) demonstrated that the two principal values $\bar{\varphi}_1$ and $\bar{\varphi}_3$ and the fabric orientation β can be determined as:

$$\left\{ \begin{matrix} \bar{\varphi}_1 \\ \bar{\varphi}_3 \end{matrix} \right\} = \frac{\left(\bar{\varphi}_{11} + \bar{\varphi}_{33} \right) \pm \sqrt{\left(\bar{\varphi}_{11} - \bar{\varphi}_{33} \right)^2 + 4\bar{\varphi}_{13}^2}}{2} = \frac{1}{2}\left(1 \pm \Delta \right) \quad \text{Equation 5.2}$$

$$\beta = \frac{1}{2} \arctan \frac{2\bar{\varphi}_{13}}{\bar{\varphi}_{33} - \bar{\varphi}_{11}} \quad \text{Equation 5.3}$$

where

$$\Delta = \frac{1}{N} \left[\left(\sum_{k=1}^{N} \cos 2\omega_k \right)^2 + \left(\sum_{k=1}^{N} \sin 2\omega_k \right)^2 \right] \quad \text{Equation 5.4}$$

The ω_k is the orientation of k-th particle in the x_1 - x_3 plane as shown in Figure 5.1(b). The Δ quantifies the degree of fabric anisotropy and is referred to as the *vector magnitude* (Curray, 1956), it. It will vary from zero when material is isotropic to unity when the long axes of particles lie strictly within the depositional plane ($\omega = \beta$ for all particles). Assuming that the principal values $\bar{\varphi}_1$ and $\bar{\varphi}_3$ in a two-dimensional image are proportional to the principal values φ_1 and φ_3 in three-dimensional space (Oda and Nakayama 1989) and knowing that $\varphi_2 = \varphi_3$ (for cross-anisotropy) and $\varphi_1 + \varphi_2 + \varphi_3 = 1$, the three principal values of the fabric tensor φ_1, φ_2 and φ_3 can be obtained. The fabric tensor of Equation 5.1 is thus rewritten as:

$$\varphi = \begin{bmatrix} \varphi_1 & 0 & 0 \\ 0 & \varphi_2 & 0 \\ 0 & 0 & \varphi_3 \end{bmatrix} = \frac{1}{3+\Delta} \begin{bmatrix} 1-\Delta & 0 & 0 \\ 0 & 1+\Delta & 0 \\ 0 & 0 & 1+\Delta \end{bmatrix} \qquad \text{Equation 5.5}$$

Equation 5.5 is the fabric tensor proposed by Oda and Nakayama (1989) which has been extensively used to characterize fabric anisotropy in granular material. It will also be used in this study.

To determine Δ and β, the ω values of many particles must be determined in the x_1-x_3 plane. An image of a long-grain rice assembly shown in Figure 5.2(a) was used as a soil surrogate to illustrate the process. The authors manually picked out 1357 full projection particles using a polygonal lasso tool of Adobe Photoshop described in chapter 3. The ω values of those labelled particles were determined and are plotted as arrows in Figure 5.2(b).

(a)

(b)

Figure 5.2 (a) Image of long-grain rice used for illustrating fabric characterization; (b) directions of long axes of rice grains.

The rose diagram of ω values in 10° increments is shown in Figure 5.3. The Δ value computed by Equation 5.4 is 0.41. The computed principal values using Equation 5.5 are φ_1, φ_2 and φ_3 are 0.18, 0.41, and 0.41 respectively. The fabric direction β is 148° by Equation 5.3.
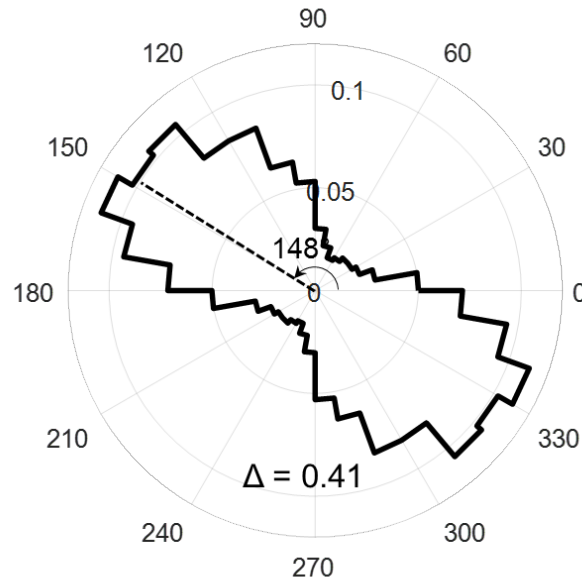

Figure 5.3 The fabric of long-grain rice using the traditional manual counting method.

5.3   Fabric characterization by simulating cognitive process

Ideally, a computer could be taught to automate detection of full projection particles. However, this is still a difficult problem due to great variations in the appearances of soil particles. It would therefore be desirable to characterize fabric without having to identify individual soil particles. By looking at the long-grain rice in Figure 5.2(a), an observer can quickly estimate the principal fabric direction and the degree of fabric anisotropy. For example, the authors felt that the principal fabric direction is about 145° which agrees reasonably well with the computed value of 148° in Figure 5.3. In our cognitive process, we essentially search for and detect repeating patterns rather than perform formal statistical

counts of individual particles. Our cognitive process divides the image into subareas containing micropatterns such as shown in Figure 5.4. For each subarea, our eyes distinguish the particle internal texture and particle edges by comparing the intensity of grayscale changes: the particle edges are associated with strong grayscale changes. We eliminate internal particle texture from our attention and focus only on the particle edges. We discriminate the long and short edges of particles and follow the long edges to estimate pattern orientation. Our eyes then scan the entire image to search for similar patterns. We then perceptually evaluate the fabric direction and the degree of fabric anisotropy. In this chapter, we aim to develop a computer algorithm that mathematically simulates this human cognitive process to automate fabric characterization.
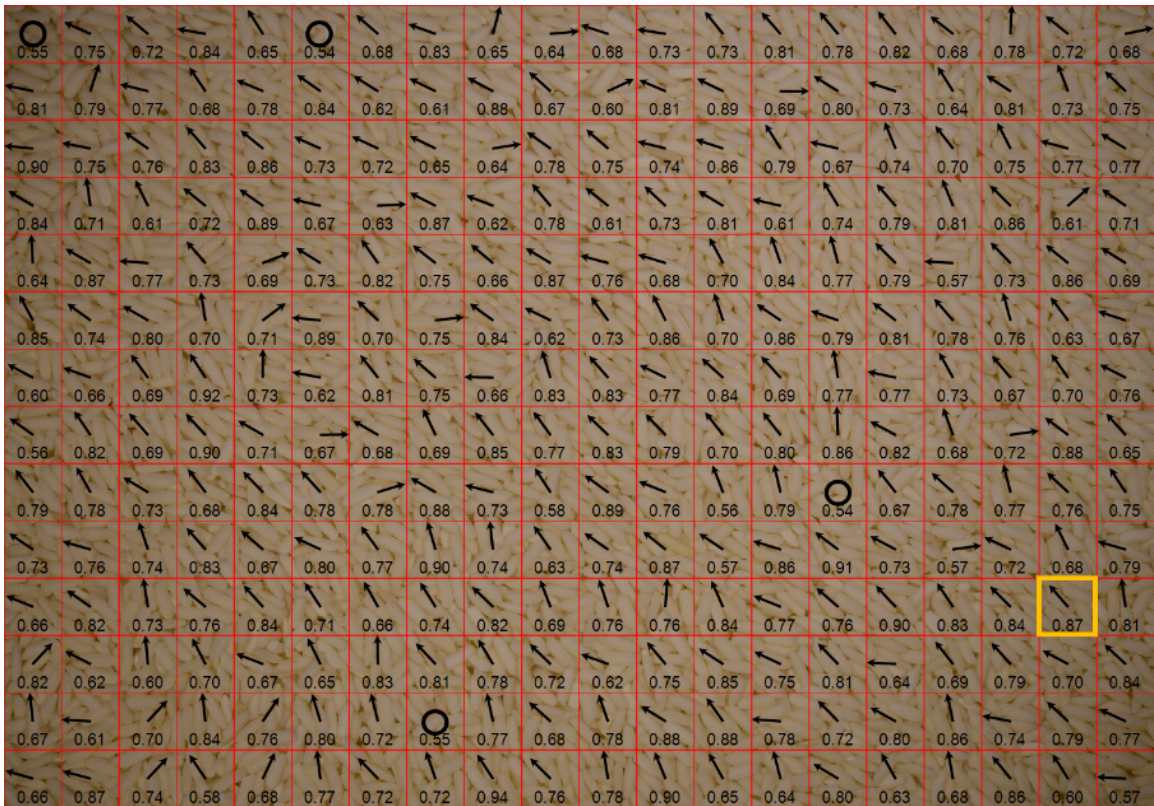

Figure 5.4 Conceptualization of the cognitive process algorithm for quantifying fabric.

It should be noted that the term "pattern orientation" is used in the rest part of chapter to represent the principal direction of particles' long axes in the small subareas while the "fabric direction" will be used to represent the principal direction of particle axes in the entire image.

5.3.1   Haar Wavelet Transform

In mathematics and computer vision, grayscale changes may be quantified by the Haar Wavelet Transform (HWT) originally proposed by Haar (1910). The detailed theoretical derivation of the Haar Wavelet Transform can be found in many textbooks on wavelet mathematics. Therefore, this chapter will not repeat it. However, the authors will explain why the HWT can be used to quantify grayscale changes in images using a simple example.

An 8 pixel × 8 pixel grayscale image A_0 is shown in Figure 5.5. The grayscale values are superimposed on the image. Larger values correspond to brighter areas in the image. In A_0, the grayscale values change only horizontally while remaining constant in the vertical direction. Thus, A_o has a vertical fabric.
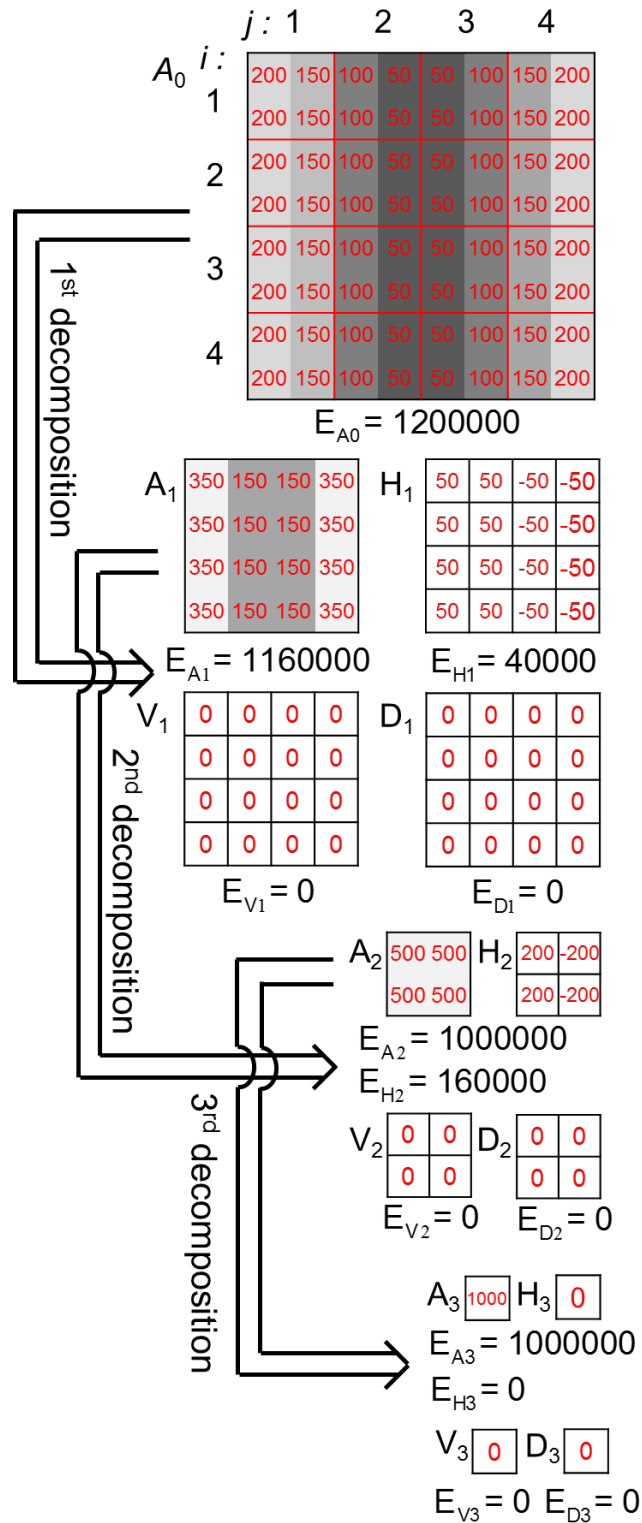
Figure 5.5 The Haar Wavelet Transform (HWT).

The HWT firstly divides the image into 2 x 2 blocks. There are a total of 16 such 2 x 2 blocks in the 8×8 image A_o as shown in Figure 5.5. For each block (i, j), the HWT computes the mathematical difference of grayscales between adjacent pixels in three directions which yields the four values $A_1 (i, j)$, $H_1(i, j)$, $V_1(i, j)$, and $D_1(i, j)$. $A_1(i, j)$ is twice the average of the four numbers. $H_1(i, j)$ is the average difference of numbers between two columns. $V_1(i, j)$ is the average difference of numbers between two rows. $D_1(i, j)$ is the average difference of numbers between two diagonals. For example, the computed results for the first block $A_0(1, 1)$ are $A_1(1, 1) = 350$, $H_1(1, 1) = 50$, $V_1(1, 1) = 0$, and $D_1(1, 1) = 0$.

These computations are repeated for each block in A_o yielding four new 4×4 matrices: A_1, H_1, V_1, and D_1 as shown in Figure 5.5. The A_1, H_1, and V_1 all have physical meaning. The matrix A_1 (can be regarded as a 4×4 image) is effectively a downscaling of the original image A_0 by a factor of 2. The matrix H_1 quantifies the difference of grayscale in the horizontal direction while V_1 quantifies the difference of grayscale in the vertical direction. In our example, the grayscale only changes in the horizontal direction, therefore, V_1 will be a zero matrix.

In computer vision, the sum of the squares of the values in a matrix is called its energy (E). The computed energies E_{A1}, E_{H1}, E_{V1}, and E_{D1} are shown in Figure 5.5. The E_{H1} and E_{V1} quantify the grayscale changes in the horizontal and vertical directions in A_0.

The Haar Wavelet Transform can now be applied to A_1 in a second decomposition as shown in Figure 5.5. It results in another four sub-matrices A_2, H_2, V_2 and D_2 whose corresponding energy values are also shown. Finally, A_2 can be further decomposed into A_3, H_3, V_3 and D_3 as shown.

The original size of A_0 was 8 pixels $\times$ 8 pixels. Therefore, three HWT decompositions could be performed on the image. It is easy to see that a 2^L pixel $\times$ 2^L pixel image can be decomposed L times. At the i-th decomposition level, the computed energies E_{Hi} and E_{Vi} quantify the magnitudes of grayscale changes in the horizontal and vertical directions in image A_{i-1}. In our example, the images A_0 and A_1 display a strict vertical fabric with grayscales changing only in the horizontal direction. Therefore, the computed E_{V1} and E_{V2} are both zero.

5.3.2 Rotational Haar Wavelet Transform

The HWT computes only horizontal, vertical and diagonal energies. However, the diagonal energy is of limited value. As such, for practical purposes, the HWT quantifies only horizontal and vertical grayscale changes. To assess grayscale changes and compute energies in other directions, a Rotational Haar Wavelet Transform (RHWT) is introduced in this study. The entire image in Figure 5.4 was divided into 280 subareas each 364 pixels × 364 pixels in size. The subarea that is highlighted in Figure 5.4 is enlarged in Figure 5.6(a). It is labelled image Z and will be used to demonstrate the RHWT.
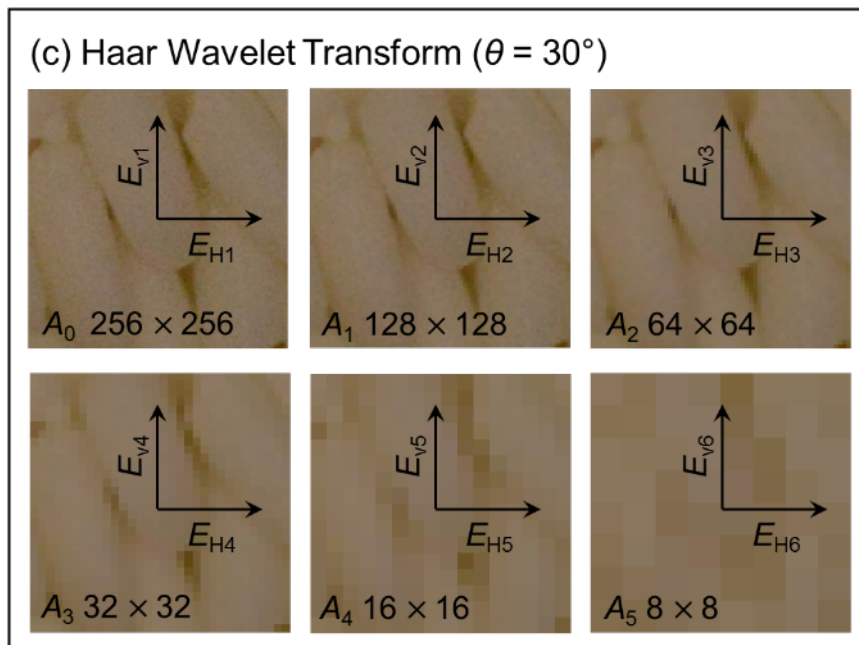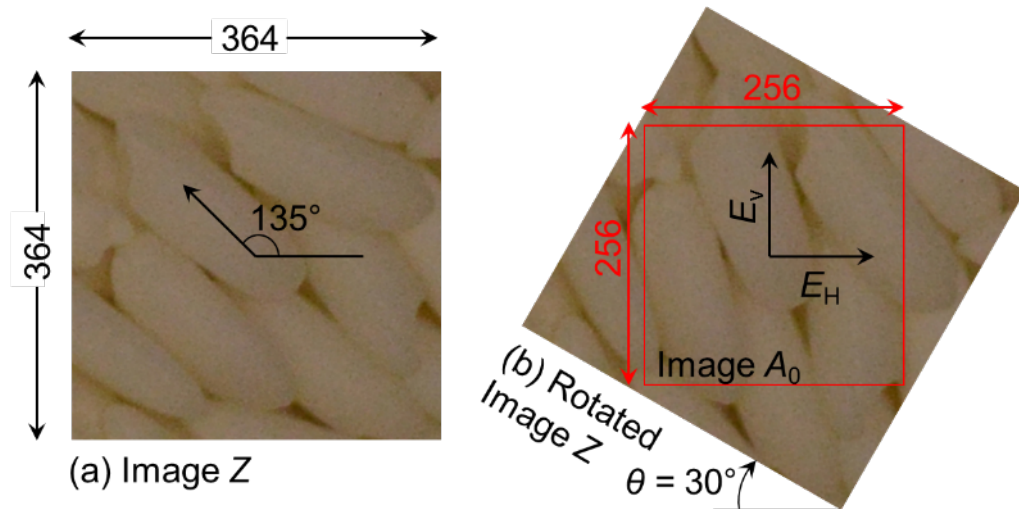
Figure 5.6 Haar Wavelet Transform at rotation of θ.

First, image Z is rotated by θ clockwise. In Figure 5.6(b), $\theta = 30°$ is used for illustration. After rotation, a HWT is performed on the central 256 pixel $\times$ 256 pixel area. This area will be referred to as A_0. A total of 8 decompositions can be performed on A_0. A series of new images $A_1, A_2, \ldots A_8$ are generated the first six of which are shown in Figure 5.6(c).

At the i-th decomposition level, the horizontal energy and vertical energy are computed as E_{Hi} and E_{Vi} respectively.

The computed E_{Hi} and E_{Vi} values for image Z are plotted in Figure 5.7. Higher E_{Hi} or E_{Vi} values correspond to larger grayscale changes in the horizontal or vertical directions in image A_{i-1}. Both E_{Hi} and E_{Vi} (i = 1, 2,…,8) display bell-shaped curves and reach maximum values at i = 5 in this example. The explanation for the bell-shaped curve is that the grayscale changes occur not only at edges but also inside the particles due to internal texture. The grayscale changes due to internal texture are much weaker than the grayscale changes at particle edges. Therefore, as the original image is consecutively approximated by smaller resolution images, the internal grayscale changes are gradually filtered out while the grayscale changes at edges become dominant as shown from A_0 to A_4 in Figure 5.6(c). Correspondingly, both E_{Hi} and E_{Vi} increase and reach peaks at A_4 meaning the majority of internal texture is eliminated and the grayscale changes occur only at edges at this decomposition level. Beyond the peak, the grayscale changes at the edges will also be filtered out and the entire image becomes increasing blurred as shown in A_5. This reduces both the E_{Hi} and E_{Vi} values. The maximum (peak) E_{Hi} and E_{vi} values essentially quantify the grayscale change in the horizontal and vertical direction only due to edges. Therefore, the maximum E_{Hi} and E_{vi} will be used to define the horizontal and vertical energies E_H and E_V in the original image A_0 in Figure 5.6(b) at rotation θ:

$$E_H = \max_{i=1...L}\left(E_{Hi}\right) \qquad\qquad \text{Equation 5.6}$$

$$E_V = \max_{i=1...L}\left(E_{Vi}\right) \qquad\qquad \text{Equation 5.7}$$

Where L is the total number of decomposition levels. In the example, $E_H = E_{H5} = 6.56 \times 10^5$ while $E_V = E_{V5} = 2.28 \times 10^5$.
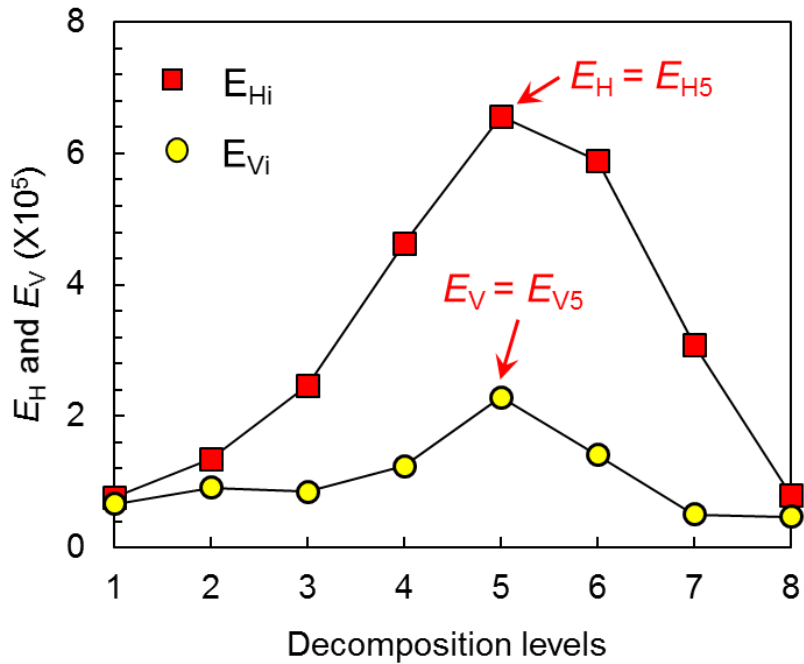
Figure 5.7 The horizontal and vertical energy at each decomposition
level for image Z at $\theta=30°$.

The rotated image Z in Figure 5.6(b) is rotated back to its original position in Figure 5.8. The $E(\theta)$ and $E(\theta+90°)$ are E_H and E_V from the previously rotated view. Therefore $E(\theta)$ and $E(\theta+90°)$ quantify grayscale changes in directions θ and $\theta+90°$. If θ is varied from $0°$ to $89°$ in $1°$ increments, a total of 90 rotations will take place. The energies $E(0°)$, $E(1°)$ all the way to $E(179°)$ are computed this way. Due to rotational symmetry, $E(\theta+180°)=E(\theta)$. Therefore, the E values for the full range of $0° \leq \theta \leq 360°$ are obtained.
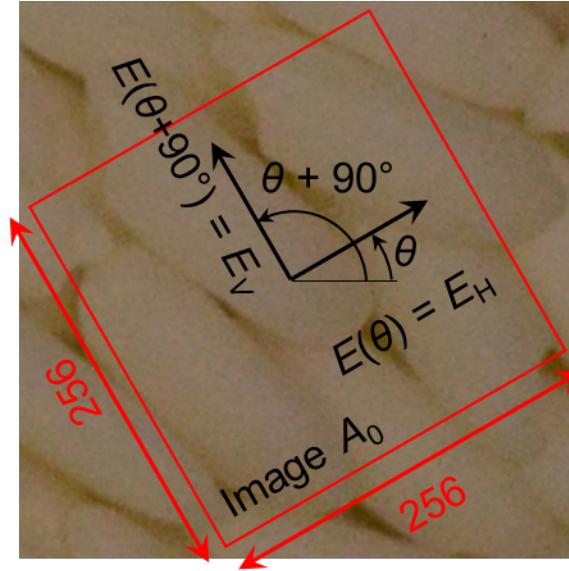
Figure 5.8 Determining energy in directions θ and $\theta+90°$ for image Z.

If we observe the image Z in Figure 5.6(a), the long edges in the fabric direction occur more frequently than the short edges perpendicular to the fabric direction. A higher edge frequency means more grayscale changes and thus a larger energy in this direction. We aim to follow the long edges parallel to the long axis of particles to determine the pattern orientation. Therefore, we should search for the direction θ having minimum energy (minimum $E(\theta)$) and the direction $(\theta+90°)$ having the maximum energy (maximum $E(\theta+90°)$). To accomplish this, we define an Energy Ratio, ER by:

$$ER(\theta) = \frac{2}{\pi} \arctan\left(\frac{E(\theta+90°)}{E(\theta)} \right)$$

Equation 5.8

The computed ER values will be in the range of 0 to 1. The θ corresponding to the ER_{max} is the long edge direction and thus the pattern orientation. The computed ER plot for image Z is shown in Figure 5.9.

124

It is a zig-zagged curve due to the random orientations of some particles and to image noise. The out-of-trend particles and image noise may bias the computed ER plot. To address this issue, a second-order Fourier series is used to fit the original ER plot with a smooth curve:

$$ER(\theta) = 0.50 + a_2 \cos(2\theta) + b_2 \sin(2\theta)$$ Equation 5.9

The coefficients a_2 and b_2 can be determined by fitting Equation 5.9 to the original ER plot as shown in Figure 5.9. The parameters are found to be $a_2 = -0.0057$, and $b_2 = -0.3669$ for our example. The ER_{max} and ER_{min} can be computed as:

$$\begin{bmatrix} ER_{max} \\ ER_{min} \end{bmatrix} = 0.50 \pm \sqrt{a_2^2 + b_2^2}$$ Equation 5.10

which are 0.87 and 0.13 for the plot in Figure 5.9. It is evident that the sum of ER_{max} and ER_{min} will be unity and their directions will always be perpendicular to each other. The computed pattern orientation (direction of ER_{max}) is 135° for the highlighted subarea in Figure 5.4. It is superimposed on Figure 5.6(a) and clearly agrees very well with the observed long axes of the particles.
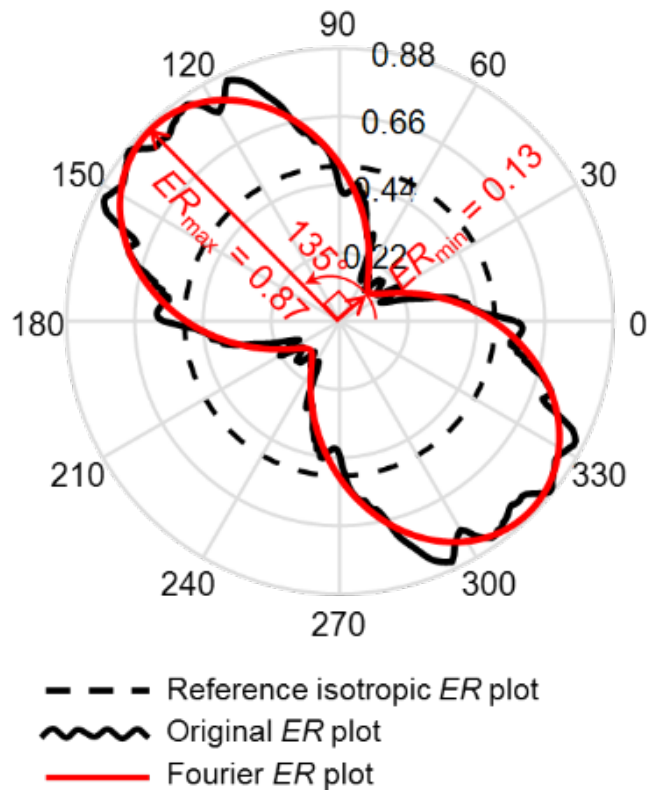
Figure 5.9 The ER plot and its Fourier smoothing for Image Z.

For an ideal isotropic fabric, E will be a constant in all directions. Therefore, the ER plot will be a circle of radius = 0.5 ($ER_{max} = ER_{min} = 0.5$) which is shown as a dashed line in Figure 5.9. For stronger anisotropic fabric, the ER plot will diverge from the isotropic circle. The ER_{max} will trend to 1.0 while ER_{min} will approach 0.0.

For practical reasons, a cut-off $ER_{max,0}$ value should logically be used to define an isotropic, or nearly isotropic fabric. This value of $ER_{max,0}$ was chosen to be 0.55 for reasons shown later in the chapter.

The above process was repeated for all of the subareas in Figure 5.4. The pattern orientations are plotted as arrows while the ER_{max} values are shown beneath the arrows. Four of the patterns were identified by circles because their ER_{max} were smaller than $ER_{max,0}$ = 0.55 meaning that the particles in those subareas showed no preferred orientation.

5.3.3 The effect of subarea size

Back to the long-grain rice example in Figures 5.2 and 5.4, the pattern orientations in each subarea can be regarded as the ω values in Equation 5.4. With these values, the Δ and β can be determined by Equations 5.2, 5.3 and 5.4. In our example, a total of 276 ω values were computed (the 4 isotropic squares were discounted). The ω values are plotted as a rose diagram in Figure 5.10(a). The computed Δ and β are $\Delta_H = 0.65$ and $\beta_H = 140°$ respectively where the subscript "H" means the RHWT method was used. The rose diagram from traditional methods and the corresponding Δ value (Δ_T) and fabric direction (β_T) such as in Figure 5.3 are also shown in Figure 5.10 where the subscript "T" means the traditional method.
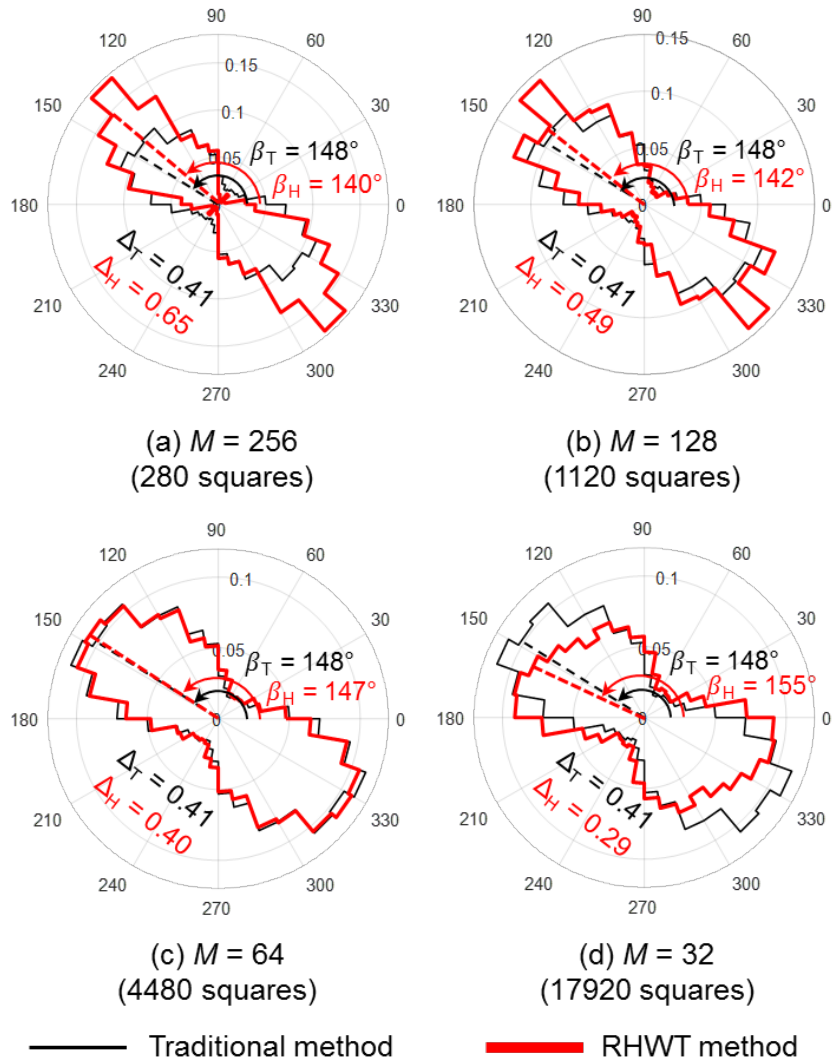
Figure 5.10 The effects of window size on RHWT results.

In our example, the subarea sizes were 364×364 pixels of which the central 256×256 pixel areas were analyzed. Generally, if the size of the analyzed subarea is M pixels $\times M$ pixels (where M must be 2^L to perform a HWT), the corresponding subarea size to allow for the rotations must be $\sqrt{2}M \times \sqrt{2}M$ pixels.

To investigate the effect of subarea sizes on the computed fabric results, three other M values were tried: $M = 128$, 64, and 32 pixels. The corresponding subarea sizes to allow for rotations were therefore set to 182×182 pixels, 91×91 pixels, and 45.5×45.2 pixels

respectively which produced 1120, 4480, and 17920 subareas for the image shown in Figure 5.2(a). The resulting rose diagrams and the corresponding Δ and β using the different M's are shown in Figures 5.10(b), 5.10(c), and 5.10(d).

Figure 5.10 reveals that the fabric characterization results will indeed be affected by the size of the subareas. A large M tends to overpredict the degree of fabric anisotropy as shown in Figures 5.10(a) and (b) while a small M tends to underpredict it as shown in Figure 5.10(d). Using $M = 64$ pixels results in a near-perfect match with the manual method as shown in Figure 5.10(c). Clearly, there is an optimum number of particles per subarea that: (a) is not so large that the subarea pattern directions all approach the fabric orientation of the full image but (b) not so small that only a few grains dictate the pattern direction of a subarea. The authors found that this dual criterion is best met by using an M related to the number of "pixels per smaller particle dimension" (PPS):

$$M = 2^{\text{int}\left(\log_2(PPS)\right)}$$

Equation 5.11

In our example, the PPS was approximately 80 pixels. Therefore, the optimum M was 64 pixels. The correctness of this value is confirmed by the results shown in Figure 5.10.

5.3.4   The effect of image magnification

Image magnification will also affect fabric characterization. The previously defined PPS can be used to quantify the required image magnification. At very low PPS (low magnifications) the edges will be blurred. This results in an underestimation of fabric anisotropy. Therefore, a minimum PPS must be established that would ensure reliable and accurate fabric characterization.

The long-grain rice in Figure 5.2 continues to be used to find this minimum PPS because this very elongated material can develop a strong fabric. If we could determine the minimum PPS that would correctly characterize such a strong fabric anisotropy we would be able to use this minimum PPS as the criterion for other less elongated materials including sands. The long-grain rice image was upscaled and downscaled to generate four other images having different PPS values. The four images were 910 × 637, 1820 × 1274, 3640 × 2548, and 14560 × 10192 pixels. The corresponding PPS values are 10, 20, 40, and

160 pixels respectively. The *M* values are computed by Equation 5.11 to be 8, 16, 32, and 128 pixels respectively. The number of subareas is 4480 for those four images.

The resulting rose diagrams for these four cases are shown in Figure 5.11 where they are also compared to the manual method results. As expected, low *PPS* values underestimated the degree of fabric anisotropy. Once *PPS* was 40 or more the results were exactly the same. Therefore, a minimum *PPS* of 40 pixels is established to produce consistently good results.
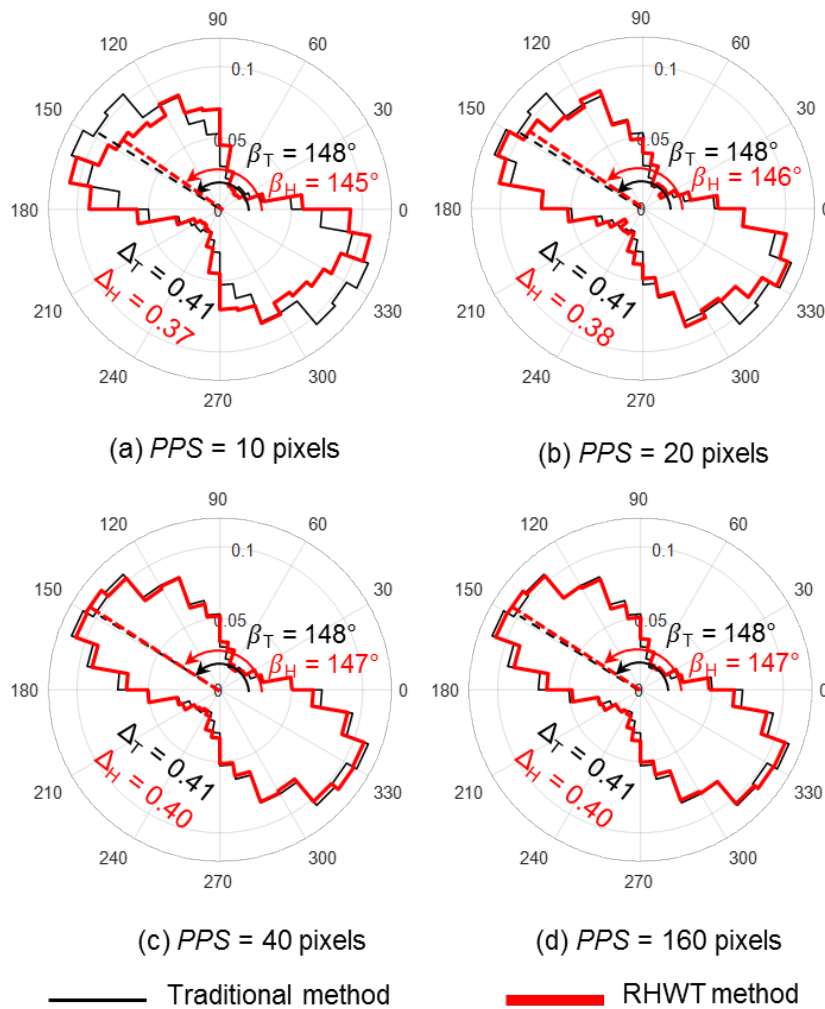

Figure 5.11 Effect of image magnification on RHWT results.

5.4   Fabric tensor of natural sands

Eleven sands (and three different kinds of rice) exhibiting a range of particle sizes, gradations, roundnesses, shapes, and particle colors were evaluated for fabric anisotropy. They are listed in Table 5.1. The particle shapes are quantified by sphericity, S, the ratio of particle width to particle length (Krumbein and Sloss, 1951). For each soil, the S was averaged from 200 maximum particle projections using computational geometry technique in chapter 2. The index void ratios e_{max} and e_{min} were determined following the ASTM D4253-14 (2014a) and ASTM D4254-14 (2014b).

The laboratory apparatus was a square glass tube with 5 cm × 5 cm (2 in × 2 in) inside opening and 30 cm height. The soils were funneled into the tube from a zero height of drop to create specimens at the loosest state. Following image capture at e_{max} the glass tube was mounted on a shaking table and a 2.5 kg surcharge was placed on top of the soil. The specimens were vibrated until they reached their known e_{min} states. A Nikon D800 camera with a magnification lens was used to capture 2912 × 5824 pixel images through the side of the glass tube. The images of six typical sands and rice at their loose states are shown in Figures 5.12(a) to 5.20(a) and at their dense states in Figures 5.12(d) to 5.20(d).

The average PPS values in the captured images ranged from 95 to 160 pixels. Based on Equation 5.11, the size of the analysis area M was set to 128 pixels and consequently, the subarea size was 182 × 182 pixels. There were 512 subareas created from each image. As before, the $ER_{max,0}$ was set to 0.55. The computed ω values at the loose and dense conditions are plotted as rose diagrams in Figures 5.12(c) to 5.20(c) and Figures 5.12(e) to 5.20(e) respectively. The Δ values at the loose and dense conditions ($\Delta_{L,H}$ and $\Delta_{D,H}$) and corresponding fabric directions ($\beta_{L,H}$ and $\beta_{D,H}$) are also shown.

The soil particles displaying full projections in Figures 5.12(a) to 5.20(a) were also manually picked out and their ω values were computed and plotted as arrows in Figures 5.12(b) to 5.20(b). This manual process took approximately 1 hour for 150 particles. The rose diagram of ω values, $\Delta_{L,T}$ and $\beta_{D,T}$ values are shown in Figures 5.12(c) to 5.20(c). The results of the RHWT and the results by the traditional method agree with each other very

well demonstrating the accuracy of the proposed RHWT method. The results also confirm that it is rational to set $ER_{max,0}$ to 0.55. The complete results for all soils and rice specimens are provided in Table 5.1.

As expected, the computed principal fabric direction (β values) are close to the horizontal direction as shown in Figures 5.12 to 5.20 and in Table 5.1. The relative density will affect the degrees of fabric anisotropy Δ. In the densified state, the particles display an even stronger preferred horizontal orientation and therefore larger Δ.
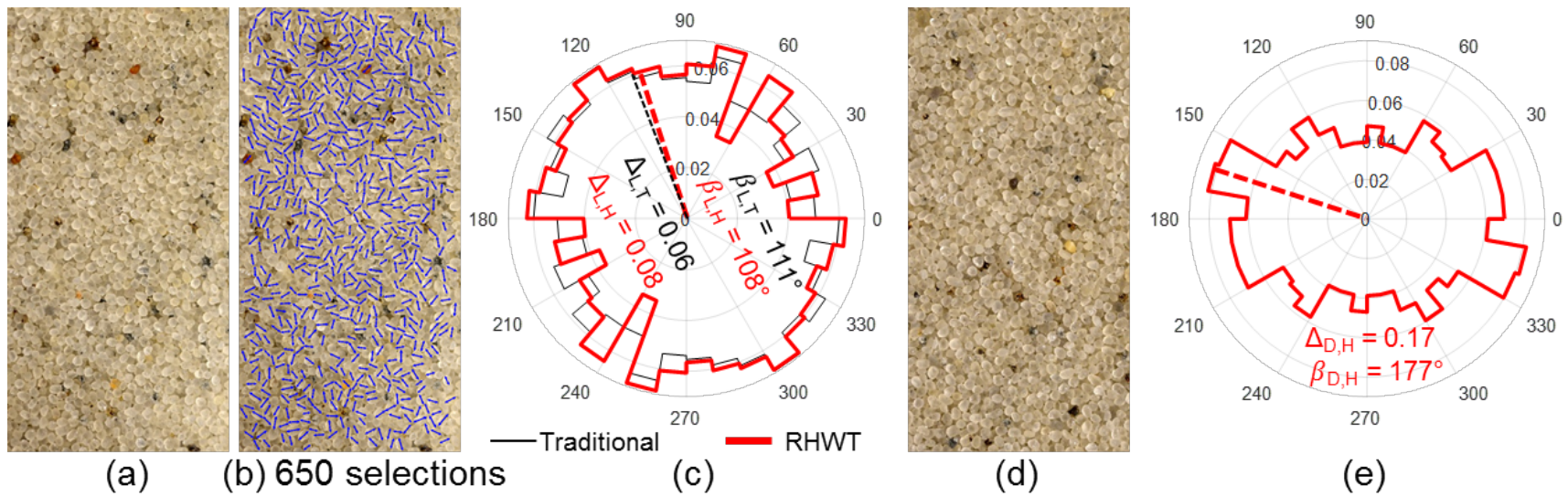
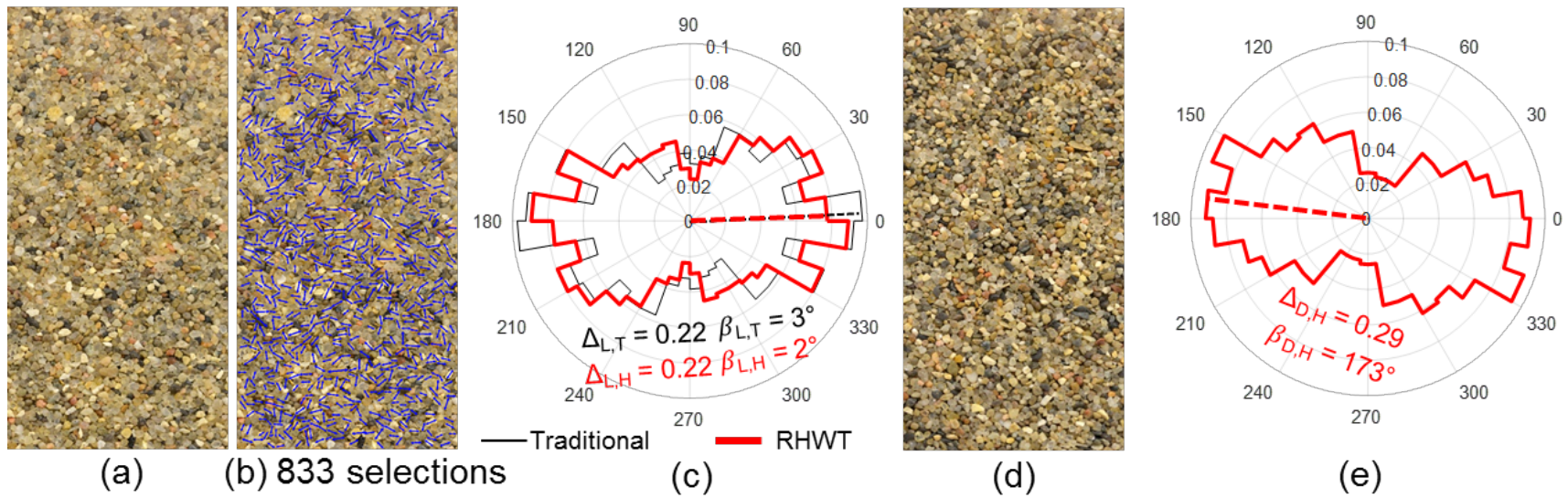Figure 5.12 The computational results for Ottawa sand.
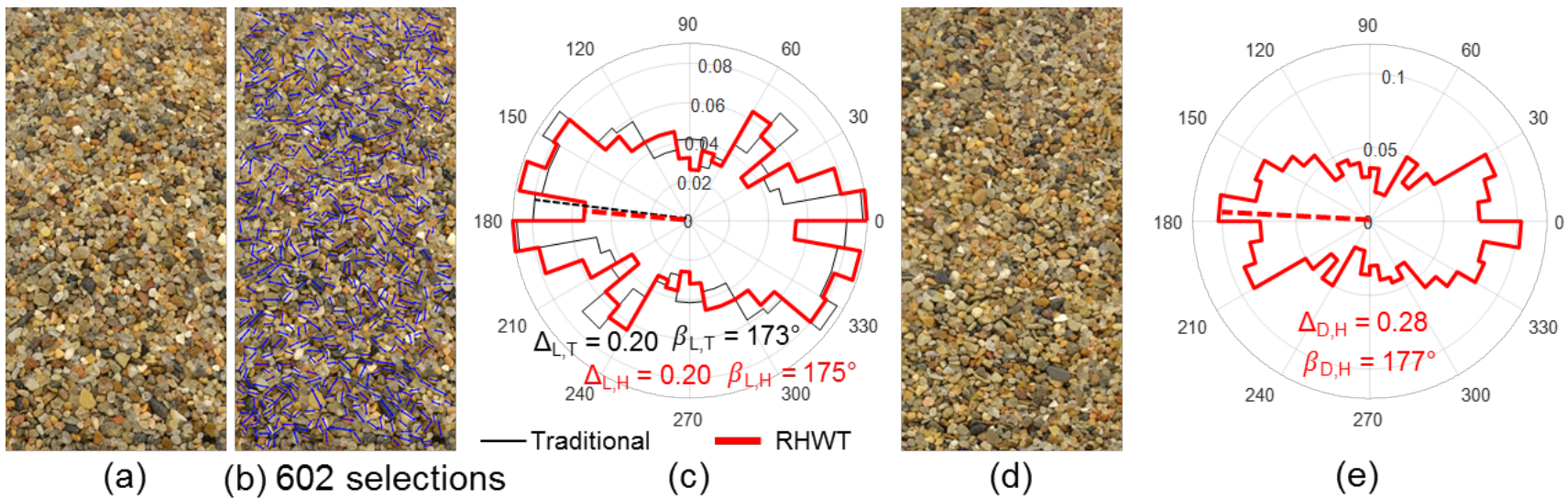
133

Figure 5.13 Results for Class IIA sand.

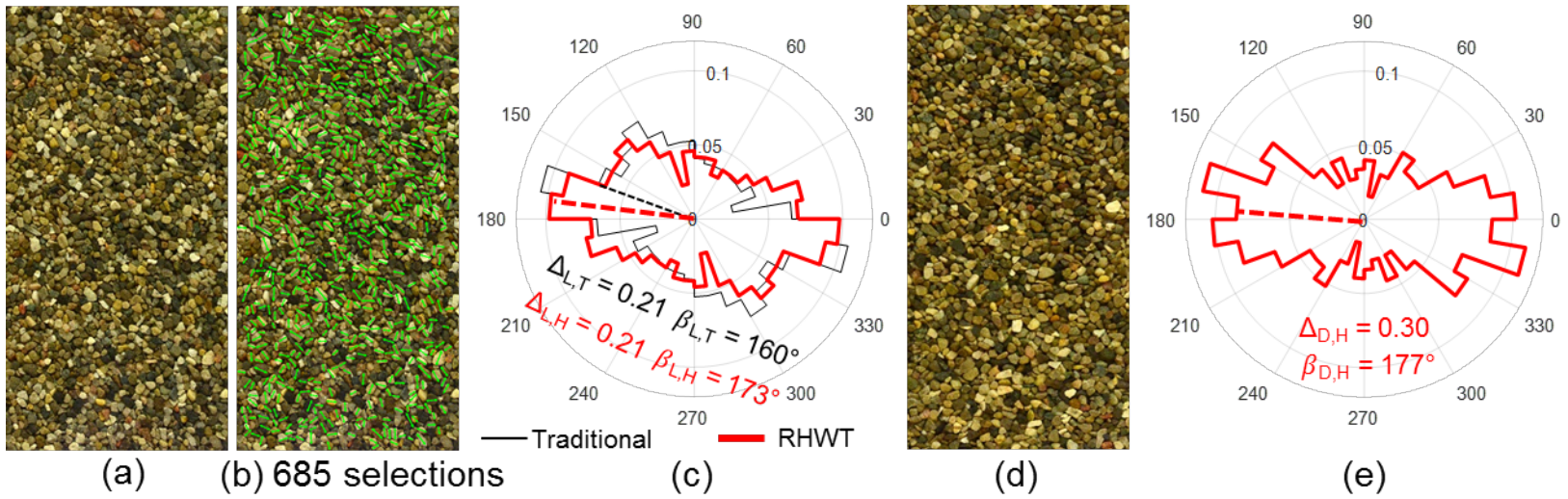Figure 5.14 Results for Indiana Beach sand.

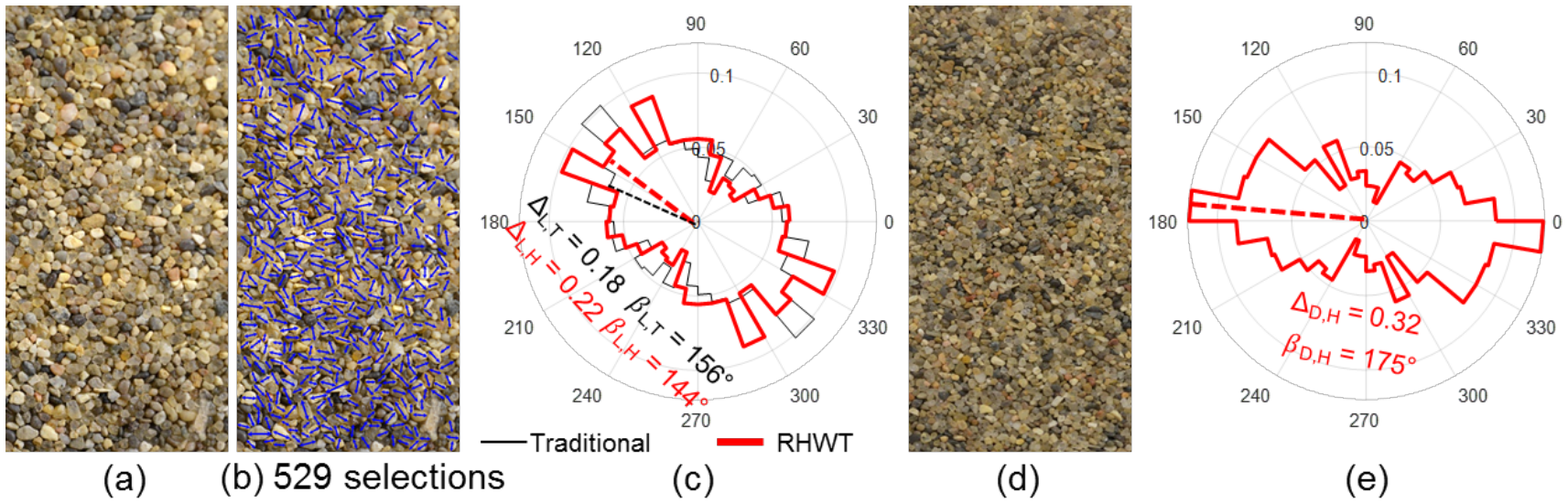Figure 5.15 Results for 2NS sand.
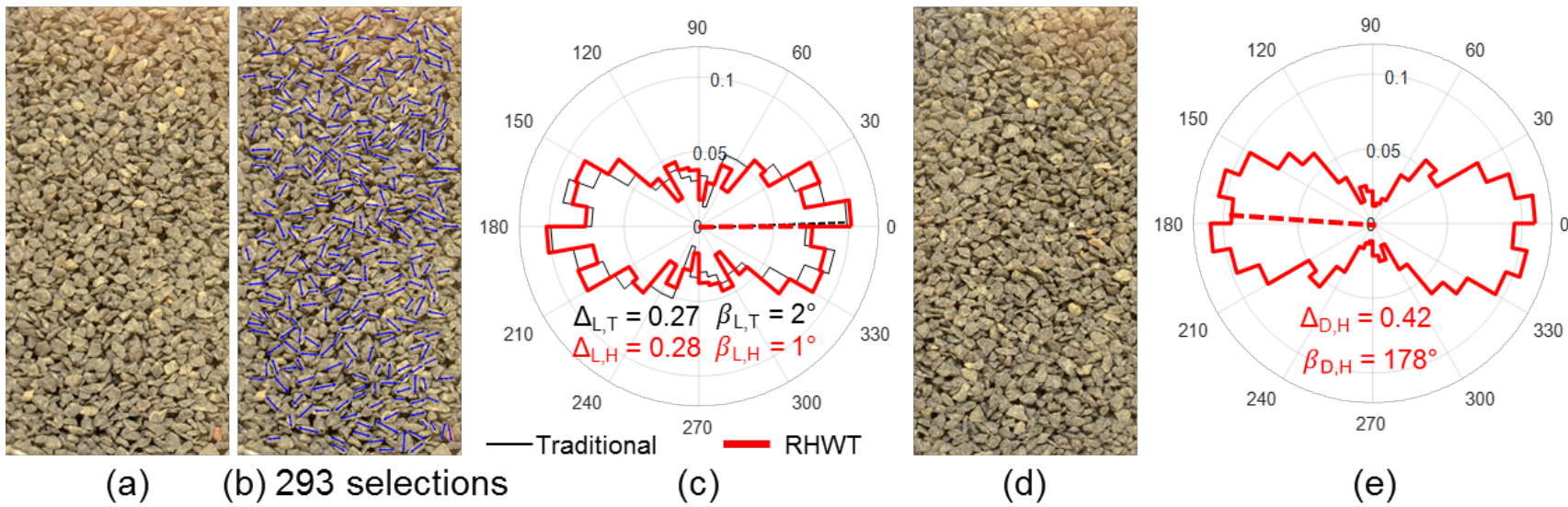
Figure 5.16 Results for Griffin sand.
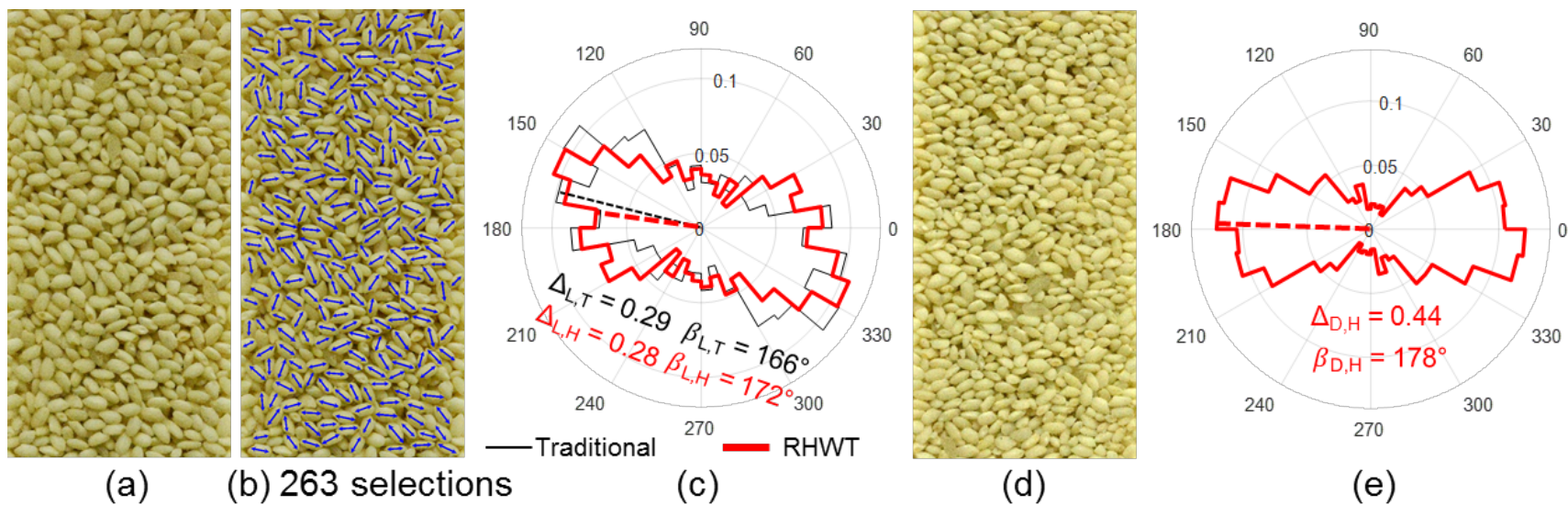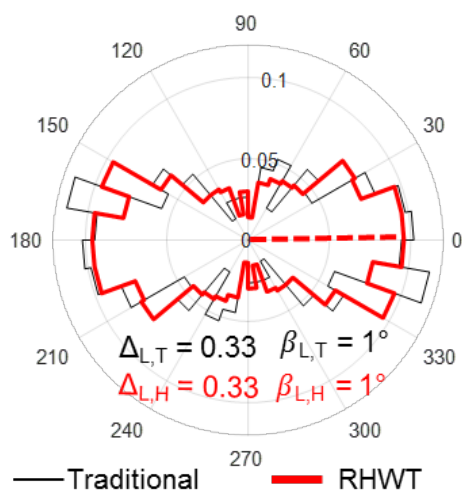
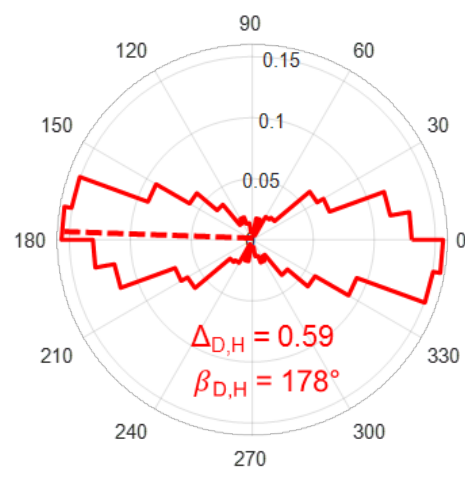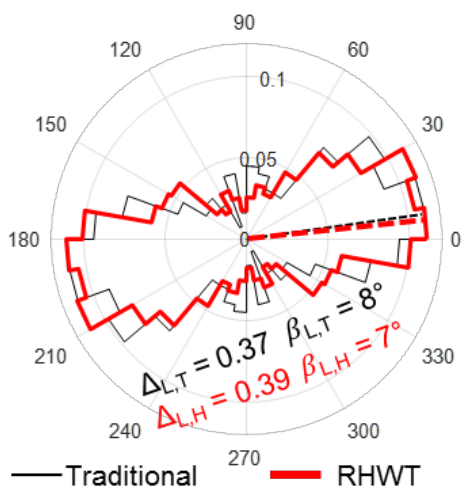Figure 5.17 Results for Crushed Gabbro sand.

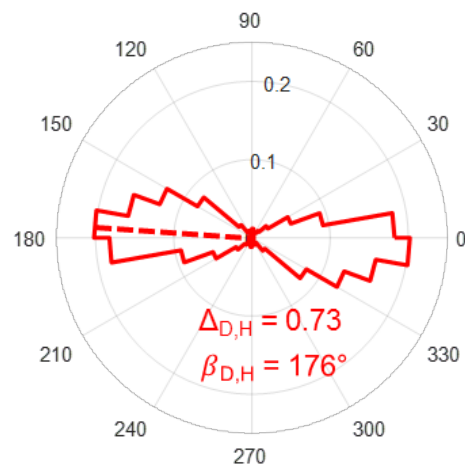Figure 5.18 Results for short-grain rice.
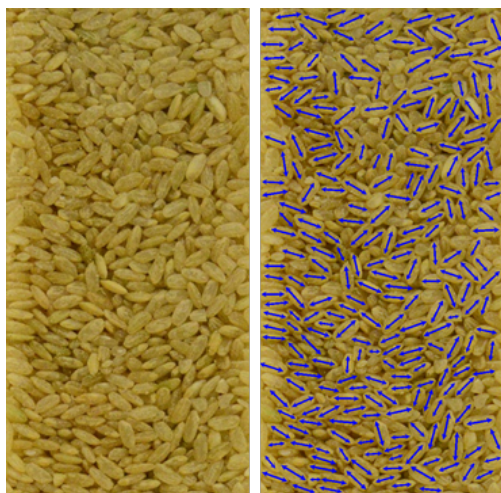
Figure 5.19 Results for medium-grain rice.
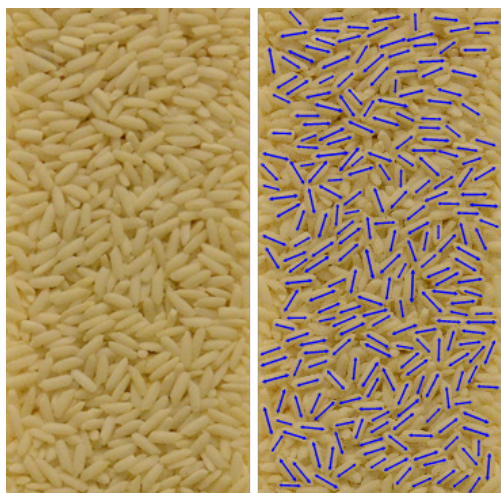
Figure 5.20 Results for long-grain rice.

Table 5.1 The computational results of natural soils

Soils	Gradation		Packing		Shape	Loose				Dense	
	D_{50}	C_u	e_{max}	e_{min}	S	$\Delta_{L,H}$	$\beta_{L,H}$	$\Delta_{L,T}$	$\beta_{L,T}$	$\Delta_{D,H}$	$\beta_{D,H}$
Ottawa 20 - 30	0.71	1.4	0.74	0.49	0.82	0.08	108°	0.06	111°	0.17	1°
Michigan Dunes	0.3	1.5	0.85	0.56	0.76	0.15	5°	-	-	0.2	2°
Muskegon	0.4	1.6	0.84	0.56	0.74	0.10	173°	-	-	0.28	5°
Oakland County, Michigan	0.31	1.6	0.86	0.53	0.72	0.18	17°	-	-	0.32	3°
Class IIA, Michigan	0.21	1.9	0.86	0.56	0.69	0.22	2°	0.22	3°	0.29	173°
Capitola, California	0.33	1.5	0.89	0.57	0.72	0.18	10°	-	-	0.26	10°
New Madrid, Missouri	0.32	2.2	0.81	0.52	0.73	0.17	0°	-	-	0.27	175°
Chesterton, Indiana beach	0.64	1.9	0.85	0.54	0.71	0.20	175°	0.2	173°	0.28	177°
Michigan 2NS	0.5	2.3	0.82	0.54	0.67	0.21	173°	0.21	160°	0.3	177°
Griffin, Indiana	0.74	3.3	0.79	0.51	0.65	0.22	144°	0.18	156°	0.32	175°
Crushed Gabbro	0.8	1.5	0.96	0.60	0.56	0.28	1°	0.27	2°	0.42	178°
Short - grain rice	1.91	1.1	0.97	0.65	0.54	0.28	172°	0.29	166°	0.44	178°
Medium - grian rice	1.62	1.1	1.01	0.72	0.47	0.33	1°	0.33	1°	0.59	178°
Long -grain rice	1.51	1.1	1.08	0.85	0.33	0.39	7°	0.37	8°	0.73	176°

Note: C_u = coefficient of uniformity; D_{50} = 50% size (mm); e_{max} and e_{min} = maximum and minimum index void ratios; NS = natural sand; S = Sphericity.

5.5   Relationship between Δ and soil properties

There is abundant evidence that the potential degree of fabric anisotropy Δ depends on particle shape. Elongated and flat particles will develop stronger fabric anisotropy compared to spherical particles (Guo 2008, Oda 1981, Lade 2008, and Tong et al. 2014). Therefore, Δ should be related to the particle flatness ratio which is the ratio of particle thickness to length. However, it is difficult to determine the particle flatness ratio. Unless specialized devices are developed (Kuo 1996; Rao and Tutumluer 2000), operators must rotate each particle to measure the length and thickness to determine flatness ratio. Major effort would be required to measure many particles this way. Furthermore, such manual measurements cannot be used to determine the flatness ratios of small particles such as Michigan Dunes and Muskegon in Table 5.1. By contrast, it is easy to determine particle sphericity, S. If soil particles are spread on a flat surface they will naturally rest with their maximum projections facing upward. An image captured from above will provide the information to compute S. If particles are very small, a close-up lens or microscope can be used. For example, in this study, for soils with $D_{50} < 1.0$ mm in Table 1, a magnifying lens was used to capture the images. For the reasons explained above, sphericity was used to quantify particle shape in this study.

The Δ and S values for the materials in this study are plotted in Figure 2.21. Both Δ_D (dense state) and Δ_L (loose state) decrease linearly with increasing S. The relationships between Δ_D and S, and Δ_L and S can be nicely approximated by:

$$\Delta_D = 1 - S \qquad\qquad \text{Equation 5.12}$$

$$\Delta_L = 0.6(1 - S) \qquad\qquad \text{Equation 5.13}$$

Equations 5.12 and 5.13 indicate that for perfect spheres ($S=1.0$) both Δ_D and Δ_L are 0, as they should be. The difference between Equations 5.12 and 5.13 is 0.4(1-S) indicating that elongated particles tend to exhibit a wider range of Δ. The Δ value at any relative density $D_r = (e_{max} - e)/(e_{max} - e_{min})$ could be estimated by linear interpolation between Equations 5.12 and 5.13:

$$\Delta = D_r \left(\Delta_D - \Delta_L \right) + \Delta_L = \left(0.4 D_r + 0.6 \right)\left(1 - S \right) \qquad \text{Equation 5.14}$$
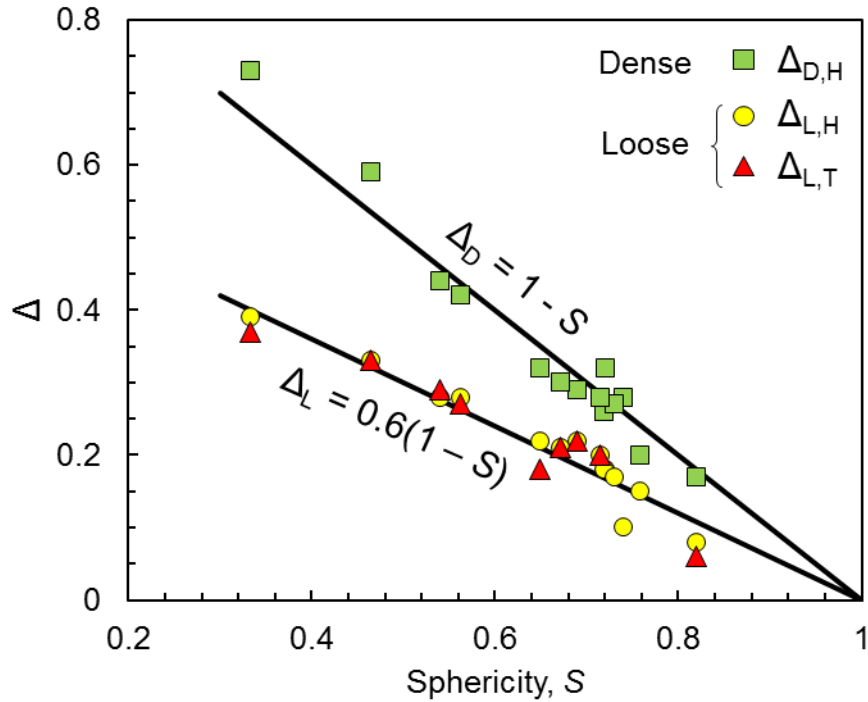

Figure 5.21 The relationship between degree of fabric anisotropy and particle shape.

The index void ratios e_{max} and e_{min} are intrinsic properties of soils. Equations 4.3 and 4.4 showed that e_{max} and e_{min} increase with decreasing particle roundness, R, decreasing sphericity, S, and increasing coefficient of uniformity, C_u. Therefore, the packing of soil particles is a reflection of the particle shape. To quantify packing, the void ratio corresponding to 50% relative density, e_{50} could be used. Figure 5.22 plots the Δ of soils at dense and loose conditions versus e_{50}. As expected, both Δ_D and Δ_L increase with increasing e_{50}. The data points are more scattered for sands with $e_{50} = 0.8 \sim 0.9$ because the e_{50} in this range is also affected by R, and C_u. The trends observed in Figure 5.22 can be approximated by:

$$\Delta_D = 1.55e_{50} - 1 \qquad \text{Equation 5.15}$$

$$\Delta_L = 0.8e_{50} - 0.5 \qquad \text{Equation 5.16}$$

As before, the Δ value at any relative density D_r can be estimated by linear interpolation between Equations 5.15 and 5.16:

$$\Delta = D_r\left(\Delta_D - \Delta_L\right) + \Delta_L = \left(0.75e_{50} - 0.5\right)D_r + 0.8e_{50} - 0.5 \qquad \text{Equation 5.17}$$

Equations 5.14 and 5.17 provide insight into the relationships between soil fabric, particle shapes and packing. Although users can always determine Δ values through the RHWT presented in this study, Equations 5.14 and 5.17 provide an alternative way to estimate Δ if D_r and either the particle sphericity or e_{50} are known. Having the Δ values, the fabric tensor of cross − anisotropic soil can be computed using Equation 5.5.
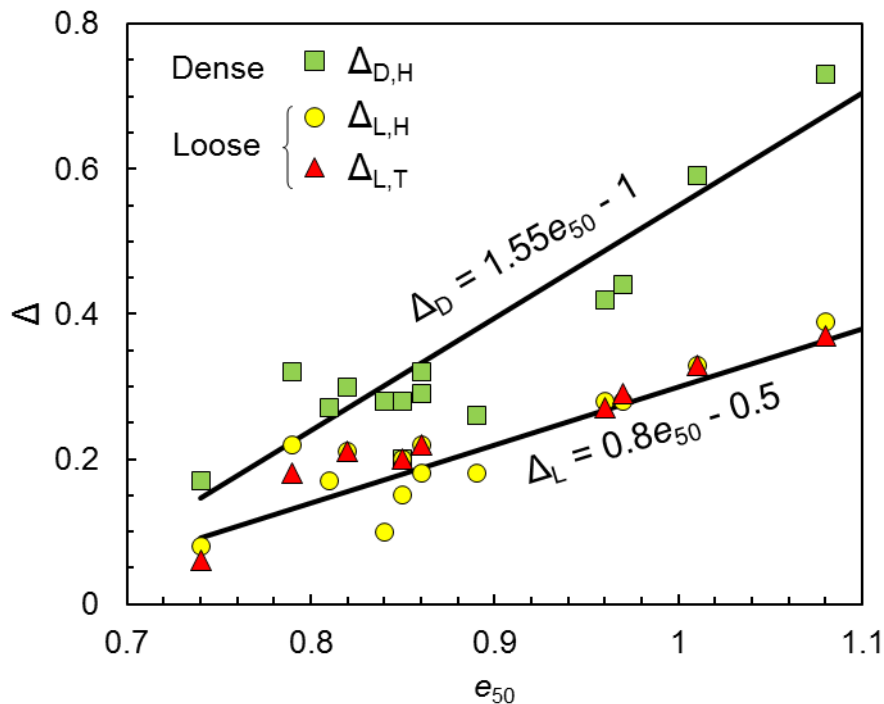

Figure 5.22 The relationship between degree of fabric anisotropy and packing.

145

5.6   Conclusions

Soil fabric is known to play an important role in soil mechanics. By virtue of depositional processes, alluvial, coastal and lacustrine sands develop cross-anisotropic fabric. The traditional manual method of characterizing fabric particle-by-particle is cumbersome. As such, a Rotational Harr Wavelet Transform (RHWT) method has been developed that mimics human cognition to automate fabric characterization. It requires dividing an image of a soil into many subareas for each of which a "pattern direction" is determined. The pattern directions from the subareas are used to create a traditional fabric rose diagram based on RHWT "Energies". The raw rose diagram can be smoothed using a second order Fourier series.

The RHWT method also yields the fabric direction β and a vector magnitude Δ that quantifies the degree of fabric anisotropy. To achieve results that replicate those by the traditional manual method the image magnification must provide at least 40 pixels per the shorter particle dimension (*PPS*). The size of the analysis subareas become a simple function of the *PPS*.

Eleven sands and three rice types were evaluated for their fabric anisotropy. Specimens were prepared in a square glass tube at a relative density, $D_r = 0\%$ then densified to $D_r = 100\%$. Images were taken and analyzed at both states and RHWT analyses were performed. The results showed the expected horizontal fabric with Δ increasing with densification.

Excellent correlations were observed between Δ and particle sphericity, S for both the loose and dense states. With linear interpolation, a simple functional relationship for $\Delta = f(D_r, S)$ was presented. Because both e_{max} and e_{min} decrease with S, an even simpler relationship of the form $\Delta = f(D_r, e_{50})$ was developed in which e_{50} is the void ratio corresponding to $D_r = 50\%$.

CHAPTER 6

A CORNER PRESERVING ALGORITHM TO GENERATE REALISTIC DEM PARTICLES

6.1   Introduction

An efficient particle clump generation algorithm for use in Discrete Element Methods (DEMs) was developed to simulate actual particles in a granular specimen. Here, the clump means bounding circles or spheres together to approximate soil particle surface. In clump generation, there will be a tradeoff between the number of circles and the fidelity of generated clumps compared to the original particle. This therefore raises questions regarding which geometrical features on a particle surface are more significant to macro mechanical behavior and therefore should be preserved in the clumps.

All properties determining a soil's mechanical behavior are either "state" or "intrinsic" (material) properties. All of the state and intrinsic properties should be preserved in a DEM model to simulate realistic soil behavior. While some state properties are expressed through the packing of clumps, intrinsic properties must be preserved at the clump level. Ideally, soil particles should be duplicated exactly by clumps. However, each of the clumps may contain thousands of circles. Therefore, some features of soil particles must be simplified in clumps to reduce the overall number of circles. However, the simplifications should not alter the overall intrinsic properties including particle size, sphericity, and roundness.

Since size and sphericity depend only on the particle length and width as observed in two–dimensional projections, the two properties are easily reproduced in DEM clumps. The Width and Length Ratio Sphericity (Equation 2.5) proposed by Krumbein and Sloss (1951) is used in this section.

By contrast, to preserve Wadell roundness (Equation 2.6), all of the corners on the particle perimeter including their sharpness and locations must be exactly duplicated. It is admittedly challenging but necessary to do so since mechanical behavior is known to be very sensitive to changes in particle roundness. For example, when Wadell roundness changes by only 0.1, the critical state angle of internal friction will change by 1.7° (Cho et al., 2006) and the peak friction angle will change by 2.4° (Bareither et al., 2008). Enormous trial and error would be required if the user wanted to faithfully reproduce actual Wadell particle roundnesses using the Ferellec and McDowell's (2010) and Taghavi's (2011) methods which merely place constraints on the smallest radius circles used in clump generation.

A corner preserving algorithm described in this section will solve the problem of accurately simulating particle roundness. The algorithm will identify corners in images of real soil particles and fit circles to them. The sharpness of corners will therefore be preserved. Then, the non-corner parts of soil particle outlines will be approximated by consecutive arcs. The reproduction accuracy will be controlled by an "*Area Ratio*" (*AR*) which is the ratio of the area of a clump to the area of the original particle. The *AR* will not be affected by particle size, angularity or image magnification. Intervention by users will not be needed to tune the *AR* for each clump. Therefore, the input to the proposed method will not be constrained to a limited number of single particle projections but will contain many soil particles having various sizes and shapes. The algorithm will automatically and quickly generate many clumps. The intrinsic properties of the generated clumps can also be determined by the algorithm. These properties in turn could be used to calibrate the DEM model.

6.2   Identification of corner circles

Human perception is able to quickly recognize the corners of a single particle. For example, the seven corners of the particle in Figure 6.1(a) are easily identified by eye. However, when numerous particles must be characterized, identification of corners and computation of roundness become impossibly laborious and time consuming efforts. Computerization of the process has been difficult since great differences exist among corners of the same

particle and certainly among corners of many particles. A second problem for computers has been elimination of the surface roughness which superimposes the smooth particle outline shown in Figure 6.1(b). Humans intuitively distinguish roughness from small sharp corners while computers must be programed to make such discriminations. These two computer challenges were overcome by chapter 3.
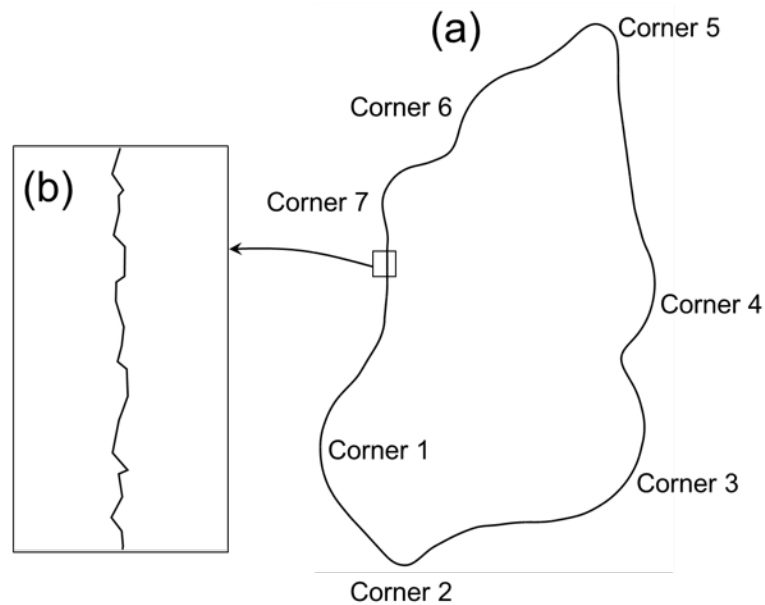

Figure 6.1 The corners and surface roughness of a particle.

The surface roughness can be removed from particle perimeters using two statistical techniques: "Locally weighted scatter plot smoothing" (LOESS) and "K-fold Cross Validation" as described in section 3.3. The particle perimeter is discretized by polar coordinates (θ, ρ) in Figure 6.2(a) and plotted as the solid line in Figure 6.2(b). The LOESS and K-fold cross validation are used to filter out the roughness resulting in a smoothed mean surface shown by the dashed line in Figure 6.2(b). Then, the mean surface is replotted to generate the new "smoothed" soil particle outline in Figure 6.2(c).
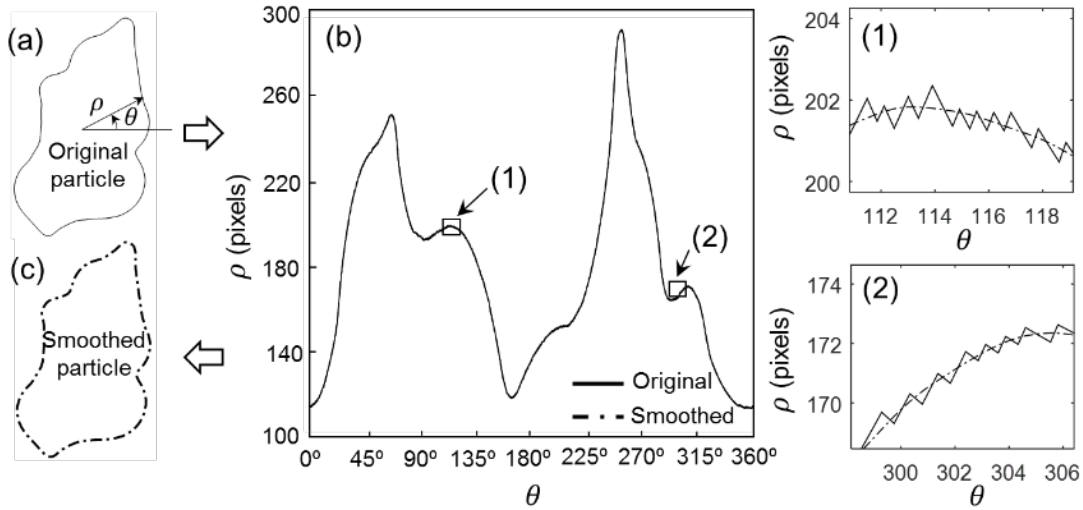
Figure 6.2 Removal of surface roughness.

Having determined the smoothed mean surface, a commonly used *root mean squared roughness* (Equation 3.3) quantifies the amplitude of the original particle surface relative to the mean surface. The computed roughness is 0.37 pixels for the particle shown in Figures 6.1 and 6.2. The image magnification was known to be 11.5×10^{-3} mm/pixel. Therefore, the roughness is 0.0043 mm.

After eliminating surface roughness from the particle perimeter, the computational geometry algorithm developed at chapter 3 is used to identify the particle corners. The results are shown in Figure 6.3. The particle length (d_1), width (d_2), and radius (r_i) of the maximum inscribed circle (C_i) can also be computed using computational geometry as shown in Figure 6.3. Finally, the intrinsic properties including sphericity and roundness can be computed using their classic definitions by Equations 2.5 and 2.6.
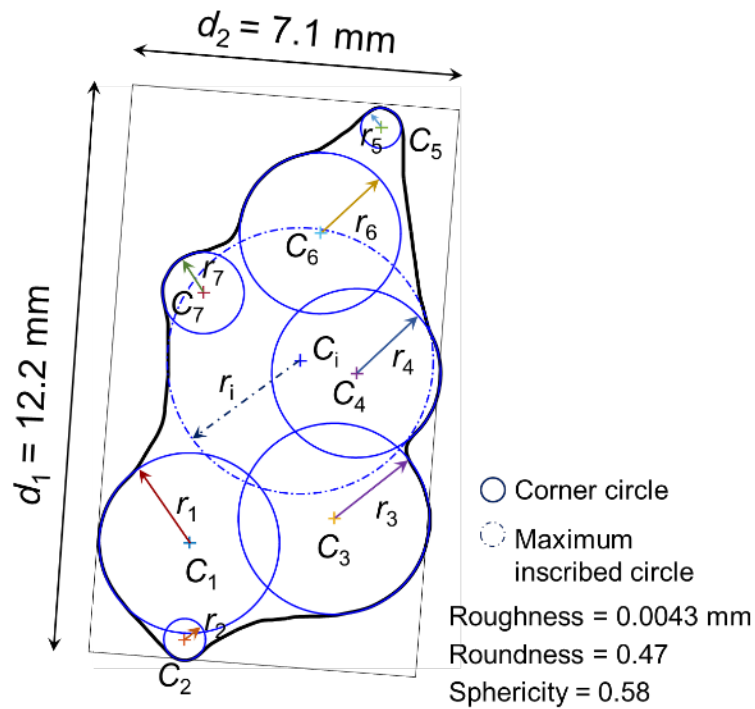
Figure 6.3 The corner circles and computed intrinsic properties.

6.3 Identification of non-corner circles

Soil particle perimeters consist of corner and the non-corner parts as shown in Figure 6.4. The non-corner parts can be further grouped into flat and concave parts. The corner parts are identified and represented by corner circles. The non-corner parts (either flat or concave) are also needed to complete the particle outlines. They will be represented by arcs of circles. For example, part $\overline{AB}$ can be represented by an arc $\widetilde{AB}$ from circle C_8 as shown in Figure 6.4. The C_8 should be as large as possible, without extending beyond the particle perimeter, to reduce the total number of circles in a clump. The allowable divergence of arc $\widetilde{AB}$ from $\overline{AB}$ is λ_0 in distance units.
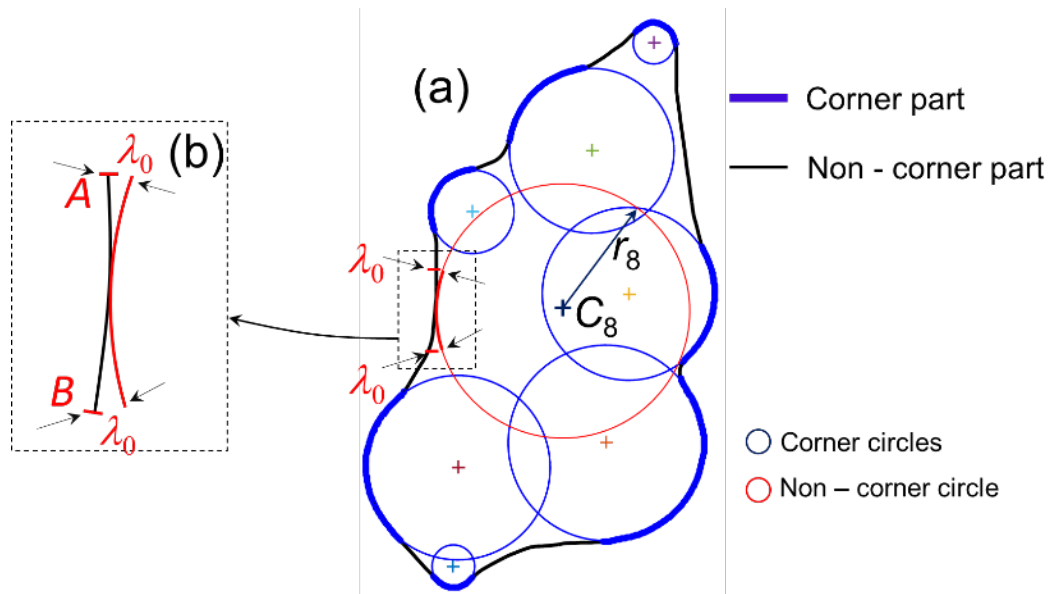
151

Figure 6.4 The structure of a soil.

The physical meaning of λ_0 is illustrated in Figure 6.5. Shown are three surfaces: the real particle surface, the mean surface, and the DEM clump model surface. As discussed before, the divergence of the real particle surface from the mean surface is quantified by the roughness. The DEM clump surface will actually be a series of consecutively connecting arcs as shown in Figure 6.5. The maximum departure of the DEM clump surface from the mean surface will be established by λ_0. As such, λ_0 will control the clump roughness.
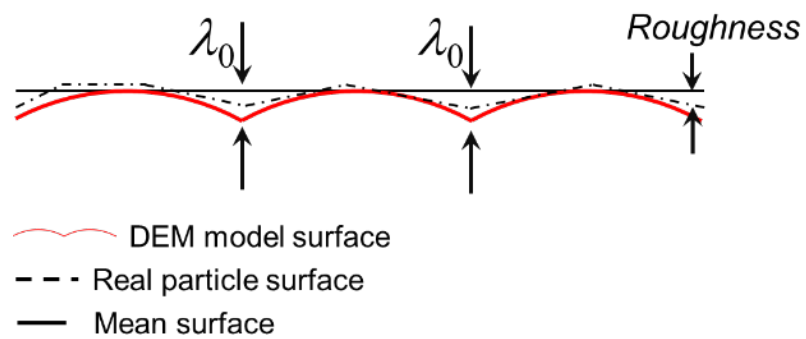

Figure 6.5 The physical meaning of λ_0.

The non-corner circles can be found through use of a Euclidean Distance Map (*EDM*). For a pixel within a particle's outline, such as pixel E in Figure 6.6(a), the nearest boundary pixel F is found and the distance EF is computed as L. The process is repeated for each point inside the soil particle resulting in the Euclidean distance map shown in Figure 6.6(b). It is evident that the line EF is perpendicular to the particle outline at F. Therefore, if a circle with a radius of L is centered at point E, that circle will be tangent to the particle outline at point F. Recall that the number of circles used to create a DEM clump should be as small as possible. Therefore, non-corner circles should be as large as possible yet not extend beyond the particle outline. To achieve this goal, the interior normal to the particle outline at point F is drawn extending through point E to the other side of the particle as shown in Figure 6.6(c). The maximum *EDM* value along this line is found and labelled as point G. It is noted that the distance FG is also the *EDM* value at point G and will be called L_{max}. Naturally, a circle centered at G having radius L_{max} will be tangent to the particle perimeter at F. This will also be the maximum tangent circle for point F. The maximum tangent circle for each point along the particle outline is found using this procedure.
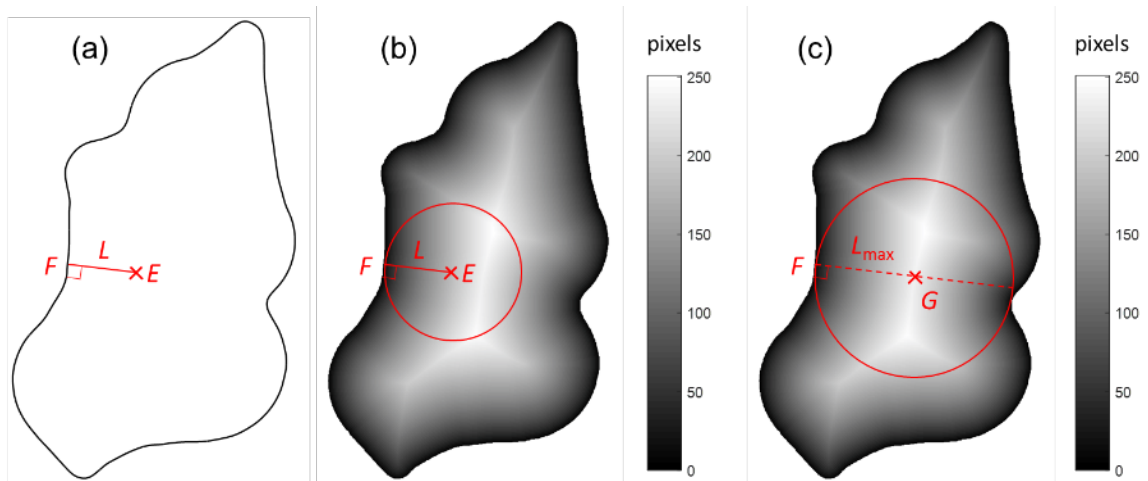

Figure 6.6 The Euclidean distance map for finding non-corner circles.

The next issue is how many tangent circles are needed to represent the non-corner parts of a soil particle outline. The previously defined departure parameter λ_0 is used for this purpose. The original soil particle perimeter with its fitted corner circles is shown in Figure 6.7(a). The perimeter contains 1266 points. For illustration, the maximum divergence is chosen to be $\lambda_0 = 40 \times$ surface roughness $= 0.172$ mm. A total of 868 perimeter points were approximated by the seven corner circles shown in Figure 6.7(a). The point range represented by each corner circle is also shown in Figure 6.7 (a). For example, points 1089 to 1189 are approximated by circle C_7.
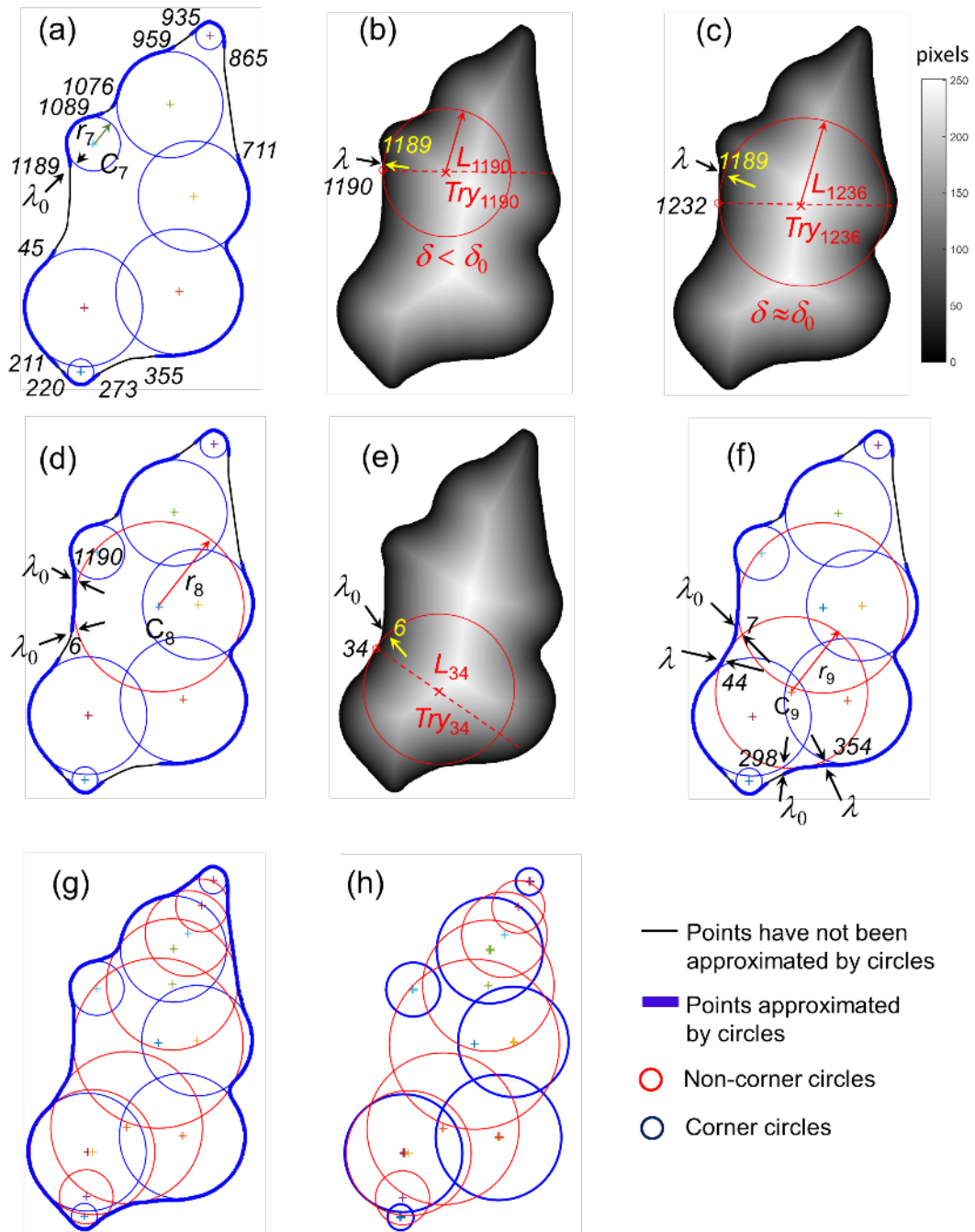
Figure 6.7 Non-corner circle.

The remaining 398 points (1266 − 868) must be represented by non-corner circles. The non-corner circle search process is as follows. The first point not yet represented by C_7 is

1190 as shown in Figure 6.7(a). Based on the Euclidean distance map shown in Figure 6.7(b), a trial circle tangent to the particle outline at point 1190 is found and called Try_{1190}. The previous point 1189 is set as a control point. The distance from 1189 to Try_{1190} is computed as λ. If λ is smaller than λ_0, Try_{1190} will not be a satisfactory circle. The next trial circle is computed using point 1191. The circle will be Try_{1191}. The distance λ from control point 1189 to Try_{1191} is compared with λ_0. If λ is still smaller than λ_0, Try_{1191} will also not be satisfactory. The next trial circle will be Try_{1192}. The process continues until a trial circle with $\lambda \approx \lambda_0$ is found. Figure 6.7(c) shows that Try_{1232} was found to be satisfactory. The non-corner circle associated with Try_{1232} is C_8. Next, the distances from all of the remaining 398 points to C_8 are computed, of which 83 were found to have distances smaller than or equal to λ_0. Those 83 points are 1190 to 1266, and points 1 to 6 as shown in Figure 6.7(d). Therefore, the section of the particle outline containing points 1190 to 1266 and 1 to 6 is represented in the clump by circle C_8 as shown in Figure 6.7(d). The number of points which have still not been represented becomes $398 - 83 = 315$.

In the next step, point 6 is set as the control point. Based on the Euclidean distance map shown in Figure 6.7(e) the next satisfactory non-corner circle with $\lambda \approx \lambda_0$ was found to be Try_{34} which identified circle C_9. The distances from the remaining 315 points to C_9 are computed. Having computed distances smaller than λ_0, points 7 to 44 and points 298 to 354 can be represented by C_9 as shown in Figure 6.7(f). This leaves 220 points having not been represented. The process continues until all the points on the soil perimeter are represented as shown in Figure 6.7(g). Figure 6.7(h) shows the final circle clump representing the original soil particle. In the end, a total of 14 circles including 7 corner circles and 7 non-corner circles were used to create the clump.

4. Accuracy control

As mentioned in the section 2.4, the accuracy of clumps in simulating a real particle cannot be assessed in current clump generation methods; it is done subjectively by the user. By contrast, in the proposed corner preserving algorithm, accuracy assessment is integrated

with clump generation through the Area Ratio (AR) previously defined as the ratio of the area of the clump to the area of the original soil particle. In Figures 6.8(b) to 6.8(e), four clumps were generated with different AR values by tuning λ_0 in the corner preserving algorithm. The λ_0 values and the corresponding number of circles constituting the clump (denoted by N) are summarized in the figure. As shown, the changing of AR does not affect the sharpness and location of corner circles. However, the non-corner parts are affected. As AR decreases (λ_0 increases correspondingly), the non-corner parts become progressively bumpier as in Figure 6.8(d) or even become relatively large arcs as in Figure 6.8(e). This alters the surface structures of the soil particle and consequently may change the macroscopic mechanical behavior in simulations.
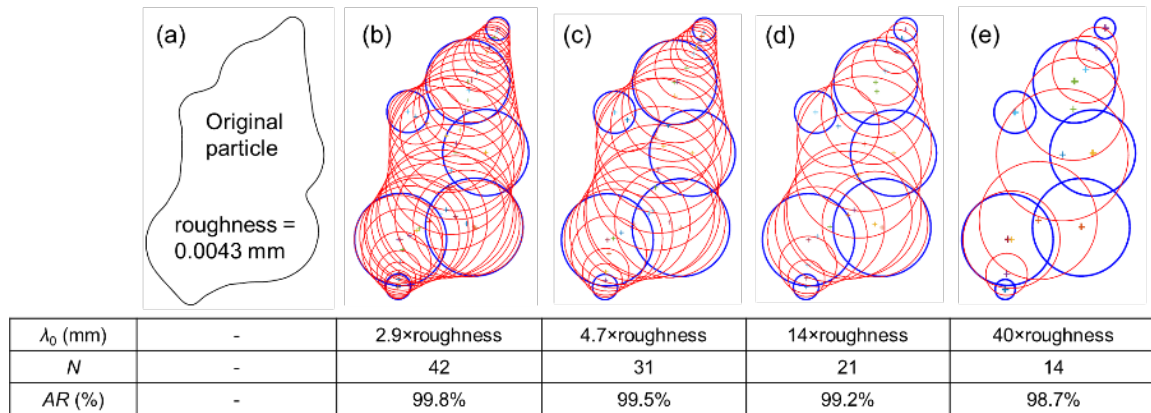

λ_0 (mm)	-	2.9×roughness	4.7×roughness	14×roughness	40×roughness
N	-	42	31	21	14
AR (%)	-	99.8%	99.5%	99.2%	98.7%

Figure 6.8 Accuracy control in clump generation.

Figures 6.9(a) and (b) illustrates the trends between AR and N depending on R and S values respectively. A total of 17 particle images shown in the figure inserts were used. The four numbers superimposed over the particle images are sequentially: the particle number, R value, S value and the roughness value. In Figure 6.9(a), the eleven particles have R values ranging from 0.08 to 0.90 while the S values are in a narrow range from 0.62 to 0.81. Expectedly, the N values increase with increasing AR for all particles. Meanwhile, to achieve the same AR, angular (low R) particles require more circles due to their complex

surface structures. Especially for particles having *R* values smaller than 0.2, the *N* values will greatly increase as *R* decreases. Figure 6.9(b) shows six particles having *S* values from 0.21 to 0.88 while *R* values are around 0.5. Naturally, elongated particles require more circles to achieve the same *AR* values. Especially for particles having *S* values smaller than 0.5, the *N* values will significantly increase as *S* decreases.
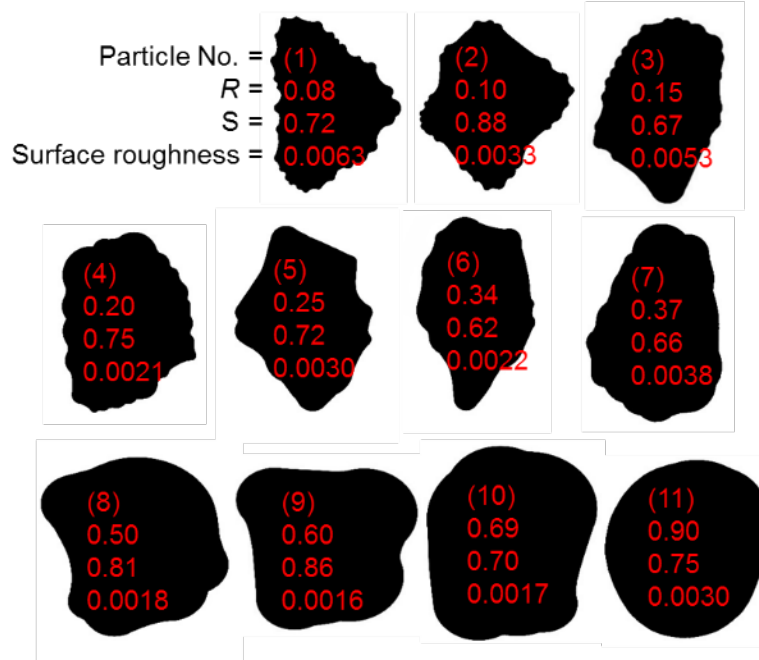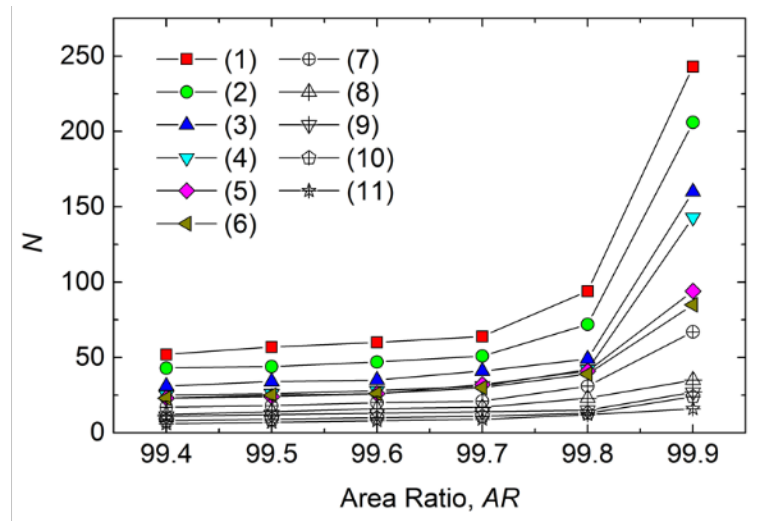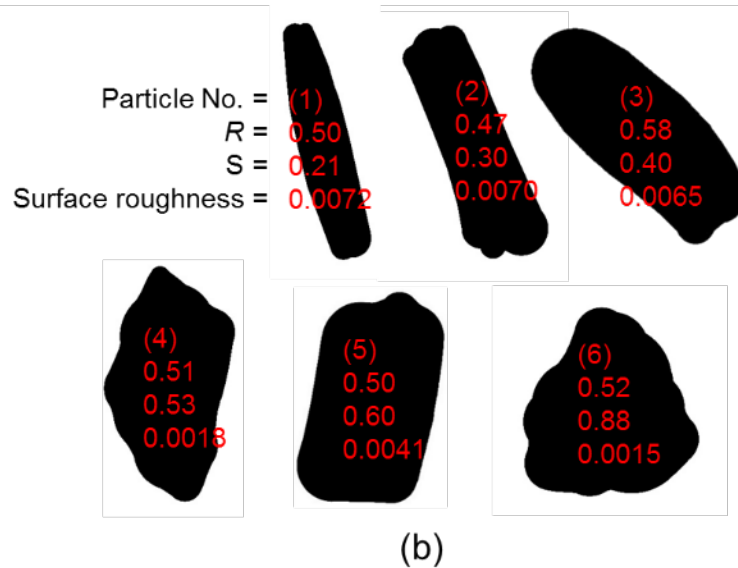

(a)
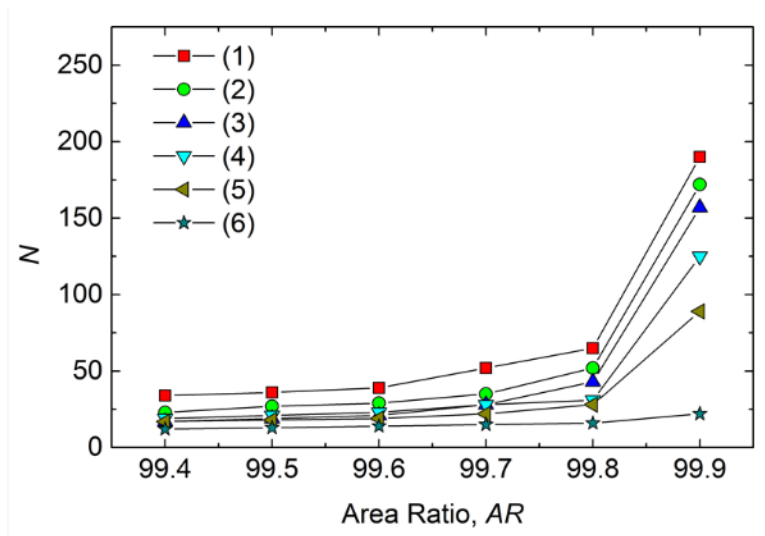
Figure 6.9 The relationship between *AR* and *N*: (a) as a function of *R*;
(b) as a function of *S*.

For a specific *AR*, the *N* depends not only on *R* and *S* but also on the number of corners, on the structure of the non-corner parts of a particle perimeter and on surface roughness. Therefore, a model between *AR* and *N* based on Figures 6.9(a) and (b) would be difficult to develop and would not be meaningful. Nevertheless, Figure 6.9 does provide general trends that could be used for initial estimation of *AR*. Based on the *R* and *S* values of a particular soil of interest, the available computational resources and the desired accuracy

of a simulation (desired N values), users can obtain a first estimate of AR values by Figure 6.9. Users can then further tune the AR value to satisfy the simulation needs.

Another important observation from Figure 6.9 is that once AR is larger than 99.8%, further increases in AR will dramatically increase the number of circles in clumps. As such, AR is maintained at 99.8% in the rest of this chapter.

Figure 6.10 summarize the frame work for the corner preserving algorithm within the broader context of determining several intrinsic soil properties from an image or images of a soil. The soil particle images are first converted into binary images. At this point, the size of each particle can be obtained and therefore the particle size distribution can be plotted. After perimeter smoothing, during which particle roughness was determined, the corner parts of soil particle outlines are identified and represented by corner circles using computational geometry method. The sphericity and roundness can now be computed. In the next step, the Euclidean Distance Maps are created and the non-corner parts are approximated by consecutive arcs.
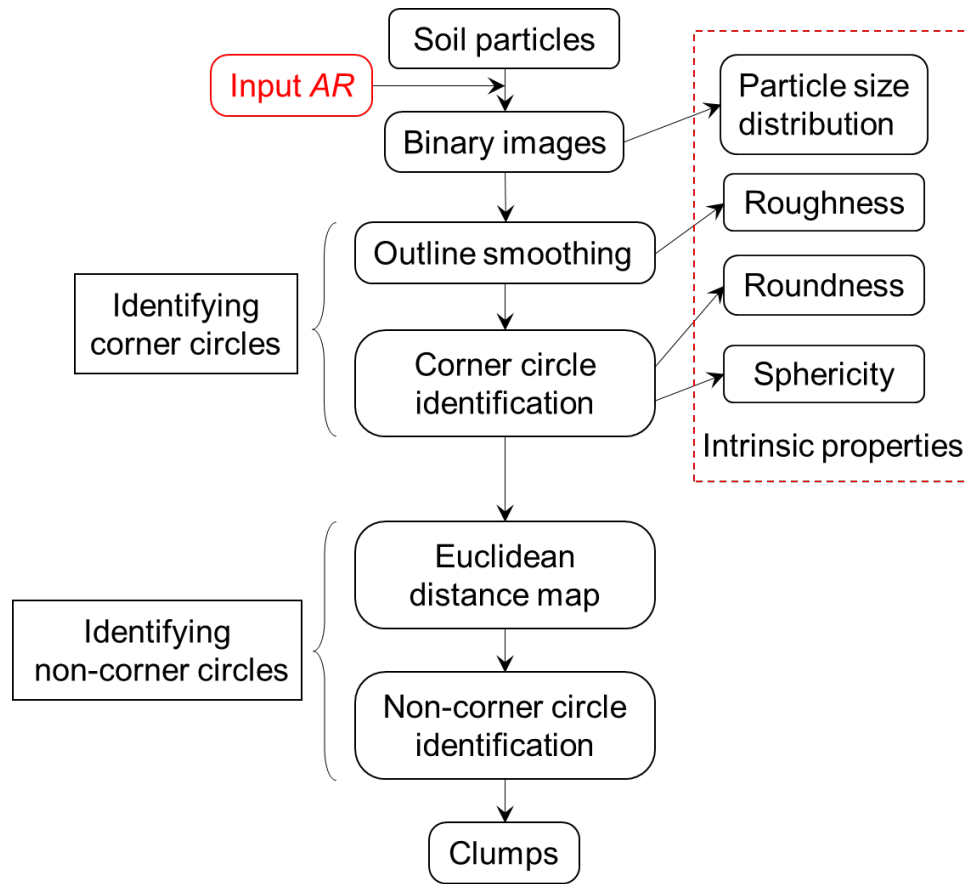
Figure 6.10 The framework of the corner preserving algorithm.

The accuracy of the clump approximation is prescribed at the outset through the user-selected value of *AR*. Based on the *AR*, the program will automatically search for the optimum λ_0. The search process starts with the computed roughness and gradually tunes it to find the λ_0 that yields the prescribed *AR*.

Compared to techniques by Ferellec and McDowell (2010), and Taghavi (2011) that involve multiple accuracy control parameters which are difficult to select, the proposed corner preserving algorithm requires only one parameter, *AR*. The *AR* is an intuitive and dimensionless parameter that can be applied universally to all of the particles in a DEM cluster simulation. It is not affected by particle size, angularity, surface roughness or image magnification.

The final clump well preserves the size, sphericity, and roundness of the original soil particle while the surface roughness is simplified by *AR* to reduce the total number of circles. This reduction in roughness would obviously affect the mechanical behavior of the particle assembly. However, this is remedied by explicitly defining the contact friction coefficient in the DEM code. With additional research the contact friction coefficient could be related to the particle roughness as defined by Equation 3.3.

6.3.1   Comparison with the bubble packing algorithm

As mentioned before, the current most popular clump generation algorithm is the bubble packing algorithm integrated in PFC. Therefore, it is useful to compare the proposed corner preserving algorithm to the bubble packing algorithm. As mentioned earlier, a soil particle outline consists of flat, concave and corner parts.

Both algorithms use a series of arcs to approximate a flat part shown in Figure 6.11(a). The approximation accuracy is controlled by λ_0 in the corner preserving algorithm and by φ in the bubble packing algorithm. Both methods could generate the same representations if appropriate λ_0 and φ values are used as shown in Figures 6.11(d) and 6.11(e).

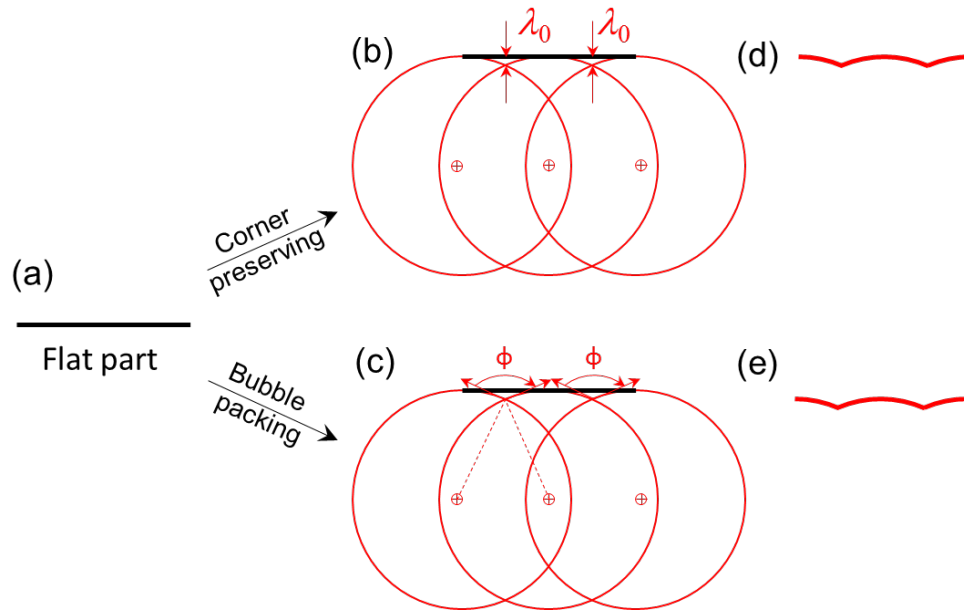Figure 6.11 Representation of flat parts of a clump.

For a concave part shown in Figure 6.12(a), the corner preserving algorithm will generate a sharp tip at the intersection of two circles as shown in Figures 6.12(b) and 6.12(d). By contrast, the bubble packing algorithm requires extra circles near the tip of the concavity to maintain a constant φ as shown in Figures 6.12(c) and 6.12(e).
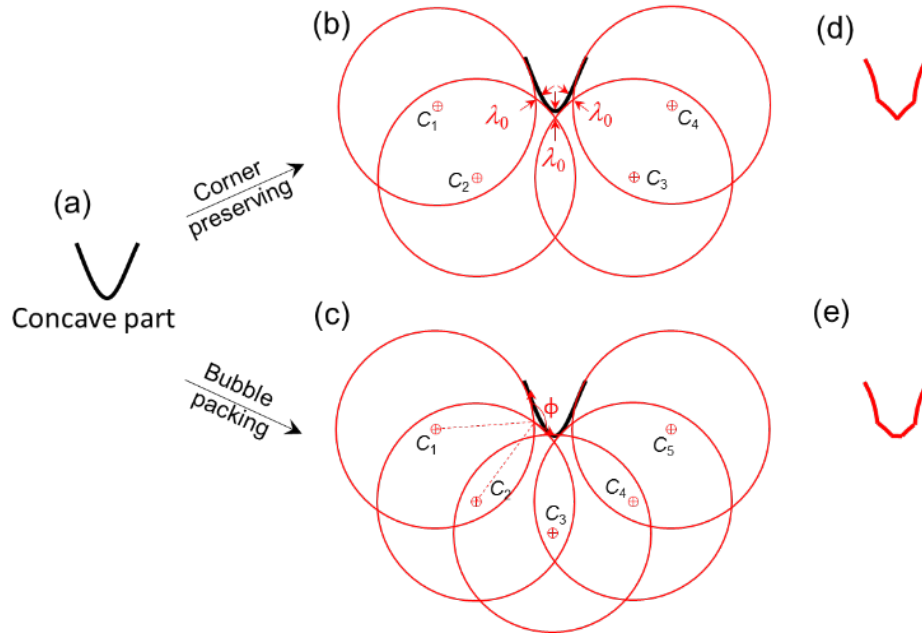
Figure 6.12 Representation of concave parts of a clump.

For corner parts, the corner preserving algorithm will automatically fit an appropriate circle to the corners as shown in Figures 6.13(a), 6.13(b) and 6.13(d). By comparison, the bubble packing algorithm requires multiple circles at circle-to-circle angle φ to approximate a corner. Therefore, the bubble packing algorithm uses more circles to represent corners and creates an artificial bumpy surface compared to the proposed corner preserving algorithm.

Figure 6.13 Representation of corner parts of a clump.

In summary, both algorithms give similar approximations for flat parts. However, the corner preserving algorithm uses fewer circles to represent concave and corner parts than the bubbl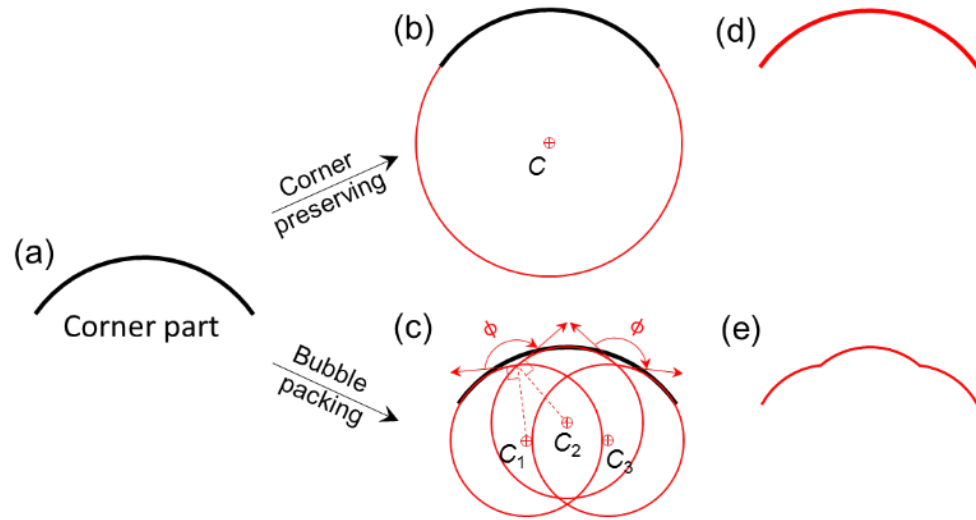e packing algorithm does. For angular particles containing many sharp corners and concavities, the corner preserving algorithm will significantly reduce the number of circles needed to represent particles. For particles with simple outlines (typically rounded particles), both algorithms yield similar accuracy with similar numbers of circles.

A series of particles with different R and S values were represented by both algorithms and the results are compared in Figure 6.14. For the corner preserving algorithm, the input accuracy control parameter AR was set to 99.8%. The algorithm automatically finds the optimum λ_0. The clumps generated by the corner preserving algorithm are shown in the second column in Figure 6.14. When using the bubble packing algorithm, the two parameters φ and ρ were carefully tuned to achieve the same AR of 99.8% while ensuring that the minimum number of circles was used. Since both algorithms preserved 99.8% of the original particles their efficiencies could be compared on an equal basis. As expected, the corner preserving algorithm used far fewer circles than the bubble packing algorithm, especially for angular particles. It is noted that in Figure 6.14 the d_1, d_2, S, R and roughness

values were computed from the corner-preserving algorithm at the same time that the clump is generated.
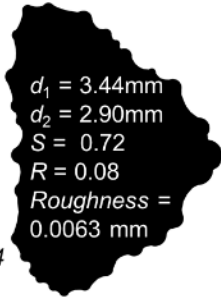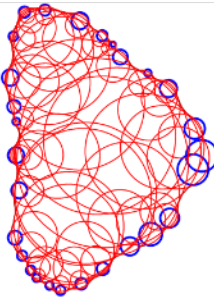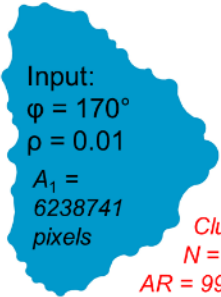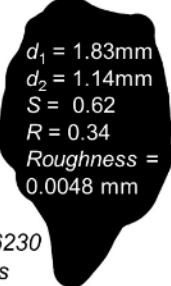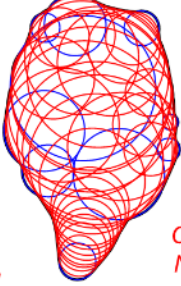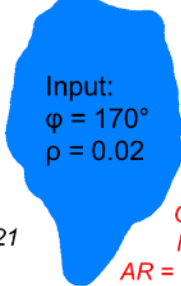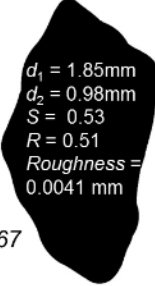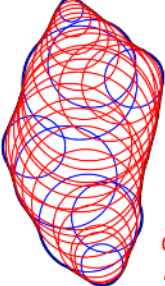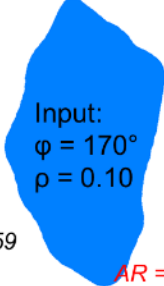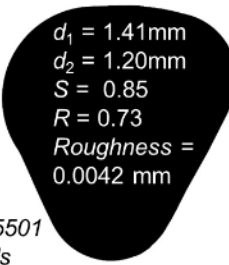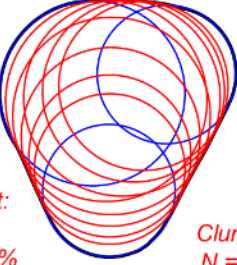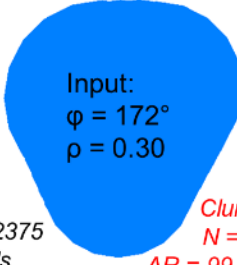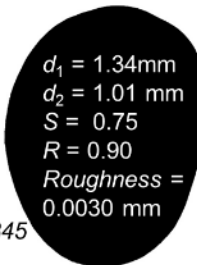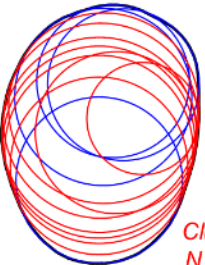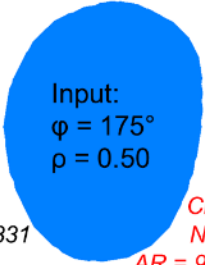
Soil particle	Corner preserving	Bubble packing
(a) d_1 = 3.44mm d_2 = 2.90mm S = 0.72 R = 0.08 Roughness = 0.0063 mm A_0 = 6251244 pixels	*Input: AR= 99.8%* *Clump: N = 94*	Input: φ = 170° ρ = 0.01 A_1 = 6238741 pixels *Clump: N = 230* *AR = 99.8%*
(b) d_1 = 1.83mm d_2 = 1.14mm S = 0.62 R = 0.34 Roughness = 0.0048 mm A_0 = 1596230 pixels	*Input: AR= 99.8%* *Clump: N = 39*	Input: φ = 170° ρ = 0.02 A_1 = 1592521 pixels *Clump: N = 95* *AR = 99.8%*
(c) d_1 = 1.85mm d_2 = 0.98mm S = 0.53 R = 0.51 Roughness = 0.0041 mm A_0 = 1384567 pixels	*Input: AR= 99.8%* *Clump: N = 31*	Input: φ = 170° ρ = 0.10 A_1 = 1381959 pixels *Clump: N = 63* *AR = 99.8%*
(d) d_1 = 1.41mm d_2 = 1.20mm S = 0.85 R = 0.73 Roughness = 0.0042 mm A_0 = 1285501 pixels	*Input: AR= 99.8%* *Clump: N = 11*	Input: φ = 172° ρ = 0.30 A_1 = 1282375 pixels *Clump: N = 24* *AR = 99.8%*
(e) d_1 = 1.34mm d_2 = 1.01 mm S = 0.75 R = 0.90 Roughness = 0.0030 mm A_0 = 1054845 pixels	*Input: AR= 99.8%* *Clump: N = 12*	Input: φ = 175° ρ = 0.50 A_1 = 1052331 pixels *Clump: N = 20* *AR = 99.8%*

Figure 6.14 Comparison of corner preserving and bubble packing algorithms.

6.3.2 Integrating the corner preserving algorithm into various image-capturing systems

Optical soil particle characterization has witnessed great advances since the 2000's. Various devices have been developed to capture particle images. Some of the systems include: the University of Illinois Aggregate Imaging System (UIAIA) (Rao and Tutumluer, 2000; Pan et al., 2006; Tutumluer and Pan, 2008), the Aggregate Imaging System (AIMS) (Mahmoud and Masad, 2007; Fletcher et al., 2003; Chandan et al., 2004), the Translucent Segregation Table system (TST) (Ohm and Hryciw, 2013), the QICPIC system (Altuhafi et al., 2013), the Vision cone penetrometer (VisCPT) (Raschke and Hryciw, 1997) and Sedimaging (Ohm and Hryciw, 2014).

In the UIAIA, AIMS, and QICPIC systems, the soil particles are separated prior to image captured either manually (UIAIA and AIMS) or through a specialized mechanism (e.g. falling particles in front of a camera in the QICPIC). These systems capture 2D non-contacting binary particle images. In the TST system, the soil particles do not need to be physically separated. An improved watershed algorithm introduced by Zheng and Hryciw (2016) digitally detaches the touching particles in the images. This system simplifies the test process and can efficiently analyze large and therefore statistically significant numbers of particle. The method presented in this chapter can readily be integrated into the systems that yield binary particle images. Figure 6.15 shows a small area cropped from a TST image in which the contacting particles have been digitally separated by the improved watershed algorithm of Zheng and Hryciw (2016). A total of 264 particles are identified.
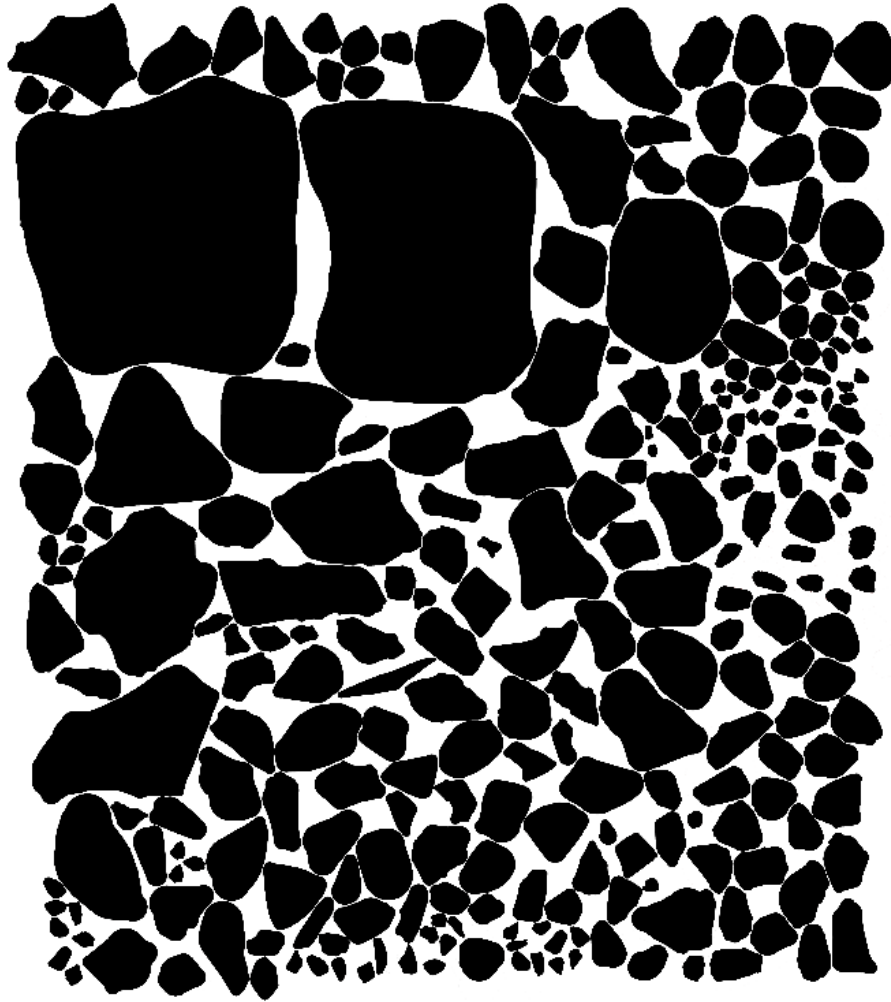
Figure 6.15 A typical image from the binary image capturing devices.

Figure 6.15 was inputted into the proposed corner preserving algorithm. The control parameter AR was set to 99.8%. The program automatically identified each particle and fit it with corner and non-corner circles. Clumps were generated for all 264 particles as shown in Figure 6.16. Volume-based intrinsic property distributions of the clumps were obtained and are shown in Figure 6.17. The volume of each clump was computed as $d_1 \times d_2 \times d_2$.
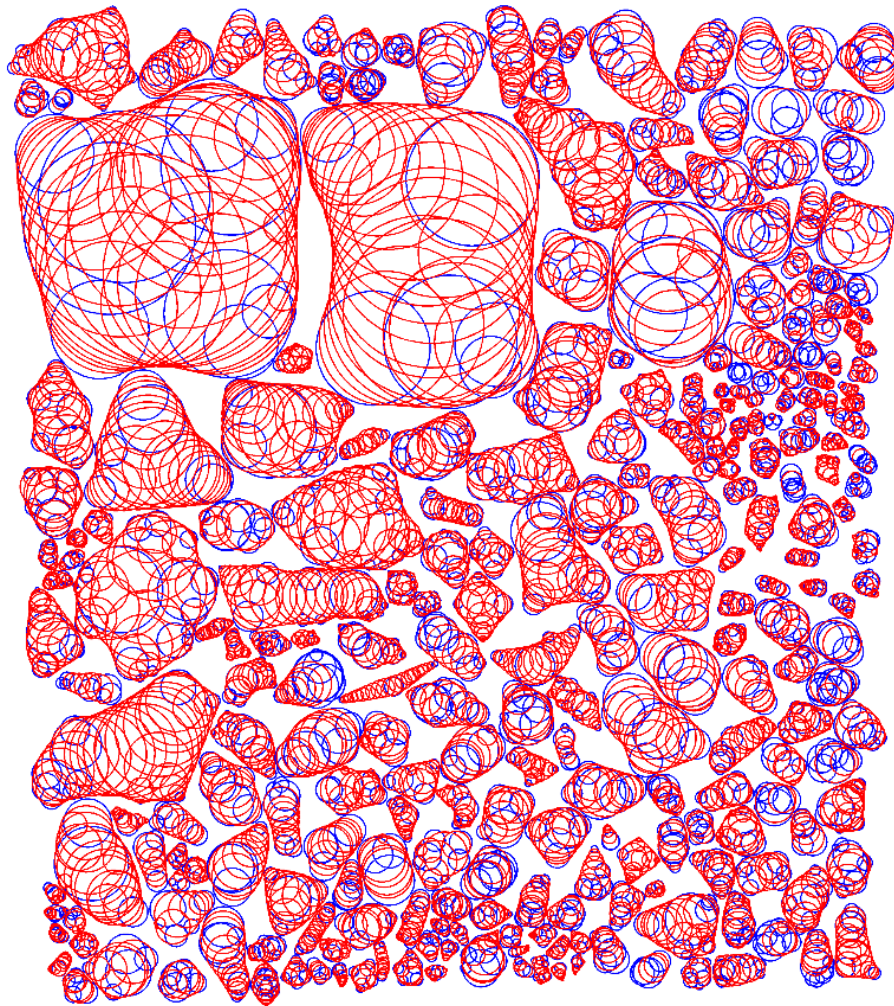
Figure 6.16 The clumps generated from Figure 6.15.
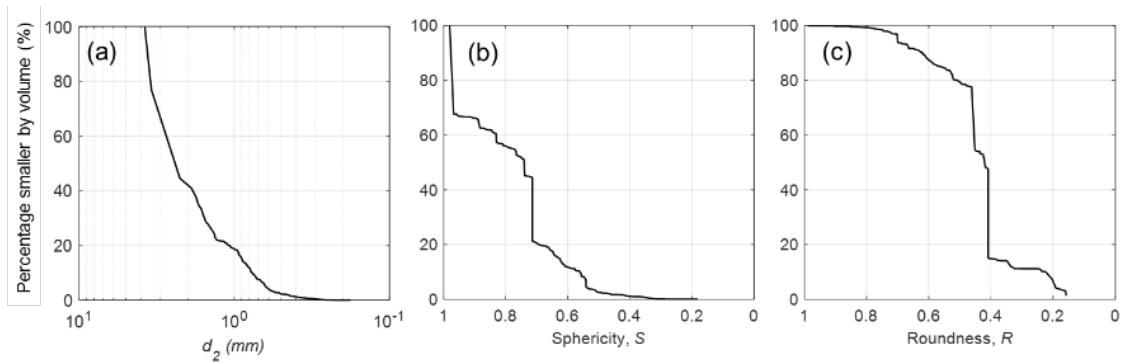
Figure 6.17 Intrinsic property distributions from clumps in Figures. 6.15 and 6.16.

By contrast with the above, the VisCPT and Sedimaging systems capture images of 2D particle assemblies in-situ and in the laboratory respectively. A typical captured soil assembly is presented in Figure 6.18(a). As shown, the particles are not only in contact with each other, many also block or are blocked from view by other particles. Some soil particles may have a full projection of their area in view while others will be occluded by foreground particles. Naturally, only particles exhibiting full projections are useful for clump generation. However, distinguishing particles with full projections from voids and occluded particles is a difficult task since soils have various colors, size distributions, internal textures, particle forms and roundnesses. The semi-automated approach developed in chapter 3 is used to pick out the particles with full projections as shown in Figure 6.18(b). For each identified particle, the corner preserving algorithm was used to generate its corresponding clump. The results are shown in Figure 6.18(c). As before, volume based intrinsic properties of the generated clumps were computed and are shown in Figures 6.19.

Figure 6.18 Clump generation from an image of a particle assembly.
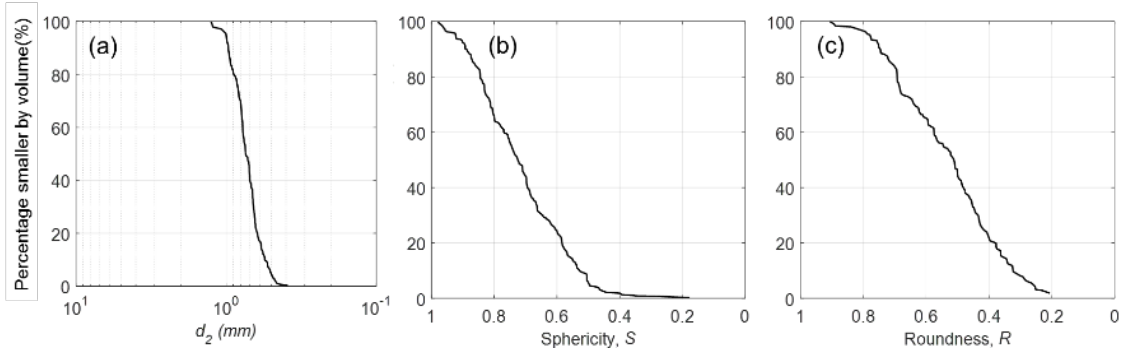
Figure 6.19 Intrinsic property distributions from clumps in Figure 6.18.

As mentioned earlier, the number of circles in a clump is determined mainly by particle roundness with some contribution from sphericity. The roundness reflects the outline complexity. As has been established in this chapter, angular particles have complex outlines and therefore require more circles to approximate them. This observation is further verified in Figure 6.20. Figure 6.20(a) summarizes the generated clumps from Figures 6.9, 6.14, 6.16, and 6.18. All the clumps have $AR = 99.8\%$. As shown before, the corner preserving algorithm uses fewer circles for generating clumps compared to the bubble packing algorithm. This difference increases as R decreases and becomes very large when R drops below about 0.5. For approximating angular to very angular particles (Wadell roundness below 0.5) with a $AR = 99.8\%$, the number of circles required for bubble packing is roughly four times the number of circles required by the corner preserving algorithm.

Figure 6.20(b) expands the results of only the corner preserving algorithm. Four abnormal points fall well outside of the observed trend line. Those points correspond to very elongated particles shown in the insert in Figure 6.20(b). Clearly, very elongated (less spherical) particles will require more circles to approximate them.

173
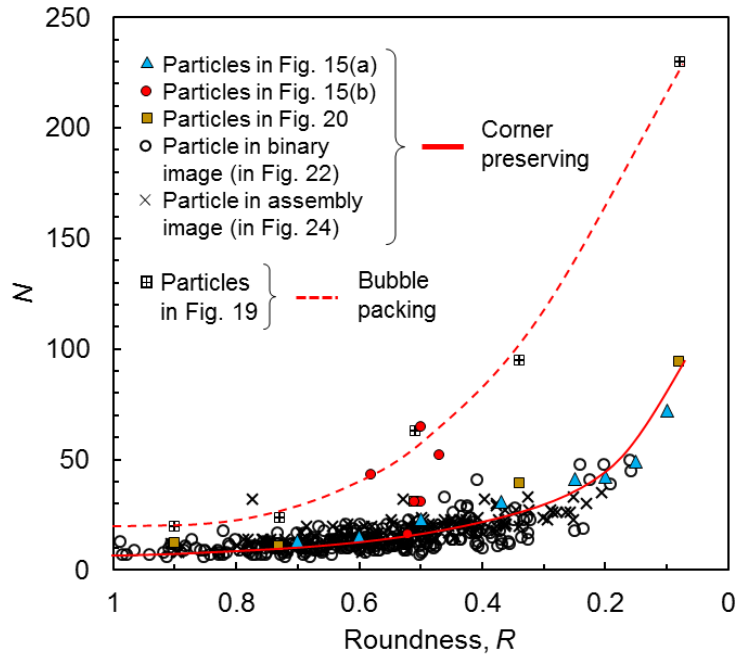
(a)
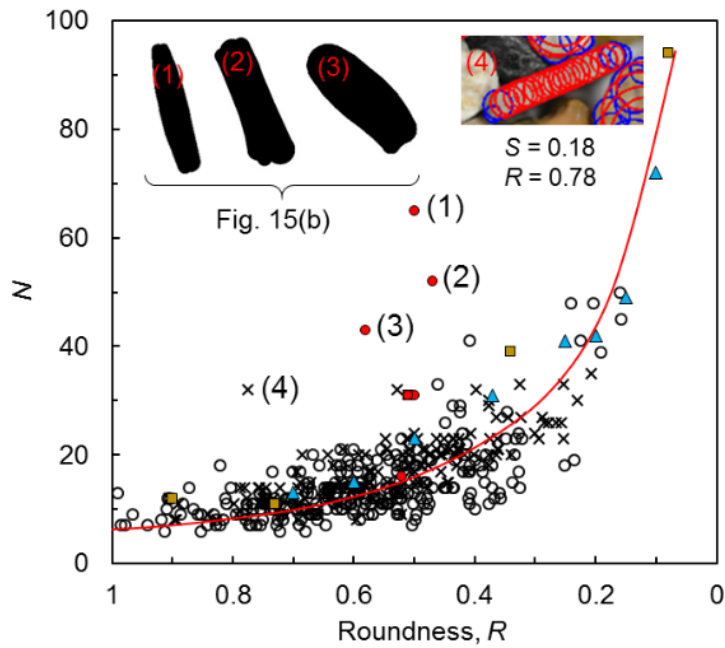
(b)

Figure 6.20 The required number of circles in clumps versus particle roundness:
comparison of the corner preserving algorithm and the bubble packing algorithm.

174

6.4 Conclusions

In summary, the corner preserving algorithm for particle clump generation proposed in this chapter possesses the following features:

1) The corner parts of soil particles are first identified and fitted by corner circles. As such, the location, size and shape of the corners is completely preserved. This also reduces the number of circles needed in the clump compared to the bubble packing algorithm which requires multiple circles to represent each corner. The non-corner parts of particles are approximated by consecutive arcs from circles. The accuracy of such approximation is controlled by AR (or λ_0). The tuning of AR (or λ_0) does not affect the corner representation. The algorithm is therefore termed as the "corner preserving" algorithm.

2) During clump generation, the particle size, sphericity, roundness and surface roughness of each soil particle in a specimen are computed. In the generated clumps, the particle size, sphericity, and roundness are preserved. The particle size distribution, sphericity, and roundness have been proven to be very important to various macro-mechanical behaviors of soils. Since the relationships between these intrinsic properties and macro-behavior of soils are known through empirical models such as developed by Cho et al. (2006), Baraeither et al. (2008) and Zheng and Hryciw (2016), they can essentially be used to calibrate DEM models. The surface roughness is simplified in the generated clump to reduce the number of circles. However, such simplification is remedied by explicitly defining contact friction coefficients in DEM models. Future research could yield correlations between the surface roughness defined in this chapter and the contact friction coefficient.

3) The surface roughness computed in the first step in the algorithm is used as a reference value to find the optimum λ_0. After a user specifies AR, the program tunes the surface roughness to find a λ_0 satisfying the AR. This significantly shortens computation time.

4) The proposed algorithm only requires one input parameter, AR. The AR is independent of particle size, angularity and image magnification. It is a very intuitive parameter. Unlike

in existing clump generation methods, users do not need to adjust the control parameters for each clump.

5) The inputs to the proposed algorithm are either binary images or images of soil assemblies that could contain many particles. Unlike existing algorithms in which clumps must be generated individually, the proposed algorithm can automatically generate clumps for many soil particles. The large number of clumps accurately representing real soil particles will be a statistically valid representation of the original soil in DEM simulations.

6) Compared to the bubble packing algorithm, the proposed corner preserving algorithm significantly reduces the number of circles required for each clump. The differences in required numbers of particles become progressively larger as particle roundness decreases. For a particle having a Wadell roundness lower than 0.5, the proposed corner preserving algorithm required only a quarter of the number of circles that would be needed by the bubble packing algorithm to achieve the same AR of 99.8%.

CHAPTER 7

GRADATION, SHAPE AND FABRIC IN DEM

7.1 Introduction

The Discrete Element Method (DEM) is commonly used to simulate particulate materials to investigate micro scale behavior that may not be easily observed or measured in physical tests. Hypothetically, if a virtual soil specimen is created that has the same intrinsic and state properties as a real soil specimen, its behavior in a DEM simulation should faithfully mimic the actual physical test. The question then becomes how to reproduce the intrinsic and state properties in the DEM model.

To reproduce an actual soil specimen perfectly, the corner-preserving algorithm developed in the chapter 6 could conceivably be used to generate as many clumps as there are particles in the soil specimen. To do so would require an image of every soil particle. It is certainly worth considering if such a large number of particle images must necessarily be collected each time a new soil is to be simulated. Instead, could virtual soil specimens be constructed from a permanent library of clumps based only on desired distributions of particle shapes and sizes? The desired distributions could be to model an actual soil specimen for which the size distribution would be determined either by conventional sieving or image analysis and for which the shape distribution would be determined by image analysis on a statistically representative number of particles. Alternatively, the library could be used for parametric studies without an actual soil to be modeled.

Some intrinsic properties including surface roughness and hardness are accounted for through defined mechanical model parameters such as the contact friction coefficient and particle stiffness. The remaining parameters including the distributions of particle size, particle sphericity and roundness have limitless possibilities and must be preserved by the

clump geometries. The question narrows down to how to create appropriate clump geometries to satisfy the desired distributions. As mentioned earlier, exhaustively reproducing all of a specific sand specimen's particles by clumps is not an efficient approach. Creation of the clump library would eliminate the need for reproducing tens of thousands of particles for each simulation.

This chapter describes the development of a large permanent clump library for use in Discrete Element Methods (DEMs). It shows how the library was constructed from numerous previously collected images of individual sand particles and how it may be used. At the present time, the library consists of only 2D particles developed from images of 2D particle projections. While soils must naturally be simulated by 3D clumps in DEMs, there are compelling reasons and distinct advantages to first developing a 2D particle library. First, the classic definitions of R and S are based on 2D particle projections and there is a long history of their usage. The corner-preserving algorithm is also presently only developed for 2D. It is easier to demonstrate the construction and usage of a 2D library. Results of 2D simulations are easier to visualize and interpret. Finally, the computational power required to create and test the library is far less demanding. Indeed, a 3D DEM simulation using a statistically valid number of clumps to faithfully simulate a real soil problem is still somewhat unrealistic.

7.2   Clump library construction

To date, a total of 98,489 images of real soil particles have been collected and modeled by clumps using the 2D corner-preserving algorithm. The "clump library" includes a wide range of particle sizes, angularities, and sphericities. The library can be expanded by adding more clumps. Ten select clumps from the library are shown in Figure 7.1. The listed R and S values have been rounded and saved in the library with two decimals. The number of circles used to construct each clump (n_c) is also shown. Having complex surface structures, the angular particles clearly require more circles to approximate them. Very elongated (low S) particles also naturally need more circles. Each clump is archived in the library by an index "$R_L\_S_L\_id$" consisting of three integers as shown in Figure 7.1. The R_L and S_L are

hundred-folds of the computed R and S values respectively. Since many clumps may have the same R_L and S_L values, the third parameter "id" is used to discriminate them. The combination of these three digits is able to catalog an unlimited number of clumps in the library. The information stored in the library for each clump also includes *basic* and *structural* information. The basic information includes the clump volume v and size d. The structural information includes the total number of circles n_c, as well as the radius and center location of each circle.

R	S	n_c	R	S	n_c	R	S	n_c	R	S	n_c	R	S	n_c
0.11	0.86	83	0.27	0.76	64	0.48	0.78	41	0.70	0.76	17	0.86	0.95	16
Index: 11_86_1			27_76_1			48_78_1			70_76_1			86_95_1		

R	S	n_c	R	S	n_c	R	S	n_c	R	S	n_c	R	S	n_c
0.47	0.20	48	0.50	0.28	56	0.11	0.43	86	0.46	0.47	30	0.65	0.66	21
Index: 47_20_1			50_28_1			11_43_1			46_47_1			65_66_1		

Figure 7.1 Ten selected clumps from the library.

A convenient map of the clump library is shown in Figure 7.2. The locations of clumps in the library are determined by their R_L and S_L values. As just mentioned, many particles may possess the same R and S combination. Thus, multiple clumps may exist at one map location. For example, there are 34 clumps at the spot $(R_L, S_L) = (55, 63)$ in Figure 7.2. The 34 clump are distinguished by the id numbers from 55_63_1, 55_63_2, … up to 50_63_34.
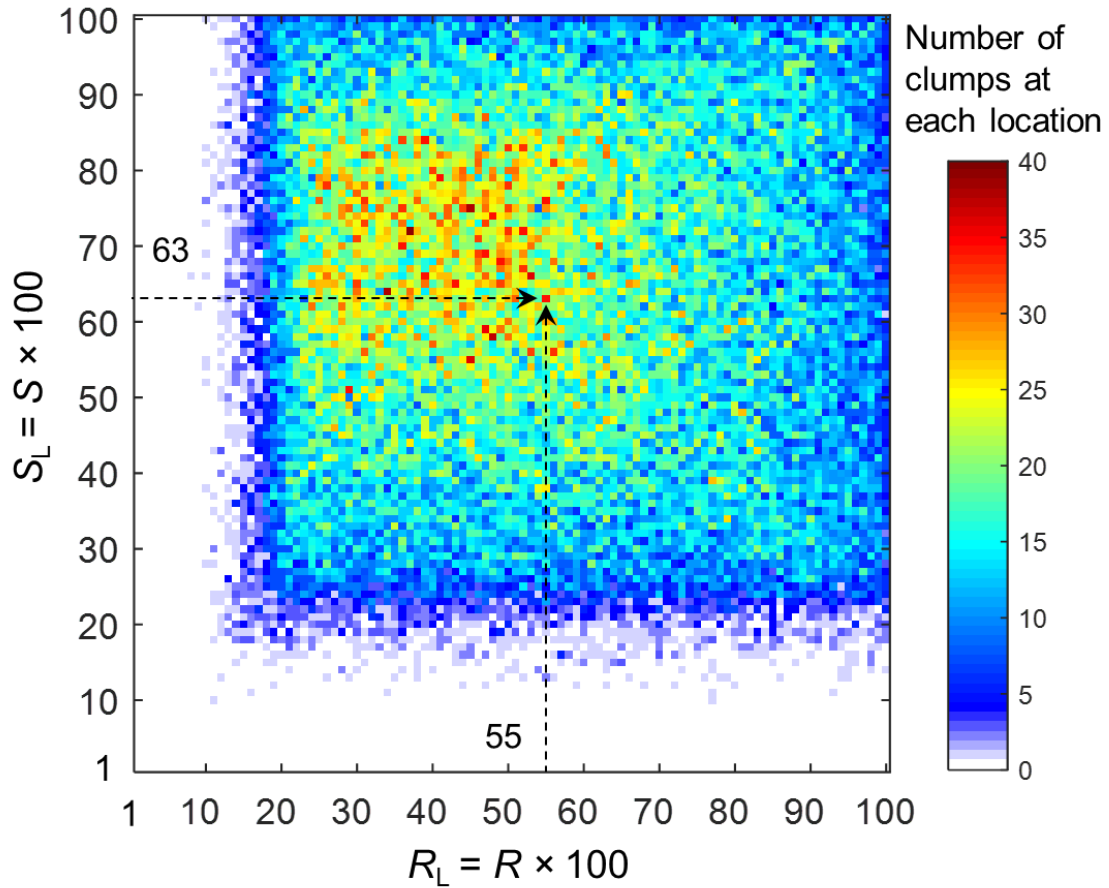
Figure 7.2 Map of the clump library.

In Figure 7.2, the library has 100×100 locations but not all locations contain clumps. Locations at $S_L < 20$ and $R_L < 15$ barely have any occupants. This is somewhat expected. Extremely elongated and angular particles are rare in nature since such particles are vulnerable to breakage (Hryciw et al., 2016). Histograms of the clumps for R_L and S_L are shown in Figure 7.3(a) and 7.3(b) respectively. Angular particles have more complex outlines than rounded particles and the variability of particle shapes increases with increasing angularity (decreasing roundness). Therefore, more angular particles in the range $20 < R_L < 50$ were deliberately collected for the library as shown in Figure 7.3(a). The S_L histogram in Figure 7.3(b) reflects the prevalence of shapes in the range $60 < S_L < 80$ found in nature.
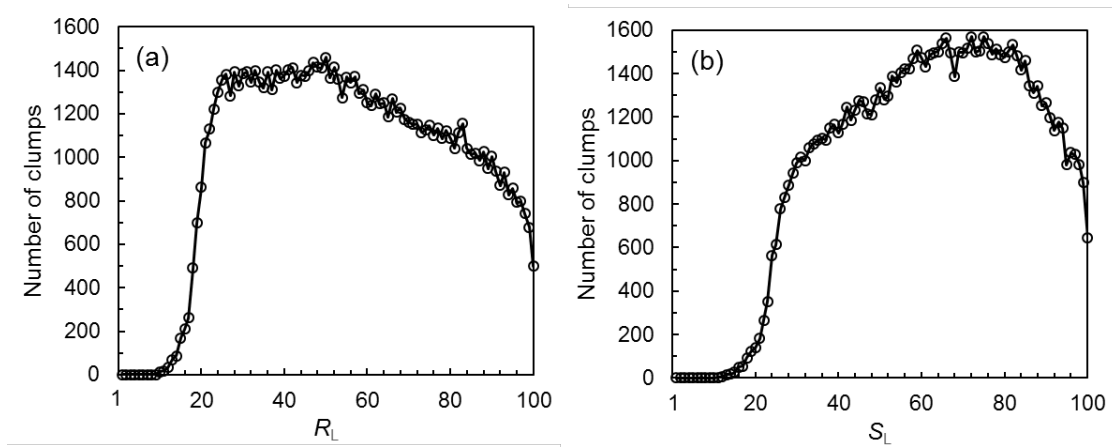
Figure 7.3 The number of clumps in the library versus R_L and S_L.

7.3 Steps in virtual soil specimen creation

The DEM virtual soil specimen creation process includes four steps as shown in Figure 7.4.
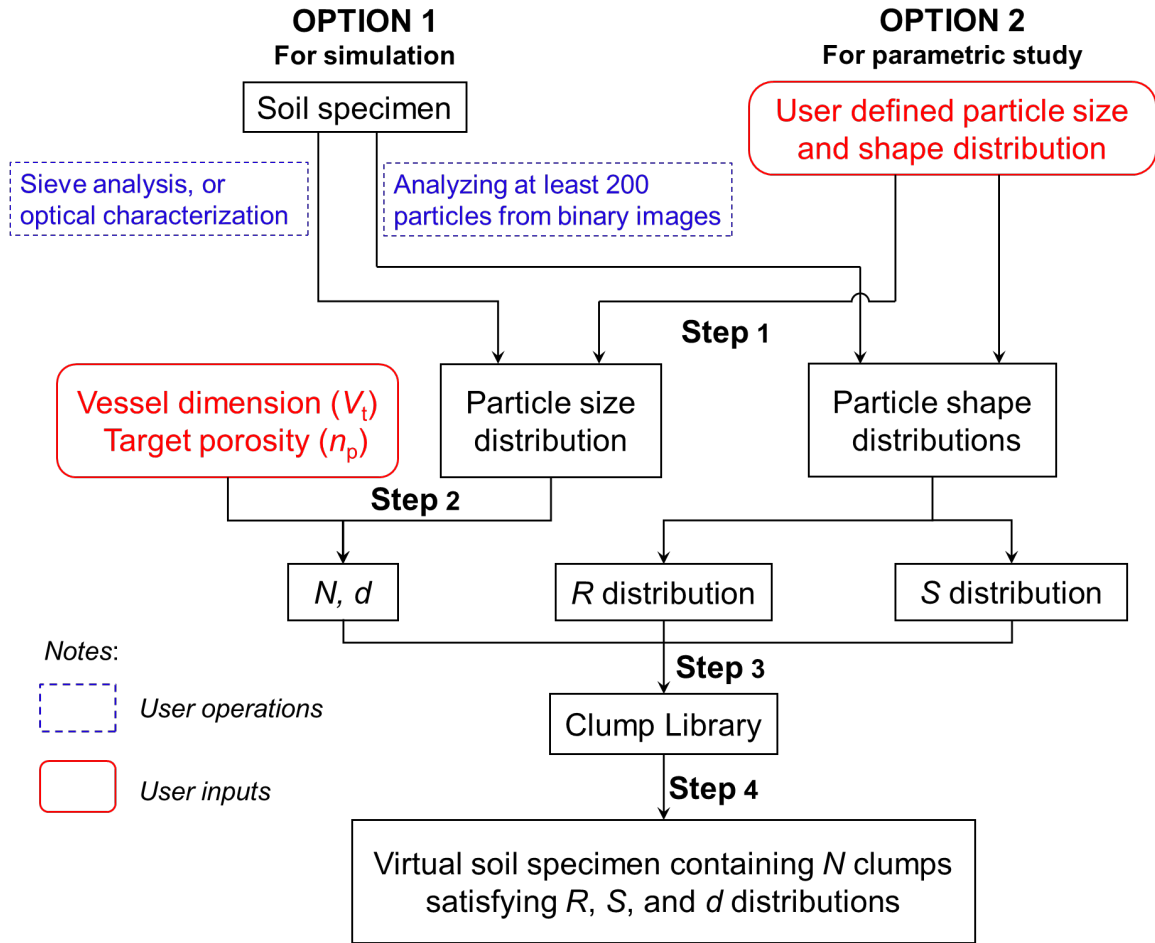
Figure 7.4 Overview of the virtual specimen preparation technique.

Step 1: Given a specific soil, users must characterize it to obtain particle d, S, and R distributions. The d can be determined by traditional sieve analysis or by optical techniques. The particle shape distributions including R and S distributions can be computed using computational geometry methods from either two-dimensional binary projections or from images of three-dimensional particle assemblies using computational geometry techniques in chapter 3. This study found that 200 particles were sufficient to provide satisfactory characterization of a real soil. However, users can create their own particle size and shape distributions to construct a customized virtual soil specimen.

Step 2: Users must input the testing vessel dimensions, a traditional weight-based particle size distribution (real or assumed) and a target packing porosity n_p. For normal (not gap-

graded) soils, weight (or volume) based particle size distributions may be fitted with the Rosin-Rammler function (1933):

$$V(d) = 1 - \exp\left[-\left(\frac{d}{D}\right)^{\lambda}\right]$$

Equation 7.1

in which D and λ are the fitting parameters related to the 50% particle size by weight, D_{50} and the coefficient of uniformity, C_u respectively. The total number of particles (N) required to fill the virtual testing vessel at porosity n_p and their distribution by size (d) are then computed.

Step 3: The distributions of R and S are unwieldy in discrete form. As such, they may be modeled by a two-dimensional Gaussian probability density functions (PDF):

$$f(x \mid \mu, \Sigma) = \frac{1}{2\pi} \frac{1}{|\Sigma|^{1/2}} \exp\left\{-\frac{1}{2}(x - \eta)' \Sigma^{-1}(x - \eta)\right\}$$

Equation 7.2

where x is a matrix of R and S values of k evaluated particles:

$$x = \begin{bmatrix} R_1, R_2, R_3, \ldots, R_k \\ S_1, S_2, S_3, \ldots, S_k \end{bmatrix};$$

η is the mean vector of R and S values:

$$\eta = \begin{bmatrix} \eta_R \\ \eta_S \end{bmatrix},$$

and Σ is the covariance matrix: $\Sigma = \begin{bmatrix} \Sigma_{RR} & \Sigma_{RS} \\ \Sigma_{SR} & \Sigma_{SS} \end{bmatrix}$.

The program retrieves the N clumps from the library based on a soil specimen's R & S PDF.

Step 4: The N clumps are input to the DEM code to assemble the virtual soil specimen. Several DEM codes are compatible with clump simulation including the commercial code Particle Flow Code (PFC) by Itasca (2015) and open source codes including the Large-

scale Atomic/Molecular Massively Parallel Simulator (LAMMPS) by Plimpton (1995) and its improved version General Granular and Granular Heat Transfer Simulations (LIGGGHTS) by Kloss et al. (2012). The PFC by Itasca was used in this study.

7.4   Example of virtual soil specimen creation

The process used to prepare virtual specimens for DEM simulation of direct shear testing is demonstrated using an Indiana Beach sand at dense and loose conditions.

In Step 1 traditional sieve analysis was used to determine the particle size distribution of an Indiana Beach sand. The result is shown in Figure 7.5(a) as a traditional weight-based cumulative distribution. A total of 200 particles were then randomly selected from the physical specimen. The particles were spread on a flat surface and binary images were captured. The computational geometry method was used to compute R and S values for every particle. The cumulative distributions of R and S values by number of particles are shown in Figures 7.5(b) and 7.5(c).
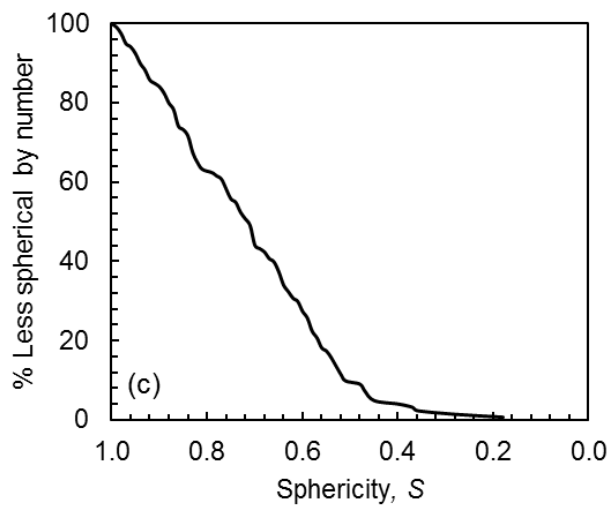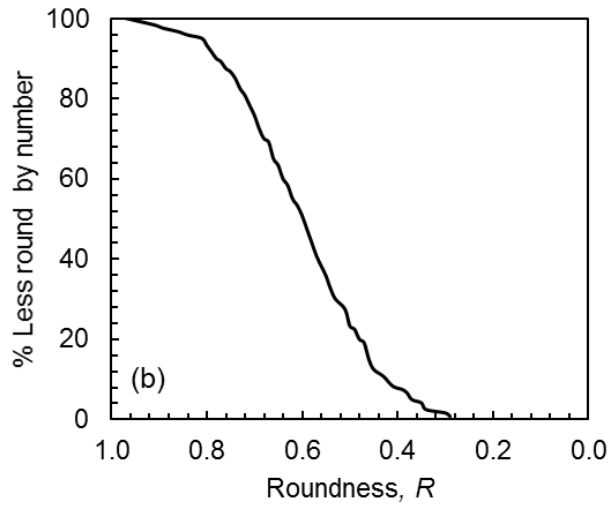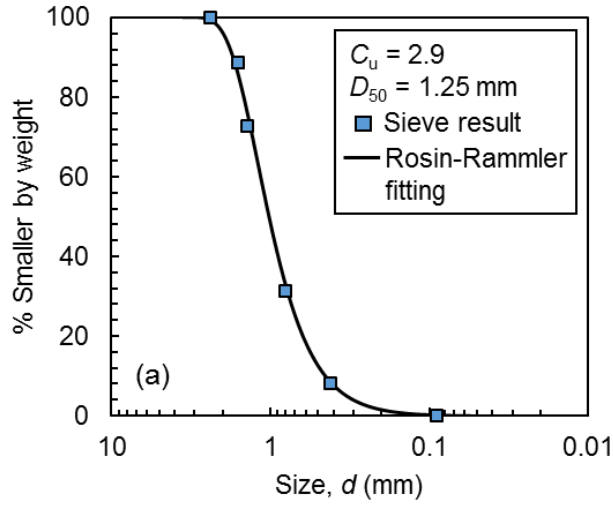
Figure 7.5 Characterization of Indiana Beach sand.

In Step 2, the particle size distribution shown in Figure 7.5(a) is fitted using Equation 7.1. The values $D = 1.2$ and $\lambda = 2.3$ were found to match the Indiana Beach Sand sieving results very well. The curve is discretized into 200 equal fractions as shown in Figure 7.6. Each fraction represents a volume increment of $\Delta V = 0.5\%$. The particle size d_i representing the i-th volume fraction can be back-calculated based on Equation 7.1. Knowing d_i, the volume v_i of each particle in the i-th volume fraction can be computed as shown in Figure 7.6.
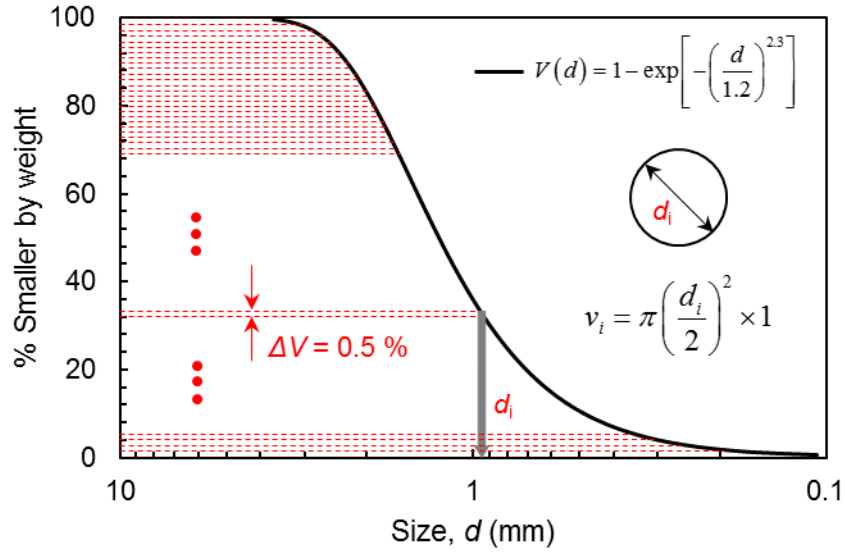
Figure 7.6 Discretization of particle size distribution curve.

To determine the number of particles in the i-th fraction, the volume of solids in this fraction must be computed as $V_t(1-n_p)\Delta V$ where V_t is the testing vessel volume and n_p is the porosity, both specified by the user. Finally, the number of particles required for the i-th volume fraction can be expressed as:

$$num_i = \frac{V_t \times \left(1 - n_p\right) \times \Delta V}{v_i} \qquad \text{Equation 7.3}$$

For example, the volume of a 2D shear box V_t used in this study was $100 \times 48 \times 1 = 4800$ mm^3 and the target porosity n_p was set to 0.2. The particle size of i-th volume fraction was

0.94 mm. Based on Equation 7.3, $num_i = 27$ particles were required to model this fraction. This computation is repeated for each volume fraction. The total number of required particles N to fill the direct shear box will be the sum of num_i. In this case, N was 12,518.

In Step 3, N clumps are retrieved from the library according to their R and S distributions as follows. The R and S distributions in Figures 7.5 (b) and (c) are fitted to the two-dimensional Gaussian probability density function, Equation 7.2. In this example, η and Σ were computed as:

$$\eta = \begin{bmatrix} 0.61 \\ 0.72 \end{bmatrix} \quad \text{and} \quad \Sigma = \begin{bmatrix} 0.0193 & -0.0019 \\ -0.0019 & 0.0293 \end{bmatrix}.$$

These were inserted into, Eqution 7.2 to determine the probability density function f which is plotted in Figure 7.7. This $f(R, S)$ map in Figure 7.7 dictates the sampling probability for each location in the clump library shown in Figure 7.2. The program will sample the library N times as was determined in Step 2. It should be noted that one location can be sampled multiple times. The number of stored clumps at each location in Figure 7.2 will generally not be the same as the needed number from that location. Statistically speaking, if the total number of particles needed from a single location in the library is m and the number of clumps at that location is k, then each clump from that library location will be used, on average, m/k times.
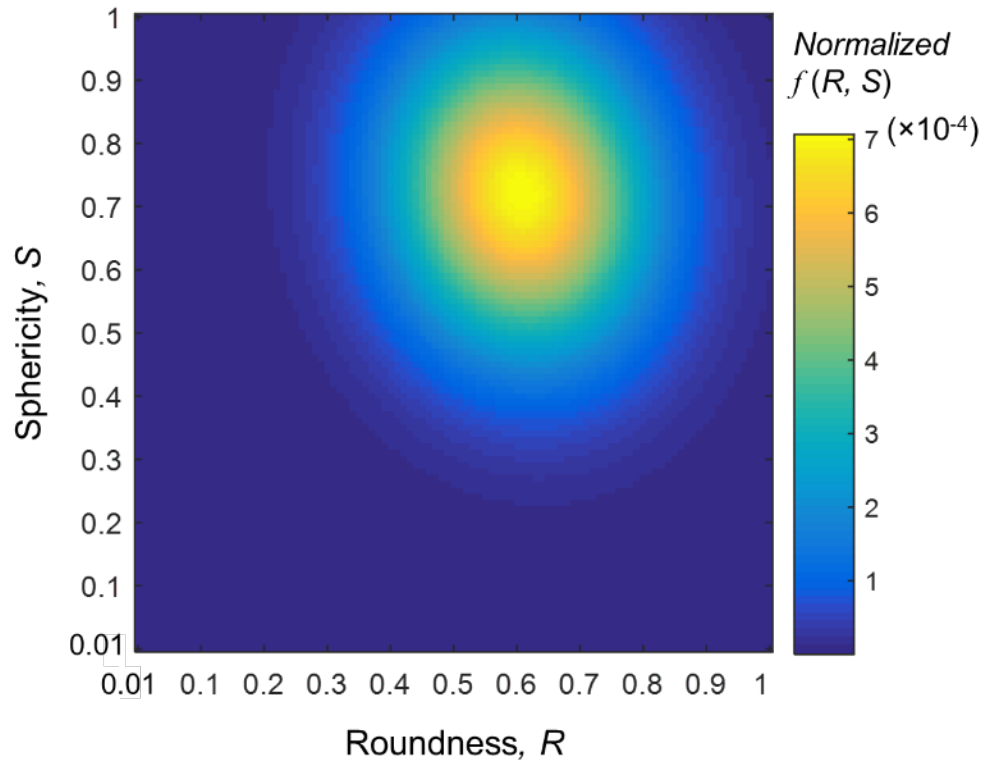
Figure 7.7 The normalized probability density map

Using the above procedure, $N = 12{,}518$ clumps were retrieved from the library for the Indiana Beach sand. Figure 7.8 shows the number of clumps sampled from each location in the library.
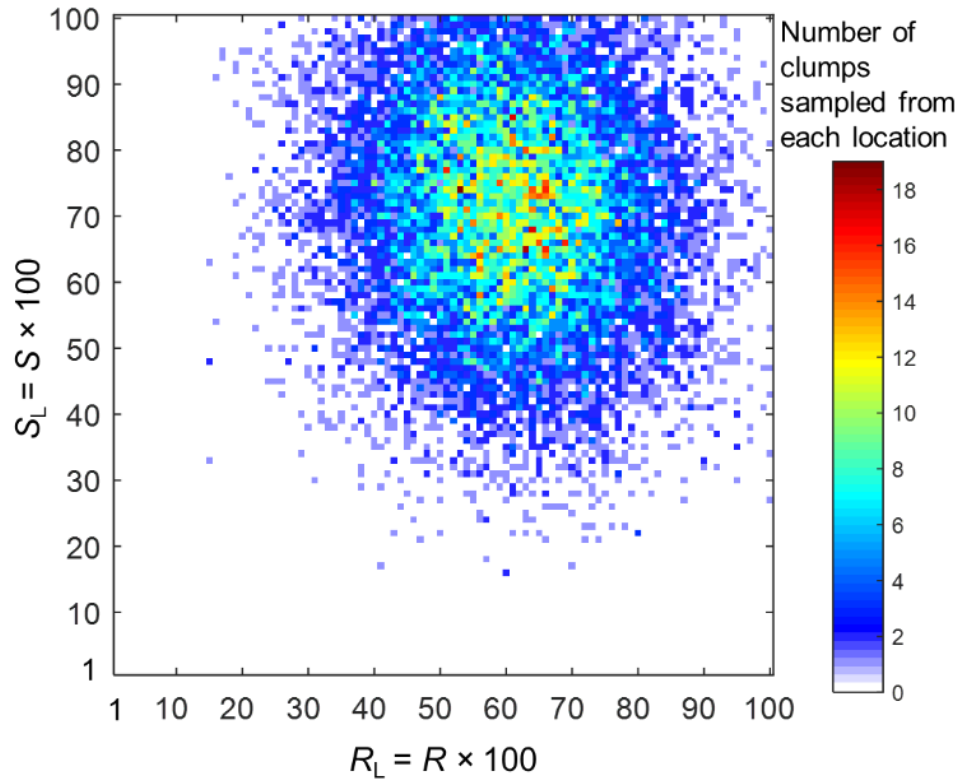
Figure 7.8 Number of clumps retrieved from each location in the library for the example.

The d values obtained in Step 1 and 2 are now randomly assigned to the N generated clumps. This is done by enlarging or reducing each clump to meet its assigned d value. The d, R and S distributions of clumps in the DEM model are compared to the distributions of the original soil in Figure 7.9. The DEM model successfully reproduced the target distributions of the original soil.
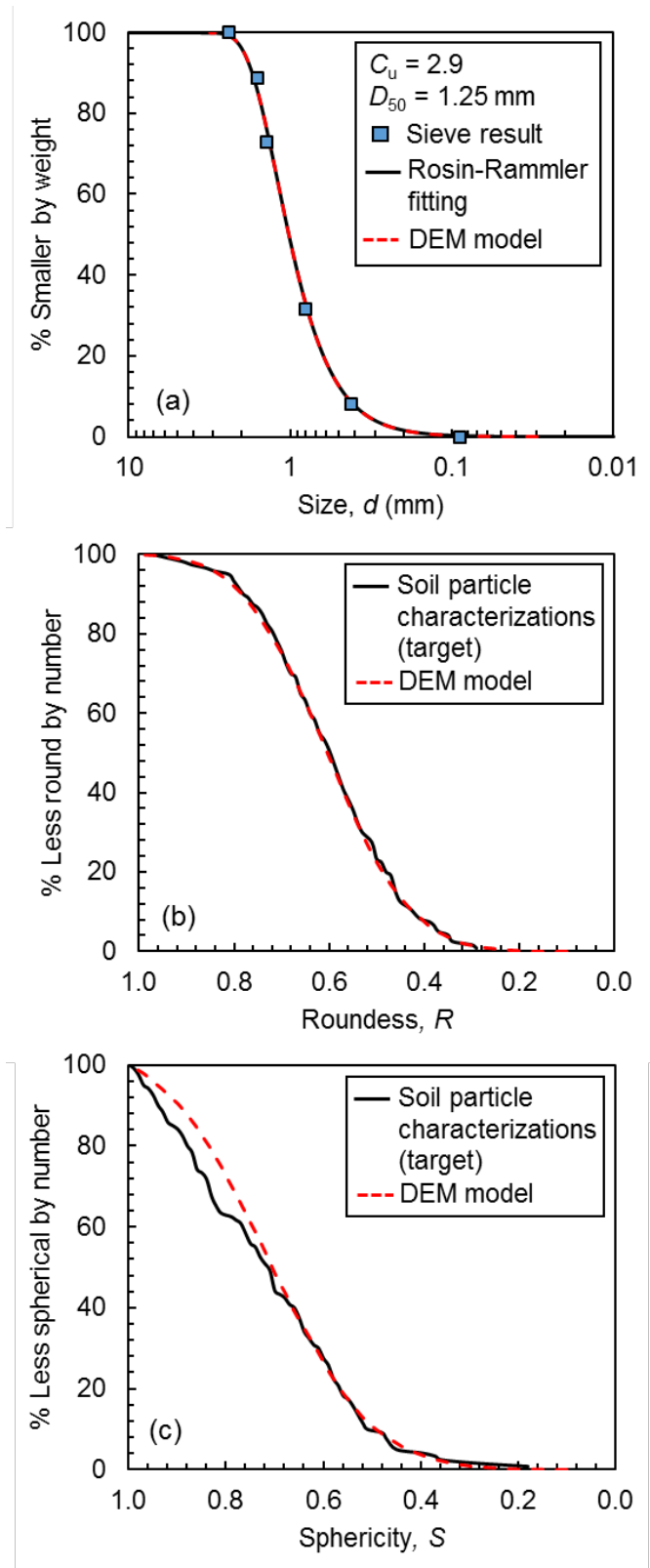
Figure 7.9 Sand size and shape distributions generated from the clump library compared to their target distributions.

In Step 4, the N generated clumps were input into PFC and rained into a direct shear box to simulate soil specimen preparation process. In this case, the fabric direction is horizontal. In PFC, users can change fabric direction by setting the particle orientations. The top cap was added and the specimen was consolidated under a normal stress of 100 kPa. A linear contact model was used in this simulation. The model parameters were set as follows: the clump density ρ was 2,650 kg/m^3; the effective modulus of the clumps E_c^* was 5×10^8 N/m^2; the effective modulus of the wall E_w^* was 5×10^9 N/m^2; the normal-to-shear stiffness ratio κ^* was 1.5; both normal and shear critical damping ratio (β_n and β_s) of the clumps were 0.5. To achieve a dense packing state, the friction coefficients for both the clump - clump and clump – wall interfaces were set to zero. The specimen is shown after consolidation in Figure 7.10(a). Two small square areas are enlarged and shown in Figures 7.10(b) and 7.10(c). As observed, each clump possesses a unique size and shape.
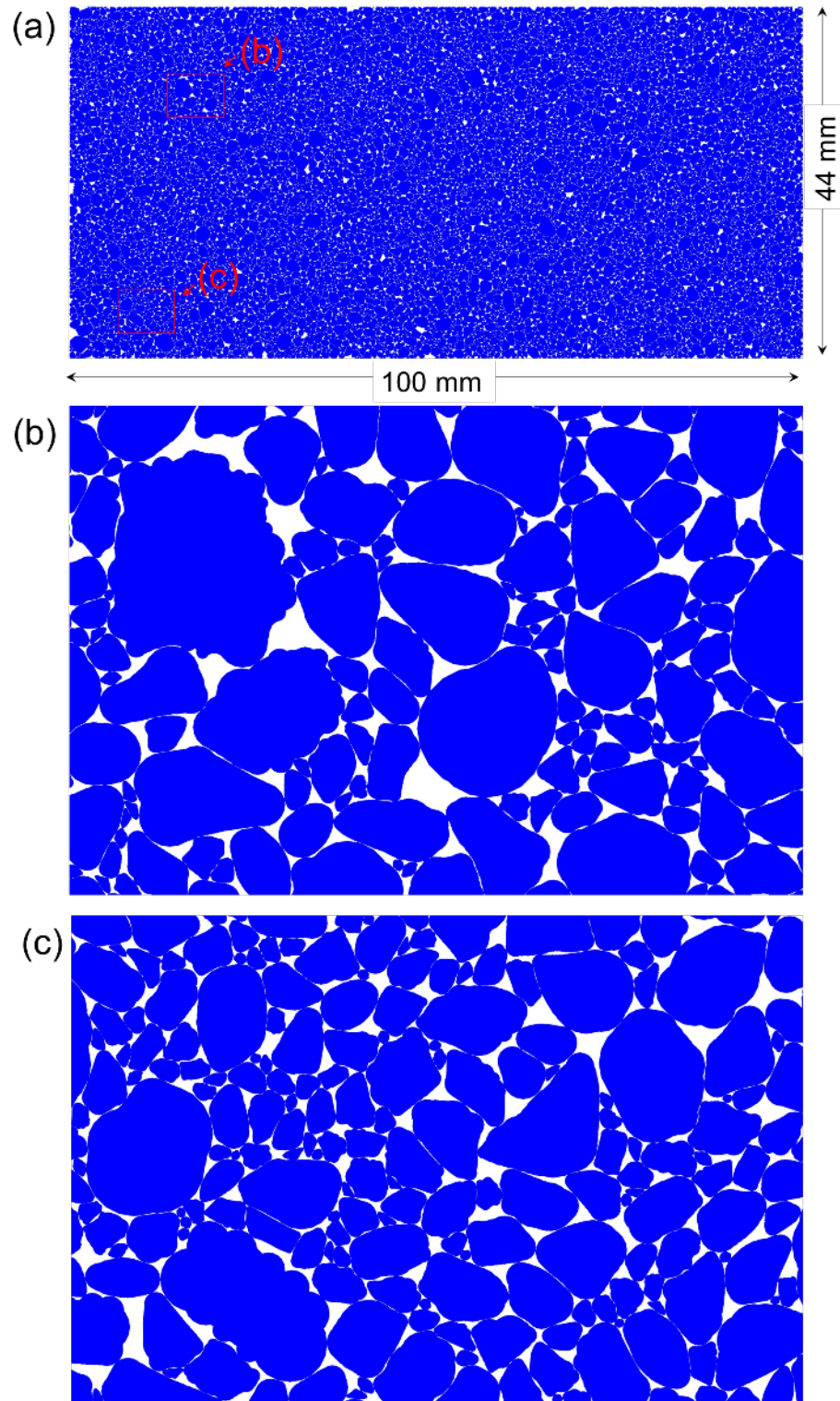
Figure 7.10 The generated DEM model at a dense condition.

After consolidation, the final porosity n was 0.13. It should be noted that the n value after consolidation is not necessarily equal to the initially specified n_p. The n_p is a presumed value for initially computing the number of clumps required to be retrieved from the library. The n after consolidation may be different than n_p. Correspondingly, the final vessel height may also be different from the previously specified value to accommodate the change in porosity due to consolidation. In this example, the height of the specimen was 44 mm after consolidation instead of previously specified 48 mm dimension. It was found in this study that such small changes in shear box height did not affect the final simulation results. Naturally, the n_p should be as close to n as possible. Therefore, steps 1-4 could be repeated using the resulting n value as the new n_p. Readers are encouraged to do so if they feel it is necessary. However, in this study, n_p was fixed at 0.2 and was not adjusted.

To achieve a loose packing condition, the friction coefficient for both the clump - clump and clump – wall interfaces were set to 0.3 for the consolidation stage. The final porosity n was 0.2 which is the same as the presumed value n_p. All other steps in setting up the loose condition were the same as for the dense state.

7.5   DEM simulation of direct shear tests

The normal stress was kept as 100 kPa during specimen shearing. The clump - clump and clump – wall contact friction coefficients were set to 0.50 and 0.95 respectively. The upper half of the box was fixed and the lower half was displaced at a constant velocity of 0.004 mm/s. The top wall was continuously adjusted via a serve-control mechanism (Itasca, 2015) to maintain the constant vertical normal stress during shearing. The horizontal displacement, vertical displacement, and shear force results are shown in Figure 7.11.
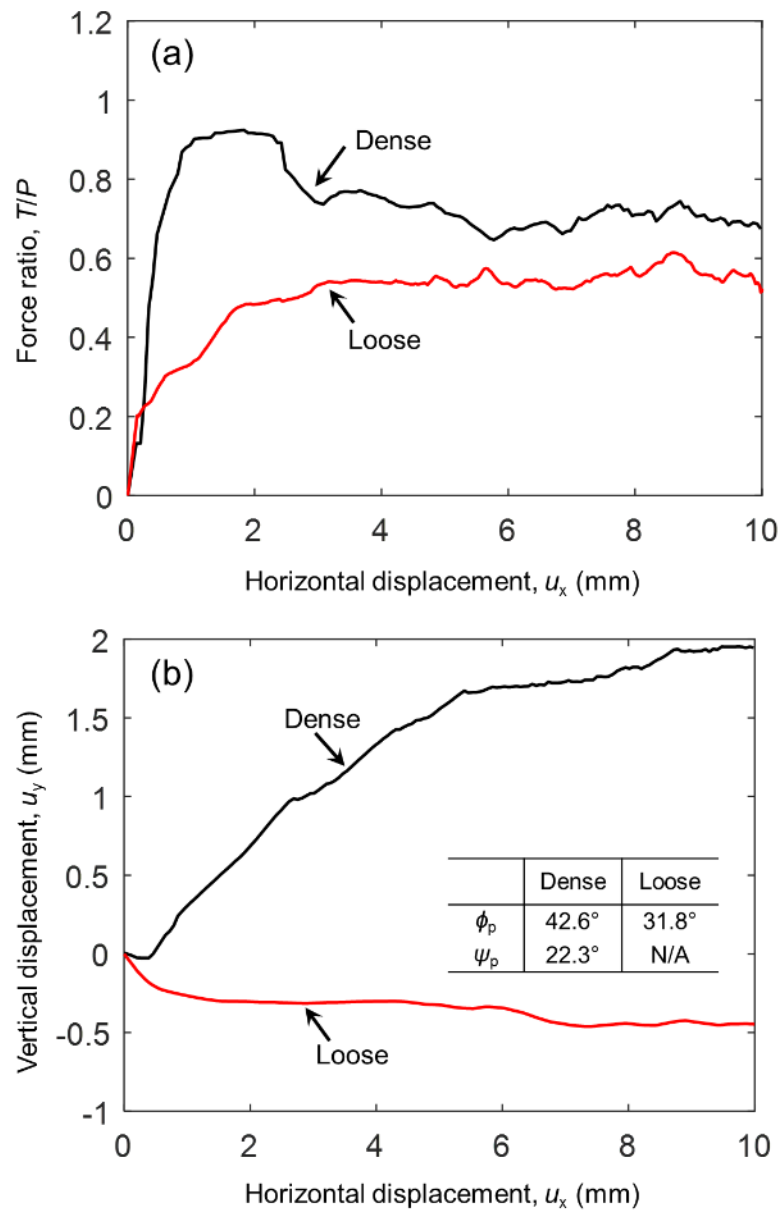
Figure 7.11 DEM simulations of Indiana Beach sand at dense and loose conditions.

The peak friction angle and dilation angle can be computed from the test curves as

$$\phi_p = \text{a} \tan\left(\frac{T_p}{P}\right)$$

Equation 7.4

$$\psi_p = a \tan\left(\frac{\Delta u_y}{\Delta u_x}\right)$$

Equation 7.5

Where P is the normal force and T_p is the shear force at the peak; Δu_x and Δu_y are the horizontal and vertical displacement rates at the peak strength state. The resulting ϕ_p and ψ_p are listed in Figure 7.11(b).

7.6   Clump library usage in parametric studies

Direct shear tests on five additional 2D versions of soils including 30A, Crushed Gabbro (CG), Leighton Buzzard (LB), Class IIA (IIA), and Glass Beads (GB) were also simulated to demonstrate the versatility of the clump library. The 30A and Crushed Gabbro are very angular and crushed angular soils respectively. The Leighton Buzzard is a subangular soil frequently used in research as reported by Lings and Dietz (2004) and Jewell (1989). The Class IIA and Glass Beads are subrounded and rounded materials respectively. The particle size distribution of Leighton Buzzard (LB) shown in Figure 7.12(b) was extracted from Lings and Dietz (2004). The particle size distributions of the remaining four sands shown in Figures 7.12(a) and (b) were determined through sieving analysis. The dashed lines are the Rosin – Rammler curves fitted to the sieving data. The fitting parameters D and λ are summarized in Table 7.1. The volume of the shear box V_t was set to $100 \times 48 \times 1 = 4800$ mm^3 and the target porosity n_p was set to 0.2 for all of the test simulations. The resulting numbers of particles (N) required to fill the direct shear box for the five soils are reported in Table 1.
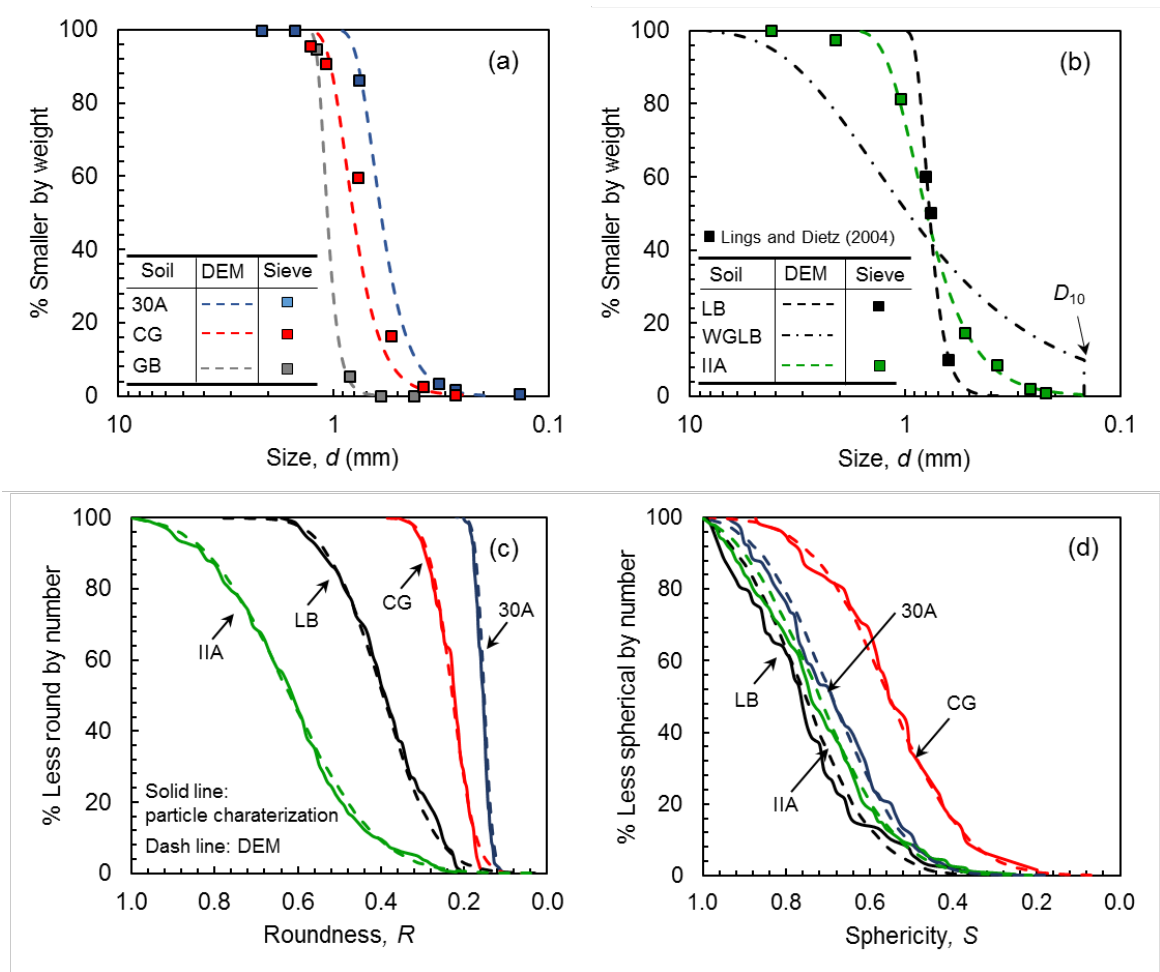
Figure 7.12 Intrinsic property distributions of the simulated soils.

For each soil except the Glass Beads, 200 particles were characterized to determine their R and S distributions. The results are shown as solid lines in Figures 7.12(c) and (d). The mean R and S values (R_m and S_m) are listed in Table 7.1. These solid lines were used to fit two – dimensional Gaussian distributions of R and S using Equation 7.2 for retrieval of clumps from the library. The resulting R and S distributions of the picked clumps are plotted as dashed lines in Figures 7.12(c) and (d). They agree well with the target distributions. For the Glass Beads, both R and S are equal to 1.0 therefore perfect disks were used in the simulation. The model parameters including ρ, E_c^*, E_w^*, κ^*, β_n, and β_s were the same as used in the earlier simulation of Indiana Beach sand. Only dense conditions were simulated. Therefore, the friction coefficient μ was set to zero for the consolidation stage and to 0.5

196

for the shearing stage. The normal stresses were set to 100 kPa. The porosities n of the five sands after consolidation are listed in Table 7.1.

Table 7.1 The parameters of virtual soils in DEM simulations

Soil	Gradation					Shape		DEM
	D_{50} (mm)	C_u	D	λ	N	R_m	S_m	n
30A	0.58	1.5	0.67	5	15681	0.15	0.69	0.21
CG	0.80	1.5	0.87	5	9196	0.23	0.56	0.19
LB	0.78	1.3	0.80	9	8802	0.41	0.76	0.15
IIA	0.80	1.9	0.90	3	13549	0.62	0.72	0.13
GB	1.00	1.1	1.10	10	4570	1.00	1.00	0.14
IIA_0.52[†]	0.80	1.9	0.90	3	13549	0.62	0.52	0.15
IIA_0.32[†]	0.80	1.9	0.90	3	13549	0.62	0.32	0.19
WGLB[†]	0.97	8.7	1.40	1	38696	0.41	0.76	0.11

Note: D_{50} is the 50% size by weight; σ_n is normal stress; μ is clump – clump friction coefficient during the shearing stage; n is porosity after consolidation, N is number of generated clumps; R_m and S_m are the mean values; superscript † means those virtual soils are created by author – defined intrinsic properties.

The simulation results are shown in Figure 7.13 while the ϕ_p and ψ_p values are plotted in Figure 7.14. As shown both ϕ_p and ψ_p increase with decreasing R (increasing angularity) which agrees with the experimental observations of Santamarina and Cho (2004), Cho et al. (2006), Bareither et al. (2008) and countless others.
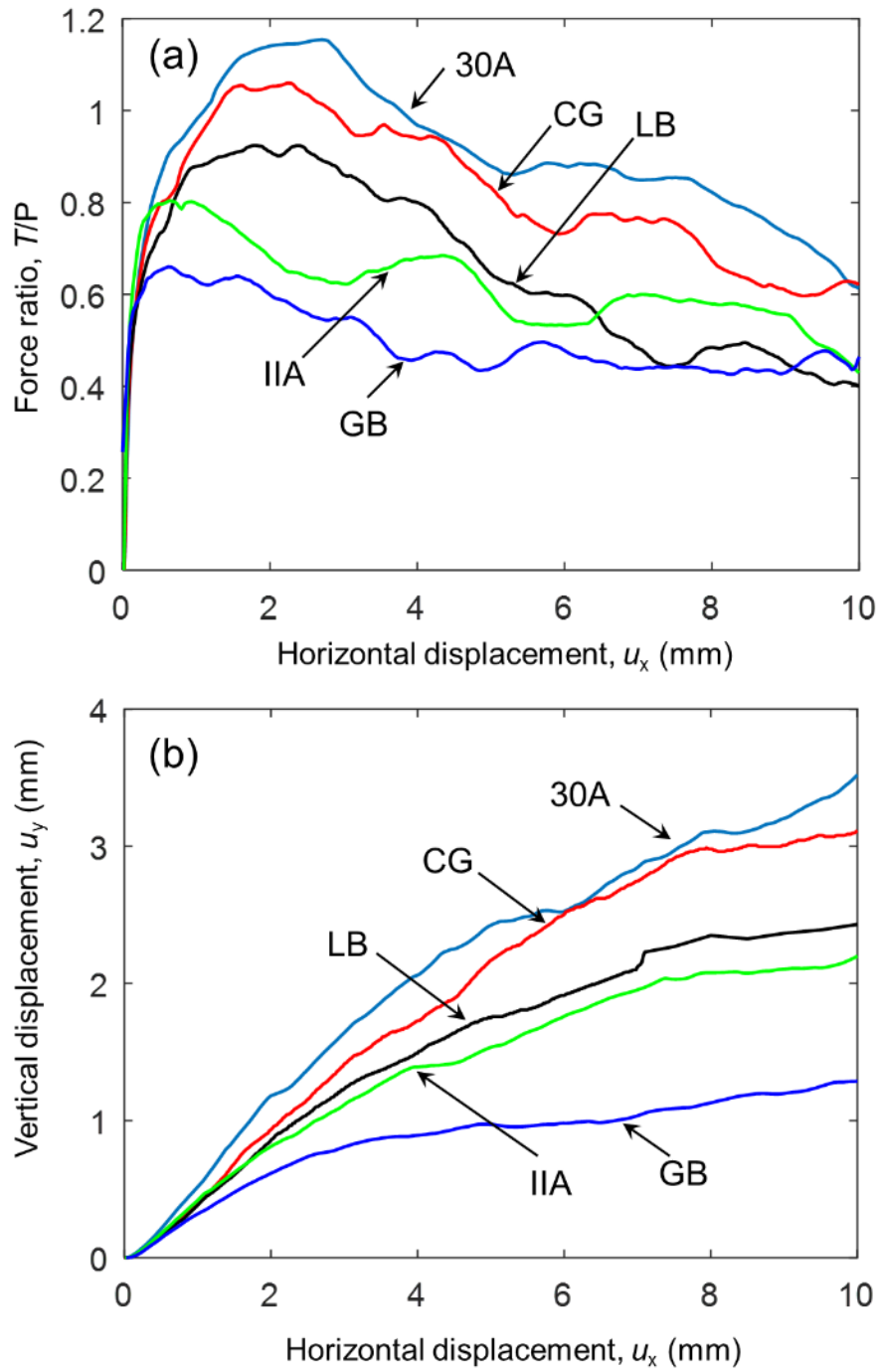
Figure 7.13 DEM simulations of five sands with different roundnesses.
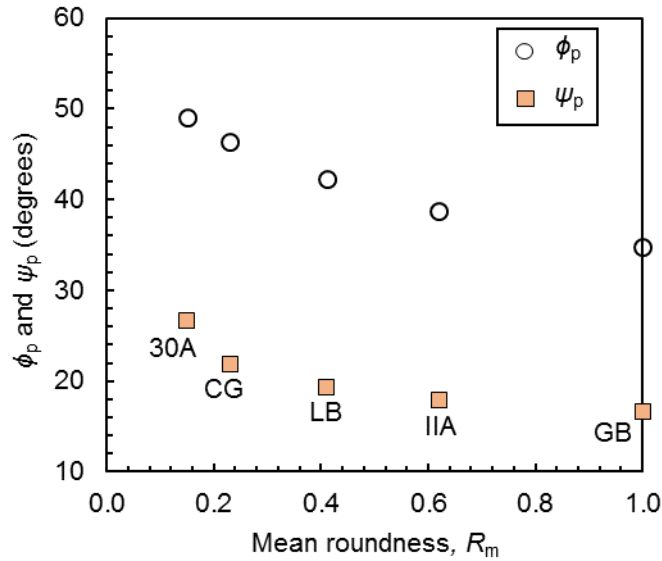
Figure 7.14 The effects of roundness by DEM simulations.

Although average S values of natural soils fall in a narrow range of 0.6 to 0.8 (Hryciw et al. 2016), it would be interesting to observe the behavior of soils having low S. This is easily facilitated using the clump library. Two virtual soils were created using the Class IIA soil but defining two additional new S distributions as shown in Figure 7.15: $S_m = 0.52$ and $S_m = 0.32$. The size and R distributions as well as other parameters were maintained the same as in the original Class IIA. After consolidation, the porosity values were expectedly different: the elongated soils had larger n. The simulation results from these newly created virtual soils are shown in Figure 7.16. The computed ϕ_p and ψ_p for each test are shown in Figure 7.17. Both ϕ_p and ψ_p increase as S decreases suggesting elongated particles increase strength and dilation. The same laboratory observation was also made by Santamarina and Cho (2004) and Cho et al. (2006).
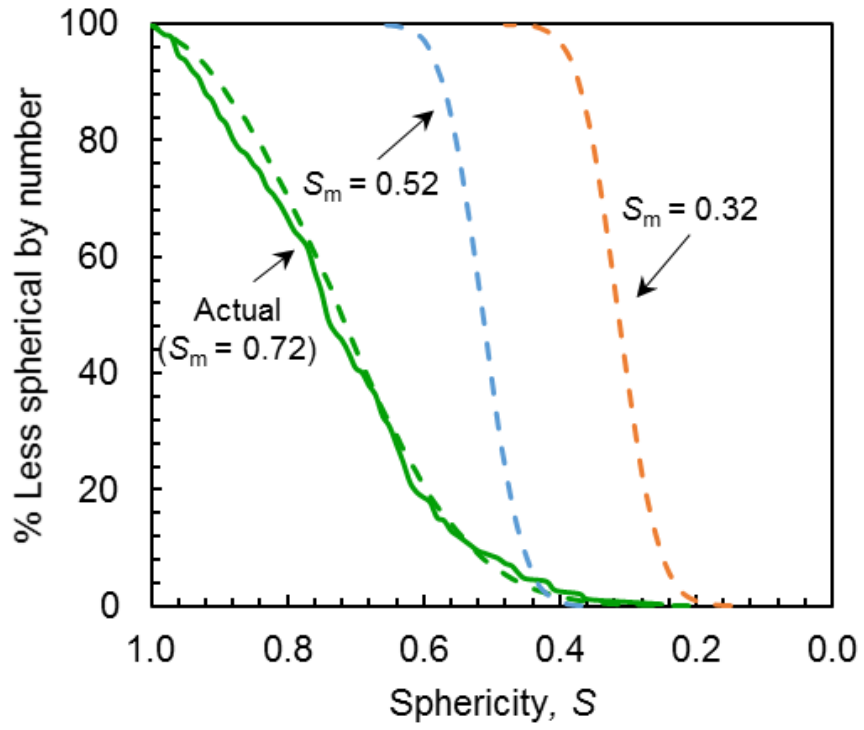
Figure 7.15 Sphericity distributions of actual and three virtual Class IIA specimens.
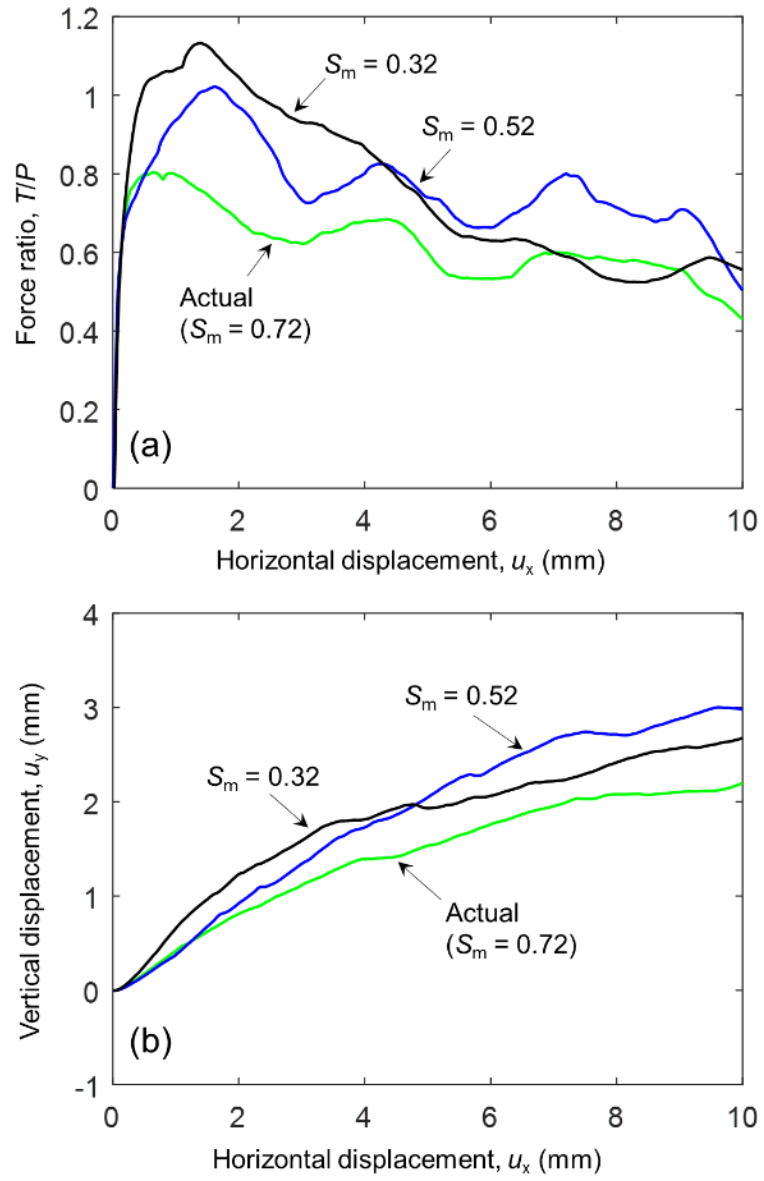
Figure 7.16 Simulations of Class IIA at three sphericities
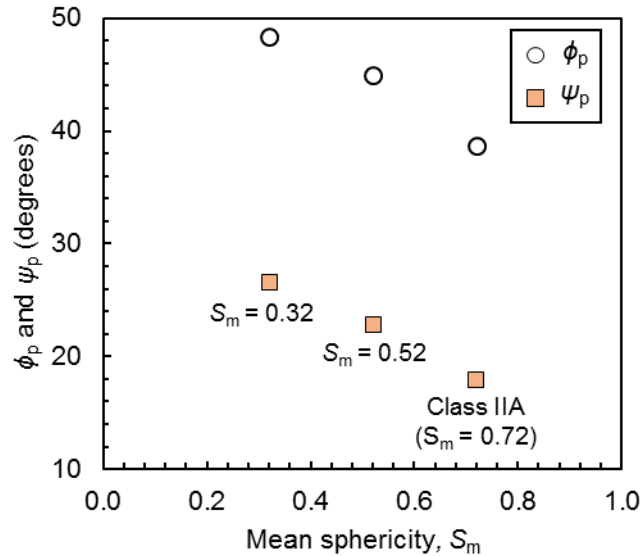
Figure 7.17 The effects of sphericity by DEM simulations.

To investigate the importance of particle gradation, the parameters D and λ for the Leighton Buzzard sand were changed to create a virtual Well-Graded Leighton Buzzard sand (WGLB) having a C_u of 8.7. The particle size distribution curve for WGLB was added to Figure 7.12(b). The fine portion smaller than D_{10} (0.15 mm) was ignored because it would dramatically increase the total number of clumps, thereby exceeding current computational ability. The R and S distributions and the remaining parameters were maintained the same as they were for the original Leighton Buzzard sand as listed in Table 1.

The DEM simulation results show that strength was enhanced slightly by increasing C_u from 1.3 (LB) to 8.7 (WGLB) as shown in Figure 7.18. Kokusho et al. (2004) performed a series of laboratory tests on sands with different C_u values and found that shear strength could either increase or decrease with increasing C_u depending on particle crushability. If particles are not crushable, the shear strength will increase with increasing C_u while the opposite trend was observed for crushable particles. The crushing of particle will suppress the relative movement and overriding of particles resulting in smaller strength and dilatancy. In this study, both ϕ_p and ψ_p increase with C_u because the clumps were not allowed to crush. This agrees with Kokusho et al.'s (2004) observation.

202
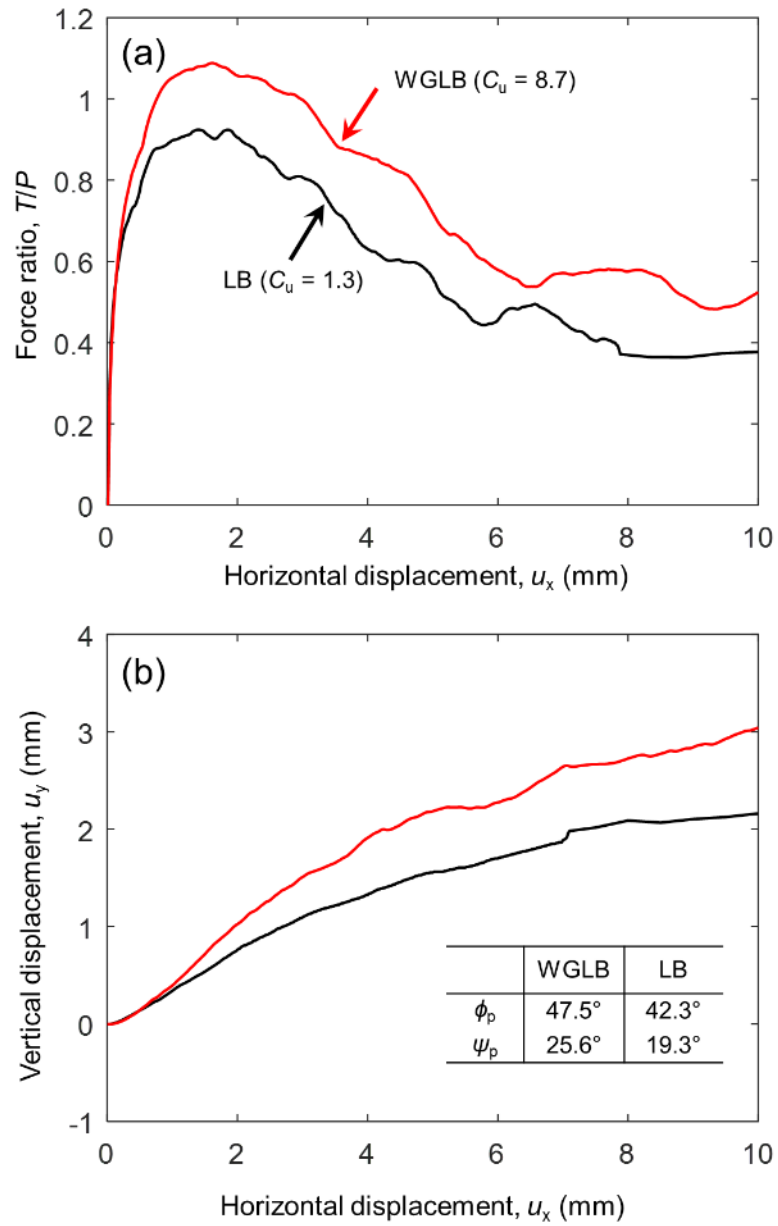
Figure 7.18 The effects of gradation in DEM simulations.

7.7   Discussion

1) The current 2D clump library consists of 98,489 geometries. In the real world, every particle, particularly if it is angular, has a unique geometry. Furthermore, even for the same particle, different scanning direction will yield different projected 2D geometries. Therefore, the 2D library obviously cannot include all possible particle geometries. However, as discussed earlier, many studies have shown that different soils with similar intrinsic properties will exhibit similar macro – mechanical behavior under the same state conditions. The 2D library does not aim to exhaustively contain all possible particle geometries encountered in nature. Rather, it contains sufficient geometries for reproducing all possible intrinsic parameter distributions.

2) To simplify image acquisition, the clumps in the library were generated from images of particles spread out on a flat surface. As such, the particles are more likely to have been displaying their maximum area projections. While it would appear that such images are most reflective of particles lying in a depositional plane, the library does not ascribe any specific orientation to the clumps. As such, the clumps in the library may be used for simulating other orientations having appropriate user-specified R and S distributions.

3) The shortcomings of two-dimensional DEMs are well known: 2D particles have only three degrees for freedom compared to six in real soils. A repercussion of these shortcomings was evidenced, for example, by the high dilation angles observed earlier in the chapter. Nevertheless, as discussed in the Introduction, 2D DEMs hold several attractive benefits including computational efficiency, simplicity of model preparation and easier visualization of particle motions. Furthermore, the direct linkage between Wadell's classic 2D definition of particle roundness, through the corner-preserving algorithm, preserves the exact shape of particles and facilitates more efficient clump generation. In the future, Wadell's definition of roundness could and should be extended to 3D thus providing a basis for 3D clump generation. Such clumps would require hundreds of spheres making them still computationally unrealistic at the present time. Nevertheless, even in 2D, the value of clump libraries towards parametric study of particle micromechanics is significant.

7.8 Conclusions

A library consisting of almost 100,000 two-dimensional clumps was developed for use with Discrete Element Methods. Each clump was created from a binary image of a sand particle. The particles in the clump library are indexed by their values of roundness (R) and sphericity (S). The R follows the classical definition of roundness developed by Wadell (1932) while S follows a simple definition proposed by Krumbein and Sloss (1951). A previously developed computational geometry technique fits circles to a particle's corners thereby facilitating the computation of R. A previously developed "corner-preserving" algorithm fits many additional interior circles to the particle perimeter. The particles in the clump library are based on sands taken from many sources and thus they possess a wide range of R and S values.

The clump library may be used to simulate an actual soil whose particle size distribution is determined by either sieving or by image analysis and whose distributions of R and S are determined by computational geometry on 200 randomly selected particles. The particle size distribution is fitted to the Rosin-Rammler function while the R and S distributions are smoothed by a two-dimensional Gaussian probability density function. The clump library may also be used in parametric studies in which the particle size, R and S distributions are designed by the user. In either case, the clumps are picked from the library to create a virtual soil specimen according to their Gaussian distributions of R and S. The clump sizes are then adjusted to match the desired particle size distribution. Example problems showed very good matches between the actual distributions of particle size, R and S and the distributions of these intrinsic properties in a virtual specimen composed of clumps from the library.

DEM simulations of direct shear tests on five vastly different sands were performed using the clump library. The simulation results qualitatively match well known trends documented in the literature. Both ϕ_p and ψ_p were observed to increase with decreasing R (increasing angularity), decreasing S, and increasing C_u (for non-crushable soils). Those simulations illustrate the usefulness and versatility of the clump library in creating virtual specimens possessing various shapes and particle gradations.

CHAPTER 8

SUMMARY AND FUTURE RECOMMENDATIONS

8.1   Summary

This research developed a computational geometry algorithm to automate the computation of particle shape descriptors including sphericity, roundness and surface roughness. The proposed computational geometry algorithm was validated by traditional sphericity and roundness charts (Krumbein, 1941; Krumbein and Sloss, 1951; and Powers, 1953). Results were in excellent agreement with values published in traditional charts thus confirming that the computational method can replace the much slower and less objective chart methods. The computational geometry algorithm can be directly incorporated into current soil characterization system capturing binary images. A semi-automated method was developed to incorporate the computational geometry algorithm to systems capturing images of three-dimensional particle assemblies.

Extensive laboratory tests were performed on various sands to develop statistical models between their intrinsic properties and macroscopic mechanical behavior including packing and compressibility. Those models show high accuracy because: (a) the computational geometry algorithm can accurately determine R and S values for a very large and statistically valid number of particles in a specimen; (b) a large database including many soils with different intrinsic properties were used to developed the models.

A Rotational Harr Wavelet Transform (RHWT) method that mimics human cognition was developed to automate soil fabric characterization. Based on images of eleven sands and three rice specimens at loose and dense conditions, strong functional relationships were observed between the degree of fabric anisotropy and particle sphericity under dense and loose conditions. Furthermore, a very simple and practical relationship was presented for

206

the degree of fabric anisotropy based only on relative density and the void ratio at 50% relative density.

A corner preserving algorithm was developed to generate realistic particle geometries. The algorithm required many fewer circles than existing methods, particularly for angular particles. The procedure is a logical extension of a computational method for determining the classic Wadell particle roundness in which circles are fitted to the corners of particles. Hence, the new method perfectly preserves the location, size and shape of particle corners and is appropriately termed as the corner preserving algorithm. The method can easily be incorporated in existing soil particle characterization systems in which binary images or even images of particle assemblies are produced.

To integrate gradation, shape and fabric in DEM modeling, a clump library was built by storing 100,000 clumps generated by the corner preserving algorithm. The clumps are based on 2D images of real soil particles and they are indexed in the library by their R and S values. A real soil can be simulated by choosing particles from the library to match the soil's actual distributions of R and S. The clumps are also enlarged or reduced to match a desired particle size distribution. The fabric of soils can be simulated by specifying clump long axis directions. The utility of the clump library in parametric studies was demonstrated by direct shear tests on five very different virtual materials created from clumps.

8.2   Recommendations for Future Research

The particle shape definitions were proposed in the period of 1920 to 1950. At that time, there were no techniques to obtain 3D particle surface models. Therefore, 3D particles had to be approximated by 2D projections for shape analysis. The 2D framework was used in this research to develop various algorithms. Admittedly, although the 2D shape descriptors can provide useful insight to 3D particle shapes, they are significantly affected by the projecting directions. For example, the 3D particle shown in Figure 8.1(a) can be viewed in three different orientations as shown in Figures 8.1 (b), (c) and (d). Those three projections result in very different R and S values. To minimize the variance in 2D shape

analysis, a very large and statistically valid number of particles should be analyzed to compute average R and S values. This approach was used in the current research.

(a)

(b)   (c)   (d)
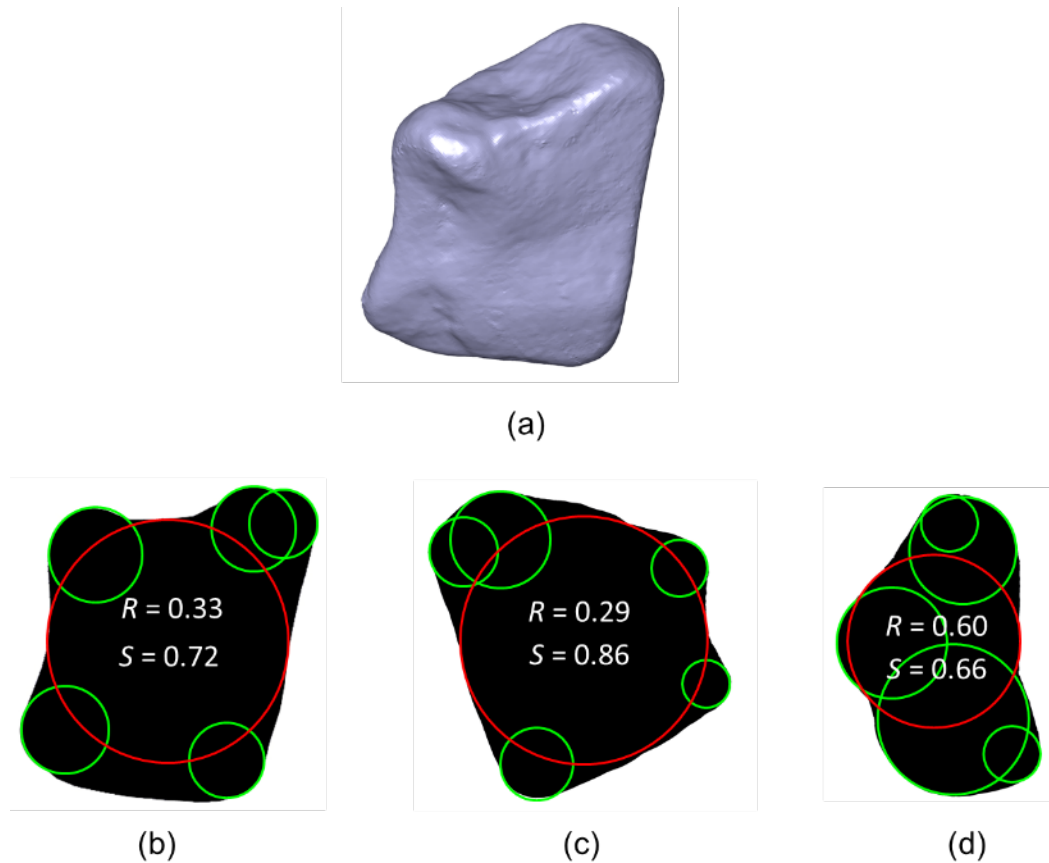
Figure 8.1 2D R and S values of three projecting directions of the same particle.

However, as 3D imaging matures, a variety of techniques will become available to easily acquire 3D models of particles such as by using stereophotography, photogrammetry, profilometry, X-ray tomography, neutron imaging, laser scanning, white light scanning, and interferometry. Therefore, direct quantification of particle shapes from 3D particles will become feasible. How to extend the current 2D particle shape characterization methods and 2D DEM clump library to 3D will be future research.

For sphericity, it is easy to extend 2D definition to 3D. In previous research, the particle length and width were measured to compute 2D sphericity. In the future, the particle length, width, and thickness can be computed from 3D particle models to define 3D sphericity.

For roundness, extension from 2D to 3D definitions will be challenging. As shown in Figure 8.2(a), the 2D surface structure includes concave, flat and corner parts. Corner parts are identified and approximated by corner circles to compute 2D roundness. However, the 3D particle in Figure 8.2(b) includes not only concave, flat, and corner parts but also a new feature: ridges. The corners and ridges create interparticle locking that controls the strength and deformation of granular soils. Therefore, the corners and ridges should be used to define 3D roundness. How to identify the corners and ridges on particle surfaces and how to fit appropriate spheres to them will be challenging. Additionally, the 3D surface contains many more points than a simple 2D perimeter. This will significantly increase the computational loads. Therefore, how to improve computationally efficiency is another challenge when developing 3D algorithm.
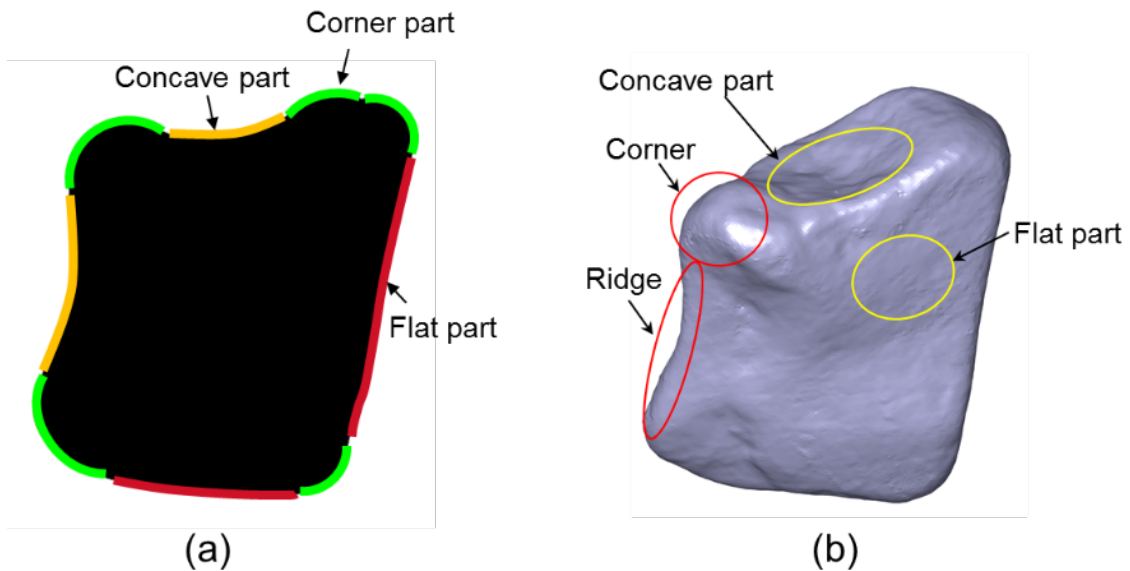
Figure 8.2 2D and 3D particle surface structures.

If the 3D roundness algorithm can be successfully developed, development of 3D corner preserving algorithms may become feasible. To compute 3D roundness, the corners and ridges have been represented by corresponding spheres. The 3D corner preserving algorithm can be developed by adding spheres to approximate the flat and concave parts on soil particle surfaces to generate 3D clumps. Based on a 3D corner preserving algorithm, a 3D clump library can be built to simulate a 3D soil specimen.

REFERENCES

Alshibli, K. A., and Alsaleh, M. I. (2004). "Characterizing Surface Roughness and Shape of Sands Using Digital Microscopy." *Journal of Computing in Civil Engineering*, 18(1), 36-45.

Altuhafi, F., O'Sullivan, C., and Cavarretta, I. (2013). "Analysis of an image-based method to quantify the size and shape of sand particles." *Journal of Geotechnical and Geoenvironmental Engineering*, 139(8), 1290-1307.

Altuhafi, F. N., and Coop, M. R. (2011). "Changes to particle characteristics associated with the compression of sands." *Géotechnique*, 61(6), 459-471.

Andrade, J. E., Lim, K.-W., Avila, C. F., and Vlahinic, I. (2012). "Granular element method for computational particle mechanics." *Computer Methods in Applied Mechanics and Engineering*, 214-244(2012), 262-274.

Arasan, S., Akbulut, S., and Hasiloglu, A. S. (2011). "The relationship between the fractal dimension and shape properties of particles." *KSCE Journal of Civil Engineering*, 15(7), 1219-1225.

Arthur, J. R. F., Chua, K. S., and Dunstan, T. (1977). "Induced anisotropy in a sand." *Géotechnique*, 27(1), 13-30.

ASTM (2009). "*Standard practice for description and identification of soils (visual-manual procedure)*." ASTM D 2488-09a, West Conshohocken, PA.

ASTM (2010). "*Standard test method for flat particles, elongated particles, or flat and elongated particles in coarse aggregate*." ASTM D 4791-10, West Conshohocken, PA.

ASTM (2011). "*Standard test methods for one-dimensional consolidation properties of soils using incremental loading*." D2435M-11 AD, West Conshohocken, PA.

ASTM. (2014a). "*Standard test methods for maximum index density and unit weight of soils using a vibratory table*." ASTM D4253-14, West Conshohocken, PA.

ASTM. (2014b). "*Standard test methods for minimum index density and unit weight of soils and calculation of relative density*." ASTM D4254-14, West Conshohocken, PA.

ASTM (2014c). "*Standard test method for sieve analysis of fine and coarse aggregates*.", C136M-14 AC, West Conshohocken, PA.

Azami, A., Pietruszczak, S., and Guo, P. (2009). "Bearing capacity of shallow foundations in transversely isotropic granular media." *International Journal for Numerical and Analytical Methods in Geomechanics*, 34(8), 771-793.

211

Azéma, E., and Radjaï, F. (2010). "Stress-strain behavior and geometrical properties of packings of elongated particles." *Physical Review E*, 81(5).

Azéma, E., Radjaï, F., Peyroux, R., and Saussine, G. (2007). "Force transmission in a packing of pentagonal particles." *Physical Review E*, 76(1).

Azéma, E., Radjai, F., and Saussine, G. (2009). "Quasistatic rheology, force transmission and fabric properties of a packing of irregular polyhedral particles." *Mechanics of Materials*, 41(6), 729-741.

Banta, L., Cheng, K., and Zaniewski, J. (2003). "Estimation of limestone particle mass from 2D images." *Powder Technology*, 132(2003), 184-189.

Barden, L., Tong, P., and Ismail, H. (1969). "Plane strain deformation of granular material at low and high pressures." *Géotechnique*, 19(4), 441-452.

Bareither, C. A., Edil, T. B., Benson, C. H., and Mickelson, D. M. (2008). "Geological and physical factors affecting the friction angle of compacted sands." *Journal of Geotechnical and Geoenvironmental Engineering*, 134(10), 1476-1489.

Barrett, P. J. (1980). "The shape of rock particles, a critical review." *Sedimentology*, 27(3), 291-303.

Baxter, C. D. P., and Mitchell, J. K. (2004). "Experimental study on the aging of sands." *journal of Geotechnical and Geoenvironmental Engineering*, 130(10), 1051-1062.

Bellotti, R., Jamiolkowski, M., Lo Presti, D. C., and O'Neill, D. A. (1996). "Anisotropy of small strain stiffness in Ticino sand." *Géotechnique*, 46(1), 115-131.

Bolton, M. D. (1987). "Discussion: The strength and dilatancy of sands." *Géotechnique*, 37(2), 219-226.

Bolton, M. D., Nakata, Y., and Cheng, Y. P. (2008). "Micro- and macro-mechanical behaviour of DEM crushable materials." *Géotechnique*, 58(6), 471-480.

Bowman, E. T., Soga, K., and Drummond, W. (2001). "Particle shape characterisation using Fourier descriptor analysis." *Géotechnique*, 51(6), 545-554.

Cabalar, A. F., Dulundu, K., and Tuncay, K. (2013). "Strength of various sands in triaxial and cyclic direct shear tests." *Engineering Geology*, 156, 92-102.

Cavarretta, I., O'Sullivan, C., and Coop, M. (2010). "The influence of particle characteristics on the behaviour of coarse grained soils." *Géotechnique*, 60(6), 413-423.

Chandan, C., Sivakumar, K., Masad, E., and Fletcher, T. (2004). "Application of imaging techniques to geometry analysis of aggregate particles." *Journal of Computing in Civil Engineering*, 18(1), 75-82.

Chapuis, R. P. (2012). "Estimating the in situ porosity of sandy soils sampled in boreholes." *Engineering Geology*, 141-142, 57-64.

Cho, G.-C., Dodds, J., and Santamarina, J. C. (2006). "Particle shape effects on packing density, stiffness, and strength: Natural and crushed sands." *J. Geotech. Geoenviron. Eng.*, 132(5), 591-602.

Chuhan, F. A., Kjeldstad, A., Bjorlykke, K., and Hoeg, K. (2002). "Porosity loss in sand by grain crushing—experimental evidence and relevance to reservoir quality." *Marine and Petroleum Geology*, 19(1), 39-53.

Chuhan, F. A., Kjeldstad, A., Bjorlykke, K., and Hoeg, K. (2003). "Experimental compression of loose sands: relevance to porosity reduction during burial in sedimentary basins." *Canadian Geotechnical Journal*, 40(5), 995-1011.

Cleveland, W. S., and Devlin, S. J. (1988). "Locally weighted regression: an approach to regression analysis by local fitting." *Journal of the American Statistical Association*, 83(403), 596-610.

Coop, M., and Lee, I. K. "The behaviour of granular soils at elevated stresses." *Proc., Predictive soil mechanics, proceedings of the wroth memorial symposium*, Thomas Telford, London 186-199.

Cox, E. A. (1927). "A method of assigning numerical and percentage values to the degree of roundness of sand grains." *Journal of Paleontology*, 1(3), 179-183.

Cubrinovski, M., and Ishihara, K. (2002). "Maximum and minimum void ratio characteristics of sands." *Soils and Foundations*, 42(6), 65-78.

Curray, J. R. (1956). "The analysis of two-dimensional orientation data." *Journal of Geology*, 64(2), 117-131.

Dafalias, Y. F., Papadimitriou, A. G., and Li, X. S. (2004). "Sand plasticity model accounting for inherent fabric anisotropy." *Journal of Engineering Mechanics*, 130(11), 1319-1333.

DeBeer, E. E. (1963). "The scale effect in the transposition of the results of deep sounding tests on the ultimate bearing capacity of piles and caisson foundations." *Géotechnique*, 13(1), 39-75.

DeJong, J. T., and Christoph, G. G. (2009). "Influence of particle properties and initial specimen state on one-dimensional compression and hydraulic conductivity." *Journal of Geotechnical and Geoenvironmental Engineering*, 135(3), 449-454.

Dickin, E. A. (1973). *Influence of grain shape and size upon the limiting porosities of sands*, ASTM, West Conshohocken, PA.

Edil, T., Krizek, R., and Zelasko, J. "Effect of grain characteristics on packing of sands." *Proceedings of Istanbul Conference on Soil Mechanics and Foundation Engineering*, Istanbul Technical University, 46-54.

Efron, B. & Tibshirani, R. J. (1993). An introduction to the bootstrap. New York, USA: Chapman and Hall/CRC.

Eisma, D. (1965). "Eolian sorting and roundness of beach and dune sands." *Netherlands Journal of Sea Research*, 2(4), 541-555.

Ezaoui, A., and Benedetto, H. D. (2009). "Experimental measurements of the global anisotropic elastic behaviour of dry Hostun sand during triaxial tests, and effect of sample preparation." *Géotechnique*, 59(7), 621-635.

Ferellec, J.-F., and McDowell, G. R. (2010). "A method to model realistic particle shape and inertia in DEM." *Granular Matter*, 12(5), 459-467.

Fletcher, T., Chandan, C., Masad, E., and Sivakumar, K. (2003). "Aggregate imaging system for characterizing the shape of fine and coarse aggregates." *Transportation Research Record: Journal of the Transportation Research Board*, 1832, 67-77.

Fonseca, J., O'Sullivan, C., Coop, M. R., and Lee, P. D. (2013). "Quantifying the evolution of soil fabric during shearing using directional parameters." *Géotechnique*, 63(6), 487-499.

Frossard, E. (1979). "Effect of sand grain shape on interparticle friction; indirect measurements by Rowe's stress dilatancy theory." *Géotechnique*, 29(3), 341-350.

Fu, P., and Dafalias, Y. F. (2010). "Fabric evolution within shear bands of granular materials and its relation to critical state theory." *International Journal for Numerical and Analytical Methods in Geomechanics*, 35(18), 1918-1948.

Galindo-Torres, S. A., and Pedroso, D. M. (2010). "Molecular dynamics simulations of complex-shaped particles using Voronoi-based spheropolyhedra." *Physical Review E*, 81(6), 061303.

Gander, W., Golub, G. H., and Strebel, R. (1994). "Least-squares fitting of circles and ellipses." *BIT Numerical Mathematics*, 34(4), 558-578.

Gao, Z., and Zhao, J. (2012). "Efficient approach to characterize strength anisotropy in soils." *Journal of Engineering Mechanics*, 138(12), 1447-1456.

Gao, Z., Zhao, J., and Yao, Y. (2010). "A generalized anisotropic failure criterion for geomaterials." *International Journal of Solids and Structures*, 47(22-23), 3166-3185.

Georgiannou, V. N., and Konstadinou, M. (2013). "Torsional shear behavior of anisotropically consolidated sands." Journal of Geotechnical and Geoenvironmental Engineering, 140(2), 1-14.

Guo, P. (2008). "Modified direct shear test for anisotropic strength of sand." *Journal of Geotechnical and Geoenvironmental Engineering*, 134(9), 1311-1318.

Guo, P., and Su, X. (2007). "Shear strength, interparticle locking, and dilatancy of granular materials." *Canadian Geotechnical Journal*, 44(5), 579-591.

ISO (2008). "*ISO 9276-6:2008: Representation of results of particle size analysis – Part 6: Descriptive and quantitative representation of particle shape and morphology*." Geneva, Switzerland: ISO.

Haar, A. (1910). "Zur theorie der orthogonalen functionensysteme." *Mathematische Annalen*, 69(3), 331–371.

Hardin, B. O. (1985). "Crushing of soil particles." *Journal of Geotechnical Engineering*, 111(10), 1177-1192.

Hendron, A. J. (1963). "The behavior of sand in one-dimensional compression." Ph.D dissertation., University of Illinois at Urbana-Champaign, Urbana. Ill.

Herle, I., and Gudehus, G. (1999). "Determination of parameters of a hypoplastic constitutive model from properties of grain assemblies." *Mechanics of Cohesive-frictional Materials*, 4(5), 461-486.

Holland, P. W., and Welsch, R. E. (1977). "Robust regression using iteratively reweighted least-squares." *Communications in Statistics - Theory and Methods*, A6(9), 813 - 827.

Holubec, I., and D'Appolonia, E. (1973). "Effect of particle shape on the engineering properties of granular soils." *Proceedings of Evaluation of Relative Density and its Role in Geotechnical Projects Involving Cohesionless Soils*, ASTM International, 304-315.

Hryciw, R. D., Zheng, J., and Shetler, K. (2016). "Particle roundness and sphericity from images of assemblies by chart estimates and computer methods." *J. Geotech. Geoenviron. Eng.*, 1-15.

Jewell, R. A. (1989). "Direct shear tests on sand." *Géotechnique*, 39(2), 309-322.

Kandasami, R., and Murthy, T. (2014). "Effect of particle shape on the mechanical response of a granular ensemble." *Proceedings of international symposium on geomechanics from micro to macro*, Taylor & Francis Group, London, UK, 1093-1098.

Kloss, C., Goniva, C., Hager, A., Amberger, S., and Pirker, S. (2012). "Models, algorithms and validation for opensource DEM and CFD-DEM." *Progress in Computational Fluid Dynamics, An International Journal*, 12(2/3), 140-152.

Koerner, R. M. (1969). "Limiting density behavior of quartz powders." *Powder Technology*, 3(1), 208-212.

Kokusho, T., Hara, T., and Hiraoka, R. (2004). "Undrained Shear Strength of Granular Soils with Different Particle Gradations." *Journal of Geotechnical and Geoenvironmental Engineering*, 13(6), 621–629.

Krumbein, W. C. (1941). "Measurement and geological significance of shape and roundness of sedimentary particles." *Journal of Sedimentary Petrology*, Vol. 11(2), 64-72.

Krumbein, W. C., and Sloss, L. L. (1951). *Stratigraphy and sedimentation*, W.H. Freeman and Company, San Francisco.

Kumar, J., and Madhusudhan, B. N. (2012). "Dynamic properties of sand from dry to fully saturated states." *Géotechnique*, 62(1), 45-54.

Kuo, C. Y., Frost, J., Lai, J., and Wang, L. (1996). "Three-dimensional image analysis of aggregate particles from orthogonal projections." *Transportation Research Record: Journal of the Transportation Research Board*, 1526, 98-103.

Kuo, C. Y., Frost, J. D., and Chameau, J. L. A. (1998). "Image analysis determination of stereology based fabric tensors." *Géotechnique*, 48(4), 515-525.

Kuo, C.-Y., and Freeman, R. (2000). "Imaging indices for quantification of shape, angularity, and surface texture of aggregates." *Transportation Research Record: Journal of the Transportation Research Board*, 1721, 57-65.

Lade, P. V. (2008). "Failure criterion for cross-anisotropic soils." *Journal of Geotechnical and Geoenvironmental Engineering*, 134(1), 117-124.

Lee, I. K., and Seed, H. B. (1967). "Drained strength characteristics of sands." *journal of The Soil Mechanics and Foundation Division*, 93(SM6), 17 - 141.

Li, B., Zeng, X., and Ming, H. "Seismic response of retaining wall with anisotropic backfills." *Proceedings of Earth Retention Conference (ER) 2010, Geotechnical Special Publication*, 688-695.

Li, X. S., and Dafalias, Y. F. (2002). "Constitutive modeling of inherently anisotropic sand behavior." *Journal of Geotechnical and Geoenvironmental Engineering*, 128(10), 868-880.

Lin, X., and Ng, T. T. (1997). "A three-dimensional discrete element model using arrays of ellipsoids." *Géotechnique*, 47(2), 319-329.

Lings, M. L., and Dietz, M. S. (2004). "An improved direct shear apparatus for sand." *Géotechnique*, 54(4), 245-256.

Mahmoud, E., Gates, L., Masad, E., Erdoğan, S., and Garboczi, E. (2010). "Comprehensive evaluation of AIMS texture, angularity, and dimension measurements." *Journal of Materials in Civil Engineering*, 22(4), 369-379.

Mahmoud, E., and Masad, E. (2007). "Experimental methods for the evaluation of aggregate resistance to polishing, abrasion, and breakage." *Journal of Materials in Civil Engineering*, 19(11), 977-985.

Majumdar, A., and Bhushan, B. (1990). "Role of fractal geometry in roughness characterization and contact mechanics of surfaces." *Journal of Tribology*, 112(2), 205-216.

Margolis, S. V., and Krinsley, D. H. (1974). "Processes of formation and environmental occurrence of microfeatures on detrital quartz grains." *American Journal of Science*, 274(5), 449-464.

Masad, E., Al-Rousan, T., Button, J., Little, D., and Tutumluer, E. (2007). "Test methods for characterizing aggregate shape texture, and angularity." *National Cooperative Highway Research Program Report 555. Washington, D.C., USA: Transportation Research Board.*

Masad, E., Tashman, L., Somedavan, N., and Little, D. (2002). "Micromechanics-based analysis of stiffness anisotropy in asphalt mixtures." *Journal of Materials in Civil Engineering*, 14(5), 374-383.

Matsushima, T., Katagiri, J., Uesugi, K., Tsuchiyama, A., and Nakano, T. (2009). "3D shape characterization and image-based DEM simulation of the lunar soil simulant FJS-1." *Journal of Aerospace Engineering*, 22(1), 15-23.

MathWorks (2016). MATLAB image processing toolbox. See http://www.mathworks.com=products=image. (accessed 23/09/2016).

Mehring, J. L., and McBride, E. F. (2007). "Origin of modern quartzarenite beach sands in a temperate climate, Florida and Alabama, USA." *Sedimentary Geology*, 201(3-4), 432-445.

Mesri, G., and Vardhanabhuti, B. (2009). "Compression of granular materials." *Canadian Geotechnical Journal*, 46(4), 369-392.

Mitchell, J. K., and Soga, K. (2005). *Fundamentals of soil behavior, 3rd edn*, Wiley, New York, USA.

Miura, N., Murata, H., and Yasufuku, N. (1984). "Stress-strain characteristics of sand in a particle-crushing region." *Soils and Foundations*, 24(1), 77-89.

Moroto, N., and Ishii, T. (1990). "Shear strength of uni-sized gravels under triaxial compression." *Soils and foundations*, 30(2), 23-32.

Mustoe, G. G. W., and Miyata, M. (2001). "Material flow analyses of noncircular-shaped granular media using discrete element methods." *Journal of Engineering Mechanics*, 127(10), 1017-1026.

Nakata, Y., Hyodo, M., Hyde, A. F. L., Kato, Y., and Murata, H. (2001a). "Microscopic particle crushing of sand subjected to high pressure one-dimensional compression." *Soils and Foundations*, 41(1), 69-82.

Nakata, Y., Kato, Y., Hyodo, M., Hyde, A. F. L., and Murata, H. (2001b). "One-dimensional compression behaviour of unuformly granded sand related to single particle crushing strength." *Soils and Foundations*, 41(2), 39-51.

Ng, T.-T. (2009). "Particle shape effect on macro- and micro-behaviors of monodisperse ellipsoids." *International Journal for Numerical and Analytical Methods in Geomechanics*, 33(4), 511-527.

Oda, M. (1972). "Initial fabrics and their relations to mechanical properties of granular material." *Soils and Foundations*, 12(1), 17-36.

Oda, M. (1981). "Anisotropic strength of cohesionless sands." *Journal of the Geotechnical Engineering Division*, 107(9), 1219-1231.

Oda, M., Koishikawa, I., and Higuchi, T. (1978). "Experimental study of anisotropic shear strength of sand by plane strain test." *Soils and Foundations*, 18(1), 25-38.

Oda, M., and Nakayama, H. (1989). "Yield function for soil with anisotropic fabric." *Journal of Engineering Mechanics*, 115(1), 89-104.

Ohm, H.-S., and Hryciw, R. D. (2013). "Translucent segregation table test for sand and gravel particle size distribution." *Geotechnical Testing Journal*, 36(4), 592–605.

Ohm, H.-S., and Hryciw, R. D. (2014). "Size distribution of coarse-grained soil by sedimaging." *Journal of Geotechnical and Geoenvironmental Engineering*, 140(4), 1-9.

Otsubo, M., O'sullivan, C., Sim, W., and Ibraim, E. (2015). "Quantitative assessment of the influence of surface roughness on soil stiffness." *Géotechnique*, 65(8), 694–700.

Ouadfel, H., and Rothenburg, L. (2001). "`Stress–force–fabric' relationship for assemblies of ellipsoids." *Mechanics of Materials*, 33(4), 201-221.

Parker, G. (2008). "Sedimentation Engineering: Theory, Measurements, Modeling and Practice." ASCE Manuals and Reports on Engineering Practice No. 110, 165–251.

Pestana, J. M., and Whittle, A. J. (1995). "Compression model for cohesionless soils." *Géotechnique*, 45(4), 611-631.

Plimpton, S. (1995). "Fast parallel algorithms for short-range molecular dynamics." *Journal of Computational Physics*, 117(1), 1-19.

Potyondy, D. O. "The bonded-particle model as a tool for rock mechanics research and application: current trends and future directions." *Proc., the 7th Asian Rock Mechanics Symposium / 2012 ISRM Regional Symposium*, Korean Society for Rock Mechanics, 73-105.

Pournin, L., Weber, M., Tsukahara, M., Ferrez, J. A., Ramaioli, M., and Liebling, T. M. (2005). "Three-dimensional distinct element simulation of spherocylinder crystallization." *Granular Matter*, 7(2-3), 119-126.

Powers, M. C. (1953). "A new roundness scale for sedimentary particles." *Journal of Sedimentary Petrology*, 23(2), 117–119.

Price, M., Murariu, V., and Morrison, G. "Sphere clump generation and trajectory comparison for real particles." *Proc., Discrete Element Methods 2007 Conference*, 1-8.

Rahim, A. (1989). "Effect of morphology and mineralogy on compressibility of sands." Ph.D. dissertation, Indian Institute of Technology Kanpur, Kanpur, India.

Rao, C., and Tutumluer, E. (2000). "Determination of volume of aggregates: new image-analysis approach." *Transportation Research Record: Journal of the Transportation Research Board*, 1721, 73-80.

Raschke, S. A., and Hryciw, R. D. (1997). "Vision cone penetrometer for direct subsurface soil observation." *Journal of Geotechnical and Geoenvironmental Engineering*, 123(11), 1074-1076.

Riley, N. A. (1941). "Projection sphericity." *SEPM Journal of Sedimentary Research*, 11(2), 94-97.

Roberts, J. E. (1964). "Sand compression as a factor in oil field subsidence."PhD thesis, Massachusetts Insitute of Technology.

Roberts, J. E., and De Souza, J. M. (1958) "The compressibility of sands." *Proceedings of, the American Society for Testing and Materials*, 1269-1272.

Rodriguez, J. M., Johansson, J. M. A., and Edeskar, T. "Particle shape determination by two-dimensional image analysis in geotechnical engineering." *Proceedings of Nordic conference on soil mechanics and geotechnics*, Danish Geotechnical Society.

Rodriguez, N. M., and Lade, P. V. (2013). "Effects of principal stress directions and mean normal stress on failure criterion for cross-anisotropic sand." *Journal of Engineering Mechanics*, 139(11), 1592-1601.

Rosin, P., and Rammler, E. (1933). "The laws governing the fineness of powdered coal." *Journal of the Institute of Fuel*, 7, 29–36.

Rousé, P. C., Fannin, R. J., and Shuttle, D. A. (2008). "Influence of roundness on the void ratio and strength of uniform sand." *Géotechnique*, 58(3), 227-231.

Saadeh, S., Masad, E., and Little, D. (2007). "Characterization of asphalt mix response under repeated loading using anisotropic nonlinear viscoelastic-viscoplastic model." *Journal of Materials in Civil Engineering*, 19(10), 912-924.

Sagga, A. M. S. (1993). "Roundness of sand grains of longitudinal dunes in saudi arabia." *Sedimentary Geology*, 87(1-2), 63-68.

Santamarina, J. C., and Cho, G. C. "Soil behaviour: the role of particle shape." *Proceedings of Advances in Geotechnical Engineering: The Skempton Conference*, Thomas Telford, London, 604–617.

Satake, M. "Fabric tensor in granular materials." *Proceedings of IUTAM Symposium on Deformation and Failure of Granular Materials*, Balkema, 63–68.

Shahanazari, H., and Rezvani, R. (2013). "Effective parameters for the particle breakage of calcareous sands: An experimental study." *Engineering Geology*, 159, 98-105.

Shin, H., and Santamarina, J. C. (2013). "Role of particle angularity on the mechanical behavior of granular mixtures." *Journal of Geotechnical and Geoenvironment Engineering*, 139(2), 353-355.

Sladen, J. A., D'Hollander, R. D., and Krahn, J. (1985). "The liquefaction of sands, a collapse surface approach." *Canadian Geotechnical Journal*, 22(4), 564-578.

Sneed, E. D., and Folk, R. L. (1958). "Pebbles in the lower Colorado River, Texas: A study of particle morphogenesis." *Journal of Geology*, 66(2), 114-150.

Sukumaran, B., and Ashmawy, A. K. (2001). "Quantitative characterization of the geometry of discrete particles." *Géotechnique*, 51(7), 619-627.

Sukumaran, B., and Ashmawy, A. K. (2003). "Influence of inherent particle characteristics on hopper flow rate." *Powder Technology*, 138(1), 46-50.

Sully, J. P., and Campanella, R. G. (1995). "Evaluation of in situ anisotropy from crosshole and downhole shear wave velocity measurements." *Géotechnique*, 45(2), 227-238.

Taghavi, R. "Automatic clump generation based on mid-surface." *Proceedings of the 2nd International FLAC/DEM Symposium*, Minneapolis: Itasca International Inc., 791-797.

Tashman, L., Masad, E., Zbib, H., Little, D., and Kaloush, K. (2005). "Microstructural viscoplastic continuum model for permanent deformation in asphalt pavements." *Journal of Engineering Mechanics*, 131(1), 48-57.

Tatsuoka, F., Sakamoto, M., Kawamura, T., and Fukushima, S. (1986). "Strength and deformation characteristics of sand in plane strain compression at extremely low pressures." *Soils and Foundations*, 26(1), 65-84.

Thomann, T. G. (1990). "Stiffness and strength changes in cohensionless soils due to stress history and dynamic disturbance." PhD Thesis, University of Michigan, Ann Arbor.

Tickell, F. G. (1931). *The examination of fragmental rocks.*, Stanford University Press, Stanford, California, USA.

Tong, Z., Fu, P., Zhou, S., and Dafalias, Y. F. (2014). "Experimental investigation of shear strength of sands with inherent fabric anisotropy." *Acta Geotechnica*, 9(2), 257-275.

Tsomokos, A., and Georgiannou, V. N. (2010). "Effect of grain shape and angularity on the undrained response of fine sands." *Canadian Geotechnical Journal*, 47(5), 539-551.

Tutumluer, E., and Pan, T. (2008). "Aggregate morphology affecting strength and permanent deformation behavior of unbound aggregate materials." *Journal of Materials in Civil Engineering*, 20(9), 617-627.

Vepraskas, M. J., and Cassel, D. K. (1987). "Sphericity and roundness of sand in coastal plain soils and relationships with soil physical properties." *Soil Science Society of America Journal*, 51(5), 1108.

Vesic, A. S., and Clough, G. W. (1968). "Behavior of granular materials under high stresses." *Journal of the Soil Mechanics and Foundations Division*, 94(SM3), 661 - 668.

Wadell, H. (1932). "Volume, shape, and roundness of rock particles." *Journal of Geology*, 40(5), 443-451.

Wadell, H. (1933). "Sphericity and roundness of rock particles." *Journal of Geology*, 41(3), 310-331.

Wadell, H. (1935). "Volume, shape, and roundness of quartz particles." *Journal of Geology*, 43(3), 250-280.

Wang, L., Park, J.-Y., and Fu, Y. (2007). "Representation of real particles for DEM simulation using X-ray tomography." *Construction and Building Materials*, 21(2), 338-346.

Wang, L., Wang, X., Mohammad, L., and Abadie, C. (2005). "Unified method to quantify aggregate shape angularity and texture using fourier analysis." *Journal of Materials in Civil Engineering*, 17(5), 498-504.

Wettimuny, R., and Penumadu, D. (2004). "Application of fourier analysis to digital imaging for particle shape analysis." *Journal of Computing in Civil Engineering*, 18(1), 2-9.

Yan, L., and Byrne, M. P. (1990). "Simulation of downhole and crosshole seismic tests on sand using the hydraulic gradient similitude method." *Canadian Geotechnical Journal*, 27(4), 441-460.

Yang, J., and Wei, L. M. (2012). "Collapse of loose sand with the addition of fines: the role of particle shape." *Géotechnique*, 62(12), 1111-1125.

Yang, L. T., Li, X., Yu, H. S., and Wanatowski, D. (2015). "A laboratory study of anisotropic geomaterials incorporating recent micromechanical understanding." *Acta Geotechnica*, 11(5), 1111-1129.

Yang, Z. X., Li, X. S., and Yang, J. (2008). "Quantifying and modelling fabric anisotropy of granular soils." *Géotechnique*, 58(4), 237–248.

Yang, Z. X., Zhu, B. T., Jardine, R. J., Tsuha, C. H. C., and Foray, P. (2010). "Sand grain crushing and interface shearing during displacement pile installation in sand." *Géotechnique*, 60(6), 469-482.

Yasin, S. J. M., and Safiullah, A. M. M. (2003). "Effect of particle characteristics on the strength and volume change behavior of sand." *Journal of Civil Engineering*, 31(2), 127-148.

Youd, T. L. (1973). "Factors controlling maximum and minimum densities of sands." *ASTM Spec. Tech. Publ., 523*, 98-112.

Yu, H., Zeng, X., Li, B., and Ming, H. (2013). "Effect of fabric anisotropy on liquefaction of sand." *Journal of geotechnical and Geoenvironmental Engineering*, 139(5), 765-774.

Zelasko, J. S., Krizek, R. J., and Edil, T. B. "Shear behavior of sands as a function of grain characteristics." *Proc., Istanbul Conference on Soil Mechanics and Foundation Engineering*, Istanbul Technical University, stanbul, Turkey., 55-64.

Zeng, X., Li, B., and Ming, H. "Effect of fabric anisotropy on seismic response of a retaining wall." *Proceedings of the 7th International Conference on Physical Modelling in Geotechnics (ICPMG 2010)*, CRC Press, 517–522.

Zhang, Y., Luo, R., and Lytton, R. L. (2011). "Microstructure-based inherent anisotropy of asphalt mixtures." *Journal of Materials in Civil Engineering*, 23(10), 1473-1482.

Zheng, J., and Hryciw, R. D. (2016). "Index void ratios of sands from their intrinsic properties." *Journal of Geotechnical and Geoenvironmental Engineering*, 142(12), 1-10.